Synthesis and Evaluation of Graphene for Polymer Electrolyte Membrane Fuel Cell Components

Submitted in partial fulfillment of the requirements for the degree of

Doctor of Philosophy

by

AVIJIT GHOSH

DEPARTMENT OF CHEMICAL ENGINEERING
INDIAN INSTITUTE OF TECHNOLOGY GUWAHATI
Guwahati – 781 039

February, 2014

Dedicated to my parents and family

Department of Chemical Engineering
Indian Institute of Technology Guwahati
Guwahati – 781 039
Assam, India

STATEMENT

I do hereby declare that the matter embedded in this thesis is the result of investigations carried out by me in the Department of Chemical Engineering, Indian Institute of Technology Guwahati, Guwahati, Assam, India, under the supervision of Dr. Anil Verma, Associate Professor, Department of Chemical Engineering, Indian Institute of Technology Guwahati, Guwahati, Assam, India.

In keeping with the general practice of reporting scientific observations, due acknowledgement has been made wherever the work described is based on the findings of other investigators.

_ _ _ _ _ _ _ _ _ _ _ _ _ _ _ _ _ _ _ _

Dated:
IIT Guwahati

(Avijit Ghosh)
Roll no. 08610710
Sustainable Environergy Electrochemical Research Group (*SEERG*)
Department of Chemical Engineering
Indian Institute of Technology Guwahati
Guwahati – 781 039

Department of Chemical Engineering
Indian Institute of Technology Guwahati
Guwahati – 781 039
Assam, India

CERTIFICATE

It is certified that the work contained in the thesis entitled "Synthesis and Evaluation of Graphene for Polymer Electrolyte Membrane Fuel Cell Components", by Mr. Avijit Ghosh, for the award of degree of Doctor of Philosophy, has been carried out under my supervision and that this work has not been submitted elsewhere for a degree.

Dated:
IIT Guwahati

_ _ _ _ _ _ _ _ _ _ _ _ _ _ _ _ _ _ _ _

Dr. Anil Verma
Associate Professor
Department of Chemical Engineering
Indian Institute of Technology Guwahati
Guwahati – 781 039

Preface

The title of this thesis, and the experimental investigations inserted in it, reflect a blend of science and engineering in the study of synthesis and performance evaluation of graphene in polymer electrolyte membrane fuel cell (PEMFC) components. The thesis provides relevant details on the development of graphene reinforced carbon-polymer composite bipolar plate and graphene as an electrocatalyst support for PEMFC. Moreover, the developed bipolar plate is evaluated for high temperature PEMFC (HT-PEMFC) applications.

The background of fuel cell, types of fuel cell, importance of PEMFC, and issues of PEMFC components are covered in the 1st chapter. However, emphasis is given on the materials development to enhance the properties of carbon-polymer composite bipolar plates as well as electrocatalyst support. The importance of graphene for these components is discussed at end of the 1st chapter.

A literature review on the graphene in composite bipolar plates and as an electrocatalyst support is included in the 2nd chapter. The literature review includes a brief discussion on the important scientific findings reported in the recent and past available literatures. The outcomes of the most significant literatures are summarized at the end of the chapter and the objective of the thesis is formulated based on the outcome of the literature review.

The 3rd chapter covers the experimental procedure for synthesis and characterize of graphene. The properties of the synthesized graphene are evaluated and discussed in this chapter.

The 4th chapter of the thesis includes the development and characterization of carbon-polymer composite bipolar plates using base compositions deduced from the literature. The effect of carbon fiber length and graphene content on the properties of carbon-polymer composite bipolar plate is discussed in this chapter. Moreover, the performance

of the developed composite bipolar plate in the PEMFC is presented at the end of the chapter.

The optimized bipolar plate is also evaluated for its potential application in HT-PEMFC. The mechanical, electrical, corrosion, and thermal properties of the developed bipolar plate are evaluated for HT-PEMFC application and discussed in the 5th chapter.

The discussion on the development and characterization of functionalized graphene are included in the 6th chapter. Materials and method to synthesis and evaluate graphene and functionalized graphene supported Pt and/or Au electrocatalysts are discussed in this chapter. Further, the performance of the developed electrocatalysts are evaluated and discussed in half-cell as well as in PEMFC at the end of the 6th chapter.

Overall conclusions of the research work are presented in the 7th chapter. Moreover, it includes the future scope of the research on the PEMFC components. The chapter will help the future researchers in formulating their research objectives to further improve the PEMFC performance as well as research pertaining to HT-PEMFC.

In the thesis, I have attempted to cover and cite all the available significant literatures relevant to the current research work. However, the off topic scientific reports are avoided carefully throughout the thesis. I have tried to organize thesis in such a manner so that it may depict a clear picture to the reader on the development and characterization of graphene to evaluate in carbon-polymer composite bipolar plates as well as an electrocatalyst support material for PEMFC.

– – – – – – – – – – – – – – – – – – –

Avijit Ghosh
Guwahati –781 039

Acknowledgements

It is my pleasure to thank those who made this thesis possible. I recollect numerous occasions and moments, which make me proud to be a part of this world class centre of excellence. It is my privilege to be amidst some intellectual genius, who guided in my pursuit of knowledge. I owe my deepest gratitude to all of them.

The first and foremost appreciation goes to my supervisor Dr. Anil Verma for his invaluable support and undaunted encouragement, throughout the research work. I appreciate his moral support and guidance from the very early stage of this research to develop an understanding of the subject as well as giving me extraordinary experiences throughout the work. I especially enjoyed his style of mentoring students from which I have benefited greatly in my professional and personal growth. I believe it will always remain with me in my future life. This thesis would not have been possible unless his guidance and enormous assistance.

I would like to thank my doctoral committee members, Dr. C Das, Dr. R.K. Upadhyay, and Dr. Md. Qureshi, for their insightful advices and suggestions throughout the research. I also wish to express my great appreciation to Prof. S. Basu, Head, Department of Chemical Engineering, IIT Delhi, for his beneficial advice and providing laboratory facilities for oxygen reduction reaction studies in his research lab.

I want to extent my sincere thanks to the Head of the Department of Chemical Engineering and also to the faculty members for their constant inspiration and valuable suggestions. The kind and constant help of the staff members of the department is also duly acknowledged. My sincere thanks go to Head, Centre for Energy, for moral support and inspiration. I would also like to convey my sincere thanks to the Head of Central Instruments Facility (CIF), IIT Guwahati, for providing me the analytical facilities such as SEM, FESEM, TEM, and Raman. My sincere thanks go to Chandan Borgohain, Dr. Kula

Kamal Senapati, and Madhurjya Borah for their help in using the analytical facilities of CIF.

I extend my sincere thanks go to Dr. Biraj, Dr. Pradip, Dr. Mehabub, Dr. Somen, Sahu, and Kaushik for helping me many times in different ways. Moreover, I am lucky enough to get very good lab-mates like Leela, Surya, Shyam, and Lepakshi and I acknowledge their constant encouragement and help during the course of the research. I would also like to acknowledge the nice company of Deepak, Srinath, Rajamahendar, Anisha, and Husen for their day to day support in the various activities of our research lab, Sustainable Environergy Electrochemical Research Group (*SEERG*).

I gratefully acknowledge the financial support of the Council of Scientific and Industrial Research (CSIR), Government of India, for providing senior research fellowship throughout my research work (Project number: 22(0498)/10/EMR-II).

At last but not least, I am highly indebted to my family members, whose support has been invaluable to me. Their constant inspiration and guidance kept me focused and motivated. Moreover, my Ph.D endeavor could not be completed without the endless love, unending support, and wishing from my wife, Ms. Rumpa. My heartfelt love and appreciation to my son Anurit for bearing with me last one year. My sincere apology goes to all of those to whom I forget to mention but helped me at any part of the research work.

– – – – – – – – – – – – – – – – – – –

Avijit Ghosh

Guwahati – 7810 39

Abstract

Polymer electrolyte membrane fuel cell (PEMFC) is one of the challenging energy conversion devices for transportation and distributed power generation systems due to its attractive features such as high power density, low operating temperature, minimal emissions, negligible noise, and high efficiency. The material selection plays a pivotal role on the performance of a fuel cell. Therefore, number of materials has been investigated in recent past for the development of efficient PEMFC components. The carbon is the key material for PEMFC component due to its unique electrical and structural properties. Carbon is used to develop various components of the PEMFC such as bipolar plate, carbon paper (gas diffusion layer), microporous layer, and electrocatalst support. The success of the PEMFC technology is largely influenced by bipolar plate as well as electrocatalyst support apart from other components.

The development of carbon-polymer composite bipolar plates for PEMFC is an important research area for materials scientists owing to its low density, good corrosion resistance, good flexibility, and ease in machining or in-situ molding of flow fields during processing as compared to pure graphite and metal. The natural graphite (NG) generally is used as primary reinforcement for polymer composite. However, the NG/polymer composite bipolar plate does not possess the properties suggested by various organizations (e.g., DoE and Plug Power Inc.). Therefore, researchers and scientists are using different type of reinforcements such as carbon black (CB) and carbon fiber (CF) into the NG/polymer composite to enhance the properties of bipolar plate. It is reported that the overall properties of NG/polymer composites are increased owing to incorporation of small amount of CB in expense of NG. However, the mechanical strength and through-plane electrical conductivity of the composite bipolar plate do not meet the stringent target. Moreover, it is found that the mechanical strength significantly improves due to the reinforcement of small amount of CF in to the CB/NG/polymer composite in expense of NG content. However, still the properties do not reached upto the required level of

stringent target. Therefore, in order to further improve the properties, the establishment of graphene (GP) nanomaterial opened up new avenues due to its highest electrical conductivity (around 10^6 $S \cdot cm^{-1}$), high thermal conductivity (5000 $W \cdot m^{-1} \cdot K^{-1}$), very good mechanical strength (100-200 times stronger than steel), and very high theoretical surface area (around 2630 $m^2 \cdot g^{-1}$). These salient features of graphene have attracted researchers across the globe to study its potential use in a variety of applications including fuel cell.

The graphene is being investigated as reinforcement in to the carbon-polymer composite bipolar plate to improve the overall properties according to US department of energy (DoE) target. Moreover, the graphene is used as an electrocatalyst support to enhance the electrochemical activity of PEMFC electrocatalyst. The aim of this research is to develope graphene reinforced efficient carbon-polymer composite bipolar plate and graphene supported electrocatalyst for PEMFC.

Monolayer graphene is synthesized by chemical oxidation followed by thermal exfoliation of NG. The synthesized graphene is characterized by XRD, Raman, AFM, FTIR, and BET. The absence of graphite C(002) and C(004) peaks in the diffractogram shows that monolayer graphene is formed, which is also confirmed by Raman analysis. The synthesis of monolayer graphene is further confirmed by XRD, Raman, FE-SEM, and TEM analyses. The thickness (around 0.5 nm) of the graphene is measured by AFM analysis.

The developed graphene (GP) is used as reinforcement along with NG, CB, and CF at various length to develop carbon-polymer composite bipolar plate. The three type of thermoset polymers such as novolac phenol formaldehyde resin (NPFR), resole phenol formaldehyde resin (RPFR), and vinyl ester resin (VER), are used as binder or matrix to fabricate composite bipolar plates using compression molding techniques. The CF/CB/NG/polymer composite bipolar plates are developed and characterized to find out

the optimum CF length. Similarly, the effects of GP content on the properties of the CF(1mm)/CB/NG/polymer composite bipolar plates are also studied. The developed bipolar plates are characterized thoroughly for flexural strength, deflation at mid-span, shore hardness, in-plane electrical conductivity, through-plane electrical conductivity, thermal conductivity, hydrogen permeability, corrosion resistance, and interfacial electrical contact resistance (ICR). It is observed that most of the properties of the CF(1mm)/CB/NG/polymer composite bipolar plates, at the optimum composition are within the stringent target. However, flexural strength, through-plane electrical conductivity, and interfacial electrical contact resistance are not achieved by the above composition. Therefore, the above compositions are used for further study to improve the desired performance. In this effort, a small amount of NG is replaced with the synthesized GP expecting to achieve the properties with the aim not to hamper the other properties. The flexural strengths of the GP reinforced composite bipolar plates, at the optimum compositions, are 63.56, 60.05, and 61.41 MPa, respectively for NPFR, RPFR, and VER polymer based composites. The in-plane electrical conductivities of the graphene reinforced composites (GP/CF(1mm)/CB/NG/polymer) are recorded as 319.42, 438.67, and 388.46 $S \cdot cm^{-1}$, respectively for NPFR, RPFR, and VER polymers. The through-plane electrical conductivities of these composites are 113.68, 139.88, 132.15 $S \cdot cm^{-1}$, respectively. The anodic and cathodic corrosion current density of the composite in simulated PEMFC environment is found to be as per stringent target for NPFR and RPFR based composite. However, the cathodic corrosion current density of VER based composite is edge above the DoE target (1.04 $\mu A \cdot cm^{-2}$ against <1 $\mu A \cdot cm^{-2}$). The hydrogen permeability of the composite is in the order of 10^{-9} $cm^3 \cdot cm^{-1} \cdot s^{-1}$ at 80°C. The ICR of the GP reinforced optimum composite bipolar plates are 14.4, 10.85, and 12.02 $m\Omega \cdot cm^2$, respectively for, NPFR, RPFR, and VER at 2 MPa applied stacking pressure. The overall properties of the graphene reinforced composite bipolar plates fulfilled almost all the stringent target values except ICR. A PEMFC setup is developed to study the

performance of the developed bipolar plates in real fuel cell. The reinforcement with 1.5% GP content into the CF(1mm)/CB/NG/polymer composite improves the peak power output of fuel cell around 12% for all the composites as compared to without GP.

The developed optimized composite bipolar plate is evaluated for high temperature PEMFC (HT-PEMFC) application. The mechanical, electrical, corrosion, and thermal characterization are investigated with an overall aim to reach stringent target for HT-PEMFC. It is observed that the flexural strength and electrical conductivity of the composites is almost stable with the increase in temperature up to 175°C. The flexural strength and shore hardness of the developed composite are around 56.42 MPa and 60, respectively, at 175^{o}C, and on further increase in the temperature the mechanical strengths deceases sharply. The composite bipolar plate maintained high in-plane and through-plane electrical conductivities, which is about 409.23 S·cm^{-1} and 98 S·cm^{-1} respectively, at 175°C.

The functionalized graphene (FGP) is prepared by chemical treatment of the synthesized GP to enhance the interaction between GP and Pt particles. The Pt/GP (20wt.%) and Pt/FGP (20wt.%) electrocatalyst is prepared by $NaBH_4$ reduction techniques. The prepared electrocatalyst is characterized for particle size using XRD, FE-SEM, TEM, oxygen reduction reaction (ORR), hydrogen adsorption desorption (HAD), and electrochemical stability using cyclic voltammetry. The Pt/FGP electrocatalyst shows the higher electrochemical activities (ORR and HAD) as compared to Pt/GP and commercial Pt/C. Therefore, FGP is used for further study and reduce the use of Pt loading. Thus, bimetallic PtAu/FGP electrocatalyst is developed and the properties are compared with Au/FGP electrocatalyst. The developed PtAu/FGP shows higher ORR activity as compared to Pt/FGP. The long term electrochemical stability of the developed electrocatalyst (Pt/GP, Pt/FGP, and PtAu/FGP) is significantly higher than the commercial Pt/C. The membrane electrode assembly is developed using the catalysts

and tested in a PEMFC. The maximum power density are obtained 314, 426, 455, and 411 $mW \cdot cm^{-2}$, using Pt/C, Pt/GP, Pt/FGP, and PtAu/FGP, respectively.

Keywords: *Bipolar plate; Cyclic voltammetry; Electrocatalyst support; Graphene; HT-PEMFC; PEMFC*

Contents

List of Tables

List of Figures

List of Symbols

°	bulk density ($g \cdot cm^{-3}$)
w	weight (g)
l	length (cm)
b	breadth (cm)
d	thickness (cm)
F	load (N)
L	support span distance (mm)
w	width (mm)
d	depth (mm)
D	maximum deflection at the center (mm)
±	electrical conductivity ($S \cdot cm^{-1}$)
I	current (A)
x	distance between two points (cm)
V	voltage (V)
A	area (cm^2)
q	heat flux ($W \cdot m^{-2}$)
T	temperature (K)
k	thermal conductivity ($W \cdot m^{-1} \cdot K^{-1}$)
¨	amount of hydrogen (cm^3)
ψ	gas permeability constant ($cm^3 \cdot cm^{-1} \cdot s^{-1}$)
t	time (s)
E	electrode potential (V)
i	current density ($A \cdot cm^{-2}$)

$i_\circ$	exchange current density ($A \cdot cm^{-2}$)
E_{corr}	corrosion potential (V)
$E_\circ$	equilibrium potential (V)
b_a	anodic Tafel constant ($V \cdot decade^{-1}$)
b_c	cathodic Tafel constant ($V \cdot decade^{-1}$)
i_{corr}	corrosion current ($A \cdot cm^{-2}$)
P	pressure (MPa)
q_{pt}	hydrogen adsorption charge ($\mu C \cdot cm^{-2}$)

List of Abbreviations

AFC	alkaline fuel cell
AFM	atomic force microscope
BET	Brunauer–Emmett–Teller
BMC	bulk molding compound
CA	citric acid
CB	carbon black
CCD	charge-coupled devices
CF	carbon fiber
CNT	carbon nanotube
CPB	composite bipolar plate
CP	carbon paper
CRPFR	cured resole phenol formaldehyde resin
CV	cyclic voltammetry
DMFC	direct methanol fuel cell
DMF	dimethylformamide
EDX	energy dispersive X-ray spectroscopy
EG	expanded graphite
EOR	ethanol oxidation reaction
ESA	electrochemical surface area
FE-SEM	field emission scanning electron microscopy
FTIR	Fourier transform infra-red
GDL	gas diffusion layer
GP	graphene
FGP	functionalized graphene

GO	graphite oxide
HAD	hydrogen adsorption desorption
HMTA	hexamethylene tetramine
ICR	interfacial contact resistance
LSV	linear sweep voltammetry
M	metal
MCFC	molten carbonate fuel cell
MEA	membrane electrode assembly
MOR	methanol oxidation reaction
MPL	microporous layer
MWCNT	multi-walled carbon nanotube
NG	natural graphite
NPFR	novolac phenol formaldehyde resin
ORR	oxygen reduction reaction
PA	phosphoric acid
PAFC	phosphoric acid fuel cell
PAN	polyacrylonitrile
PBI	polybenzimidazole
PDS	poly(acrylenedisulfide)
PDDA	poly(diallyldimethlammonium chloride)
PEM	proton exchange membrane
PEMFC	proton exchange membrane fuel cell
PE	polyethylene
PFSA	perfluorosulfonic acid
PF	phenol formaldehyde

PP	polypropylene
PPS	polyphenylene sulfide
PVDF	poly(vinylidene fluoride)
PNGV	new generation vehicles program
RDE	rotating disc electrode
RPFR	resole phenol formaldehyde resin
SAED	selected area electron diffraction
SEM	scanning electron microscope
SG	synthetic graphite
SHE	standard hydrogen electrode
SWCNT	single-walled carbon nanotube
TEM	transmission electron microscopy
TPB	triple phase boundary
DoE	Department of Energy, United State
VER	vinyl ester resin
XRD	X-ray diffractometer

Chapter 1

Introduction

Chapter 1

Introduction

Background of the fuel cell is discussed in this chapter with an emphasis on polymer electrolyte membrane fuel cell along with its importance and various issues.

1.1 Background

The International Energy Outlook in 2013 (IEO 2013) estimated that the global energy consumption may increase around 35% by 2040 from its current usage of 89 million barrels per day. It is predicted that 70% of this increase may come from developing nations, led by China and India. The present energy demand of the world is primarily met by the conventional fuel resources. However, the present world energy scenario reveals that within the next few decades, the world would face severe shortage of the present conventional fuel resources. Moreover, the uses of fossil fuel pose unwanted side effects to the environment such as emission of toxic and greenhouse gases (Devanathan 2008). Therefore, owing to the probable shortage of the conventional fuels, scientists and technologists are in search of non-conventional sources and efficient energy conversion devices. There are various non-conventional energy sources and a lot of research work is being carried out worldwide to make the technologies economically viable. In this aspect, fuel cell is found to be one of the most stringent and promising power conversion devices in near future (Li and Sabir 2005). Fuel cells are basically galvanic cells, which directly convert the chemical energy of a fuel into electrical energy (Li 2007).

The hydrogen is considered as an ideal fuel for fuel cells. The primary by-product of a H_2/air fuel cell is water. No air pollutants such as NO_x, SO_x, CO or particulates are produced if pure hydrogen is used. Fuel cells emit 40-60% less CO_2 than conventional

energy sources when hydrogen is reformed from carbon-based fuels (Song 2002; James and Andrew 2003). Emissions of CO_2 can be completely eliminated when hydrogen is produced using solar or wind power. The fuel cell may provide the electrical energy continuously if the fuel and oxidant is supplied continuously similar to devices using Carnot engine. However, fuel cells are not limited by thermodynamic limitations of heat engines, such as the Carnot efficiency, as the intermediate steps of producing heat and mechanical work are avoided and thus the fuel cells may generate the electrical power with high efficiency without noise (Chen 2003; Li 2007). These salient features attracted researchers, scientists, government agencies as well as industrialist to develop fuel cell systems for future energy economy.

1.2 Brief history of fuel cell

The first working concept of chemical energy to electrical energy in a primitive fuel cell was demonstrated by Sir Willam Groves in 1839 (Grove 1839). Later there have been several research attempts to develop efficient fuel cell for more than 100 years, however much success could not be achieved. Since the early applications of PEMFC in NASA's Gemini space flights in 1962 (Maget 1968; Bockris and Srinivasan 1969) followed by the new generation of vehicles program (PNGV) conducted with the joint collaboration of US Government and automobile manufacturer companies in 1993 (Costamagna and Srinivasan 2001), it has taken more than a decade to reach the demonstration or partial commercialization stage. Later, various technical and associated fundamental breakthroughs have been achieved during last decades, but many challenges such as increasing durability and reducing cost while maintaining maximum power output are still need to be overcome prior to the commercialization of PEMFC technology.

1.3 Type of fuel cells

Fuel cells are classified primarily by the kind of electrolyte they use. The type of electrolyte determines the kind of chemical reactions that take place in the cell, the catalysts required, temperature range in which the cell operates, and the fuel required among other factors. These characteristics, in turn, affect the applications for which these cells are most suitable. There are several type of fuel cells currently under development, each with its own advantages, limitations, and potential applications. Table 1.1 represents the classification of most common type of fuel cells along with their operating temperature ranges and other details. Among the various type of fuel cells, polymer electrolyte membrane fuel cell (PEMFC) offers several advantages including low temperature (around 80^{o}C) operation, rapid start-up and shut-down, higher power density, and all solid-state components. Moreover, the US-DoE (DoE) has identified PEMFC as the main candidate to replace the internal combustion engine in transportation as well as stationary applications (Barbir 2005; Hogarth and Ralph 2002). The level of interest in PEMFC is increasing continuously with the advancement of hydrogen storage solutions and involvement of high profile companies.

1.4 Polymer electrolyte membrane fuel cell and associated issues

Polymer electrolyte membrane fuel cell (PEMFC) is one of the challenging energy conversion devices for transportation and distributed power generation systems due to its attractive features such as high power density, modularity, solid state construction, low operating temperature, longer lifetime, minimal emissions, quick startup, negligible noise, and high chemical to electrical energy conversion efficiency. The PEMFC may generate power in the range of Watt to kilowatts.

Table 1.1: Details of different type of fuel cells (Larminie and Dicks 2003; DoE, 2013)

Fuel cell type	**PEMFC**	**DMFC**	**HT-PEMFC**	**AFC**	**PAFC**	**MCFC**	**SOFC**
Operating temperature (°C)	25-80	25-60	100-200	60-220	170-220	600-650	600-1000
Fuel	H_2	CH_3OH	H_2	H_2	H_2	H_2 and CH_4	H_2, CH_4, and CO
Catalyst	Pt	Pt and/or Pt-Ru	Pt	Pt	Pt	Ni	Ni
Carrier ion	H^+	H^+	H^+	OH^-	H^+	CO_3^{2-}	O^{2-}
Electrolyte	Solid polymer	Solid polymer	Solid polymer	Aqueous KOH	Aqueous H_3PO_4	Molten carbonate	Ceramic
Output Power range	Watts/kilowatts	Watts	Watts/kilowatts	Watts/kilowatts	kilowatts	kilowatts/megawatts	Megawatts
Limitations	High catalyst cost, water management, and catalyst poisoning	Low efficiency and methanol crossover	Solid polymer electrolyte and composite bipolar plate	Expensive catalyst, sensitive to poisoning, and water management	Expensive catalyst, corrosive electrolyte, and electrolyte management	Corrosive electrolyte, high cost materials, and degradation	Expensive materials and degradation
Application	Portable devices, electrical equipment, Automotive, and domestic	Vehicles, and small appliances	Portable devices, electrical equipment, automotive, and domestic	Space, military	Electrical equipment, transportation, and stationary application	Stationary and distributed power generator	Power plants, combine heat and power, and stationary.
Advantages	High power density, short start-up time, and low temperature	Short start-up time and low temperature	High CO tolerance, separate water management is not required	Low cost materials and high performance	Low cost electrolyte, long time performance, and reliable	High quality waste heat and high efficiency	High quality waste heat, fuel flexibility, and high efficiency

The major application of PEMFC is focused on transportation, because of its potential impact on the environment, such as the control of greenhouse gas emission. Figure 1.1 shows schematic representation of a single PEMFC (fig. 1.1a), whereas fig. 1.1b shows the exploded view of a PEMFC stack (two single-cells in series). It can be seen in the fig. 1.1 that PEMFC mainly consists of anode and cathode compartments separated by a proton exchange membrane (PEM). Both the compartments have similar components like monopolar plate/bipolar plate, carbon paper, and catalyst coated microporous layer (MPL) on which the catalyst is coated. The anode and cathode, both comprising of carbon paper, MPL, and catalyst layer, along with PEM is known as membrane electrode assembly (MEA) as shown in the fig. 1.1b. It may be noted that the bipolar plate accommodates both fuel and oxidant as well as connects the single-cells in series. Many cells may be stacked with the help of bipolar plate for higher power output. The anode, which provides an interface to the fuel (H_2 gas) and the electrolyte, catalyze the fuel oxidation reaction, and provides a path through which free electrons are conducted to the load via external circuit. The cathode provides an interface to the oxidant (O_2 gas) and the electrolyte, catalyze the oxygen reduction reaction. The electrolyte provides conductive path to the protons and acts as a separator between anode and cathode compartment to prevent the mixing of hydrogen and oxygen and thus preventing direct combustion. The basic principle of PEMFC is that the H_2 and O_2 electrochemically react to produce electricity along with water, and heat as by-product. The hydrogen gas is supplied to the anode side of the PEMFC, where H_2 molecule splits into two protons (H^+) and two electrons (e^-) in the presence of catalyst as shown in eq. 1.1. The monopolar plates provide a pathway through which the generated electrons are collected and conducted to cathode via external circuit through a load. Protons generated at the anode migrate to cathode through the PEM.

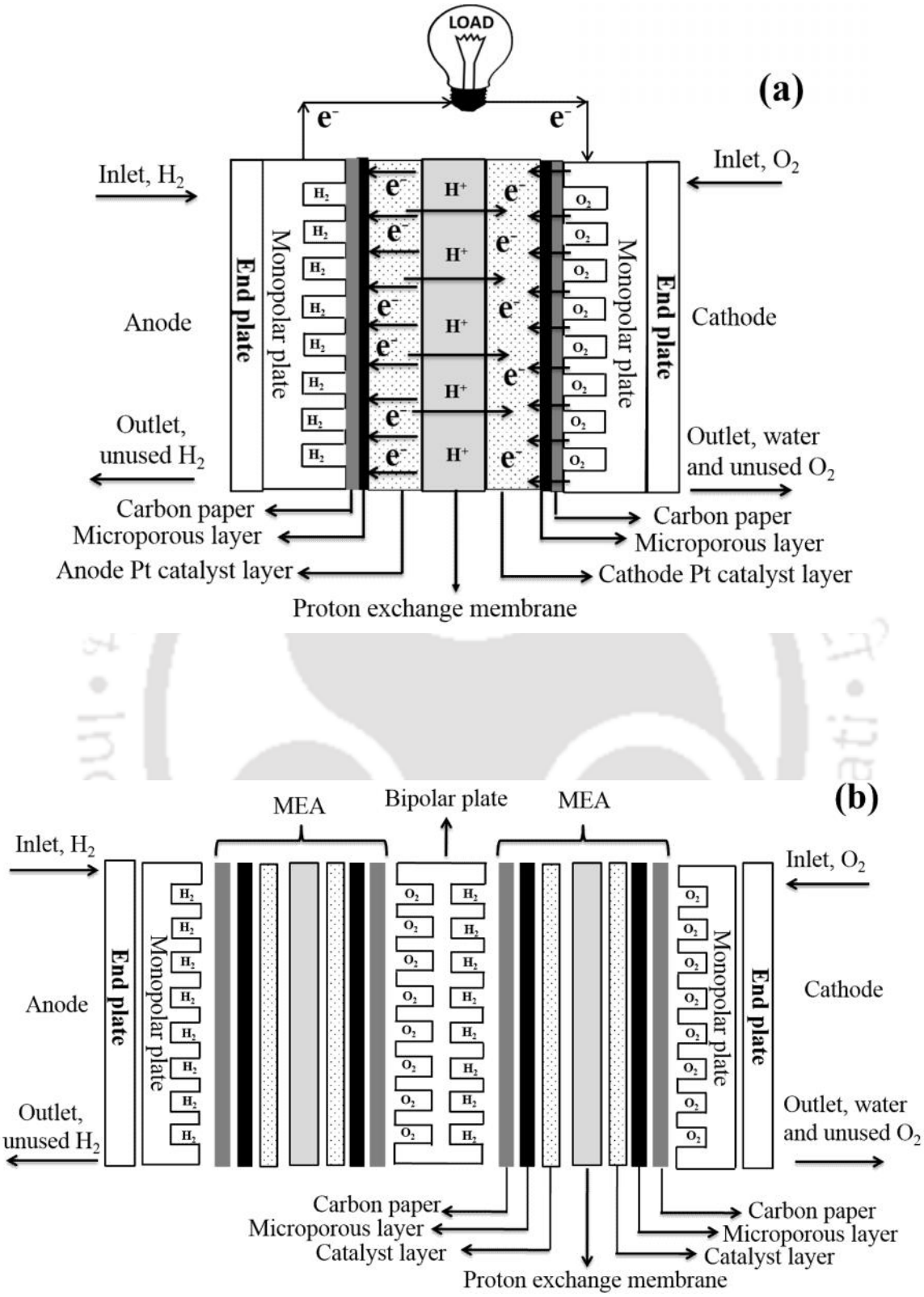

Figure 1.1: Schematic of (a) single-cell PEMFC, and (b) an exploded view of a PEMFC stack (two unit cells in series)

At cathode, the protons, electrons, and oxygen react as per eq. 1.2 to form water. The overall reaction is shown in eq. 1.3.

Anode reaction: $H_2 \rightarrow 2H^+ + 2e^-$ (1.1)

Cathode reaction: $\frac{1}{2}O_2 + 2H^+ + 2e^- \rightarrow H_2O$ (1.2)

Overall reaction: $H_2 + \frac{1}{2}O_2 \rightarrow H_2O$ (1.3)

At present, the most effective catalysts for these reactions are noble platinum metal supported on carbon. The standard Gibbs free energy of the overall reaction (considering liquid water product) is around −237.13 kJ·mol^{-1}, which corresponds to theoretical cell voltage of 1.229 V.

However, a single cell does not generate any useful power and therefore, stacking is essential. It is worth mentioning that though the fuel cells generate high currents but are very low voltage sources. Therefore, in order to have useful voltage output, the single cell PEMFCs need to be stacked in series, which generate the requirement of efficient bipolar plate. The high costs of noble metal catalyst (and durability), and lack of efficient bipolar plate are the main constraints for the world-wide commercialization of low temperature PEMFC (Pander 2009; Toyota 2009). The cost analysis of the components of a PEMFC stack is shown in the fig. 1.2. From the fig. 1.2 it can be seen that the bipolar plate is the most costly component contributing to around 38% PEMFC stack cost followed by the cost of electrodes (MPL on carbon paper), membrane, and catalysts as 32, 12, and 11%, respectively.

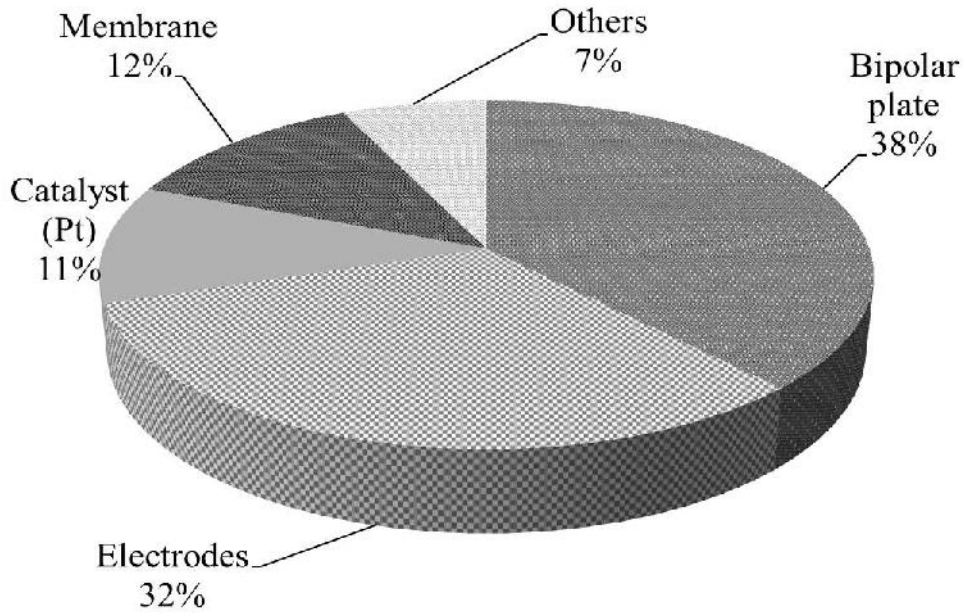

Figure 1.2: PEMFC stack cost analysis (Kamarudin et al., 2006)

Moreover, the bipolar plate is the heaviest component of the PEMFC stack having 80% weight of the stack (Kamarudin et al., 2006; Jayakumar et al., 2006). Figure 1.3 shows the time-line of PEMFC system cost along with the target cost to be achieved by 2017 (Spendelow and Jacos 2012). The fuel cell system cost involves stack cost as well as cost for balance of plant. It is targeted to achieve 30 $\$\cdot kW^{-1}$ by 2017 considering 80 kW PEMFC stack with a production of 5,00,000 units per year. This cost reduction would be achieved by advances in the science and technology using efficient and durable fuel cell components. It may be noted that various components of PEMFC contain carbon in some or the other form. Present research pattern of bipolar plate is focused on carbon-polymer composites (graphite, carbon black, carbon fiber, etc), whereas platinum catalyst is supported on carbon black (Pt/C).

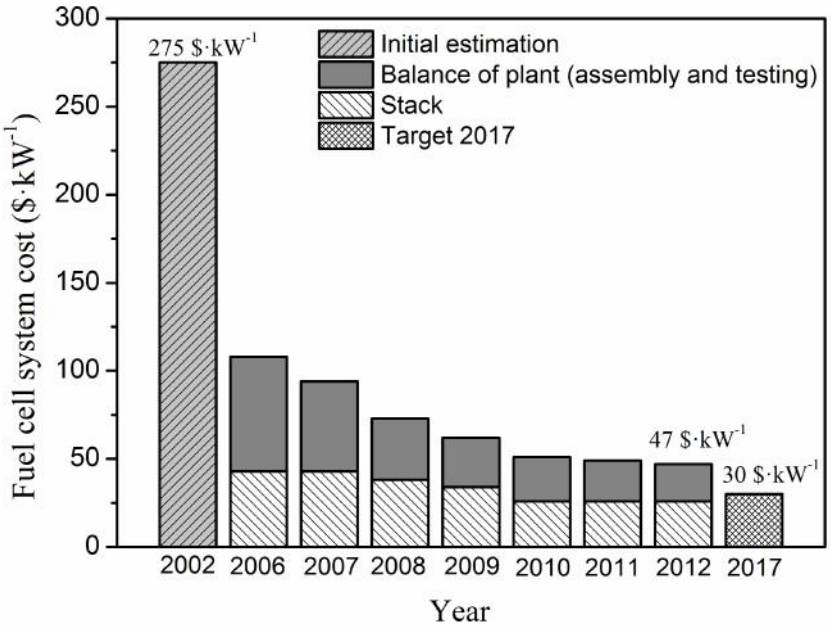

Figure 1.3: Projected cost of a 80 kW PEMFC system considering high volume manufacturing (500,000/yr) (FuelCellToday 2013)

The carbon paper and the microporous layer too contain carbon. Thus it can be understood that carbon greatly influences the performance of the PEMFC (Dicks 2006). On the other hand cost of electrocatalyst (commonly Pt-based) is very high. The Pt loading has been reduced by two orders of magnitude in the past decade and still research is going on to reduce the Pt loading by improving the properties of the electrocatalyst support material (Shao et al., 2010; Liu et al., 2010). The less durability of Pt support also hinders the long term operations (Gittleman et al., 2010). The expected lifetime of commercial fuel cell is 5,000 h for transportation and 40,000 h for stationary application with maximum 10% performance decay as projected by DoE 2015 (Borup et al., 2008; Schmittinger and Vahidi 2008). Recently, the durability of single cell was achieved over

7,500 h in laboratory scale by 3M company which make sense to meet DoE target 2015 (Papageorgopoulos 2010).

The material selection plays a pivotal role on the performance of a fuel cell as discussed in the earlier sections. Number of materials has been investigated in recent past for the development of efficient PEMFC components, on the basis of physical and electrochemical properties. In particular, electrical conductivity and excellent chemical stability in acidic and redox environment are a few of the most important requirements. It is reported that carbon in the form of its different allotropes is extremely attractive for use in the PEMFC components such as bipolar plate, microporous layer, gas diffusion layer, and electrocatalyst support, due to its high electrical conductivity and electrochemical stability in PEMFC (Hou et al., 2011; John et al., 2011; El-kharouf et al., 2012). Moreover, the establishment of graphene nanomaterial has attracted the research focus due to its unique properties.

Therefore, the researchers are attracted to study the graphene used in the manufacturing of the bipolar plate as well as an electrocatalyst support for PEMFC components to evaluate the fuel cell performance and durability.

1.5 Graphene: A potential candidate for PEMFC components

Graphene (GP) is one of the most exciting nanomaterials being explored during recent years, not only out of academic interest but also for its potential applications. Graphene is an atomically thin sp^2 hybridized 2D sheet of carbon atom, packed in a hexagonal lattice structure with a carbon-carbon bond length of 0.142 nm. The graphene is recognized as the basic building block of all graphitic materials such as 3D-graphite, 1D-carbon nanotube (CNT), and 0D-fullerene (Novoselov et al., 2004; Geim 2009). Initially, the existence of 2D crystal was assumed to be thermodynamically unstable. However, in

2004 Geim and his co-workers have established single layer 2D crystal from graphite using scotch tape method (Geim and Novoselov 2007). The carbon atoms in the graphene crystal lattice are bonded together with σ bonds, and one π electron (due to delocalized p_z orbital) is freely suspended to each of the carbon atoms that contribute to a delocalized network of electrons (Zhu et al., 2010). This distinct structure of graphene has received considerable attention because of its fascinating properties including very high theoretical surface area (around 2630 $m^2 \cdot g^{-1}$) (Stankovich et al., 2006), highest electrical conductivity (around 10^6 $S \cdot cm^{-1}$) (Geim and Novoselov 2007), very good mechanical strength (100-200 times stronger than steel), inherent flexibility, high aspect ratio, and unique basal plane structure (Novoselov et al., 2004; Geim and Novoselov 2007; Xu et al., 2008). Therefore, the graphene has attracted a great deal of attention in a variety of applications including fuel cell components such as in bipolar plate and as an electrocatalyst support (Sun et al., 2011; Tjong 2011; Devanathan 2008; Brownson et al., 2011; Liu et al., 2012; Zhang et al., 2013).

An extensive literature survey on the recent advances of carbon-polymer composite bipolar plate as well as on electrocatalyst support materials has been carried out and reported in next chapter.

Chapter 2

Literature Review

Chapter 2

Literature Review

The properties of graphene as a potential candidate for the PEMFC components were discussed in the previous chapter. The importance of graphene in the PEMFC components such as in bipolar plate and as an electrocatalyst support is discussed in this chapter along with an extensive literature review on recent advancement in the research and development of composite bipolar plate and electrocatalyst support for PEMFC.

2.1 Graphene in bipolar plate

The bipolar plate is one of the vital components of PEMFC, which accounts for 80% of the total weight, around 90% of the total volume, and also consumes around 38% of total cost of the PEMFC stack (Mehta and Cooper 2003; Cunningham and Baird 2007). The various functions of the bipolar plates of a PEMFC stack are to (Cooper 2004),

(i) support the membrane electrode assembly,

(ii) distribute the fuel and oxidant over the active electrode surface,

(iii) facilitate water management within the cell,

(iv) prevent leakage of reactant gases and coolant,

(v) carry current away from the cells, and

(vi) dissipate the generated heat from the cells.

In order to meet the above functions, the bipolar plate should have several properties including (Middelman et al., 2003; Cunningham and Baird 2007),

(i) high through-plane as well as in-plane electrical conductivity,

(ii) good mechanical strength,

(iii) high thermal conductivity,

(iv) low hydrogen permeability,

(v) excellent electrochemical stability,

(vi) low interfacial contact resistance,

(vii) high stability, and

(viii) easy processability for designing flow field.

Therefore, many agencies have given benchmarks for bipolar plate properties. Table 2.1 shows the stringent target properties out of the benchmarks provided by the DoE and Plug Power Inc. (Hwang et al., 2008; Wang and Turner 2010; Tjong 2011; Mamlouk and Scott 2011). The above stringent targets can only be achieved using suitable materials for the bipolar plate.

Table 2.1: Stringent target properties for bipolar plate in PEMFC application (Mamlouk and Scott 2011; Tjong 2011; Chandan et al., 2013)

Required properties		**Unit**	**DoE target 2017**
Density		$g \cdot cm^{-3}$	<2
In-plane electrical conductivity and through-plane electrical conductivity		$S \cdot cm^{-1}$	> 100
Flexural strength		MPa	>59[α]
Deflection at mid-span		%	3–5
Thermal conductivity		$W \cdot m^{-1} \cdot K^{-1}$	> 10
Hydrogen permeability (at 80°C and 3atm)		$cm^3 \cdot cm^{-2} \cdot s^{-1}$	$< 2 \times 10^{-6}$
Scleroscope shore hardness		C type	> 40[α]
Corrosion current density	Anodic	$\mu A \cdot cm^{-2}$	< 1
	Cathodic		
Interfacial contact resistance		$m\Omega \cdot cm^2$	<10
HT-PEMFC operating temperature	Transportation applications	°C	120
	Stationary applications	°C	150

[α] Plug power Inc.

2.1.1 Different type of materials for bipolar plate

Different type of materials, including graphite, metal sheet, coated metal, and carbon-polymer composite, have been used for the development of bipolar plates (Davies et al., 2000b; Tawfik et al., 2007; Yang et al., 2007; Fu et al., 2008; Wu et al., 2009). However, developing suitable bipolar plate, which can satisfied all the stringent target properties is still in progress. Pure graphite is the most common material used to develop bipolar plates. The graphite bipolar plates have very good corrosion resistance, excellent chemical stability, good electrical conductivity, and high thermal conductivity. However, the main limitation of graphite bipolar plate is its brittleness, which poses difficulty in machining the flow channels in the plate for the reactant flow (Antunes et al., 2011). In addition, cutting and machining of the flow channels is time consuming and costly, owing to the brittleness of graphite. In view of all these issues, pure graphite may not be suitable for automobile and portable devices (Oliveira et al., 2012). Therefore, metal bipolar plate is the other option, which may exhibit high electrical conductivity, excellent mechanical strength, high thermal conductivity, easy flow channels processability, and high hydrogen gas impermeability. Different types of metal, metal-alloy, and metal-foam have been studied for possible replacement of pure graphite bipolar plates. They include aluminum, stainless steel, titanium, nickel, copper, and their alloys (Davies et al., 2000b; Tawfik et al., 2007; Yang et al., 2007). However, metals are susceptible to corrosion upon exposure to harsh acidic, humid and redox environment of fuel cell at about 80°C (Lafront et al., 2007; Hermann et al., 2005). The degradation of fuel cell may start by electrocatalyst poisoning and membrane contamination due to leaching of the metal ions from the bipolar plate (Davies et al., 2000b). To overcome the corrosion issue, a protective layer is coated on the metal surface to resist the corrosion in acidic PEMFC environment (Hermann et al., 2005). However, it should be ensured that the electrical conductivity of

the coated metal bipolar plate should not be much compromised. In addition, the coating must be adhered well to the metal surface. However, this protective layer increases the surface resistivity of the metal bipolar plate due to the formation of micro-pores and micro-cracks in the coating layer by uneven thermal expansion between metal and coating layers (Davies et al., 2000b; Hong and Weil 2007; Nam and Lee 2007; Ren and Zeng 2007; Hsiao et al., 2010).

Considering the above issues, it was felt necessary to find alternative material to fulfill the stringent requirements of the PEMFC bipolar plate. In this concern, the carbon-polymer composite bipolar plate is being studied extensively to replace the pristine graphite and metal/or coated metal bipolar plate (Du and Jana 2007; Maheshwari et al., 2007; Thepkaew et al., 2008; Hui et al., 2010; Taherian et al., 2011; Oliveira et al., 2013).

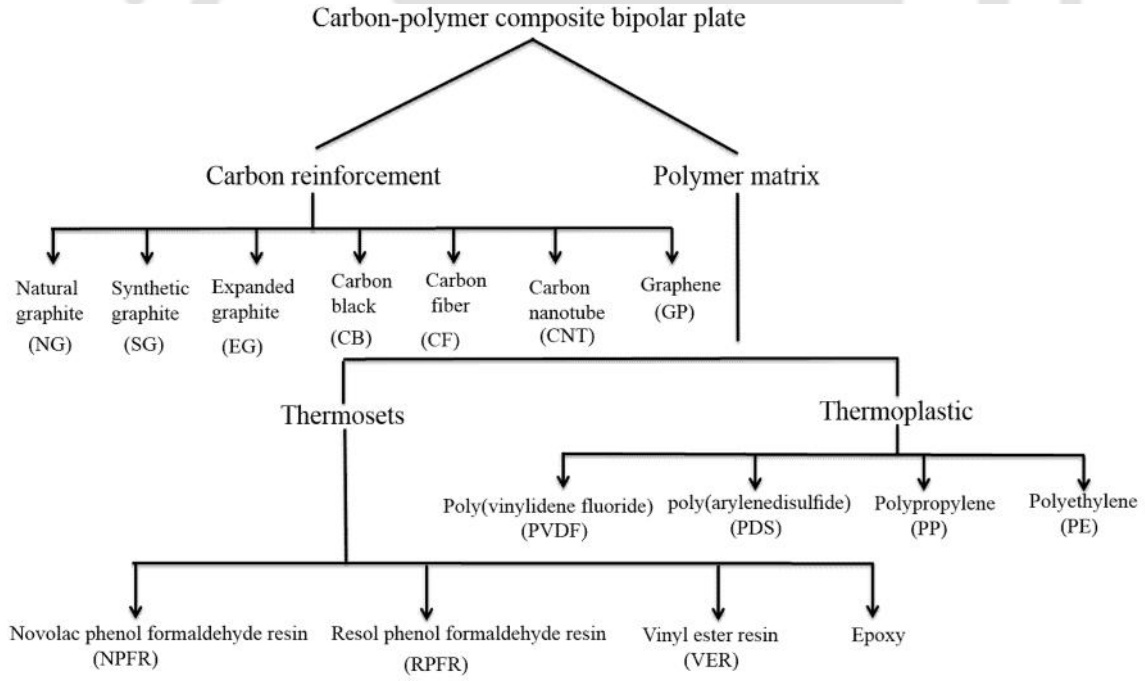

Figure 2.1: Classification of carbon-polymer composite bipolar plate materials (Mehta and Cooper 2003; Hermann et al., 2005)

Table 2.2: Properties of different carbon materials (Dai et al., 2012; Dhakate et al., 2010; Park and Ruoff 2009; Rodwick 2008)

Properties	**Unit**	**NG**		**CB**	**CF**		**CNT**	**GP**
Density	$g \cdot cm^{-3}$	2.26		1.12	1.76		1.33	>1
Electrical conductivity	$S \cdot cm^{-1}$	$\sim 10^4$		$\sim 10^2$	$\sim 10^3$		$\sim 10^4$	$\sim 10^6$
Thermal conductivity	$W \cdot m^{-1} \cdot K^{-1}$	500 (∥)	6 (⊥)	174	10.46 (∥)	70 (⊥)	3000	5000
Specific surface area	$m^2 \cdot g^{-1}$	10		254	12		400	2630
Fracture strength	GPa	$\sim 10^{-1}$		$\sim 10^{-2}$	1.87		45	124

∥: in-plane; ⊥: Through-plane

Figure 2.1 shows the different types of additives, reinforcements, and matrix, which are commonly used for the development of carbon-polymer composite bipolar plate (Mehta and Cooper 2003; Hermann et al., 2005; Dhakate et al., 2010). Table 2.2 shows the comparison of the different carbon material properties, which are commonly being under investigation for the preparation of efficient composite bipolar plate. Natural graphite (NG) or synthetic graphite (SG) or expanded graphite (EG) is commonly used as a primary reinforcement for the polymer composite bipolar plate. The critical primary reinforcement to matrix ratio should be around 60-75 vol.% or 25-40 wt.% to maintain proper dispersion of reinforcement into the polymer matrix (Tjong 2011). Moreover, the different types of additives such as carbon black (CB), carbon fiber (CF), carbon nanotube (CNT), and graphene (GP) are introduced into the primary reinforcement/polymer matrix to tune the various properties of the composite bipolar plate in order to achieve the stringent benchmark (Huang et al., 2005; Hwang et al., 2008; Tjong 2011; Sohi et al., 2011; Taherian et al., 2012; Blunk et al., 2006a). It has been seen that combining NG with the additives such as CB, CF, and CNT shows an effective way to develop the carbon-polymer composite with higher electrical and good mechanical

properties (Mehta and Cooper 2003; Kim et al., 2010b; Chen et al., 2011; Guo and Leu 2012). Generally, thermosetting or thermoplastic polymer is used for the development of carbon-polymer composite bipolar plate as a matrix.

The composite bipolar plates are usually prepared by compression molding and injection molding techniques. One of the main advantages of these preparation techniques is that the flow channels can be prepared in-situ in the bipolar plate at the time of compression/injection molding, thus eliminating the cost associated with the machining steps. The injection molding method is preferred for large scale production of carbon composite bipolar plate using thermoplastic resin due to short processing time, automated production, and accurate size (Mighri et al., 2004). However, it has some disadvantages, such as excessive mold wear for high viscosity of the materials, limited flow ability, and poor through-plane electrical conductivity of the composite due to flow induced orientation of the continuous fillers (Du 2008).

In this regard, compression molding may be a good choice for the development of composite bipolar plates due its high accuracy, higher electrical conductivity, good thermal conductivity, handling capabilities, and high filler loadings (Wolf and Willert-Porada 2006; Blunk et al., 2006a; Dweiri and Sahari 2007; Yin et al., 2007). However, compression molding technique has slow output (in terms of time to prepare the bipolar plate) as compared to injection molding technique (Lee et al., 2009; Antunes et al., 2011; Oliveira et al., 2013). The subsequent section will discuss on recent advances of carbon-polymer composite bipolar plate for PEMFC.

2.1.2 Carbon-polymer composite bipolar plate

Natural graphite (NG) is used as main reinforcement along with different matrix (Kuan et al., 2004; Yin et al., 2007; Kang et al., 2010). Kuan et al., (2004) prepared the composite bipolar plate by mixing bulk molding compound (BMC) and NG using compression molding technique. The BMC formulation used by Kuan et al., (2004) is shown in table 2.3. Different proportions of the BMC and natural graphite were used and the optimum performance of the developed composite bipolar plate was found at 75% NG content (mean size 177 µm) and 25% BMC. The in-plane electrical conductivity and flexural strength were found to be 114 $S \cdot cm^{-1}$ and 31.25 MPa, respectively. However, it may be noted that the flexural strength is quite low as compared to the target values shown in the table 2.1. Moreover, the through-plane electrical conductivity of the developed composite bipolar plate is not reported. Yin et al., (2007) optimized the operating preparation parameters and composition of NG/NPFR composite. They have studied molding temperature and molding time on the electrical and mechanical properties of the composite bipolar plate and studied the effect of NPFR content. It was found that the electrical conductivity of the composite decreased initially up to 220°C and 45 min of molding time. Thereafter, further increase in the molding temperature and time the electrical conductivity achieved maxima for molding temperature of 240°C and molding time of 1 h. However, the electrical conductivity decreased on further increase in temperature and molding time. The optimum temperature and time of the compression molding was utilized to fabricate composites using various composition of NG/NPFR. The flexural strength of the above composites also followed the same trend for molding temperature and time. The best in-plane electrical conductivity and flexural strength was found for NG/NPFR 85/15 wt.% composite were 142 $S \cdot cm^{-1}$ and 61.6 MPa, respectively.

Table 2.3: Formulation of BMC (Kuan et al., 2004)

Component	**Composition**	
	Resin	**BMC**
VER (wt.%)	75	25
Low profile agent (wt.%)	8	
Styrene monomer (wt.%)	17	
tert-Butyl peroxybenzoate (phr)	1.8	
Zinc stearate (phr)	3.5	
MgO (phr)	1.8	
Graphite powder (wt.%)		75
Total (wt.%)	100	

phr: parts per hundred parts of resin

However, the other properties of the composite were not reported. The effect of graphite particle size (mean size 75 and 150 µm) and its content on the properties of NG/polymer composite bipolar plate was studied by Kang et al., (2010). The through-plane electrical conductivity of the optimum composite NG/RPFR 80/20 wt.% was reported as 31.1 and 39.1 $S \cdot cm^{-1}$ using average NG particle sizes of 75 and 150 µm, respectively, which was significantly lower than the DoE target. Moreover, the air permeability of the optimum composites were around 1.7×10^{-5} $cm^3 \cdot cm^{-2} \cdot s^{-1}$ and 7.6×10^{-5} $cm^3 \cdot cm^{-2} \cdot s^{-1}$ for average NG particle sizes of 75 and 150 µm, respectively, which was quite high in comparison to the stringent benchmark for hydrogen permeability (table 2.1). It was found that only the use of graphite might not be suitable to improve the various properties of the composite bipolar plate.

Various literature reports the use of NG, EG, CB, and CF along with the resin matrix for the development of composite bipolar plate (Du and Jana 2007; Kakati et al., 2010; Mathur et al., 2008; Dhakate et al., 2007; Lee et al., 2009; Suherman et al., 2013). For example, Dhakate et al., (2007) as well as Lee et al., (2009) reported similar electrical and

mechanical behavior of CB/NG/NPFR and CB/NG/epoxy composites, respectively. The optimum carbon black content was found to be 20% Dhakate et al., (2007) as compared to 5% Lee et al., (2009). These difference arise from intrinsic electrical properties, and from morphology-related issues of both graphite and carbon black particles (Antunes et al., 2011). It is reported that the properties, particularly conductivities of the NG/polymer and EG/polymer (Dhakate et al., 2008; Du 2008) composites may be benefitted from the addition of small CB content. It is also reported that CF is the primary source of mechanical strength for carbon-polymer composite bipolar plate (Tjong 2011).

Table 2.4 shows the comparison of some of the recent and past literature data on the properties of carbon-polymer composite bipolar plates. It can be seen that the in-plane electrical conductivity of the composite bipolar plate was extensively studied but through-plane electrical conductivity was reported by a few researcher only. The through-plane electrical conductivity for bipolar plate is more important than in-plane electrical conductivity, as the electrons are collected by the plate at the anode side and transported though the bipolar plate to cathode side (other side of the bipolar plate) in a fuel cell stack. In addition, the high through-plane electrical conductivity not only increase the electron mobility but also decrease the interfacial contact resistance of carbon-polymer composite bipolar plate. The interfacial contact resistance constitutes a significance part of the ohmic resistances, especially when carbon-polymer composite is chosen as the bipolar plate (Davies et al., 2000a). The performance of a PEMFC system can be significantly improved if the interfacial contact resistance can be minimized (Kraytsberg et al., 2007; Mishra et al., 2004). Reported values of interfacial contact resistance in PEMFC literature largely vary, from 25 $m\Omega \cdot cm^2$ (Davies et al., 2000a; Avasarala and Haldar 2009) to 150 $m\Omega \cdot cm^2$ (Blunk et al., 2003) depending on the bipolar plate material, diffusion media, compression pressure, surface roughness of contacting materials and

other prevailing conditions during the measurements; thus making it difficult to compare. However, according to DoE target, the contact resistance of the bipolar plate is required to be less than 10 $m\Omega \cdot cm^2$ (table 2.1).

It is obvious that the electrical conductivity and flexural strength are the most important properties among the others stringent benchmarks. Therefore, research is going on to increase the mechanical strength and electrical conductivities (particularly through-plane) of the carbon-polymer composite bipolar plate using different types of carbon nanofillers. In the other words, it is difficult to obtain simultaneous high electrical conductivity and high mechanical strength, for the same reinforcement in the composite bipolar plate (Oliveira et al., 2013; Jiang and Drzal 2012). Polymer matrix distributes the various stresses/loads throughout the composite (NG/polymer) and provides the mechanical strength. However, achievement of the higher mechanical strength is adversely accompanied by the reduction of electrical conductivity. Therefore, balancing these two properties are the main challenges in the development of carbon-polymer composite bipolar plate for PEMFC. Moreover, the pathway to reach high power density is closely related to the ohmic losses within the PEMFC stack. In this regards, the optimization of the electrical conductivity of the composite bipolar plate plays a leading role thereby demanding many efforts to the development of highly conductive materials. A common approach reported to improve the electrical conductivity and mechanical strength is to reinforce minor amount of highly conductive carbon nanofillers into the NG/polymer composites. In this concern, researchers and scientists studied carbon nanomaterial, which may overcome these problems. Among the various reinforcements single-walled carbon nanotube (SWCNT), multi-walled carbon nanotube (MWCNT), and graphene (GP) have attracted considerable attention as potential candidates for fabricating multi-fillers reinforced efficient carbon-polymer composite bipolar plate.

It is found that in general the reinforcement loadings fall in 60-75% to reach adequate electrical conductivity by the polymer composite bipolar plate (Oliveira et al., 2013). However, there is lack of polymer matrix to fill all the interstices among graphite particles at high carbon filler loadings. Therefore, the mechanical strength of highly reinforced carbon-polymer composite bipolar plate is insufficient as well as susceptible to hydrogen permeability (Blunk et al., 2006a; Blunk et al., 2006b; Antunes et al., 2011). The carbon nanotubes (CNT) are used as reinforcement for carbon-polymer composite to increase the mechanical properties. For example, the tensile strength of the pure epoxy bipolar plate could be increased by 159% (89.1 to 231.5 MPa) using CNT/epoxy 16.5/83.5 wt.% composite bipolar plate (Cheng et al., 2010). Although the in-plane electrical conductivity of the CNT/epoxy composite achieved the DoE target (table 2.1) but other target properties including the through-plane electrical conductivity were not reported. Moreover, it is reported that the high aspect ratio of CNT has the tendency to agglomerate at higher loadings into the polymer matrix, which may decrease the properties of the CNT/polymer composite (Dhakate et al., 2010). Moreover, it is found that 2% CNT content at the expense of SG in the optimum polymer composite increased the corrosion current density of the composite bipolar plate from 0.5 to 1.25 $\mu A \cdot cm^{-2}$ (Oliveira et al., 2013), which is higher than DoE target (table 2.1). However, they have not evaluated the corrosion current density of the composite bipolar plate under accelerated PEMFC anodic and cathodic environment. Therefore, CNT may be used as a low loading additive in the NG/polymer composite to improve the electrical and mechanical properties (Liao et al., 2008a; Liao et al., 2008b; Liao et al., 2010a; Liao et al., 2010b) without an adverse effect on the other properties.

An investigation by Lee et al., (2009) was conducted on the electrical and mechanical properties of a compression molded SG/polymer composite bipolar plate reinforced with

different additives such as CB, MWCNT or CF. They have found that the optimum in-plane electrical conductivity of 254.7 $S \cdot cm^{-1}$ was achieved for 73 vol.% SG, 25 vol.% epoxy, and 2 vol.% of MWCNT, which was 105% higher than SG/epoxy composite with the same amount of conducting filler (75/25 vol.%). This may be attributed to the high aspect ratio of MWCNT, which formed good conducting path as well as connected the graphite particles. The flexural strength of the MWCNT/SG/epoxy composite was found to be 48 MPa, that was also 83% higher that SG/epoxy composite. It was shown that the electrical conductivity of MWCNT reinforced composite bipolar plate decreased with the increased content of MWCNT beyond 2%. It was due to the cluster formation of MWCNTs at higher loading, due to lack of polymer matrix in the composite resulting incomplete binding during the molding process. Thus the generated voids act as insulator and reduced the electrical conductivity (Choi et al., 2005). However, the through-plane electrical conductivity of the MWCNT reinforced composite bipolar plate was not reported. Later, Dhakate et al., (2010) reported a similar beneficial effect of MWCNTs in forming additional conductive paths in MWCNT/NG/NPFR composite. The through-plane electrical conductivity of the optimum MWCNT/NG/NPFR 1/35/64 vol.% composite was 30 $S \cdot cm^{-1}$, which was around 233% higher than without MWCN reinforced composite bipolar plate. The in-plane electrical conductivity, flexural strength, and thermal conductivity of the optimum composite was increased by 106%, 25%, and 100%, respectively due to the reinforcement of 1vol.% MWCNT into the NG/NPFR composite as compared to without MWCNT composite bipolar plate. This significance improvement can be attributed to the MWCNTs, which were oriented in all directions and having higher intrinsic thermal conductivity and mechanical strength. Moreover, the MWCNT oriented in z-direction (through-plane) facilitate pathway for electrical conduction and heat transfer along the composite. However, it has been reported that the

shore hardness of the composite (MWCNT/NG/NPFR) bipolar plate was decreased continuously due to addition of above 1vol.% MWCNT content into the NG/NPFR composite. It was seen that though the various polymer matrices and carbon reinforcements were used in the studies but the composite bipolar plates either not achieve the required benchmark given in table 2.1 or the properties were not reported. Moreover, it can also be seen that many of the other crucial properties of the composite bipolar plate have not been studied thoroughly. The hydrogen permeability, thermal conductivity, corrosion resistance, and interfacial contact resistance are the foremost properties among them. Therefore, the research is going on to improve the overall properties of the composite bipolar plate.

Graphene can be a potential reinforcement into the polymer composite bipolar plates owing to attractive electrical and mechanical properties as compared to CNTs. It can be seen from the table 2.2 that the electrical, mechanical, and physical properties of the GP is significantly high as compared to other carbon materials. The specific surface area is around 10 times higher than CNT, which is one of the most important and desired properties for various components of a PEMFC. Furthermore, it can be dispersed uniformly into the polymer matrix without any entanglement with suitable treatment (Tjong 2011).

2.1.3 Graphene reinforced carbon-polymer composite bipolar plate

The GP nanoparticles exhibit low percolation threshold in GP/polymer composites, typically in the range of 0.1% to 2%, depending on the dispersion in the polymer and processing conditions employed. The GP nanoparticles affect the behavior of the surrounding polymer matrix and improve the electrical and mechanical strength at lower filler content (Ramanathan et al., 2008; Rafiee et al., 2009; Rafiee et al., 2010).

GP/polystyrene composite exhibits a percolation threshold of 0.1vol.%, the lowest reported value, this composite has the electrical conductivity of 0.001 $S \cdot cm^{-1}$ (Stankovich et al., 2006). This electrical conductivity is sufficient for many electrical applications, but it is not suitable for the bipolar plate. Moreover, it is reported that the electrical conductivity of the polymer nanocomposite can further be increased by increasing the GP content beyond percolation threshold value (Tjong 2011). Song et al., (2009) patented a process on the development of GP/polymer composite using 15wt.% GP. They have reported that the GP/polymer 15/85 wt.% nanocomposite exhibits in-plane and through-plane electrical conductivities around 100 and 20 $S \cdot cm^{-1}$, respectively (Song et al., 2009). Thus GP nanomaterial may also be reinforced in high content to improve the properties of polymer composite.

Recently, the GP/polyphenylene sulfide (PPS) nanocomposite with high loading of GP nanoparticles was prepared by Jiang and Drzal (2012). They found that the in-plane electrical conductivity increased with the increased GP content. However, the conductivity was still below the DoE target even at 60wt.% GP content (Jiang and Drzal 2012). It indicate that using GP as the single conductive filler may not be able to provide enough conductive pathways for the desired electrical conductivity. It may be due to the presence of polymer matrix in the micro-pores and/or micro-gaps between GP particles, which impede the through-plane electrical conductivity in the composite.

It is often reported that the carbon-polymer composite bipolar plates should be comprised of more than one types of conductive reinforcement to achieve the desired properties of the bipolar plate, where NG may be commonly used as a primary reinforcement as can be seen in table 2.4. The interactions between reinforcements determine the bulk electrical behavior of the polymer composite. The major problem in the carbon-polymer composite

is a thin insulating layer often forms by polymer resin around the conductive fillers and these decreases the effective electrical conductive pathway along the filler particles. Therefore, the NG/polymer composite requires micro and/or nano-fillers to increase the conductivity of the composite. One key issue to solve this problem is to reinforce one or more appropriate conductive fillers (NG and/or CB and/or CF and/or EG and/or CNTs, and/or GP) that may improve electrical and mechanical properties at relative low filler loadings (Kuilla et al., 2010; Liao et al., 2010b; Spendelow and Jacos 2012).

It is found that the in-plane electrical conductivity of the NG/VER 70/30 wt.% composite was increased by 67.7% due to the reinforcement of 0.5 phr MWCNT content. However, the in-plane electrical conductivity of the same composite was increased by 83.9% due the reinforcement of only 0.2 phr GP content. On the other hand, the flexural strength of the NG/VER composite bipolar plate was improved by 60.7% and 75.7% due to reinforcement of MWCNT (0.5 phr) and GP (0.2 phr), respectively. Therefore, it is understood that the GP is much effective than MWCNT for not only improving the electrical conductivity but also the mechanical strength of the polymer composite bipolar plate (Hsiao et al., 2010). The in-plane electrical conductivity of the MWCNT reinforced composite bipolar plate decreases at higher loading of MWCNT (beyond 0.5 phr). It can be attributed from the fact that the formation of local clusters due to lack of compatibility between MWCNT and polymer matrix increases the resistance between the clusters for electron migration, thus causing decreased in-plane electrical conductivity. Moreover, the effect of GP content on the NG/VER composite was studied only at 0.2 phr. The PEMFC fuel cell performance in terms of power density was improved by using different composite bipolar plates while the other parameters were kept same. The fuel cell power density using NG/VER nanocomposite bipolar plate was enhanced around 21.2% and 16.9% for incorporation of 0.2 phr GP and 0.5 phr MWCNT, respectively (Hsiao et al.,

2010). However, the through-plane electrical conductivity of the GP reinforced NG/VER composite bipolar plate was not reported. The flexural strength of the GP (0.2 phr) reinforced NG/VER composite bipolar plate was found to be 49.2 MPa, which is far below the stringent target (table 2.1). Therefore, it is obvious that GP can be more favorable reinforcement into the NG/polymer composite than MWCNT, which is attributed from the difference in the intrinsic properties between GP and MWCNT (table 2.4).

The comparisons of the properties of GP reinforced composite bipolar plates are summarized in the table 2.4. It can be seen that the CF/CB/NG/RPFR composite bipolar plate (Kakati and Verma 2011) exhibits better electrical and mechanical properties as compared to GP (0.2 phr) reinforced NG/VER composite bipolar plate (Hsiao et al., 2010). Therefore, there is a need to study the effect of GP content on the electrical and mechanical properties of the CF/CB/NG/polymer composite bipolar plate.

In this regard, exhaustive and systematic study, which explains the effects of each of these carbon conductive fillers (reinforcements, and additives) on the final composite, was conducted by several researchers using various matrices. The final composites were prepared by compression molding and cured at required curing temperatures to obtain composite bipolar plates (Lee et al., 2009; Mathur et al., 2008). It was observed that the NG/polymer composite bipolar plate with an optimized combination was able to achieve the desired in-plane and through-plane electrical conductivities (Kakati and Verma 2011). However, the flexural strength (31.99 MPa) and deflection at mid span (2.85%) of the optimum NG/RPFR 75/25 vol.% composite was significantly lower as compared to the benchmark. Moreover, the through-plane electrical conductivity (103.30 $S \cdot cm^{-1}$) of the

above optimum NG/RPFR composite was just reached to the target, which is required to be increased for better fuel cell stack performance.

Therefore, shortfall in the required properties may be achieved by replacing some of the NG with the other relevant additives without much compromising the other properties including density, corrosion current, and hydrogen permeability (Kakati and Verma 2011). For example, the high through-plane electrical conductivity was achieved by introducing spherical conductive particles between the flaky graphite particles and the mechanical strengths by the fibrous conductive material. Therefore, CB and/or CF were used not only to increase the mechanical strength but also to increase the in-plane and through-plane electrical conductivities of the composite (Kakati and Verma 2011). It can be noted that the in-plane electrical conductivity, through-plane electrical conductivity, flexural strength, and deflection at mid-span of the CB/NG/RPFR composite was increased by around 17%, 12%, 43%, and 34%, respectively, due to reinforcement of 5vol.% CB at the expense of NG in the NG/RPFR 75/25 vol.% composite. This improvement in the properties of composite bipolar plate was attributed to positive synergetic effect between NG and CB. The synergetic effect can be explained in terms of formation of electrical bridge between two neighboring NG flakes. As the CB content increases, they may not be fully coated by the polymer resin due to high surface area of the CB as compared to NG, leading to decreased electrical and mechanical performance of the composite. However, flexural strength and through-plane electrical conductivity of the above composite (CB/NG/RPFR 5/70/25%) were below the benchmark. To further improve the mechanical and electrical properties of the above CB/NG/RPFR composite, the CF was reinforced in to the CB/NG/RPFR composite at the expanse of NG content. The in-plane and through-plane electrical conductivity of the optimum composite CF/CB/NG/RPFR 5/5/65/25 vol.% bipolar plate were slightly reduced to 415.09 and

99.70 $S \cdot cm^{-1}$, respectively, as compared to CB/NG/RPFR 5/70/25 vol.%. However, the flexural strength and deflection at mid-span of the composite were significantly improved (55.28 MPa and 5.2%) as compared to the CB/NG/RPFR 5/70/25% composite.

It is reported that the CB particles help to increase the electrical conducting path by occupying the gap between NG-NG and/or NG-CF (Kakati et al., 2009). Moreover, from the table 2.4 it can be seen that the overall properties of the CF/CB/NG/polymer is significantly higher as compared to the CB/NG/polymer composite. The through-plane electrical conductivity and flexural strength of optimized composite (without GP), CF/CB/NG/RPFR 5/5/65/25 vol.%, was edge below the stringent benchmark. Therefore, graphene was used as low loading additive to increase the electrical and mechanical properties of the CF/CB/NG/RPFR composite (Kakati and Verma 2011). It can be seen in the table 2.4 that the incorporation of graphene in the above optimized composite improved the electrical and mechanical properties. It is found that 1% GP content at the expense of NG in the above mentioned optimized composite increased the in-plane electrical conductivity, through-plane electrical conductivity, and flexural strength of the composite from 415.05 to 435.31 $S \cdot cm^{-1}$, 99.07 to 130.17 $S \cdot cm^{-1}$, and 54.23 to 57.28 MPa, respectively. Moreover, the corrosion current density of the composite bipolar plate was not affected due to the incorporation of the GP content (table 2.4). It may be due to the reinforcements were well bonded within the composite and as a result, the properties of the above composite were increased significantly (table 2.4). However, the interfacial contact resistance and accelerated PEMFC corrosion current density were not reported for GP reinforced composite bipolar plate. It is also reported that the power densities of PEMFC were increased significantly for GP reinforced carbon-polymer composite bipolar plate as compared to without GP reinforced composite bipolar plate (Hsiao et al., 2010; Kakati and Verma 2011).

Table 2.4: Properties of the carbon-polymer composite bipolar plates reported in literatures of recent past

Composition	Density ($g \cdot cm^{-3}$)	Flexural strength (MPa)	Deflection at mid-span (%)	Shore hardness	Electrical conductivity ($S \cdot cm^{-1}$)		Thermal conductivity ($W \cdot m^{-1} \cdot K^{-1}$)	Hydrogen permeability (10^{-10} $cm^3 \cdot cm^{-2} \cdot s^{-1}$)	Corrosion current density ($\mu A \cdot cm^{-2}$)		Interfacial contact resistance ($m\Omega \cdot cm^2$)	References
					∥	⊥			i_a	i_c		
Bipolar plate	**<2**	**59[α]**	**3-5**	**40[α]**	**>100**		**>10**	**10^4**	**<1**		**<10**	**US-DoE target 2017**
NG/NPFR 85/15 vol.%	-na-	-na-	-na-	-na-	142	-na-	-na-	-na-	-na-	-na-	-na-	Yin et al., 2007
CF/NG/PVDF 6/70/24 wt.%	-na-	60	-na-	-na-	292	32	-na-	-na-	-na-	-na-	-na-	Cunningham et al., 2007
EG/NG/NPFR 7.5/67.5/25 wt.%	-na-	50	-na-	-na-	250	-na-	-na-	-na-	-na-	-na-	-na-	Heo et al., 2007
CF/NG/PVDF 6/70/24 wt.%	-na-	60	-na-	-na-	292	32	-na-	-na-	-na-	-na-	-na-	Cunningham et al., 2007
CNT/NG/NPFR 3/82/15 wt.%	-na-	68.6	-na-	-na-	145.2	-na-	-na-	-na-	-na-	-na-	-na-	Yin et al., 2008
CNT/NG/PP 4phr/76/24 wt.%	-na-	32.6	-na-	-na-	548	-na-	-na-	-na-	-na-	-na-	-na-	Liao et al., 2008
Composite graphite	-na-	-na-	-na-	-na-	-na-	-na-	-na-	-na-	0.419[r]		22.13 at 2 MPa	Yue hung et al., 2008
EG/NG/NPFR 7.5/67.5/25 wt.%	-na-	50	-na-	-na-	250	-na-	-na-	-na-	-na-	-na-	-na-	Heo et al., 2007
CNT/NG/NPFR 3/82/15 wt.%	-na-	68.6	-na-	-na-	145.2	-na-	-na-	-na-	-na-	-na-	-na-	Yin et al., 2008
CF/NG/Epoxy 7/68/25 vol.%	-na-	67	-na-	-na-	240	-na-	-na-	-na-	-na-	-na-	-na-	Lee et al., 2009
NG/BMC 70/30wt.%	-na-	-na-	-na-	-na-	-na-	-na-	-na-	-na-	-na-	-na-	27 at 2.5 MPa	Avasarala et al., 2009
CNT/NG/NPFR 1/64/35 vol.%	1.78	56	-na-	55	178	30	50	-na-	-na-	-na-	-na-	Dhakate et al., 2010
NG/RPFR 80/20 wt.%	-na-	41.9	-na-	-na-	324.7	31.1	-na-	7.6×10^4 (air)	-na-	-na-	-na-	Kang et al., 2010
NG/BMC 80/20 wt.%	-na-	-na-	-na-	-na-	167	35.2	-na-	-na-	-na-	-na-	-na-	Hui et al., 2010
CNT/NG/VER 0.5phr/70/30 wt.%	-na-	45	-na-	-na-	261.1	-na-	27.3	-na-	-na-	-na-	-na-	Hsiao et al., 2010

Composition	Density ($g \cdot cm^{-3}$)	Flexural strength (MPa)	Deflection at mid-span (%)	Shore hardness	Electrical conductivity ($S \cdot cm^{-1}$)		Thermal conductivity ($W \cdot m^{-1} \cdot K^{-1}$)	Hydrogen permeability ($\times 10^{-10}$ $cm^3 \cdot cm^{-2} \cdot s^{-1}$)	Corrosion current density ($\mu A \cdot cm^{-2}$)		Interfacial contact resistance ($m\Omega \cdot cm^2$)	References
					∥	⊥			i_a	i_c		
GP/NG/VER 2phr(only)/70/30 wt.%	-na-	49.2	-na-	-na-	286.4	-na-	27.2	-na-	-na-	-na-	-na-	Hsiao et al., 2010
CF/EG/NG/NPFR 5/5/40/50 wt%	-na-	84	-na-	-na-	1518	76	-na-	-na-	-na-		-na-	Taherian et al., 2011
CF/CB/NG/NPFR 5/5/60/30 vol.%	1.845	55.28	5.2	46	285.54	91.79	128	9.51	0.986[p]		-na-	Kakati and Verma 2011
CF/CB/NG/RPFR 5/5/65/25 vol.%	1.81	54.23	5.47	50	415.05	99.7	145	6.22	0.997[p]		-na-	
CF/CB/NG/VER 5/5/65/25 vol.%	1.825	53.5	5.37	49	355.05	95.95	132	15.59	1.215[p]		-na-	
CF/EG/NG/NPFR 10/5/45/40 wt.%	-na-	74	-na-	-na-	101	-na-	9.6	No leakage detected	-na-	-na-	9 at 1.5 MPa	Taherian et al., 2012
CF/SG/NG/NPFR 10/10/45/35 vol.%	-na-	40	-na-	-na-	125	-na-	-na-	-na-	-na-	-na-	-na-	Guo et al., 2012
GP/CF/CB/NG/RPFR 1(only)/5/5/64/25 vol.%	1.804	57.28	5.85	-na-	435.31	130.17	-na-	-na-	0.998[p]		-na-	Kakati et al., 2013
SG/ABS/CNT 83/15/2 wt.%	-na-	-na-	-na-	-na-	200	38	-na-	-na-	1.25[q]		-na-	Oliveria et al., 2013

NG: natural graphite
SG: synthetic graphite
EG: expanded graphite
CB: carbon black
CF: carbon fiber

CNT: carbon nanotube
NPFR: novolac phenol formaldehyde resin
RPFR: Resole phenol formaldehyde resin
VER: vinyl ester resin
PPS: polyphenylene sulfide
PVDF: polyvinylidene fluoride

PP: polypropylene
BMC: bulk molding compound
-na- : not available
[α] Plug power Inc.
∥: in-plane;
⊥: through-plane

i_a: anodic corrosion current density
i_c: cathodic corrosion current density
[p]process condition (1 M H_2SO_4 at 50°C)
[q]process condition (0.5 M H_2SO_4 + 2 ppm HF at 70°C)
[r]process condition (0.5 M H_2SO_4 + 200 ppm HF at room temperature)

In almost all the cases the maximum gain in the power density is about 10% as compared to without GP reinforced composite bipolar plate. The gain in the power density is due to the increased electrical conductivity and reduced contact resistance (Hsiao et al., 2010; Kakati and Verma 2011). The graphene reinforced composite bipolar plate (GP/CF/CB/NG/RPFR 1/5/5/64/25%) meet most of the stringent benchmark shown in the table 2.1. Moreover, there is further scope to study the effect of graphene content on other properties of the composite bipolar plate.

It has been discussed at the beginning of the chapter that the graphene can be used in various components of the PEMFC. Therefore, the subsequent section discuss about the role of graphene as an electrocatalyst support.

2.2 Graphene as an electrocatalyst support

The electrocatalyst plays a vital role in the performance of PEMFC. High electrocatalytic activity is necessary for efficient performance of the fuel cell. In this concern, the research work is going on to develop highly durable, highly efficient, and cost effective catalyst for PEMFC applications. For example, the DoE has set target for PEMFC stability as 5000 h for car applications, 20,000 h for bus applications, and 40,000 h for stationary applications, which are about two times more than the presently achieved stability (Spendelow and Jacos 2012). The failure of any of the components limits the stability of the fuel cell. Therefore, in this section, stability and the performance of electrocatalyst pertaining to its support are being discussed.

Commonly, platinum is used as an active electrocatalyst in PEMFC for not only hydrogen electrooxidation at anode but also for oxygen electroreduction at cathode. However, the use of bulk platinum (noble metal) does not yield good performance of the PEMFC due to

low surface area per unit weight of platinum. Moreover, due to the limited natural resource, the cost of Pt noble metal is gradually increasing with the time (Zhang et al., 2013). It is thus necessary to reduce the Pt loading by increasing the surface area of the platinum per unit weight. Although many attempts have been made in the last few decades to develop non-noble metal electrocatalysts to replace platinum catalysts in PEMFCs and other low temperature fuel cells, platinum still remains the catalyst of choice. Therefore, Pt nanoparticles are dispersed on supporting material to increase the active electrochemical surface area (ESA) of Pt electrocatalyst (Shao et al., 2010; Liu et al., 2010). Generally, the requirements for catalyst support material are (Shao et al., 2010) (i) high surface area to improve the dispersion of the metal electrocatalyst, (ii) high electrical conductivity to provide low ohmic resistance, (Shan et al., 2009) (iii) long term electrochemical stability under fuel cell operating conditions, and (iv) good interaction between support material and metal catalyst.

Commonly, carbon black (Vulcan XC-72) is commercially used as a support material for Pt and Pt-alloy nanoparticles in PEMFC application (Antolini 2009; Choi et al., 2011). However, it is reported that the carbon black as a support for the PEMFC catalyst is easily oxidized as compared to graphitized form of carbon at higher potential (greater than 0.8 V vs. standard hydrogen electrode) (Wang et al., 2011; Kangasniemi et al., 2004). Moreover, it is well established that the corrosion of carbon black increases due to the presence of Pt nanoparticles, which leads to detachment of Pt from the support and agglomeration of the Pt nanoparticles (Kulikovsky 2011) as shown in fig. 2.2. The agglomeration results in lowering the active electrochemical surface area over the time (Sharma and Pollet 2012).

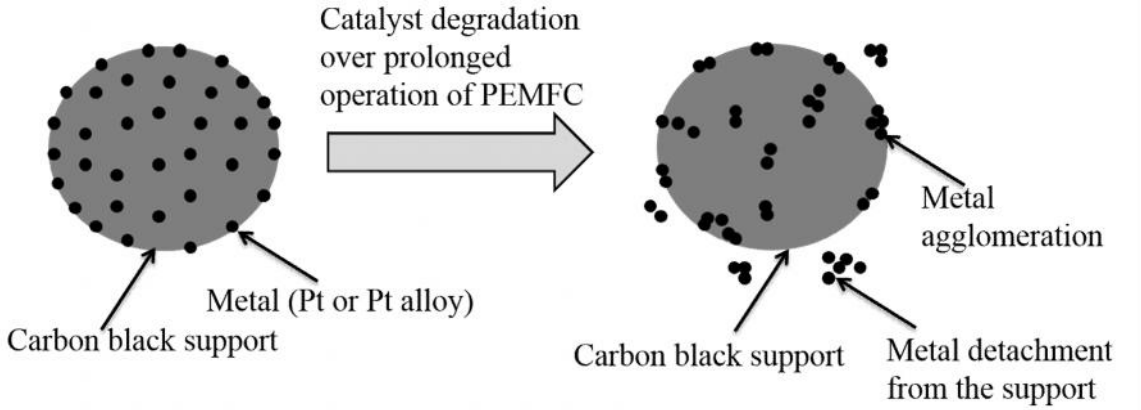

Figure 2.2: Schematic of M/C (M: Pt, Pt-alloy) catalyst degradation process

Moreover, during the preparation of catalyst layer on the electrode surface, around 30% of the catalyst either does not form triple phase boundary (TPB) or the Pt catalyst deposit into the deep cracks of the carbon black, resulting in lower catalyst activity than expected (Zhang et al., 2013). At TPB in the catalyst, ionomer, and reactant are simultaneously present for the electrochemical reaction for the transport of ion and electrons apart from reactant and byproduct. Owing to the above stated problems, graphene is being exploited as a promising candidate for fuel cell electrocatalyst support due to its high corrosion resistance, attractive basal plane structure with high electrical conductivity and high surface area (Park et al., 2011; Li et al., 2009; Kou et al., 2009; Shao et al., 2010; Bong et al., 2010; Zhang et al., 2009; Yoo et al., 2009; Liu et al., 2012). However, functionalization of graphene is required to enhance the interaction of Pt with the graphene. In this regards, numerous research efforts have been made to exploit the unique features of graphene and functionalized graphene (FGP) to develop fuel cell electrocatalyst with enhanced activity and increased stability.

Different types of synthesis methods such as impregnation method (Sogaard et al., 2001), colloidal method (Kim et al., 2003), ethylene glycol reduction method (Marinkas et al.,

2013), green electrochemical method (Liu et al., 2010), sonochemical method (Xing 2004), and sputtering (Caillard et al., 2006) method have been reported for the preparation of Pt electrocatalyst supported on carbon based materials. The above methods can be categorized into two groups such as physical and chemical method (Saha et al., 2013). The physical methods are atomization of Pt in vacuum by thermal evaporation or sputtering on the support, whereas the chemical methods are used to form neutral Pt atom on the support by reducing Pt ions. It is also reported that support material, particle size, and dispersion of the Pt nanoparticles on the support materials can strongly effect the utilization of the catalyst and its electrocatalytic activity in PEMFC. In this concern, chemical methods have the significant advantages due to ease in controlling the size, shape, and composition as compared to physical methods (Subhramannia and Pillai 2008; Saha et al., 2013). However, it may be noted that as-synthesized graphene does not have very good interaction with Pt nanoparticles. Moreover, the functionalized graphene may have better interaction than as-synthesized graphene (Antolini 2012). The presence of functional groups such as carboxyl (-COOH), hydroxyl (-OH), ether (-O-), and carbonyl (-C=O) on the graphene surface are responsible for physico-chemical adsorption of the Pt on the support. In addition, the functional groups on the graphene help to provide the hydrophilicity, which help in efficient dispersion of the electrocatalyst during the electrode ink preparation. Functionalization of the graphene (Choi et al., 2011; Kou et al., 2009; Park et al., 2011; Kuila et al., 2012) is usually done by (diallyldimethylammonium chloride) (PDDA) (He et al., 2012; Shao et al., 2010), and nitrogen doped graphene (Geng et al., 2011; Jafri et al., 2010).

2.2.1 Properties of graphene supported metal electrocatalyst

Electrochemical properties of the graphene supported electrocatalyst were evaluated by many researchers for fuel cell application. ESA is one of the important characteristics of the electrocatalyst. The ESA is usually done by cyclic voltammetry (CV) using hydrogen adsorption/desorption (HAD) on the Pt/GP electrocatalyst. Electrocatalytic activity of the supported Pt catalyst depends on the presence of nano-sized (around 1-5 nm) Pt particles on the support material (Yano et al., 2006). Table 2.5 shows various properties of graphene supported Pt electrocatalyst. Significant improvement in the electrocatalytic activities is observed, when GP is used instead of CNT and carbon black as electrocatalyst supports (Li et al., 2009). On comparison of the electrochemical activities of the Pt/GP with Pt/C electrocatalyst, the ESA of Pt/GP is found to be 44.6 $m^2 \cdot g^{-1}$Pt, which is higher than the commercial electrocatalyst Pt/C (30.1 $m^2 \cdot g^{-1}$) (Li et al., 2009). The higher ESA of Pt/GP is attributed to the high surface area of GP, better interaction between Pt and GP nanoparticles, the good charge transport property of GP sheets, and easy loading of noble metal nanoparticles on GP surface. Another example of high ESA for the Pt/GP electrocatalysts with 40, 60, and 80 wt.% Pt loading was reported as 53, 51, and 36 $m^2 \cdot g^{-1}$, respectively, while the ESA of commercial Pt/C (40wt.%) was around 26 $m^2 \cdot g^{-1}$ Pt (Choi et al., 2011). The Pt particle sizes for the 40wt.%, 60wt.%, and 80wt.% Pt/GP electrocatalysts were found to be around 1.8, 2, and 2.9 nm, respectively (Choi et al., 2011). It also reported that the Pt nanoparticles are highly dispersed on GP surface even at high Pt loadings (60wt.%). Generally, well dispersed high Pt loading on the carbon black support is very difficult to obtain, because the Pt nanoparticles tends to sinter due to weak interactions between Pt nanoparticles and low surface area carbon support (Liu et al., 2010). ESA mainly depends on the dispersion of Pt on the support materials and the size of Pt particles. Pt/GP electrocatalysts exhibit much higher stability

and enhanced current density as compared to Pt/C catalyst even for methanol oxidation reaction (MOR) analyzed by CV analysis (Bong et al., 2010; Dong et al., 2010; Liu et al., 2010; Wang et al., 2011; Choi et al., 2011; Xin et al., 2011). However, the electrochemical stability of the GP supported Pt electrocatalyst is not studied.

In this regards, Pt/GP electrocatalyst was prepared and activity as well as stability towards electrochemical oxygen reduction reaction (ORR) of the GP based electrocatalyst were evaluated (Kou et al., 2009). The Pt/GP (20wt.%) shows an initial ESA of 108 $m^2 \cdot g^{-1}$Pt, which decreased to 67.6 $m^2 \cdot g^{-1}$Pt (around 38% degradation) after 5000 cycles of cyclic voltammetry operation. It has also been reported that beyond the 5000 cycles the Pt particle size of the Pt/GP electrocatalyst increased from 2.5 nm to 5.5 nm. On the other hand, the Pt particle size of the commercial Pt/C increases from 2.8 nm to 6.9 nm after 5000 cycles of CV analysis. However, the smaller Pt particle size in Pt/GP electrocatalyst is required for high ESA and activity of electrocatalysts. However, it is reported that the electrocatalytic activities of GP based Pt electrocatalysts can further be improved using functionalization of GP particles.

He et al., (2012) found a severe degradation (49.2%) of Pt/GP electrocatalyst as compared to PDDA functionalized Pt/FGP (22.1%) after 3000 cycles of CV analysis using ORR. However, it is reported that PDDA functionalized graphene support improves the dispersion of Pt nanoparticles as well as stabilizes GP sheets against restacking during the reaction (Ha et al., 2011). On the other hand, the nitrogen doped graphene (N-GP) was found to be an effective way to improve the anchoring sites as well as better exploitation of the electrochemical activity of the Pt particles (Zhang et al., 2010). The dispersion of Pt nanoparticles on N-GP support was better than on GP support. Moreover, the MOR current density using CV analysis of Pt/N-GP was three times higher than the commercial

Pt/C electrocatalyst. Similarly, four times higher MOR current density using CV analysis was observed for Pt/GP (0.12 $mA \cdot cm^{-2}$) as compared to Pt/C (0.03 $mA \cdot cm^{-2}$) (Yoo et al., 2009).

Another alternative procedure against functionalization was reported to prevent the staking of GP sheets, in which the CNT was used along with GP as electrocatalyst support for Pt electrocatalyst (Yang et al., 2010). The 1D CNTs act as nano-spacer between 2D graphene nanosheets to effectively inhibit the face-to-face stacking and/or agglomeration of GP layers. The ESA of the Pt/C, Pt/CNT, Pt/GP, and Pt/GP/CNT was found to be 43.63, 51.46, 94.06, and 127.78 $m^2 \cdot g^{-1}$Pt, respectively. In addition, the incorporation of CNT also improved the pathway for mass transfer of the chemical reactants and products and work as an electrical bridge between the GP sheets. The representative electrochemical properties of GP supported Pt electrocatalysts are summarized in table 2.5.

Recently, the supported Pt-alloy electrocatalysts were found to be more electrochemically active due to their enhanced catalytic properties relative to individual carbon supported Pt electrocalatyst (Rao et al., 2011; Lobato et al., 2011; Dutta et al., 2011). Amongst the many Pt-alloy, Pt-Co, and Pt-Cr were found to be more efficient to enhance the ORR activity at low overpotential (Rao et al., 2011). The ESA of the Pt-alloy electrocatalysts was found to be 65, 57, and 55 $m^2 \cdot g^{-1}$ Pt for Pt/GP, Pt_3Co/GP, Pt_3Cr/GP electrocatalysts, respectively. Moreover, it was found that the ORR activity of the Pt_3Co/GP and Pt_3Cr/GP electrocatalyst was 3-4 times higher than that of Pt/GP electrocatalyst. The overpotential for ORR of the Pt-M/GP (M: metal) is 45-70 mV less than the Pt/GP. The stability of the graphene supported Pt, Pt_3Co/GP, and Pt_3Cr/GP electrocatalyst was conducted using ORR analysis. The marginal degradation was observed in ORR activity using CV after

500 cycles of Pt/GP, Pt_3Co/GP, and Pt_3Cr/GP electrocatalyst, which was within 5%. Therefore, the graphene as electrocatalyst support for Pt-alloy can also improve the electrochemical activities and stability of the electrocatalyst. In addition, the graphene based Pt electrocatalyst enhance the CO tolerance as compared to commercial Pt/C electrocatalyst, which is one of the most important desired properties of PEMFC hydrogen fuel cell electrocatalyst. It is well known that the major source of hydrogen as fuel is steam reforming of hydrocarbons (James and Andrew 2003). The hydrogen gas obtained by steam reforming process generally contains trace amount (Cross 1999) of carbon monoxide (CO), which easily adsorbed irreversibly on the surface of Pt and thus poison the PEMFC anode electrocatalyst. Therefore, the high CO tolerance of the electrocatalyst is required for the hydrogen fuel cell (Yoo et al., 2009; Yoo et al., 2011). Pt/GP electrocatalyst is evaluated for the CO stripping analysis and compared with commercial Pt/C electrocatalyst and it is found that the CO adsorption rate of Pt/GP is significantly (about 40 times) lower than Pt/C electrocatalyst (Yoo et al., 2009). In their further studies a more significant support effect is observed in the presence of H_2 and 500 ppm CO mixture for Pt/GP, Pt/C, and Pt-Ru/C electrocatalysts and compared the performance using pure hydrogen gas (Yoo et al., 2011). The hydrogen oxidation reaction (HOR) activity of the Pt/GP in H_2+CO mixture was found to be 52% of pure H_2. In contrast, the electrocatalytic activity exhibited by Pt/C was around 11% of the pure H_2. In comparison, Pt-Ru/C which is well known CO tolerant electrocatalyst, maintained electrocatalytic activity upto 45% (of pure H_2) under mixture of 500 ppm CO and H_2. It was found that the catalytic activity towards CO tolerance of Pt/GP was significantly superior as compared to Pt/C and that the substrate carbon material altered the catalytic properties of the Pt for the PEMFC. The two possible reasons attributed to the excellent CO tolerance for HOR activity of the Pt/GP electrocatalyst are the presence of sub-nano-

Pt cluster on the graphene surface, which promoted CO tolerance, and the modification of the Pt electronic structure by graphene support.

Therefore, to minimize the CO poisoning on the Pt surface, various GP supported bimetallic nanoparticles, such as PtPd, PtAu, AuPd, PdRu, and PtAg, significantly attracted researchers due to their enhanced catalytic activity relative to individual Pt-based nanoparticles (Rao et al., 2011; Guo et al., 2011; Dong et al., 2010; Tan et al., 2013). Core-shell nanoparticles as particular type of arrangement of binary metals have attracted much attention in electrochemical energy conversion (Giorgio and Henry 2002; Sobal et al., 2003; Sao-Joao et al., 2004; Zhang et al., 2005; Mani et al., 2008; Strasser et al., 2010; Hasche et al., 2011). Dependent on the shell thickness, the improved long-range geometric effects such as lattice strain. It can be seen that the enhanced electrochemical activities was observed for both MOR and ethanol oxidation reaction (EOR) with PtRu/GP electrocatalyst as compared to Pt/C (Dong et al., 2010). Moreover, the adsorption of CO species on the surface of Pt particles was greatly reduced due to introduction of Ru metal into the Pt/GP electrocatalyst. Furthermore, ternary metal-alloy electrocatalysts also attracted the scientific community due to their superior electrocatalytic activities and stability than single and bimetallic electrocatalysts (Zhang et al., 2009). It is reported that the PtPdAu/GP electrocatalyst provides higher electrocatalytic performance with reduced overpotentials as compared to GP supported single metallic and bimetallic electrocatalyst.

Graphene is evaluated not only as electrocatalyst support but also attracted significant attention as metal free electrocatalyst for fuel cell applications. Significantly higher ORR activity was found using metal free N-GP as compared to commercial Pt/C electrocatalyst (Gong et al., 2009).

Table 2.5: Properties of graphene or functionalized graphene supported electrocatalysts

Developed ectrocatalyst (electrocatalytic activity of comparison with other catalyst)	**Electro-chemical analyses**	**ESA ($m^2 \cdot g^{-1}$)**	**Pt particle Size (nm)/loading (wt.%)**	**Evaluated in anode or cathode of PEMFC**	**Comparison of single cell PEMFC performance with commercial catalyst**	**References**
Pt/GP(>Pt/C)	HAD;MOR	44.6	5-6/45	-na-	-na-	Li et al., 2009
Pt/FGP(>Pt/CNT>Pt/C)	HAD;ORR	-na-	3.5/20	-na-	-na-	Shao et al., 2010
Pt/(GP-CNT) (>Pt/GP>Pt/CNT>Pt/C)	HAD	127.78	2-2.4/20	-na-	-na-	Yang et al., 2010
Pt/FGP (>Pt/C)	HAD;ORR	108	2/20	-na-	-na-	Kou et al., 2009
Pt/GP (> Pt/C)	ORR	-na-	2.9/70	Cathode	Pt/GP>Pt/C	Ha et al., 2011
Pt/GP	HAD;ORR	65	3.5/40	Cathode	Pt/GP	Rao et al., 2011
Pt/GP (>Pt/C)	HAD	24.01	2-3/20	-na-	-na-	Yoo et al., 2011
Pt/GP (>Pt/C)	MOR	53	1.8/40	-na-	-na-	Choi et al., 2011
Pt/GP	-na-	81.8	2.4/20	-na-	-na-	Song et al., 2009
Pt/GP (>Pt/C)	HAD;ORR	-na-	5-8/20	-na-	-na-	Wu et al., 2011
Pt/GP (>Pt/C)	ORR	-na-	3-5/10	-na-	-na-	Xin et al., 2011
Pt/FGP (>Pd-Pt/GP>Pt/GP)	HAD;ORR	-na-	1.95/~40	-na-	-na-	He et al., 2012
Pt/GP (>Pt/C)	MOR	-na-	2-4/-na-	-na-	-na-	Sun et al., 2013

-na-: not available

The current research work indicated that the GP and its derivatives doped with other heteroatoms such as boron-doped, phosphorous-doped, and sulfur-doped could also enhanced ORR electrocatalytic activities (Yang et al., 2011b; Liu et al., 2011; Yang et al., 2011a). Recently, boron and nitrogen doped GP (BN-GP) was synthesized for electrochemical ORR activity. It was observed that the electrocatalytic activity of metal-free BN-GP electrocatalyst was better than the commercial Pt/C electrocatalyst (Wang et al., 2012).

It can be seen that the graphene and functionalized graphene supported Pt and/or Pt-alloy electrocatalyst show superior electrocatalytic activities as compared to Pt/C and Pt/MWCNT (Lee et al., 2011) for PEMFC applications. However, from the practical point of view, the fuel cell test is the ultimate evaluation criterion for the supported electrocatalyst. For example, Seger and Kamat reported a single-cell PEMFC performance using Pt/GP or Pt electrocatalyst at cathode whereas at anode commercial Pt/C was used. They have reported that the Pt/GP as a cathode electrocatalyst showed a maximum power density of 0.161 $W \cdot cm^{-2}$ as compared to 0.091 $W \cdot cm^{-2}$ for an unsupported Pt electrocatalyst (Seger and Kamat 2009). The similar kind of support effect was reported, where graphene supported electrocatalyst was evaluated only as the cathode electrocatalyst for PEMFC (Rao et al., 2011; Ha et al., 2011; Jafri et al., 2010). Furthermore, regarding efficient PEMFC electrocatalysts, the main issues are long-term electrochemical stability while maintaining high electrochemical active surface area. The presence of CO content in the reformate hydrogen accelerated the poisoning of Pt electrocatalyst. The CO is easily adsorbed on the Pt surface and start to degradation of its electrocatalytic activity within very short period of time. One possible solution of combating issues is the use of the high temperature (100–200°C) PEMFC (HT-PEMFC), instead of using pure hydrogen which is costly and also difficult to production as per

increased future demand. The subsequent section will be discussed about the importance of HT-PEMFC and its issues in details.

2.3 High temperature PEMFC components

Increasing attention has been given recently to HT-PEMFC (100–200°C) systems due to their several advantages namely, reduction of CO poisoning of the platinum, use of reformed natural gas instead of purified hydrogen, faster reaction kinetics, simple cooling device and water management system, and flexibility to use non-noble metal catalyst. All of these factors also contribute to the highly durable and reduced Pt platinum loading in the HT-PEMFC. However, operating HT-PEMFC has some issues also such as higher temperature results in more rapid degradation, including corrosion of bipolar plates and catalyst support, alongside degradation of seals, and membranes. As a result, stability of HT-PEMFC is still remain a primary focus of research.

Therefore, there is need to develop PEMFC components, which can be sustained at elevated temperature (100-200^{o}C) in HT-PEMFC without any adverse effect on their physicochemical properties. As discussed earlier that the different form of carbon materials are key materials for the development of efficient PEMFC components such as composite bipolar plate (NG, CB, CF, and GP) and electrocatalyst support (CB and GP). It is also reported that the carbon and its derivatives hardly degrade within the temperature range of 100-200^{o}C (Shao et al., 2014). Moreover, the polymer present in the carbon-polymer composite may start degrading when it is operated at high temperature. However, there is no report available on the mechanical and electrical properties of carbon-polymer composite bipolar plate at elevated temperature. Therefore, it is required to evaluate the composite bipolar plate properties at elevated temperature.

2.4 Summary of literature review

This chapter has shown the research findings on bipolar plate, electrocatalyst support, and stability issues of HT-PEMFC especially bipolar plate. The emphasis was given to the literatures using graphene as one of the ingredients in these components. From the literature review, it is quite evident that many of the properties have not been studied thoroughly as well as some of the crucial properties are far away the stringent target properties given in table 2.1 (page 18). The flexural strength, through-plane electrical conductivity, hydrogen permeability, thermal conductivity, interfacial contact resistance, as well as anodic and cathodic corrosion resistance are the main properties among them.

The through-plane electrical conductivity of a bipolar plate, in a fuel cell stack, is more important than the in-plane electrical conductivity, as electrons are collected by the plate at the anode side and migrate through the plate to the cathode side of the cell. In addition, high through-plane electrical conductivity not only increase the electron mobility but also decrease the ohmic losses of PEMFC stack. At the same time, anodic and cathodic corrosion poses one of the big challenges in selecting the bipolar plate materials. Therefore, research is going on to improve the graphite-polymer composite bipolar plate using different types of carbon fillers, which include natural graphite (NG), synthetic graphite (SG), carbon black (CB), carbon fiber (CF), and carbon nanotube (CNT) (Allaoui et al., 2002; Huang et al., 2005; Blunk et al., 2006a; Hwang et al., 2008; Kakati et al., 2010; Sohi et al., 2011; Tjong 2011; Taherian et al., 2012). It is reported that the CF was mainly reinforced into the carbon-polymer composite to change the mechanical strength in order to meet the stringent target values. However, it is also reported that at higher loading of CF the electrical conductivity is adversely affected owing to the percolation threshold of the carbon-polymer composite (Lee et al., 2009; Kakati et al.,

2010; Guo and Leu 2012). It was found by many authors and by our research group also that 5% CF loading was an optimum content in the composite bipolar plate (Taherian et al., 2011). However, the electrical conductivity (especially through-plane) of the composite bipolar plate was found below the benchmark for 5% CF loading (Kakati and Verma 2011).

The development of graphene opened up many possibilities to be used in various applications due to its extraordinary properties. The use of graphene in energy conversion devices such as fuel cell is being explored in full extent. The present state-of-art of PEMFC is not competitive enough to penetrate the market due to various challenges. These challenges include high cost, low performance as well as stability issues of various components. Carbon is used in many components of PEMFC such as composite bipolar plate and electrocatalyst support material. The different forms of carbon material such as graphite, carbon black, carbon fiber, carbon nanotube are widely studied for the PEMFC components. However, it is quite evident from the literature review that the graphite alone with CB and CF cannot offer the sufficient properties to the bipolar plate, which is required for PEMFC application. It has been found that incorporation of graphene in bipolar plate improves the performance by great extent, especially electrical conductivity. The systematic approach to replace a small part of NG in the composite by CB, CF, and GP has achieved a suitable carbon-polymer composite bipolar plate. It is observed that that the through-plane electrical conductivity and flexural strength of the NG/polymer (Hsiao et al., 2010) or CF/CB/NG/polymer (Kakati and Verma 2011) composites were increased significantly due to the incorporation of only 0.2 phr and 1% GP content, respectively. However, still the flexural strength (49.2 MPa or 57.28 MPa against 59 MPa) was not reached to the stringent target as set in the table 2.1. Moreover, the other important properties of bipolar plate such as hydrogen permeability, thermal conductivity,

thermal conductivity, and interfacial contact resistance are not reported. Furthermore, the anodic and cathodic corrosion current density of the composite bipolar plate is hardly reported in any literature, which is one of the most important properties of the bipolar plate according to DoE. Therefore, it is expected that the flexural strength can be improved by incorporating CF suitably.

It may be noted that the effect of CF loading in carbon-polymer composite is investigated by many researchers and scientist but the investigation on CF length is hardly discussed. Similarly, graphene is evaluated at a particular loading (Hsiao et al., 2010; Kakati and Verma 2011) in carbon-polymer composite bipolar plate but hardly any literature shows the effect the graphene content on the composite bipolar plate.

It is found that the graphene and functionalized graphene supported Pt and/or Pt-alloy electrocatalysts are superior as compared to Pt/C and Pt/MWCNT for fuel cell electrocatalytic activity. The better dispersion was responsible for the higher electrochemical activity of Pt/GP as compared to commercial Pt/C electrocatalyst. In order to reduce the cost of PEMFC systems, optimum utilization of Pt with narrow particle size distribution, good dispersion and high electrochemical activity should be achieved because platinum plays a critical role in the PEMFC system. It is found that the electrochemical long term stability of Pt/GP and Pt/FGP for HAD are not studied thoroughly. It is also reported that the graphene supported bimetallic electrocatalysts are more favorable as compared to single metal to increase the electrochemical activity. Although enhanced half-cell electrochemical properties have been observed using graphene supported electrocatalyst. However, from the practical point of view, the fuel cell test is the ultimate evaluation criterion for the supported electrocatalyst. Only a few research work are reported in which the performance of the PEMFC is evaluated using

Pt/GP as the cathode electrocatalst whereas commercial Pt/C was used as the anode electrocatalst (Seger and Kamat 2009; Rao et al., 2011; Ha et al., 2011; Jafri et al., 2010). It is found that the research work is being conducted on graphene but the work on graphene as a support material for fuel cell is feeble. Moreover, the potential of the graphene in PEMFC is still under exploited. There is hardly any report with graphene supported platinum catalyst replacing the anode and cathode catalysts of PEMFC. Furthermore, it is reported that the functionalization of GP improved the dispersion of nanosized Pt electrocatalyst. However, hardly any systematic study is reported in the open literature, where both GP and FGP are used as an electrocatalyst support.

On the other hand, it is expected that the HT-PEMFC technology emerged from the research stage within the recent years and considerable progress has been made towards commercialization. The phosphoric acid doped polybenzimidazole (PBI) membranes meet the DoE targets for high temperature membranes operating under no humidification on both anode and cathode sides (barring the stability). This eliminates the stringent requirement for humidity. However, HT-PEMFC has many drawbacks including increased degradation, leaching of PA acid and incompatibility with carbon-polymer composite bipolar plate. Therefore, it is required to evaluate the stringent target properties of the carbon-polymer bipolar plate at elevated temperature.

2.5 Aim and Objectives

It is evident from the literature review that the graphene has great role in the PEMFC components. However, it is not explored in great extent. Therefore, the main aim of the research work is to synthesis, characterize, and utilize GP in the carbon-polymer composite bipolar plate for PEMFC, as an electrocatalyst support as well as to evaluate the suitability of the developed bipolar plate for HT-PEMFC application. To obtain the

main aim, the research work is divided into four objectives. In the first objective, graphene will be synthesized and characterized. In the second objective, the graphene will be used in carbon-polymer composite bipolar plate. It may be noted that we have used the base composition of the bipolar plate as CF/CB/NG/NPFR 5/5/60/30%, CF/CB/NG/RPFR 5/5/65/25%, and CF/CB/NG/VER 5/5/65/25% (Kakati and Verma 2011). The properties of the above composite are shown in the table 2.4. This base composition was further reinforced by graphene and carbon fiber in order to enhance the properties of the carbon-polymer composite bipolar plate to achieve the benchmark as shown in the table 2.1. In the third objective, the optimized bipolar plate is evaluated for its applicability for HT-PEMFC application. In the fourth and last objective, the graphene is evaluated as an electrocatalyst support for PEMFC. The various investigations under these objectives are shown below to achieve the research aim.

I: Synthesis and Characterization of Graphene

- The developed graphene is characterized using physicochemical (XRD, Raman, AFM, FTIR), thermal, morphological (FE-SEM and TEM), elemental (EDS), and BET surface area analysis.

II: Graphene Reinforced Carbon-polymer Composite Bipolar Plate Development, Characterization, and Evaluation in PEMFC

- The developed bipolar plate is developed and characterized
- PEMFC performance is evaluated using developed composite bipolar plate

III: Evaluation of Carbon-polymer Composite Bipolar Plate for HT-PEMFC Application

- The mechanical, electrical, corrosion and thermal properties of the bipolar plate is evaluated at elevated temperature

IV: Synthesis and Characterization of Graphene Supported Electrocatalyst

- The characterization of electrocatalsts is carried out using structural (XRD), morphological (FE-SEM and TEM), and electrochemical (ORR and CV) analysis.
- PEMFC performance is evaluated using synthesized electrocatalyst

Chapter 3

Synthesis and Characterization of Graphene

Chapter 3

Synthesis and Characterization of Graphene

This chapter covers experimental procedures for synthesis and characterization of graphene. The chemical oxidation followed by thermal exfoliation of natural graphite is used to synthesis the graphene. The formation of graphene is confirmed by various characterization techniques and described in details.

3.1 Background

Graphene, a single-atom-thick 2D sheet of carbon atoms (sp^2-hybridized) arrayed in a honeycomb pattern is the ever known thinnest, and strongest material, having excellent electrical conductivity and mechanical strength (Novoselov et al., 2004; Geim 2009). No wonder that this two-dimensional material is considered, from the application point of view, to be even more promising than other nanostructured carbon allotropes such as 1D carbon nanotubes and 0D fullerenes. Since its discovery in 2004 (Novoselov et al., 2004), a major focus of experimental research has been concentrated on the development of new synthetic routes enabling an effective production of well-defined graphene sheets (Geim and Novoselov 2007; Stankovich et al., 2006; Xu et al., 2008b; Park and Ruoff 2009). The commonly applied methods include the micromechanical cleavage of graphene with adhesive tape (Novoselov et al., 2004), chemical vapour deposition (CVD) on metal surfaces (Reina et al., 2008), epitaxial growth on SiC (Emtsev et al., 2009), direct sonication of graphite powder (Lotya et al., 2009), hydrothermal reduction (Kaniyoor et al., 2010), and chemical oxidation followed by thermal exfoliation of natural graphite (Stankovich et al., 2006). Among the various methods of graphene synthesis, the

chemical oxidation followed by one-step thermal exfoliation of natural graphite has been regarded as one of the most attractive for large volume production of single and a few layer of graphene sheets (Li et al., 2008; Lotya et al., 2009; Kim et al., 2009). The carbon atoms in the graphene crystal lattice are bonded together with σ bonds and one π electron (due to delocalized p_z orbital) is freely suspended to each of the carbon atoms that contribute to a delocalized network of electrons (Zhu et al., 2010). This distinct structure of graphene has received considerable attention because of its fascinating properties including very high theoretical surface area (around 2630 $m^2 \cdot g^{-1}$) (Stankovich et al., 2006), highest electrical conductivity (around 10^6 $S \cdot cm^{-1}$) (Geim and Novoselov 2007), very high thermal conductivity (5000 $W \cdot m^{-1} \cdot K^{-1}$) (Dai et al., 2012) (very good mechanical strength (100-200 times stronger than steel), inherent flexibility, high aspect ratio, and unique basal plane structure (Novoselov et al., 2004; Geim and Novoselov 2007; Xu et al., 2008b).

These unique physicochemical properties make it a potential material providing new approaches and critical improvements in many fields of science and technology including, electrochemistry and fuel cell. For example, the high surface area of electrically conductive graphene sheets can be reinforced to carbon-polymer composite bipolar plate to increase the electrical and mechanical properties as well as it can be used as an electrocatalyst support materials to increase the electrochemical activity. The graphene was synthesized using chemical oxidation followed by thermal exfoliation of NG so as to use in the PEMFC components. The synthesis and characterization procedures of graphene are discussed in the subsequent sections.

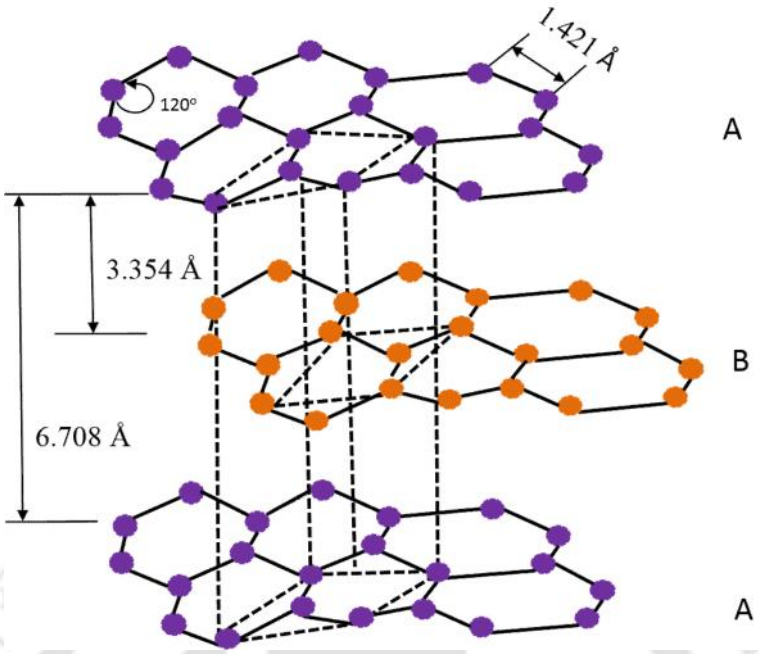

Figure 3.1: Schematic of natural graphite structure (solid circle shows carbon atoms; solid line shows σ-bonds; dotted line shows π-bonds)

3.2 Experimental

3.2.1 Materials

Industrial grade NG with purity of 98% and average size of 63 μm was supplied by Jayesh Trading Co., Mumbai, India. The pure graphite structure shown in fig. 3.1 consists of hexagonal net planes of carbon, stacked along the c-axis in a staggered array usually denoted as ABAB… (Solin 1997).

The stacked layer in the graphite plane is separated by 3.354 Å. The unit layer of graphite is named graphene. Each carbon atoms in the graphene sheet are attached with three covalent bond (bond length 1.421 Å). The fourth valence electron takes part in weak van der Waal bonding (π-bonding) with another layer of graphene sheet to form graphite structure (Liu et al., 2008). Sulfuric acid (H_2SO_4), sodium nitrate ($NaNO_3$), potassium permanganate ($KMnO_4$), hydrogen peroxide (H_2O_2), and dimethylformamide (DMF) were procured from Merck, India.

3.2.2 Methods

3.2.2.1 Synthesis of graphene

The synthesis of graphene (GP) from NG using chemical oxidation followed by thermal exfoliation method can be broadly divided to two steps, (i) chemical oxidation of NG to synthesize graphite oxide or graphite intercalated compound and (ii) thermal exfoliation of GO to finally prepare graphene. Figure 3.2 shows the different steps involved in the synthesis of GP.

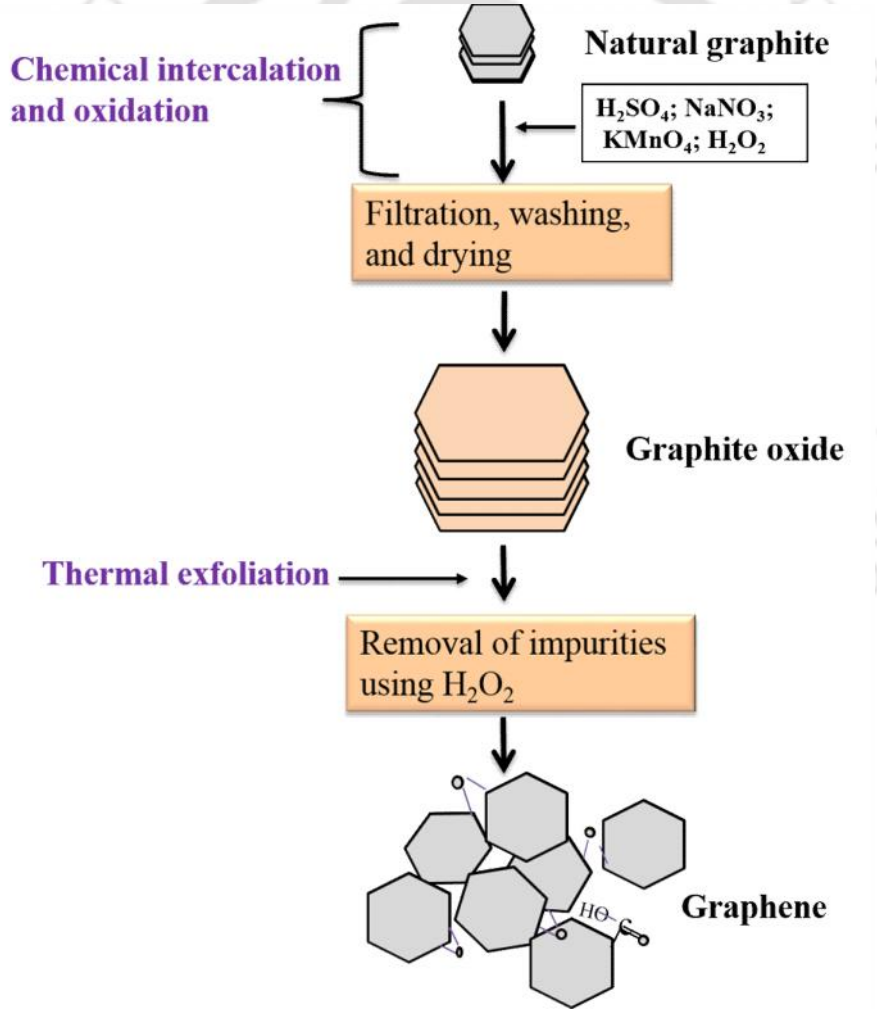

Figure 3.2: Synthesis route of single layer graphene by chemical oxidation followed by thermal exfoliation of NG

The graphite oxide was prepared from NG flakes using modified hummer's method (Hummers and Offeman 1958). The NG was first dried in vacuum oven for overnight to remove the moisture content before using. Required amounts of NG, concentrated H_2SO_4, and $NaNO_3$ were mixed in a conical flask. The above mixture was thoroughly stirred with the help of a mechanical stirrer for 30 minutes. The ingredients were mixed and cooled to subzero temperature in an ice-bath. Then $KMnO_4$ was added to the above mixture and rigorously stirred for 1 h. The rate of addition was controlled carefully to keep the temperature of the suspension below 20°C. The above mixture was then diluted with warm water and treated with 30% H_2O_2 to reduce the residual permanganate to colorless soluble manganese sulfate. The resultant suspension turned to yellow-brown color. Thereafter, the final mixture was filtered, washed thoroughly with running millipore water, and dried in a vacuum oven at 135°C for 12 h to obtain the GO.

The obtained GO was further processed to synthesized graphene. Thus the above dry GO was ground to powder form and then transferred to a silica crucible and subjected to thermal shock at about 1050°C in a muffle furnace for a few seconds. The thermally exfoliated graphite oxide may also have trace amount of metal ions such as potassium and manganese. Therefore, it was further treated with H_2O_2 and dispersed with the help of ultrasonication for 1 h. Then the treated mixture was centrifuged and washed thoroughly using millipore water. The sample was then kept in a vacuum oven at 75°C for 12 h. Finally, the GP was obtained and it was stored in an air tight vacuum desiccator for further characterization.

3.2.3 Characterization

The developed GP was characterized using X-ray diffractometer (XRD), Raman spectroscope force microscope (AFM), thermogravimetric analyzer (TGA), Fourier

transform infrared spectroscope (FTIR), field emission scanning electron microscope (FE-SEM), transmission electron microscope (TEM), selected area electron diffractometer (SAED), energy dispersive X-ray spectroscope (EDX), and Brunauer–Emmett–Teller (BET) surface area analyzer.

3.2.3.1 In-situ XRD analysis

The XRD analysis of the GP was carried out in an advanced diffractometer (Bruker, D8 Advanced, USA) and compared with the NG and GO. The measurements were performed using CuKα source at a scan rate of 0.05° s^{-1}. The wavelength of the CuKα X-ray was approximately 1.5406 Å at 40 kV and 40 mA operating voltage and current, respectively. The samples were dried and kept over a glass slide which was later fixed in the XRD analyzer.

3.2.3.2 Raman analysis

Raman spectroscopy analysis is defined by the molecular and crystal lattice vibrations and therefore it is sensitive to the composition, bonding, chemical environment, phase, and crystalline structure of the sample material. These characteristics make it an exceptional method for unambiguously identifying materials in any physical form: gases, liquids, solutions, and crystalline or amorphous solids. The synthesized GP was characterized using Raman (LabRAM HR: IGA-512X1-50-1700-3LD; USA) instrument equipped with a confocal microscope (SPEX 500M), a charge-coupled devices (CCD) camera (1024 × 256 pixel) cooled with liquid nitrogen with 633 nm wavelength laser line, and homemade sample stage. The powder form of GP sample was dried over night before sampling on glass slide for Raman analysis.

3.2.3.3 AFM analysis

The AFM (Molecular Imaging: PicoScan^{TM} 2500; USA) of the developed GP was carried out to study the nano-level morphology. GP in powder form was mixed with isopropanol and dispersed thoroughly using ultrasonication. The homogeneously dispersed GP slurry was then spread over an ultra-flat mica substrate and kept in a vacuum oven to remove the volatile content. The mica slide was then used to carry out the AFM analysis. The thickness of the graphene sample was measured by the height profile at the edge of a graphene sheet (Chandra et al., 2010; Soldano et al., 2010).

3.2.3.4 BET surface area analysis

The surface area of the developed GP was measured in BET surface area analyzer (Beckman Coulter, SA 3100, Russia) using nitrogen adsorption isotherm at 77 K and compared with the NG. Approximately 80 mg of the sample was degassed at 250°C for 2 h to remove moisture content and volatile content. The sample was then weighed under air tightened, after which it was inserted into the analysis port and analyzed automatically at liquid nitrogen temperature.

3.2.3.5 TGA analysis

The thermal behavior of the GP was studied using TGA analyzer (Mettler Toledo: SDTA 851e, Switzerland) and compared with NG. Approximately 10 mg of sample was taken in a 70 µL alumina crucible and analyzed in the temperature range of 25–600°C at a heating rate of 10°C·min^{-1} under nitrogen gas.

3.2.3.6 FTIR analysis

The developed GP was analyzed using FTIR spectrometer (Perkin Elmer: Spectrum One spectrometer; USA) to identify the presence of functional groups and compared with NG.

The dry and purified graphene sample was finely ground with KBr pallet in a marble mortar and pestle. This powder mixture was then pressed in a mechanical press to form a translucent thin pellet. The pellet was scanned in the range of 500–4000 cm^{-1}. The NG sample was also prepared in a similar manner.

3.2.3.7 FE-SEM analysis

The surface morphology of developed GP was studied using FE-SEM (Carl Zeiss: Sigma; Germany) and compared with GO. The powder samples were dispersed in isopropanol with the help of an ultrasonic bath. The thoroughly dispersed solution was spread over a conductive aluminum sheet and kept in the oven to remove the volatile content. The dried samples were directly mounted on the FE-SEM stub and subjected to morphological analysis without any conductive coating owing to all the carbon materials used in this study are conductive.

3.2.3.8 TEM and SAED analyses

The nanoscale morphology of GP particles was conducted using TEM (JEOL: JEM 2100; Japan). The samples were dispersed ultrasonically in isopropanol for 30 min. for TEM analyses. The homogeneously dispersed sample was then put on 300 mesh size copper grid with holey carbon film using micropipette. The grid along with the sample was then transferred to a petridish and dried in a vacuum oven to remove the volatile content. The TEM grid along with the sample was mounted on a single axis tilt sample holder and inserted into the TEM goniometer. The sample was optically aligned for further analysis. The SAED was also studied separately using TEM instrument over a limited area of GP samples to know the crystalline nature.

3.2.3.9 EDX analysis

The composition of the synthesized GP was analyzed quantitatively using scanning electron microscope equipped with a cold field emitter and an energy dispersive X-ray spectroscopy (Oxford Instruments: INCA X-sight; USA). The EDX scans for each samples were analyzed and averaged about a large range on different samples.

3.3 Results and discussion

3.3.1 XRD analysis of graphene

The powder XRD analyses of NG, GO, and GP particles were carried out and the diffractograms are shown in fig. 3.3. The C(002) graphite peak is visible at around 26.54°, which corresponds to the d-spacing of the graphite crystal. The length of the C-axis of the graphite crystal was calculated from the XRD analysis of NG, and it was found to be 6.712 Å. The detailed analysis of the XRD pattern shows that the lengths of the other two axes were 2.456 Å. The graphite C(004) peak was also visible in the fig. 3.3 at 54.70°. From the fig. 3.3 it can be seen that the C(002) and C(004) peaks of NG was disappeared in the diffractogram of GO. During the treatment of the NG with harsh chemical environment the van der Waals bonding between two consecutive graphene layers (of the NG) may be broken and/or covalent bonding may be created through oxide ions.

Therefore, the C(002) and C(004) diffraction peaks disappeared in the diffractogram of GO. However, a new peak appears at around 9.26° (insect fig. 3.3) with d-spacing of 9.267 Å, indicating that the complete conversion NG to GO (Jiang and Drzal 2012). It was found that the interlayer distance between the two consecutive graphene layers was increased from 3.39 Å in NG to 9.267 Å in the GO.

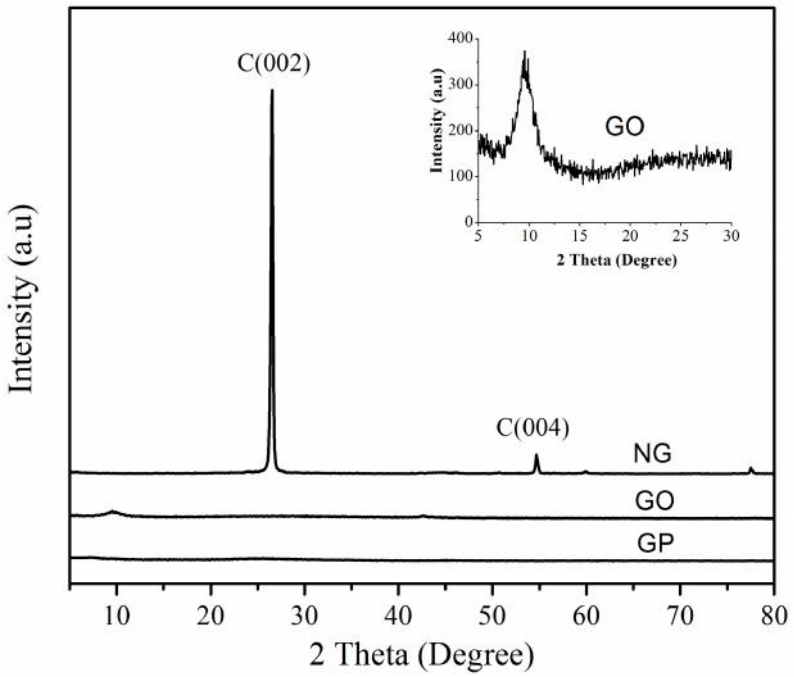

Figure 3.3: XRD diffraction pattern of NG, GO, and GP

The developed GO was later reduced by thermal exfoliation and violently expanded to produce graphene layers. At this stage, all the graphene layers separated to form individual graphene sheets, without having any chemical bonding with another graphene sheets (Geng et al., 2009). The GP is a 2D crystal with chicken wire structure of sp^2 hybridized carbon atoms and the graphene should align parallel to the substrate. Therefore, C(002) and C(004) peaks were also not visible in the GP diffractogram (fig. 3.3) (Kakati et al., 2013). Raman spectra (fig. 3.4) also supported the XRD results, as discussed in subsequent section.

3.3.2 Raman analysis of graphene

Raman scattering is an intense non-destructive technique, which is especially used to examine the ordered and disordered crystalographic structures (Kakati et al., 2013;

Akhavan 2010). The Raman spectra shows in fig. 3.4 is used to distinguish NG and GP which are shown in. The D peak at 1360 cm^{-1} is due to the breathing mode of the sp^2 atoms and is active in the presence of defects and impurities in GP. It can be seen that the intensity of the D peak in GP (fig. 3.4) is increased as compared to NG. It is due to the formation of defects in the graphene sheet during the synthesis of graphene from NG. The G peak at 1595 cm^{-1} is due to the E_{2g} phonon of sp^2 hybridized carbon atoms. Moreover, an intense 2D peak observed at around 2700 cm^{-1} for GP, which is more intense than the 2D peak of NG. It is reported that the intensity of the 2D peak decreases gradually with the increase in graphene layers and reaches minimum for the stack of multilayered graphene, which is nothing but the graphite (Ferrari 2007; Kakati et al., 2013). However, it is well known that the 2D peak is the second order of the D peak. The shape, position, and intensity relative to the D band of this peak depend markedly on the number of layers (Soldano et al., 2010).

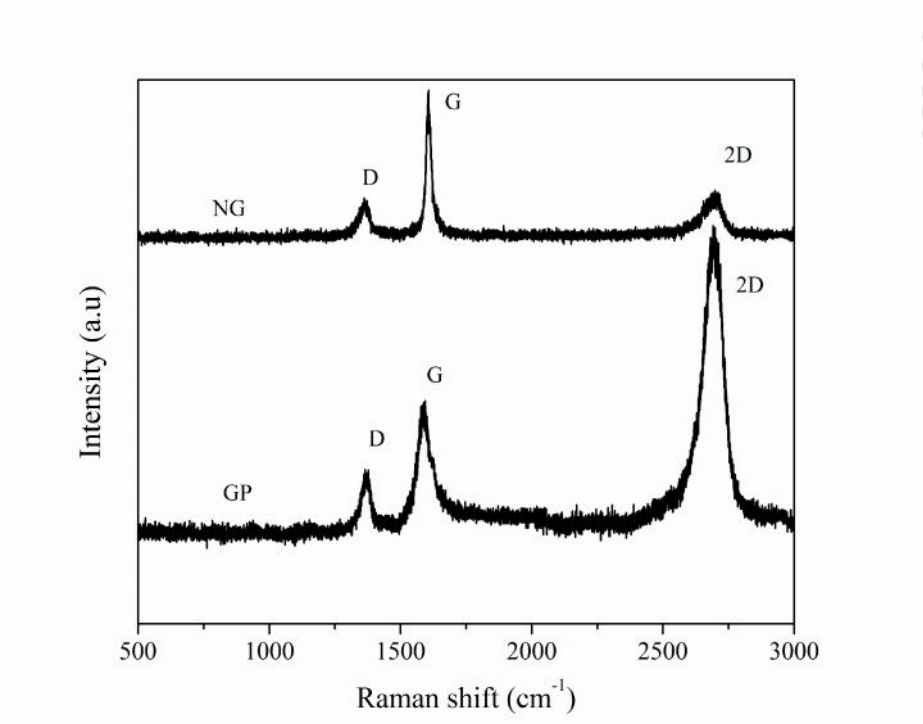

Figure 3.4: Raman scattering of NG and synthesized GP

Therefore, sharp 2D peak confirmed that graphene has been produced successfully. It is confirmed from the above analyses (XRD and Raman) that GP was developed. Therefore, evaluation of the GP thickness is to be done now. Thus the AFM analysis (section 3.2.3.3) of the GP was conducted to determine the thickness of the graphene sheet.

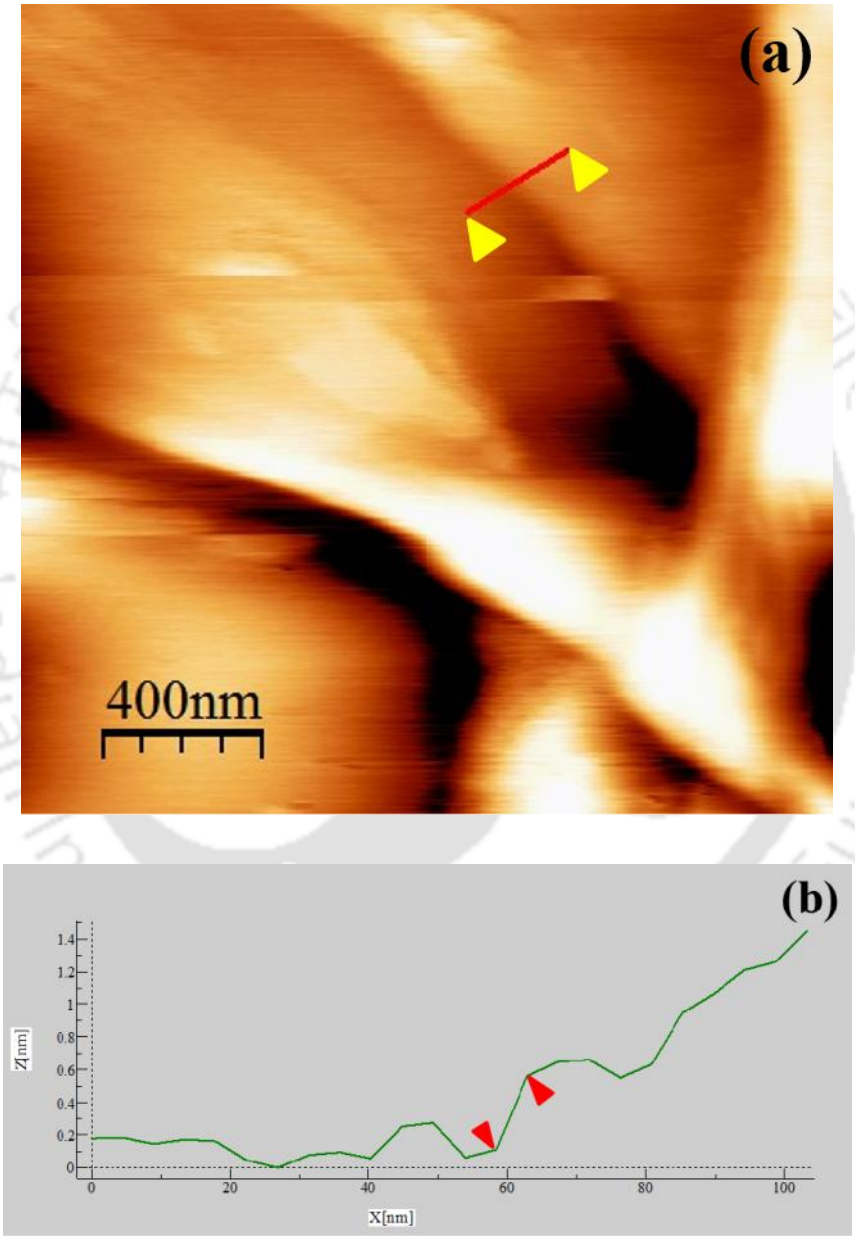

Figure 3.5: (a) AFM micrograph of a graphene sheets, and (b) corresponding height profile at the edge of the graphene layer at a position shown by the marking

3.3.3 AFM analysis of graphene

Figure 3.5(a) shows the deflection profile of the AFM analysis of a GP sheet on the mica substrate. The thickness of the GP sheet was calculated by measuring the height profile at the edge of the sheet. The line of interest is shown in the deflection profile with a red colored line and marked with yellow arrow. The corresponding height profile at the edge of the graphene sheet is shown in fig. 3.5(b).

It was found from the height profile that the thickness of the graphene sheet is around 0.5 nm. It can be noted that the AFM measured thickness is higher than the theoretical thickness of a graphene sheet, which is around 0.35 nm (Schniepp et al., 2006; Stankovich et al., 2006; Ramanathan et al., 2008; Geng et al., 2009; Avinash et al., 2010). It may be due to the difference in tip attraction/repulsion between the insulating substrate and semimetallic GP sheet but also preferential adsorption of thin layer of water on graphene under ambient conditions (Allen et al., 2009).

3.3.4 BET surface area analysis of graphene

The BET surface area analysis of the developed GP was carried out as per the procedure described in section 3.2.3.4. The BET surface area of the NG and GP were found to be around 23.97 and 750.85 $m^2 \cdot g^{-1}$, respectively (Ghosh et al., 2013). The large surface area of GP indicates a near uniform distribution of pores. Although the theoretical surface area of graphene is 2630 $m^2 \cdot g^{-1}$ (Novoselov et al., 2004), this surface area would only be observed in a hypothetical case where no overlap of sheets exists. In a real system, a significant amount of surface area is not available for nitrogen adsorption because of overlap of the exfoliated sheets. Therefore, the resultant surface area of the graphene was less than the ideal surface area of an individual graphene sheet.

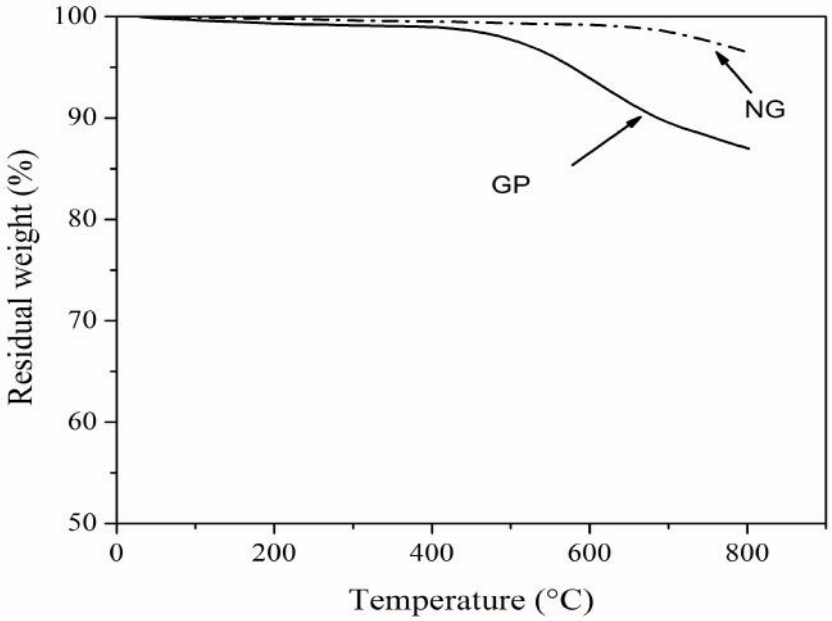

Figure 3.6: TGA curves of NG and GP

3.3.5 TGA analysis of graphene

The thermal stability of the developed GP was evaluated with the help of thermogravimetric analyzer. The thermogram of GP along with the NG is shown in fig. 3.6. It can be observed in the thermogram that, up to 425°C, the weight loss of the GP is almost identical to the weight loss of NG. However, the weight loss of graphene was slightly more than the NG. It suggests that the graphene has more moisture content than the graphite owing to the high specific area of the GP than NG. It can be seen in the fig. 3.6 that the weight loss of graphene increases above 425°C. It may be a result of reduction of the functional groups present on the high surface area GP sheets. However, the total weight loss of the graphene up to 800°C was only around 13.5%.

3.3.6 FTIR analysis of graphene

The FTIR analysis of the GP was carried out to investigate the presence of any functional group in the synthesized GP.

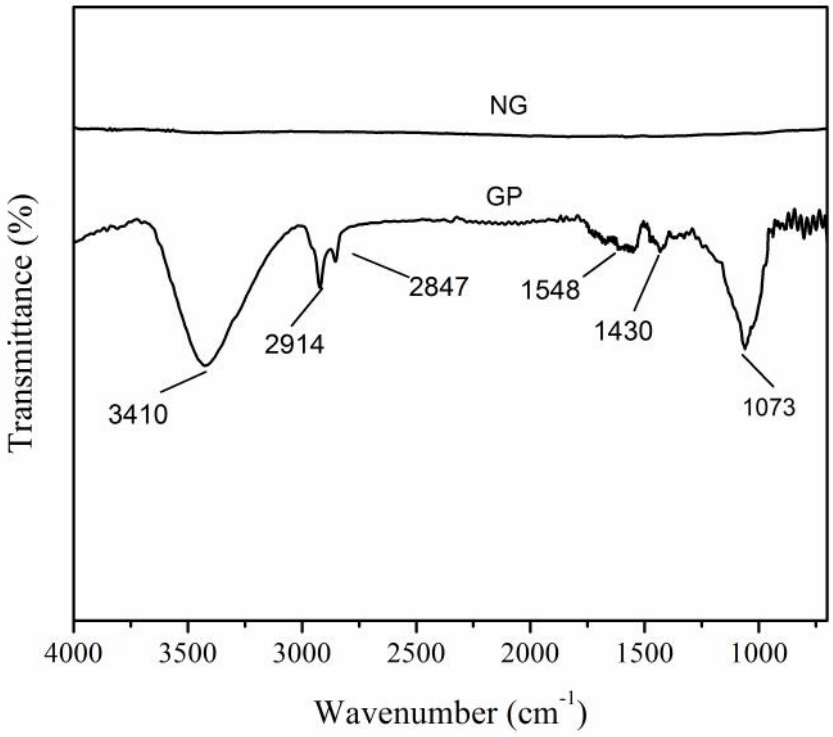

Figure 3.7: FTIR spectra of NG and GP

Figure 3.7 shows that the pristine natural graphite does not contains any significant functional groups (Min et al., 2013; Geng et al., 2013). However, though the GP is produced after thermal exfoliation at 1050°C but shows some characteristic bands of surface oxidized groups between 3500-1000 cm^{-1} (Ghosh et al., 2013). The broad peak at 3410 cm^{-1} can be attributed to the stretching vibration mode of O-H groups (Aravind et al., 2011; Poh et al., 2008). The peaks at 2914 cm^{-1} and 2847 cm^{-1} are due to the asymmetric and symmetric stretching of alkyl C-H groups (Vinayan et al., 2012). The peak at 1548 cm^{-1} is due to the presence of C=C groups (Geng et al., 2011). The peak at 1419 cm^{-1} may be attributed to C-O stretching (Park et al., 2008) and at 1073 cm^{-1} due to the stretching vibrations of C-O groups of alcohol or ether (Kou et al., 2009; Huang et al., 2011; Shen et al., 2013).

3.3.7 FE-SEM analysis of graphene

Figure 3.8 shows the morphological analysis of the NG, GO, and GP. The FE-SEM image of as prepared GO (an intermediate while synthesizing graphene) is shown in fig. 3.8(b). Figure 3.8(b) shows that the GO, where smooth leafy structure of graphite flakes was completely changed into the rough structure after chemical oxidation processes in strong acidic medium (Metin et al., 2012). Figure 3.8(c) shows the micrograph of a developed monolayer graphene in different magnification. The rough surface structure of the GO changed into more uniform topology and the thickness of the layer become thinner (Metin et al., 2012).

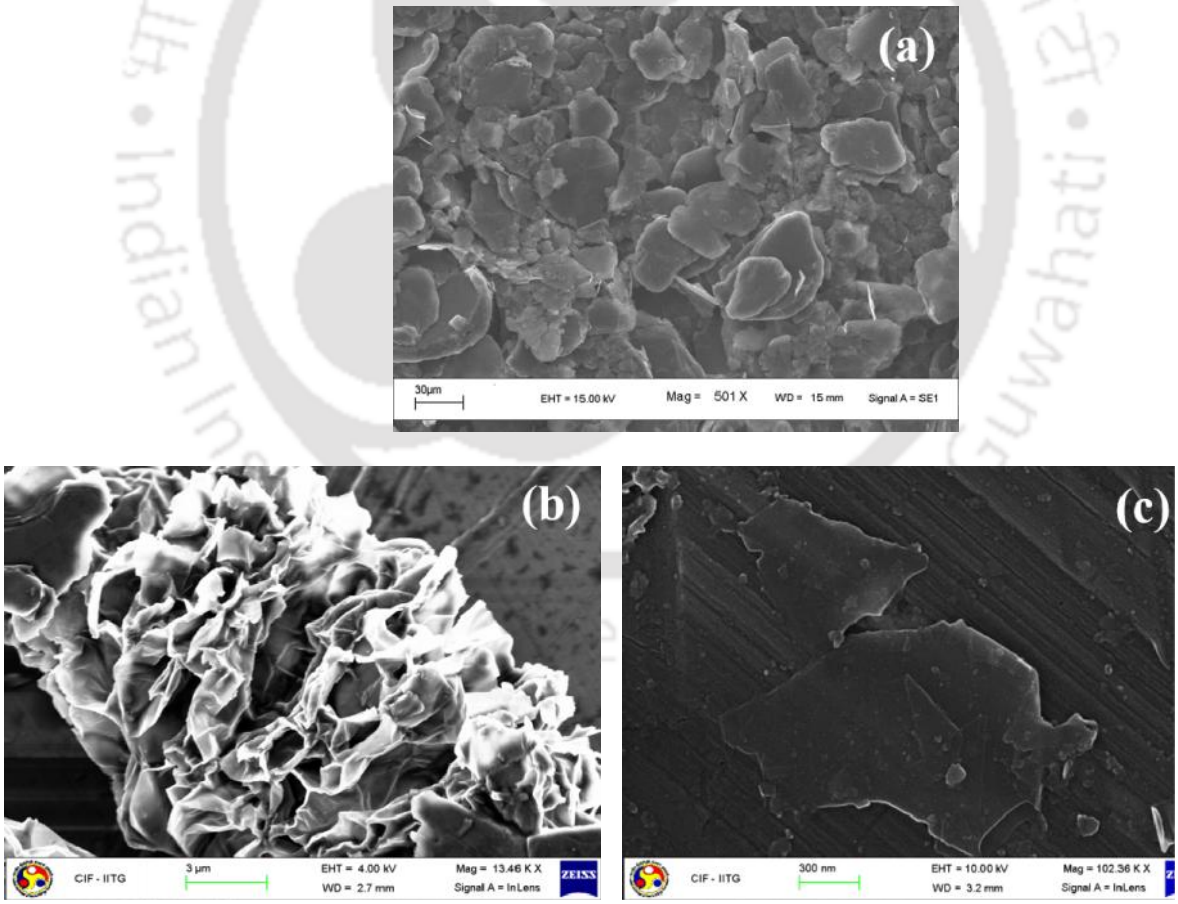

Figure 3.8: FE-SEM image of (a) NG, (b) GO, and (c) GP

The atomically thin graphene monolayer is seen semi-transparent in the micrograph (Ghosh et al., 2013). It is possible as the graphene monolayer has a thickness equal to the diameter of a sp^2 hybridized carbon atom (Novoselov et al., 2004). The electron beam from the electron gun of the FE-SEM penetrates the graphene layer upon irradiation. Therefore, texture of the aluminum sample holder is clearly visible through the monolayer graphene. The developed GP was further analyzed using TEM for better understanding of the surface morphology.

3.3.8 TEM and SAED analyses of graphene

A TEM image of developed GP is shown in fig. 3.9. From the figure, it is seen that the developed graphene is nearly flat. The presence of single layer of GP on the irradiated sample was also confirmed with the SAED analysis.

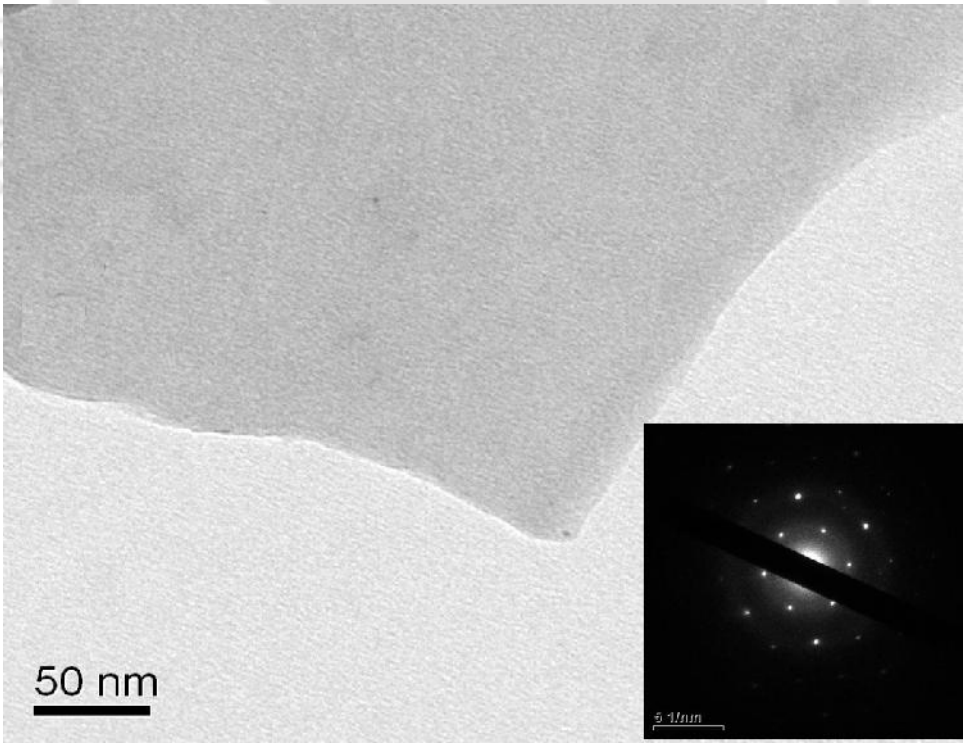

Figure 3.9: TEM micrograph of synthesized GP sheet (inset is the SAED pattern of the GP)

The selected area electron diffraction (SAED) pattern (inset in fig. 3.9) clearly reveals the typical six-fold symmetry of graphene, which is consistent with a hexagonal lattice pattern (Guo et al., 2009). The simple hexagonal pattern of the sharp spots is similar to those obtained from monolayer graphene (Meyer et al., 2007; Valles et al., 2008; Park et al., 2011).

3.3.9 EDX analysis of graphene

The elemental analysis was carried out with the help of EDX. Figure 3.10 shows the EDX spectra along with the elemental analysis. The EDX analysis showed that the atomic proportion of carbon (C) and oxygen (O) content in the GP were found to be 99.41% and 0.59%, respectively. The weight percent of the carbon content in the graphene was around 99.22%. It is to be noted that a harsh chemical environment of involving $NaNO_3$, $KMnO_4$, and H_2SO_4 was used to synthesize the monolayer graphene. However, the absence of Na, K, and Mn in the EDX spectrum reveals that the metal ions were completely removed from the graphene during washing, cleaning, and purification procedures.

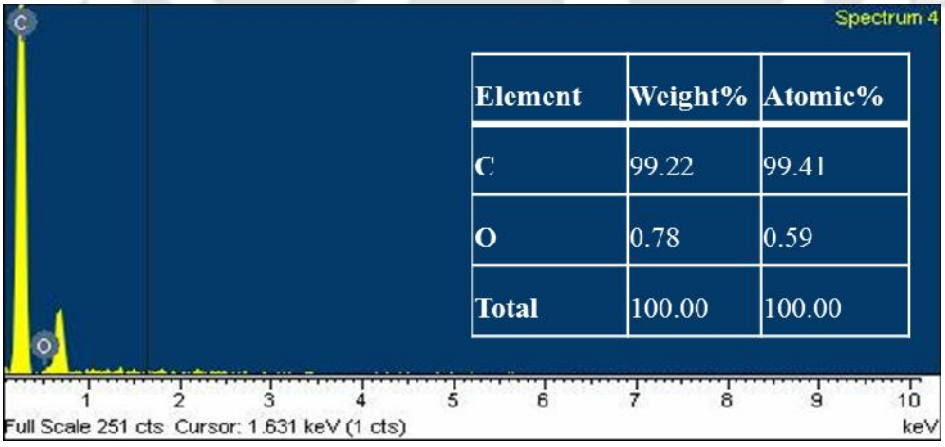

Figure 3.10: EDX analysis of the synthesized GP

Chapter 4

Graphene Reinforced Carbon-polymer Composite Bipolar Plate for PEMFC

Chapter 4

Graphene Reinforced Carbon-polymer Composite Bipolar Plate for PEMFC

This chapter describes the potential evaluation of graphene in carbon-polymer composite bipolar plate for PEMFC. The carbon-polymer composite bipolar plate is prepared using compression molding technique. The developed composite bipolar plate is characterized with an overall aim to achieve the desired properties as per the stringent target properties chosen out of DoE and Plug Power Inc. Moreover, the single cell PEMFC performance is evaluated using optimized composition of the developed composite bipolar plate.

4.1 Background

It has been discussed that the carbon-polymer composites are being considered in the PEMFC as viable material for bipolar plate as compared to pure graphite and metal bipolar plate. Research is going on to improve the carbon-polymer composite bipolar plate using different types of carbon reinforcement, which include carbon black (CB), carbon fiber (CF), and graphene (GP) (Huang et al., 2005; Blunk et al., 2006b; Hwang et al., 2008; Kakati et al., 2010; Sohi et al., 2011; Taherian et al., 2011; Tjong 2011; Allaoui et al., 2002). It was concluded in the chapter 2 that there is a need of systematic study on evaluation of CF length and graphene content for carbon-polymer composite bipolar plate in order to further enhance the required properties of the base composite bipolar plate.

In this chapter, the investigation on CF length and graphene content in carbon-polymer composite bipolar plate is reported. The NG, CB, CF and/or GP was used as the

conductive reinforcement. The thermosetting resins are good choice as matrix for the development of composite bipolar plate owing to its high dimensional stability, good thermal stability, high flame resistant, and excellent corrosion resistant (Knop and Pilato 1985; Wu and Chu 2010; Hsiao et al., 2010). Therefore, three types of thermosetting polymer resin such as novolac phenol formaldehyde resins (NPFR), resole phenol formaldehyde resin (RPFR), and vinyl ester resin (VER) were used as the polymer matrices for the development of composite bipolar plates. The optimized base compositions using these three polymer matrix are selected from our previous research work (Kakati and Verma 2011; Lee et al., 2011) (CF/CB/NG/NPFR 5/5/60/30%, CF/CB/NG/RPFR 5/5/65/25%, and CF/CB/NG/VER 5/5/65/25%) are used for the evaluation of CF length and graphene content. It may be noted that in that study 2mm CF length was only used. The subsequent section of the chapter report about the development, characterization, optimization, and evaluation of the optimized composite bipolar plate in the PEMFC.

4.2 Experimental

4.2.1 Materials

NG was the choice for the primary conductive reinforcement due to its high intrinsic electrical conductivity, excellent corrosion resistance in acidic environment. Vulcan XC-72 grade CB, PAN based CF, and in-house synthesized GP (the synthesis method is described in chapter 3) were chosen as the other reinforcements into the NG/polymer composite to improve the properties of the composite. In this study, three different type of polymer matrix (NPFR, RPFR, and VER) was used for the evaluation of CF length and

GP content in composite bipolar plate. The subsequent section describes the details properties of the procured raw materials as received.

4.2.1.1 Conductive reinforcement

The in-house synthesis of GP is described in chapter 3. The details of other carbon raw materials used for the development of carbon-polymer composite bipolar plates are discussed in the following section.

Natural graphite is an inexpensive and one of the most stable materials, which is commonly used as conductive filler to polymer composite. Graphite is a good electrical and thermal conductor with in the laminea but the opposite is true in the perpendicular direction due to its anisotropic characteristics (Chung 2002). These characteristics make graphite effective as a conductive filler for the composite bipolar plate of a PEMFC.

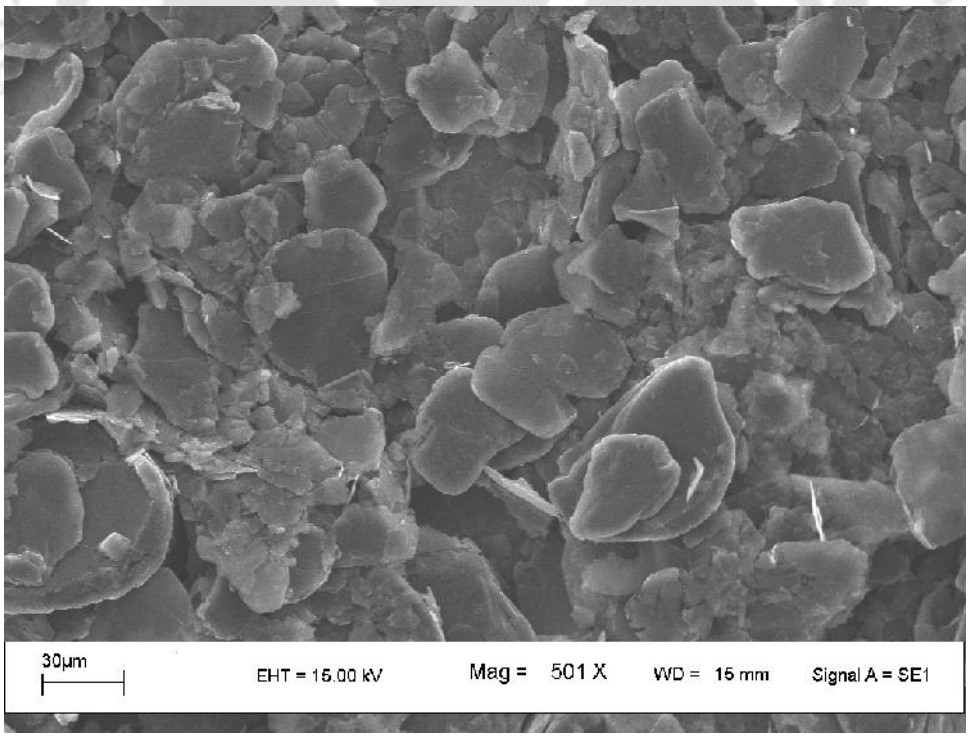

Figure 4.1: SEM image of the NG particles

NG not only has good conductivity but is also helpful for improving processability due to its lubricating effect in the melt (Wang et al., 2006). A SEM micrograph of the natural graphite flake can be seen in fig. 4.1 and table 4.1 lists additional physical properties of this filler.

Electrically conductive carbon black (CB) was selected for its synergetic effect on electrical conductivity when combined with NG as the conductive filler in polymer composite. The CB is a particular form of carbon that is produced in industry using thermal cracking or thermal decomposition of a hydrocarbon (Accorsi and Yu 1998). There are different types of carbon blacks used commercially, which vary in their application and production processes. Carbon blacks are currently sold in the form of hundreds of commercial grades, which vary in particle size, aggregate size and shape, porosity, and surface chemistry. The CB is used for imparting excellent electrical conductivity when it is used in electronic components, cables, electrodes, electrode additives, and so on (Frysz et al., 1996; Lu and Chung 2002).

Table 4.1: Properties of as received NG powder

Typical property	**Typical value**
Appearance	Fine black powder
Bulk density	2.26 $g \cdot cm^{-3}$
Particle size (average)	63 μm
Purity	≥ 98%
Ash content	5%
Moisture content	0.2–0.5%
BET surface area ($m^2 \cdot g^{-1}$)	23.97

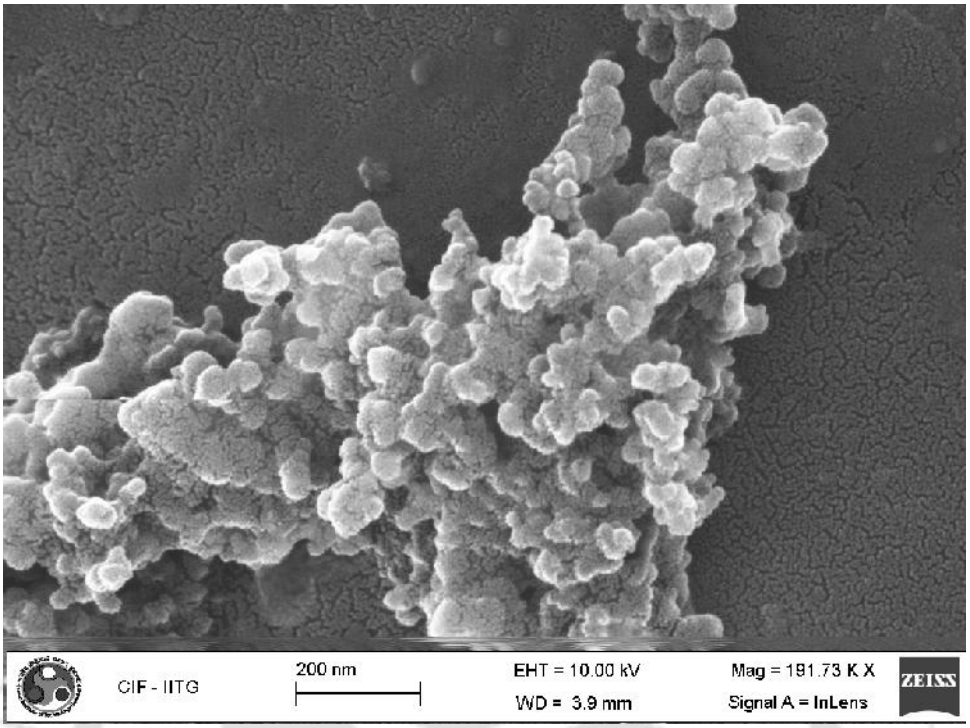

Figure 4.2: FE-SEM image of the CB particles

Moreover, the CB is extensively studied for potential reinforcement into the NG/polymer composite owing to the high electrical conductivity, as well as the good chemical resistance (Chung 2004). The different types of CB have been studied by the scientists and researchers as reinforcement to NG/polymer composite for the enhancement of electrical conductivity of the composite bipolar plate (Mighri et al., 2004; Wu and Shaw 2005; Chen and Kuo 2006; Kakati et al., 2010). In this study, Vulcan XC-72 CB has been used to enhance the electrical property of the composite bipolar plates. Vulcan XC-72 grade CB was received from CABOT India Ltd., Mumbai, India. Figure 4.2 shows the FE-SEM image of the CB particles. It is observed that the CB particles are almost spherical in nature. Though the CB particles are in agglomerated form but the diameter of most of the CB particles are around 80 nm. The size of the CB particles was further analyzed with the help of particle size analyzer which also showed similar results. The typical properties of the Vulcan XC-72 grade CB is listed in the table 4.2.

Table 4.2: Properties of as received Vulcan XC-72 CB

Typical property	**Typical value**
Physical appearance	Black powder
Bulk density	1.2 g·cm^{-3}
Average particle size	3 µm
Purity	≥ 95%
Volatile content	≤ 2%
Moisture content	< 1%
Ash content	≤ 0.1%
BET surface area	249.64 m^2·g^{-1}

The carbon fiber is commonly used for enhancing the mechanical properties of the polymer composite. The CF made up of mostly carbon atoms, which are more or less aligned in microscopic crystals parallel to the in-plane. There are several precursors that can be used to synthesize carbon fibers, however, each produces fibers with different cross-sectional morphologies. Most commercial carbon fibers exploit the great strength of carbon materials under tension, which is achieved when the carbon fibers are prepared from a polymer precursor, such as polyacrylonitrile (PAN). Moreover, PAN based CFs are thermally stable, have highly oriented molecular structure, and possess excellent mechanical strength (Katz and Brandmaier 1987). The SEM image of the carbon fibers is shown in fig. 4.3. The diameter of the fiber was around 6 µm. It is obvious from the micrograph that the diameter of the fibers are almost uniform. The micrograph shows that the surface of the fibers was not perfectly smooth.

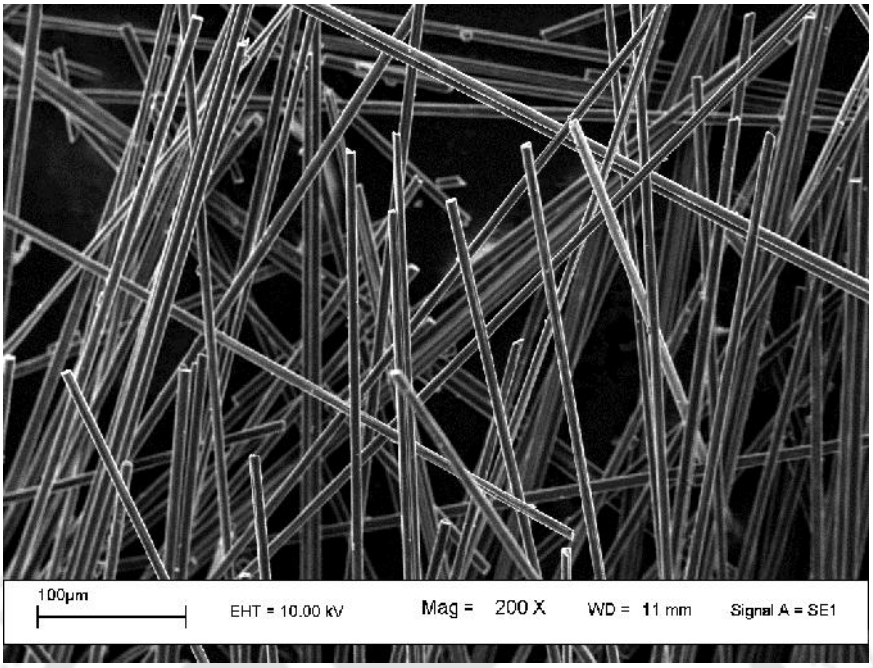

Figure 4.3: SEM image of the CF

Table 4.3: Properties of as received T-300 grade CF

Typical property	**Typical value**
Physical appearance	Fine thread
Bulk density	1.76 g·cm^{-3}
Fiber diameter	6 µm
Purity	99.9%

The longitudinal grooves on the periphery of the fiber may be due to the manufacturing defects. PAN based CF (T-300 grade) was supplied by Torayca, Japan. The typical properties of the as received CF is listed in the table 4.3.

4.2.1.2 Polymer matrix

The reaction of formaldehyde with phenol can led to either a novolac or resole type phenol formaldehyde polymer, which depends upon the mode of catalysis and molar ratio of formaldehyde to phenol. Table 4.4 shows some basic information of the phenol formaldehyde resin preparation (Gardziella et al., 2000; Kurachenkov and Igonin 1971).

The NPFR and RPFR were supplied by Rishab Phenolic Pvt. Ltd., Hyderabad, India. The resins were stored in an airtight container to prevent unwanted crosslink before use it. The details of the NPFR and RPFR properties are listed in table 4.5.

Table 4.4: Different parameter for synthesis phenol formaldehyde resins

Resin type	**Catalyst**	**Formaldehyde /Phenol**	**Functional group**	**Mode of cure**
NPFR	Acid	<1	Phenolic	Hexamethlenetetramine
RPFR	Base	≥1	Methylol, Phenolic	Acid, base, Thermal

Table 4.5: Properties of as received phenolic matrix

(a) NPFR

Typical property	**Typical value**
Appearance	Cream to pink color free flowing powder
Melting point	80-95°C
Flow @ 125°C	35-50 mm
Gel time @ 160°C	30-45 s
HMTA content	8-10%
Shelf life @ 25°C	6 months
Curing temperature range	160-210°C

(b) RPFR

Typical property	**Typical value**
Appearance	Reddish brown viscous liquid
Viscosity@ 25°C	230 cP
Solid content @ 135°C	58–62%
Gel time @ 150°C	85–130 s
Specific gravity@ 25°C	1.16 $g \cdot cm^{-3}$
Water solubility	1:3
Solvent solubility	Alcohols, glycols
Shelf life @ 25°C	6 months
Curing temperature range	130-210°C

Vinyl ester resins (VER) are widely used as thermosetting resin because of their low cost, excellent chemical and corrosion resistance, outstanding heat performance and favorable mechanical properties. The industrial grade VER (MECHSTER 5310) was supplied by Alchem Polymer, Kolkata, India. The promoter, accelerator, and catalyst were also supplied along with the resin. The typical properties of the VER is shown in table 4.6.

Table 4.6: Properties of as received VER

Typical property	**Typical values**
Appearance	Yellowish brown liquid
Viscosity@ 25°C	450±50 cps
Specific gravity@ 25°C	1.16 $g \cdot cm^{-3}$
Peak exotherm temperature	140–145°C
Solid content @ 140°C	64–66%
*Gel time @ 25°C	15–20 min
Solvent solubility	Alcohols, ketones
Shelf life @ 25°C	6 months
Curing temperature range	120-180°C

* with 1.5% promoter, 1.5% accelerator, and 1.5% catalyst

4.2.2 Methods

4.2.2.1 Development of carbon-polymer composite bipolar plate

The carbon-polymer composite was prepared using solution blending and compression molding technique. The three types of polymer matrix such as NPFR, RPFR, and VER were used for the development of carbon-polymer composite bipolar plate. The 70% NG content was used for NPFR based polymer composite, whereas the 75% NG was used for RFPR and VER based polymer composite, respectively. Initially, the NPFR (30%), RPFR (25%), or VER (25%) polymer matrix was dissolved in acetone and blended with required amount of NG using mechanical stirring. Separately, CB (5%) was dispersed in acetone using sonication to obtain CB slurry. The CB slurry was then added slowly into the continuously stirred NG/polymers mixture in expense of NG. Subsequently, CF (5%) of a particular length was added. For VER based composite, catalyst, promoter, and accelerator were also added to the polymer matrix. Then the homogeneous mixture was allowed to dry at a room temperature. The mixture was stirred with a glass rod in regular interval to avoid formation of lumps. Furthermore, the completely dried mixture was thoroughly. The obtained mixture was used to develop the bipolar plate using a three-part mold in a compression molding machine. The mixture was transferred in to the mold and pressed at around 80°C and subsequently the temperature was slowly maintained upto 210^{o}C for full curing for NPFR and RPFR polymer based composites. However, the final curing of VER based composites was done upto 180^{o}C. The applied pressure was maintained at 100 kg·cm^{-2} for all the polymer matrix. The curing time was 1 h for all the polymer. The cured samples were removed after proper cooling. The developed bipolar plates were then used for characterizations.

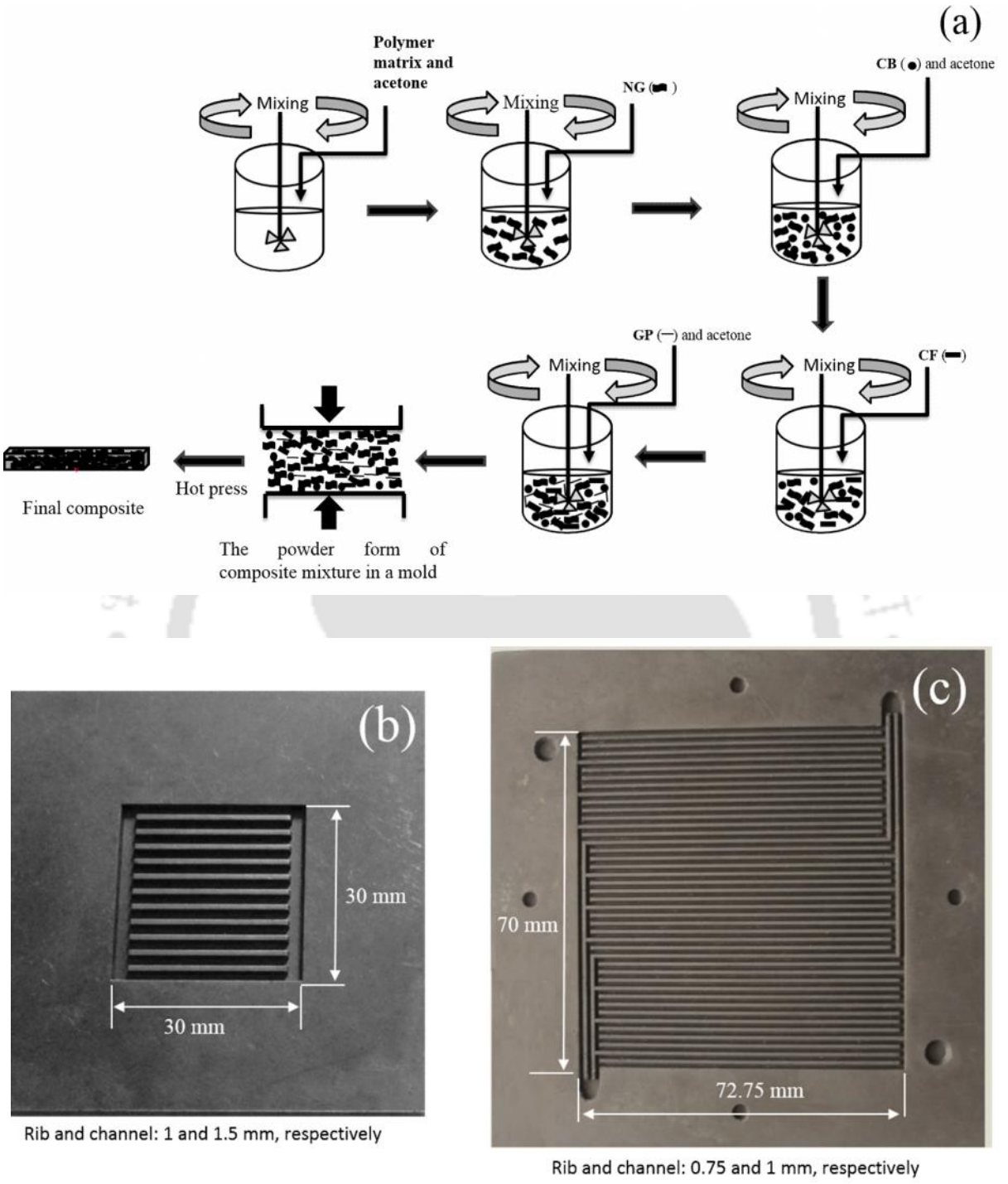

Figure 4.4: (a) Different steps followed for the carbon-polymer composite bipolar plate fabrication, (b) snapshot of a bipolar plate used to evaluate fuel cell performance, and (c) another bipolar plate sample

To prepare graphene reinforced carbon-polymer composite bipolar plate, the GP slurry in acetone was prepared separately using sonication. The dispersed GP slurry was added into the mixture of CF/CB/NG/polymer at the expense of NG content. It means if x % of GP was added in to the mixture then the NG loading was reduced by x % from its original content, which was present in CF/CB/NG/polymer composite. Figure 4.4(a) shows the schematic route for the development of composite bipolar plate and the fig. 4.4(b,c) shows two representative photograph of the developed composite bipolar plate with inbuilt flow channels.

The electrical conductivity of the composite is strongly affected by the volume of conducting reinforcement that make electrical path-networks. Therefore, the amount of conducting reinforcement (as well as polymer) in the composite was measured and controlled by the volume percentage, unless otherwise specified.

4.2.3 Characterization

The developed bipolar plates were tested for density, flexural strength, deflection at mid-span, shore hardness, electrical conductivity, thermal conductivity, thermal stability, hydrogen permeability, anodic and cathodic corrosion current density, and interfacial electrical contact resistance (ICR). Moreover, developed bipolar plates were also tested in a PEMFC as described in the section 4.3.3. The FE-SEM analyses of the developed composite bipolar plate have been carried out as per the procedure described in the chapter 3.

4.2.3.1 Bulk density

The bulk density of the developed composite bipolar plates was measured as per the ASTM C559 standard, which is used to determine the bulk density of manufactured items

of carbon and graphite. The dimensions of the sample were measured using vernier caliper having least count of the vernier caliper was 0.002 cm (make: Aerospace instruments). The weight (w) of the sample was measured using a high precision electronic balance (Denver Instrument, model: SI-234) that has a least count of 0.1 mg. The length (l), breadth (b), and thickness (d) of the sample were measured to calculate the density (Kakati and Verma 2011). The density of the bipolar plate was calculated as per the eq. 4.1.

$$\rho = \frac{w}{lbd}\ \mathrm{g\cdot cm^{-3}} \tag{4.1}$$

4.2.3.2 Flexural strength and deflection at mid-span

The flexural test measures the force required to bend a beam under three-point loading conditions. The three-point bending test was performed to measure the flexural strength and deflection at mid-span of the bipolar plate using universal testing machine (Dipak Polyplast Pvt. Ltd., UTM DUTT-101, India). The span length was kept 16 times to that of thickness of the sample as per the ASTM D790. The crosshead speed of the loading point was maintained at 0.5 $\mathrm{mm\cdot min^{-1}}$.

Most commonly, the specimen lies on support span and the load is applied to the center by the loading nose producing three-points bending at a specified crosshead rate and the simultaneous load-deflection data was monitored with the help of a computer. The break load and the maximum deflection were recorded accordingly. The flexural strength of the composite bipolar plate was calculated using eq. 4.2.

$$\textit{Flexural strength} = \frac{3FL}{2wt^2}\ \mathrm{MPa} \tag{4.2}$$

where F = breaking force of the specimen (N),

L = support span distance (mm),

w = width of the test sample (mm), and

d = depth of the test sample (mm).

Similarly, the deflection at mid-span (D_{mid}) of the bipolar plate samples were also calculated using eq. 4.3 (Kakati et al., 2011).

$$D_{mid} = \frac{D}{L/2} \times 100\% \tag{4.3}$$

where, D = maximum deflection at the center of the beam in mm.

4.2.3.3 Shore hardness

The shore hardness is a mechanical property which represents the resistance of the material for penetration and scratching. The shore hardness of the developed composite bipolar plate was measured as per ASTM C886 method using scleroscopic hardness tester (Imai Testing Machine Manufacturing Company Limited, Hardscope) (Ghosh and Verma 2014). It is a rebound hardness test in which a diamond tipped hammer drops vertically and strikes onto the surface of the specimen being tested. The height of the rebound of the hammer can be noted with the help of the scale marked on the apparatus, which provide the shore hardness of the composite bipolar plate.

4.2.3.4 Electrical conductivity

The in-plane and the through-plane electrical conductivities of the composite bipolar plates were measured as per the ASTM C611 method using conventional four probe

method. Prior to use, the bipolar plate sample was polished with fine grade silicon carbide emery paper to reduce the skinning effect. Later, the polished sample was cleaned with acetone. The surface treated sample was sandwiched between two carbon papers, which was then placed in the electrical conductivity experimental setup as shown in the fig. 4.5 (a). The use of carbon paper ensures the good electrical contact between the sample and the flat plate metallic current supplier. The digital multimeter was used as the constant current source through two outermost probes and the voltage drop across the two inner probes was measured.

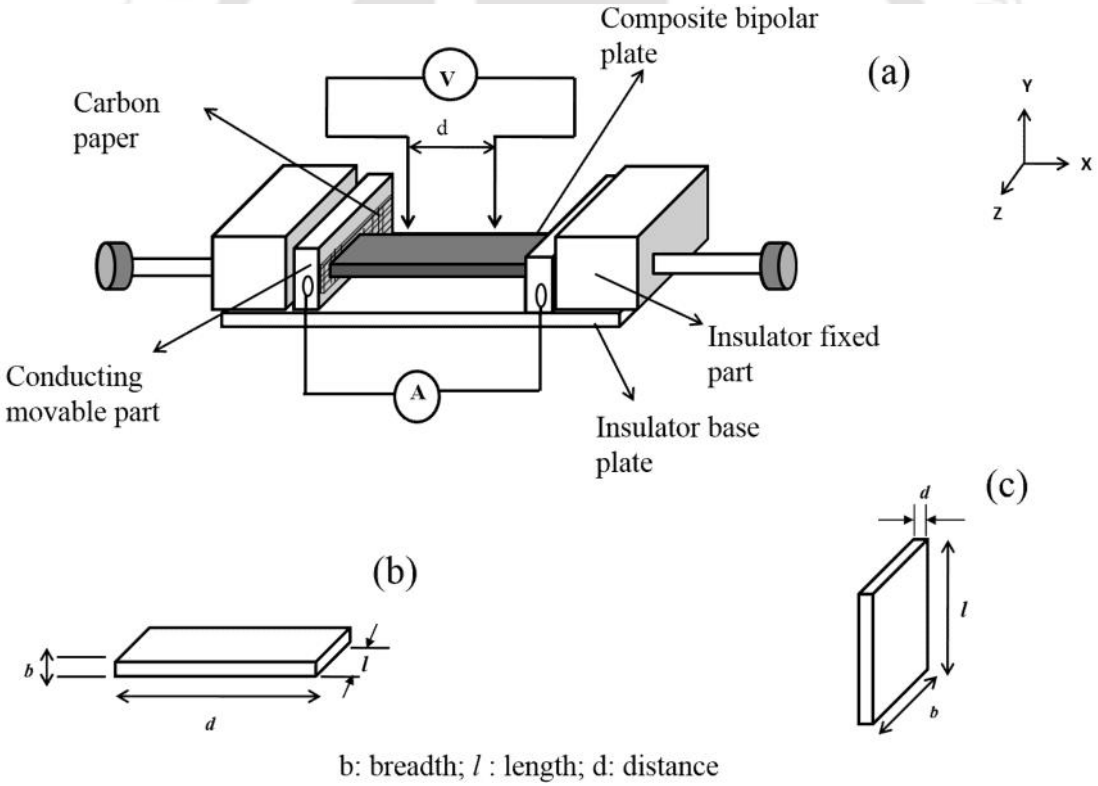

Figure 4.5: (a) schematic of the electrical conductivity measurement setup and orientation of the sample for (b) in-plane, and (c) through-plane electrical conductivity measurement (Kakati et al., 2010)

The electrical conductivity (σ) of the bipolar plate was determined using eq. 4.4,

$$\pm = \frac{I}{V} \times \frac{x}{A} \ \mathrm{S \cdot cm^{-1}} \tag{4.4}$$

where, I is the applied current (A), V is the measured voltage (V), A is the cross section area of the sample (cm^2), and x is the distance between inner probes (cm). The through-plane electrical conductivity was measured by changing the orientation of the bipolar plate (Kakati et al., 2010).

4.2.3.5 Thermal conductivity

The thermal conductivity of composite bipolar plate was measured using thermal conductivity measuring instrument (Gunt: WL376, Germany) (Kakati and Verma 2011). The constant power was supplied in the heating zone, while the tap water was supplied from the cooling zone to achieve the steady state heat conduction. The temperature at different points along the sample was measured with the help of thermocouple. There were eight different points to measure the temperature during the analysis of sample. The temperature at first three-points and last three-points were in the heating and cooling zone, respectively. The temperature across the bipolar plate was measured at the 4^{th} and 5^{th} points in steady state condition. The thermal conductivity of the composite bipolar plate was measured using one dimensional steady state heat conduction of Fourier's law, as shown in eq. 4.5.

$$q = -k \frac{T_4 - T_5}{x} \ \mathrm{W \cdot m^{-2}} \tag{4.5}$$

where, k ($W \cdot m^{-1} \cdot K^{-1}$) is thermal conductivity, T_4 and T_5 (K) are the temperature at 4th and 5th points, q ($W \cdot m^{-2}$) is the heat flux, transfer from the heating zone to cooling zone, and x (m) is the distance between 4th and 5th points. The other four surfaces of the sample were insulated.

4.2.3.6 Hydrogen permeability

The hydrogen permeability of the composite was measured under pressurized condition at 80°C. A schematic of the experimental setup is shown in fig. 4.6. The samples were cut into the size of 30 mm×30 mm. The bipolar plate were polished with fine grade emery paper before analysis. The sample was fixed in a sample holder made up of two stainless steel flanges. The anabond red silicon paste was used as gasket on both the sides of the sample edges to prevent leakage of the gas. The hydrogen was passed from the one side from the cylinder at a fixed pressure. A bypass valve was provided to release pressure, particularly at the end of the experiment. A ceramic band heater was used to heat the sample holder and temperature was controlled with the help of a digital temperature controller. The hydrogen permeates through the composite was collected in a cylinder connected on the other side of the sample holder. The hydrogen gas permeability was checked at a pressure difference of 2 bar across the bipolar plate at particular temperature.

The gas was sampled from the downstream side and analyzed. The bipolar plate was kept up to 10 h under pressure to measure the hydrogen permeability at different temperatures. The hydrogen permeability (ν) of the composite bipolar plate, at a particular pressure, was calculated as per the following equation (Kakati et al., 2011).

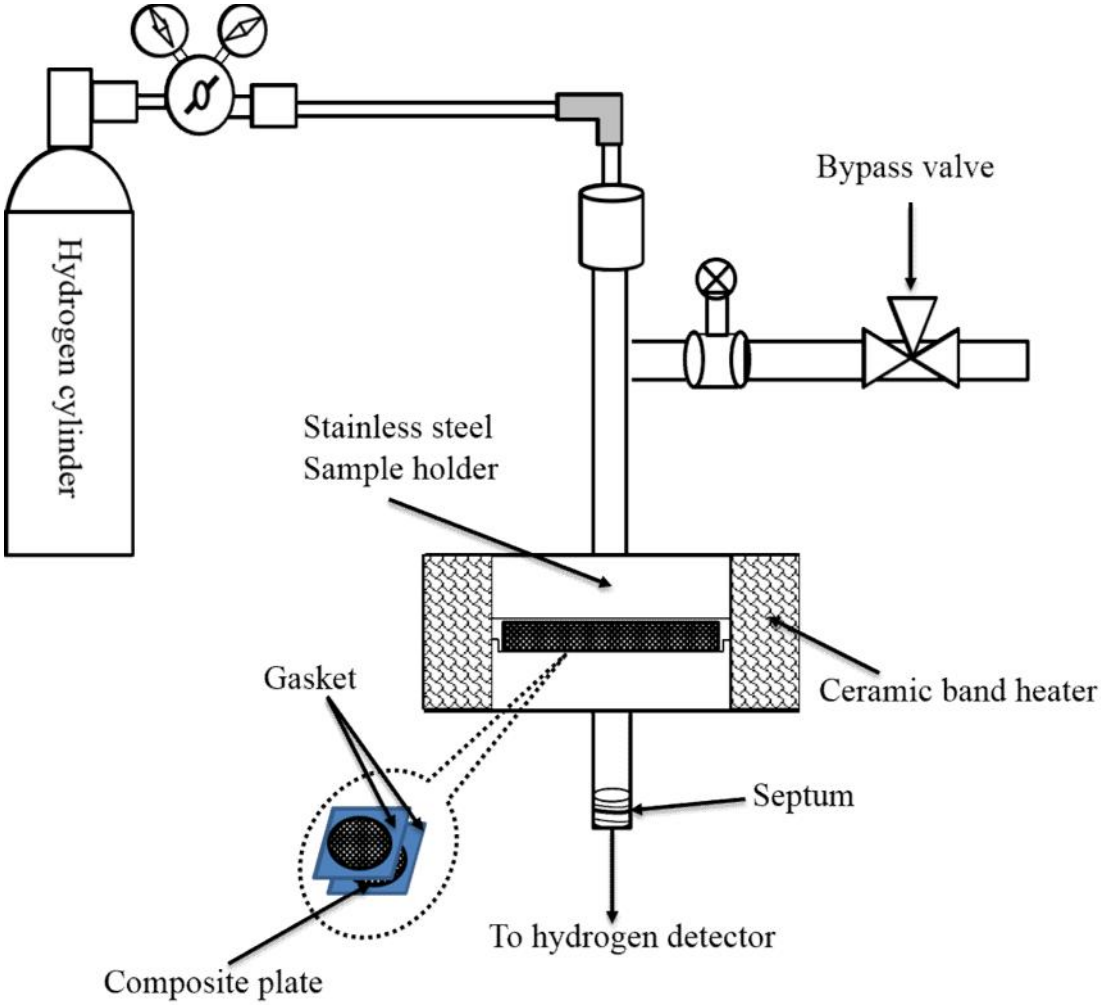

Figure 4.6: Schematic of the hydrogen permeability measurement setup

$$\mathrm{V} = \frac{\ddot{}}{A} \times \frac{d}{t} \ \mathrm{cm^3 \cdot cm^{-1} \cdot s^{-1}} \tag{4.6}$$

where, d is the thickness of the plate (3 mm), and $\ddot{}$ is the amount of hydrogen (cm^3) passed through an area (A) $(4.91\ cm^2)$ of the bipolar plate over a time t (s).

4.2.3.7 Corrosion current density

The corrosion current density of the developed composite bipolar plate was measured using potentiodynamic polarization test by linear sweep voltammetry (LSV) using potentiostats/galvanostats in a simulated PEMFC environment. The conventional three-electrode system was used in the electrochemical measurements. The Ag/AgCl was used as a reference electrode and platinum wire was used as a counter electrode. The developed bipolar plate was used as a working electrode. The experiments were conducted using 1 M H_2SO_4 solution with 2 ppm HF concentration. The reason to add HF is that it is a highly oxidizing agent and its presence provides the accelerated corrosion resistance. Moreover, it is a well-known fact that the source of HF in PEMFC is nafion (Liu et al., 2006).

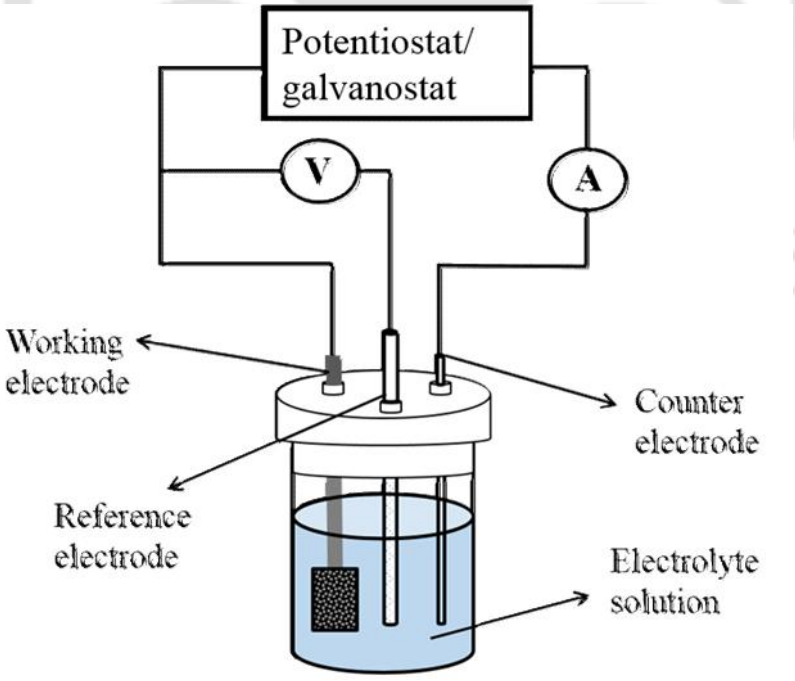

Figure 4.7: Schematic of the LSV experimental setup

A very low concentration of HF, in ppm range, is released due to degradation of nafion at prolonged operation of PEMFC (Liu et al., 2006). The solution was purged with hydrogen and oxygen to provide simulated anodic and cathodic environment of PEMFC, respectively. The electrochemical measurements were conducted at 80°C. The potential was swiped at a scan rate of 1 $mV \cdot s^{-1}$ with the help of a potentiostat. Figure 4.7 shows the schematic of three-electrode experimental setup in which the potential was applied between working and reference electrode and current was measured between working and counter electrode. The whole experimental analyses was conducted in an unstirred electrolyte solution (Ghosh and Verma 2014). The Tafel analysis was performed by extrapolating the linear portions of a log current density versus potential plot to obtain the corrosion current density and potential at their intersection as shown in the fig. 4.8.

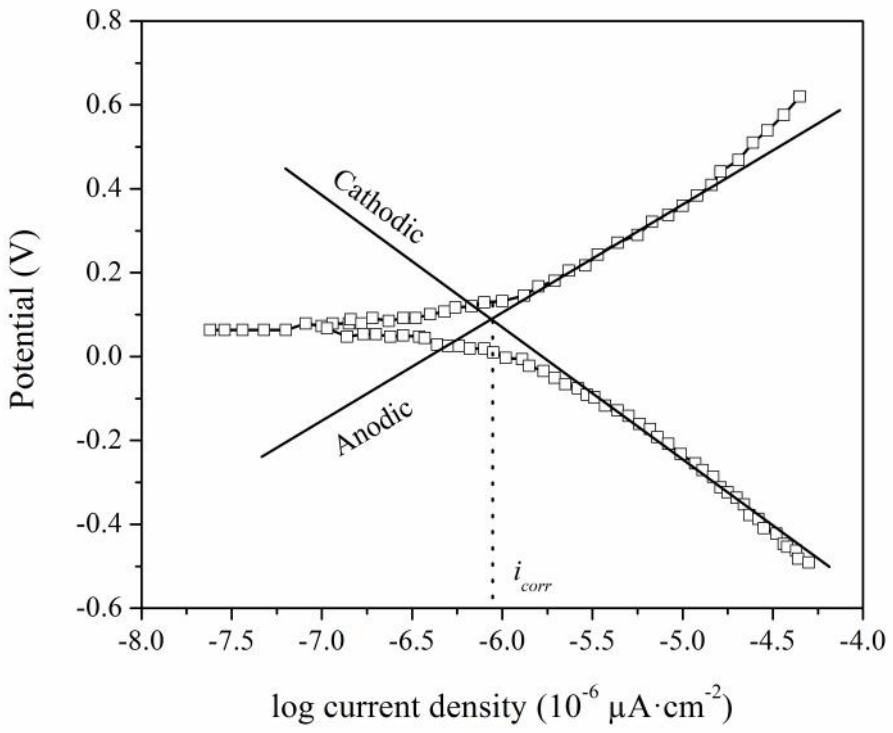

Figure 4.8: Tafel plot showing corrosion current density (i_{corr})

It was assumed that the rate of the corrosion process was controlled by the kinetics of the electron transfer reaction at the working electrode, in general the case for corrosion reaction (Wang et al., 2004). An electrochemical reaction under kinetic control region follows the Tafel equation (eq. 4.7),

$$i = i_O \exp(2.303\frac{E - E_O}{b}) \quad (4.7)$$

where, i = current density ($A \cdot cm^{-2}$) resulting from the reaction, $i_\circ$= a reaction dependent constant called the exchange current density ($A \cdot cm^{-2}$), E = electrode potential (V), $E_\circ$ = equilibrium potential (V), and b = Tafel constant (constant for a particular reaction).

The Tafel equations for both the anodic and cathodic reactions in a corrosion system can be combined to generate the Butler-Volmer equation as follows.

$$i = i_{corr}[\exp(2.303\frac{E - E_{corr}}{b_a}) - \exp(-2.303\frac{E - E_{corr}}{b_c})] \quad (4.8)$$

where, i_{corr} = corrosion current (A), E_{corr} = corrosion potential (V), b_a = anodic Tafel constant (V/decade), b_c = cathodic Tafel constant (V/decade). The voltage reported in the thesis is with respect to the standard hydrogen electrode (SHE) unless otherwise stated (Ghosh and Verma 2014).

4.2.3.8 Interfacial electrical contact resistance

In a PEMFC stack, under a particular pressure, gas diffusion layer contacts directly to the bipolar plate. Therefore, the interfacial electrical contact resistance (ICR) is one of the most important factors, which affect the cell voltage especially at higher current densities

and in turn can affect the fuel cell performance. The schematic of the experimental setup along with the corresponding analogous electrical circuit for measuring ICR is shown in fig. 4.9. The toray carbon paper (CP) was sandwiched between two pieces of developed composite bipolar plate (CBP) and placed in between two pieces of copper plates. Electrical insulator was used above the upper and below the lower copper plate in different arrangements to find out the total resistance of the assemblies shown (fig. 4.9). The compaction load was applied using hydraulic press. A constant current was applied through the copper plates and the voltage was measured at a particular compaction load (Kim et al., 2010a; Taherian et al., 2011; Avasarala and Haldar 2009).

Total resistance of the assemblies (R_1 and R_2) corresponding to the fig. 4.9(a and b) is shown by eq. 4.9 and 4.10), respectively.

$$R_1 = 2R_{Cu} + 2R_{CP} + 2R_{Cu/CP} + 2R_{CBP/CP} + R_{CBP} \quad (4.9)$$

$$R_2 = 2R_{Cu} + R_{CP} + 2R_{Cu/CP} \quad (4.10)$$

The interfacial contact resistance of the two materials are shown by $R_{material\text{-}1/material\text{-}2,}$ whereas R_{CBP} and R_{CP} are the bulk resistance of composite bipolar plate and carbon paper (gas diffusion layer), respectively. The resistances (R_1 and R_2) were found out experimentally using the following eq. 4.11,

$$R_n = \frac{V}{I} \quad (4.11)$$

where (n= 1,2), R is the resistance, I is the applied current, and V is the total voltage of the assembly.

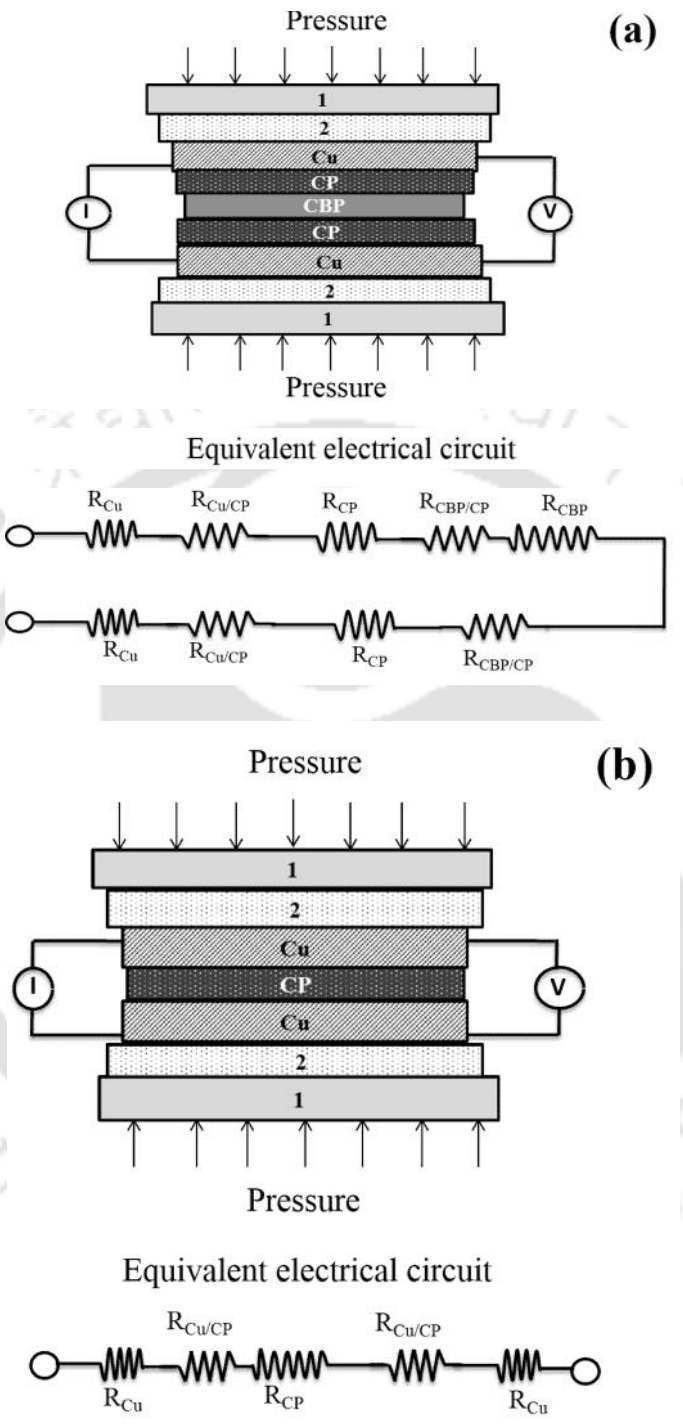

Figure 4.9: Experimental setup for interfacial electrical contact resistance measurement (1: Plates of compression machine; 2: Electrical insulator; Cu: Copper plate; CBP: Composite bipolar plate; CP: Carbon paper)

The equations (3 and 4) can be solved to find out $R_{CBP/Cu}$ and $R_{CBP/CP}$. The ICR (area specific) for CBP and CP interface was then evaluated using eq. 4.12,

$$ICR = (R_{CBP/CP} \times A) \ \ m\Omega \cdot cm^2 \qquad (4.12)$$

where, A is the geometric interface area in contact.

4.3 Fuel cell testing

A single cell PEMFC was developed using the composite bipolar plates. The developed fuel cell was used to characterize the composite bipolar plate in the real environment of PEMFC. The membrane electro assembly (MEA) was prepared for the evaluation of developed composite bipolar plate, which is discussed in following sub-section.

4.3.1 Fabrication of MEA

Nafion-117 solid polymer electrolyte membrane was used to development of MEA for all the experiments. The nafion-117 membrane was cut in required size and pretreated to improve the proton conductivity. The membrane was first treated in 0.5 M H_2O_2 for an hour at 80°C. The peroxide treated membrane was then boiled and cleaned in hot water for an hour at 80°C.

The membrane was then treated in 0.5 M H_2SO_4 solution for an hour at 80°C followed by cleaning with water as mentioned above. Finally, the treated membrane was wiped with tissue paper to remove the surface water. The in-house MEA was fabricated using the nafion-117 membrane by the conventional hot-press method. The commercial 20wt.% Pt/C catalyst was employed at anode (Pt with 0.4 $mg \cdot cm^{-2}$) as well at cathode (Pt with 0.6 $mg \cdot cm^{-2}$). The required amount of Pt/C catalyst was then dispersed in 3 ml isopropyl alcohol together with 1 ml water by sonicating it for 30 min.

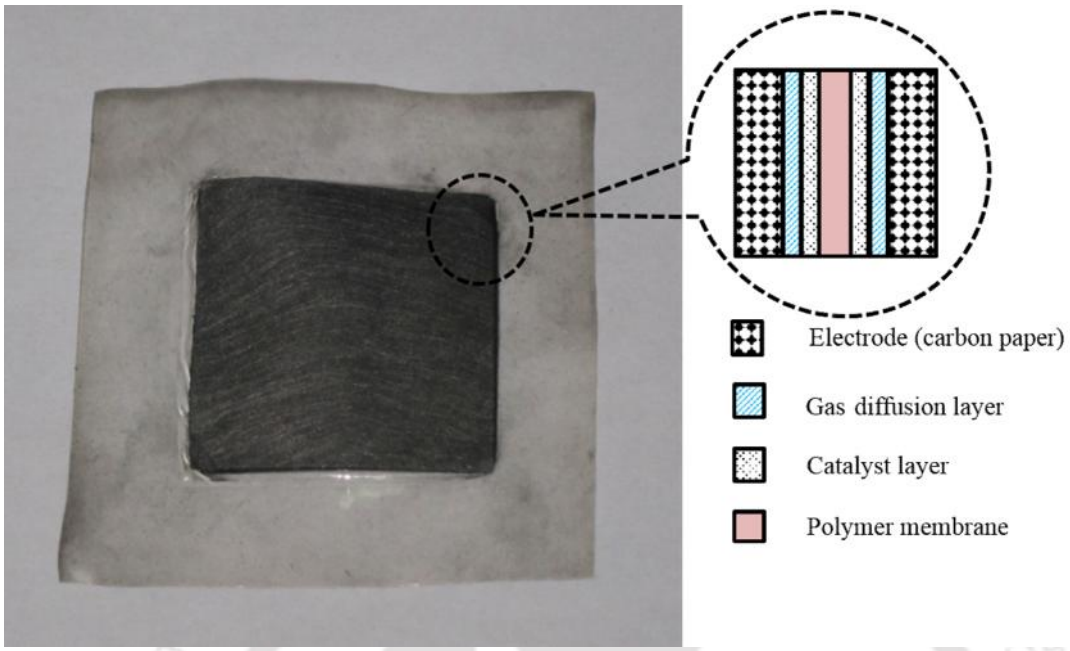

Figure 4.10: Snapshot of the developed MEA and its schematic

The fairly well-mixed catalyst slurry was coated on a respective commercial gas diffusion layer (GDL) (carbon paper coated with microporous layer) using spraying gun at 110°C. Before hot pressing, the naturally cooled GDL with the catalyst layer were heat treated in an air oven for about 12 h at 80°C. Then the MEA was fabricated by sandwiching the nafion-117 membrane between the anode and cathode. Hot pressing was done at 110°C under the pressure of 45 $kg \cdot cm^{-2}$ for 3 min to obtain the MEA. The MEA was then cooled down to room temperature and then the final MEA was tested in the fuel cell using the developed bipolar plate. A photograph of the developed MEA and its schematic, showing sequence of different layers, are shown in fig. 4.10.

4.3.2 Fabrication of PEMFC setup for the evaluation of composite bipolar plate

The schematic of experimental setup and photograph of the single cell PEMFC testing arrangement is shown the fig. 4.11.

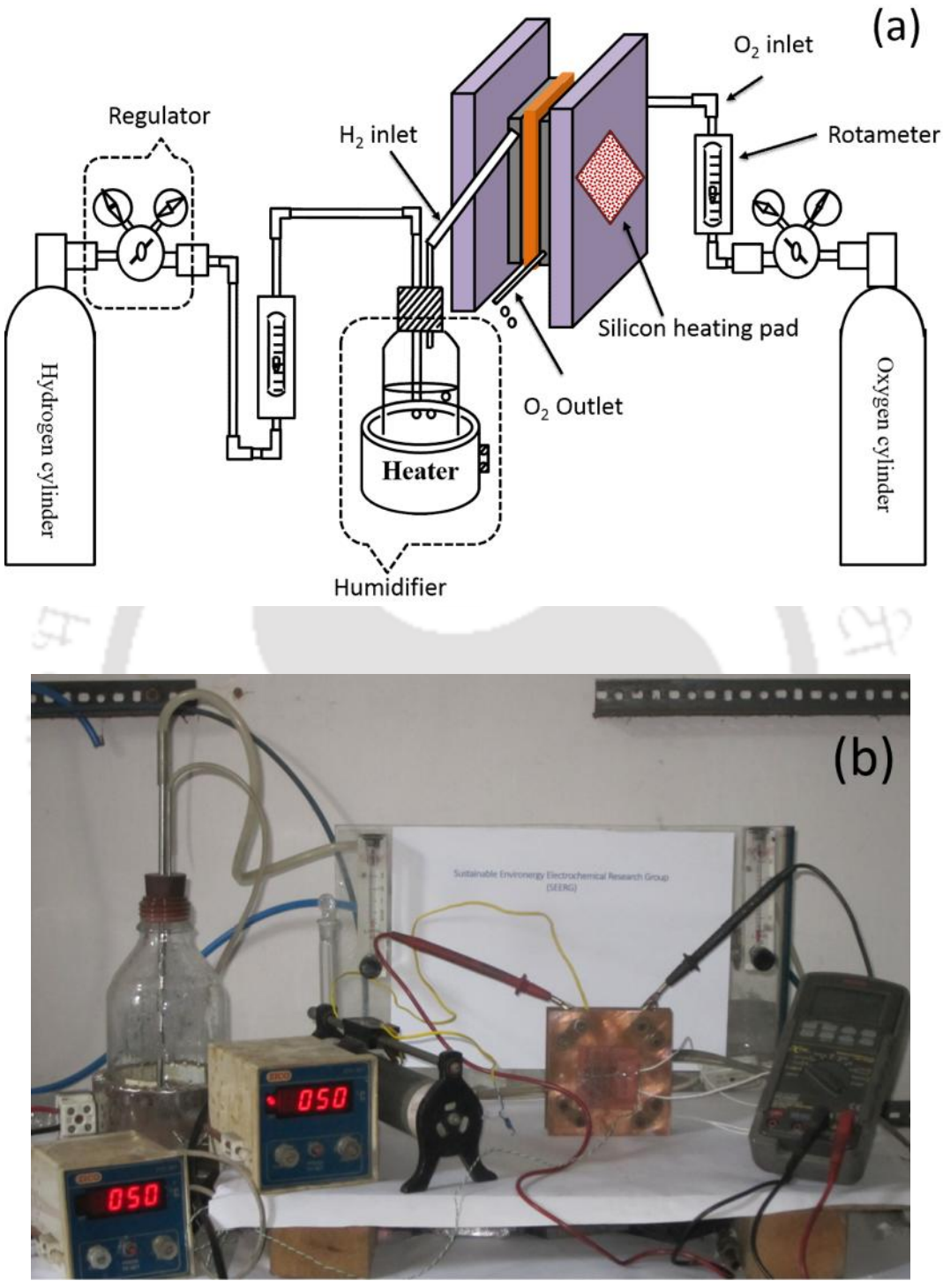

Figure 4.11: (a) Schematic of the PEMFC testing setup and (b) snapshot of the in-house developed PEMFC system

The humidified hydrogen was supplied from the cylinder through a bubbler humidifier to the anode side, whereas oxygen was directly supplied to the cathode side of the fuel cell. The flow rate of hydrogen and oxygen was controlled with the help of two rotameters. The temperature of the fuel cell was controlled with the help two heating pads attached to each end plate. The current and voltage across the cell was monitored with the help of help of a precision multimeter (Sanwa, PC 5000).

4.3.3 Fuel cell performance analysis using developed composite bipolar plates

The developed MEA was sandwiched between two similar bipolar plates and tested for $i-V$ performance of the fuel cell. The hydrogen and oxygen flow rates were maintained to be 0.5 and 1.0 lpm, respectively. The temperature of the fuel cell was controlled with the help of a digital temperature controller. The output current and voltage was measured with the help of two digital multimeters. A rheostat was used as a variable load to obtain the $i-V$ performance of the fuel cell. It may be noted that the composite bipolar plate was tested using indigenously fabricated PEMFC hardware as shown in fig. 4.11.

4.4 Results and discussion

4.4.1 Effect of CF length on the properties of composite bipolar plate

The CF/CB/NG/polymer composite bipolar plates with different CF length were developed to find out the optimum CF length with the overall aim to improve the mechanical strength of the composites. All the composites were prepared using compression molding technique.

The developed bipolar plates were characterized thoroughly for bulk density, flexural strength, shore hardness, morphological analysis, electrical conductivity, thermal conductivity, hydrogen permeability, corrosion current density, and interfacial contact resistance. The developed bipolar plates were later tested in single cell PEMFC.

4.4.1.1 Bulk density of the CF/CB/NG/polymer

The effect of CF length on the density of the NPFR, RPFR, and VER polymer composite bipolar plate is shown in fig. 4.12. It is observed that the density of the CB/NG/polymer composites decreases sharply due to addition of CF (5%) content as compared to without CF content (corresponding to zero mm CF length). This can be attributed to the difference in density of the NG (2.26 $g \cdot cm^{-3}$) and CF (1.76 $g \cdot cm^{-3}$).

It can be seen that the density of the composites does not change with the addition of CF (5%) for the studied CF length. Moreover, it can be seen that the CF/CB/NG/NPFR composite shows the lower density, which is obvious as the content of the NG is lowest in this composite.

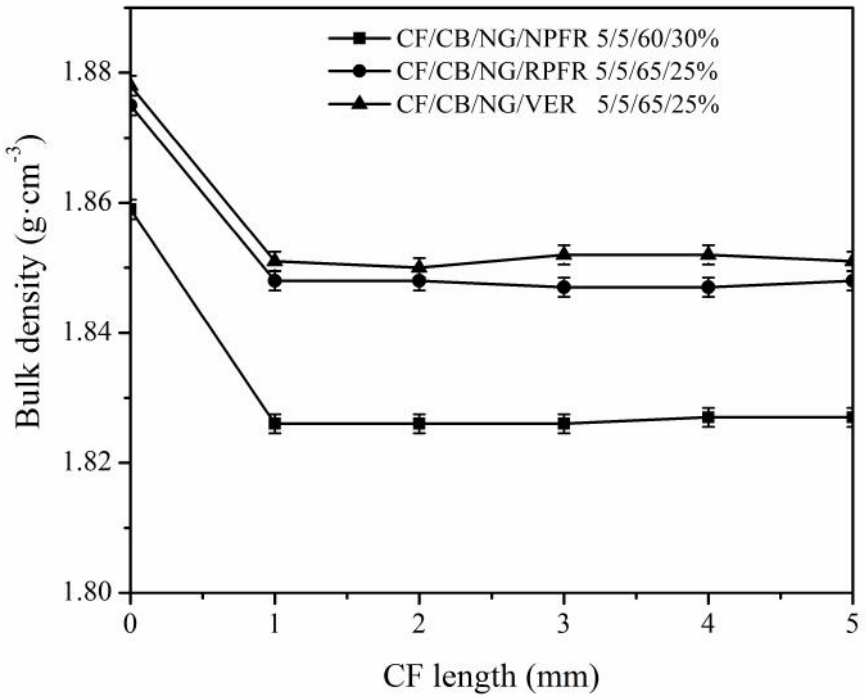

Figure 4.12: Effect of CF length on the bulk density of the CF/CB/NG/polymer composite bipolar plates

4.4.1.2 Flexural strength and deflection at mid-span of the CF/CB/NG/polymer

Figure 4.13 shows the effect of CF length on the mechanical properties of CF/CB/NG/polymer composites. It can be seen that the flexural strength and deflection at mid-span increases sharply from no CF (zero mm CF) to 1 mm CF (5%) for all three polymer matrix. However, on further increase in the CF length, the mechanical strength decreases comparatively slowly up to 2 mm length and then quickly. In fact the uniform distributions at 1 mm and 2 mm length help to increase the mechanical strength for all three polymer matrix. However, the non-uniform distribution due to the agglomeration leads to the decrease in flexural strength and deflection at mid-span.

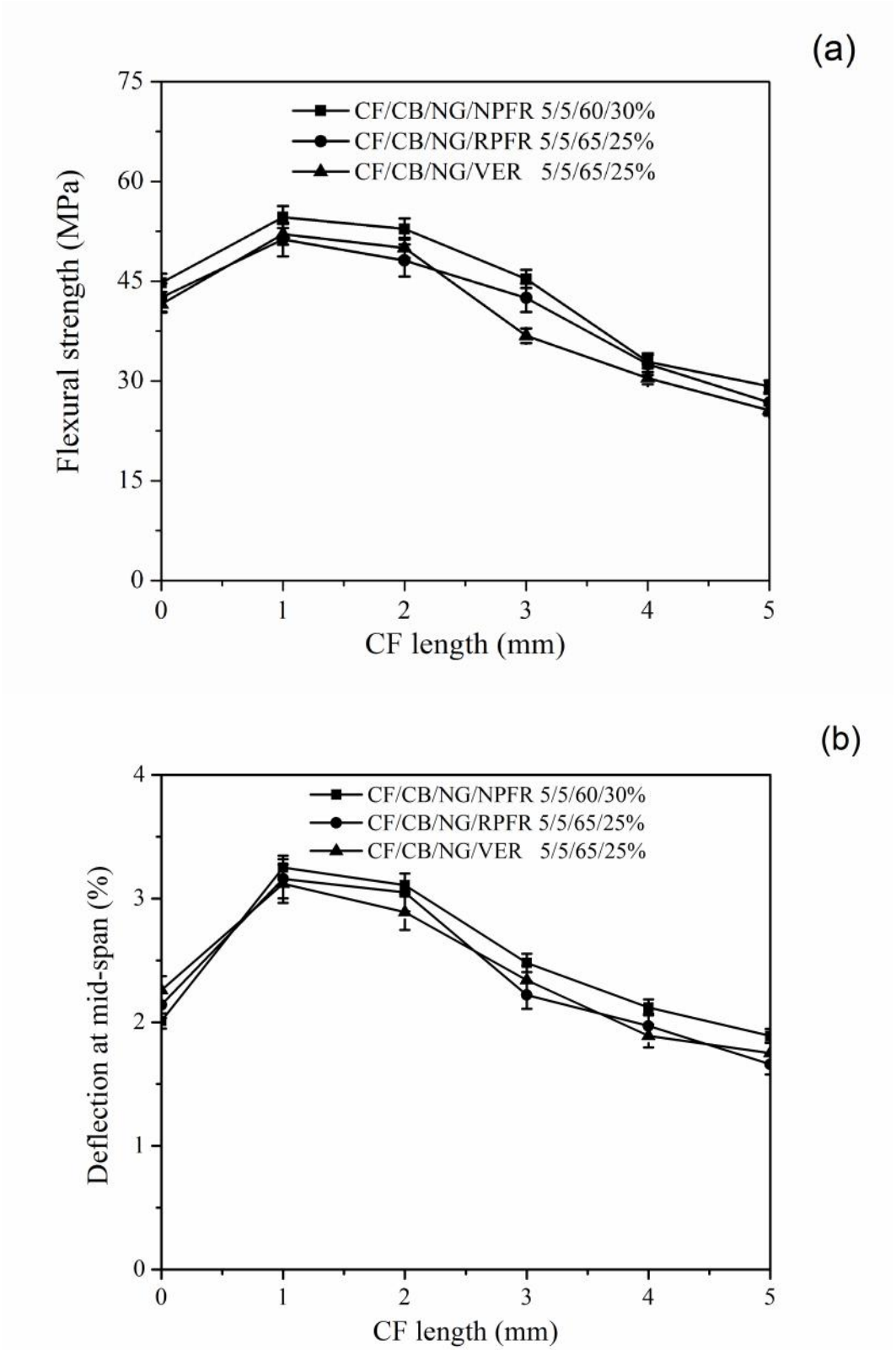

Figure 4.13: Effect of CF length on the (a) flexural strength, and (b) deflection at mid-span of the CF/CB/NG/polymer composite bipolar plates

The non-uniformity of CF distribution at different CF length at fixed CF loading (5%) can be seen in the fractured surface representative SEM morphology of CF/CB/NG/NPFR 5/5/60/30% shown in section 4.4.1.4. The flexural strengths of the NPFR, RPFR, and VER resin based composite were around 54.64, 51.27, and 52.05 Mpa, respectively, corresponding to 1mm CF length. However, the deflection at mid-span of these three composites followed the similar pattern and were found to be within the target value.

4.4.1.3 Shore hardness of the CF/CB/NG/polymer

Figure 4.14 shows the effect of CF length on the shore hardness of the developed composite bipolar plates. It can be seen that the shore hardness of the composite increases initially due to the addition of CF as compared to without CF content composite bipolar plate.

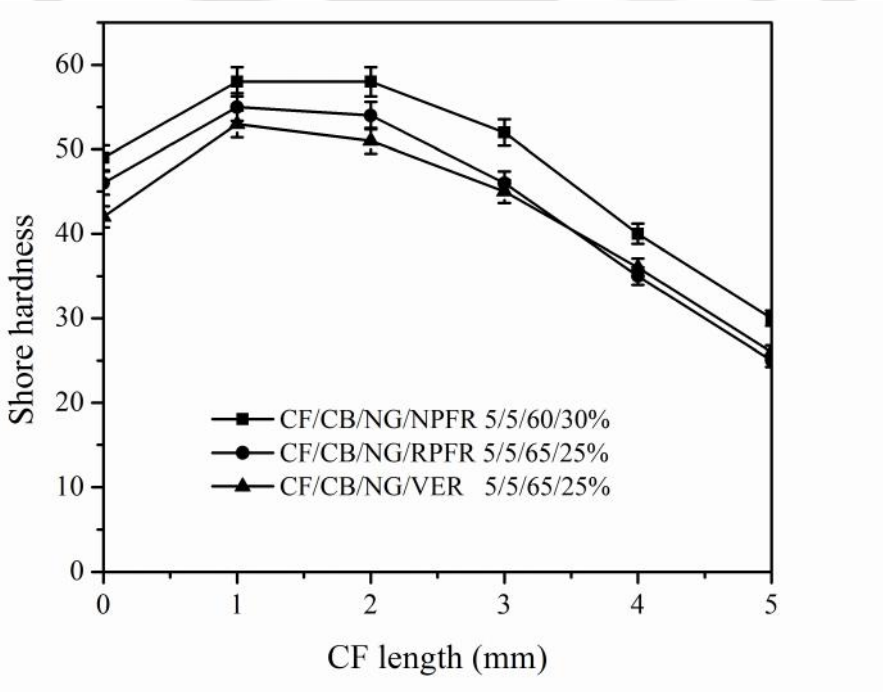

Figure 4.14: Effect of CF length on the shore hardness of the CF/CB/NG/polymer composite bipolar plates

This increase of shore hardness can be attributed to the well-known ribbon or glassy carbon structure of CF, which provides cushioning effect to the surface of the composite. It can also be seen that the shore hardness of the composite was almost same up to CF length of 2 mm. However, after that the shore hardness was decreased with the increase of CF length. The CF was reinforced primarily to improve the mechanical properties therefore 1 mm of CF length was taken as the optimized length for further study considering the highest mechanical properties discussed earlier. The shore hardness of the composite bipolar plate at the optimum compositions was 58, 55, and 53 for NPFR, RFPR, and VER based composites, respectively.

4.4.1.4 Morphological study of the CF/CB/NG/polymer

The micrographs of the CF/CB/NG/polymer composite bipolar plates were evaluated. However, fig. 4.15 shows the SEM of the fractured surfaces of CF/CB/NG/NPFR 5/5/60/30% composite bipolar plate for different CF lengths. It can be seen in the micrograph that the carbon fibers are sandwiched between several NG particles and thus help in improving the mechanical strength of the composite bipolar plates. Similar, pattern was also observed in the case of RPFR and VER based composite bipolar plates (not shown in fig 4.15). Moreover, the CF strands were found to be spread in the interstices between NG-NG, NG-CB, and CB-CB. This effect ensures the contact between the NG and CB thus helps in increasing the mechanical strength. However, increase in CF length clearly shows the agglomeration of the CF strands. It may be noted that the volume fraction of CF was 5% in all the composite.

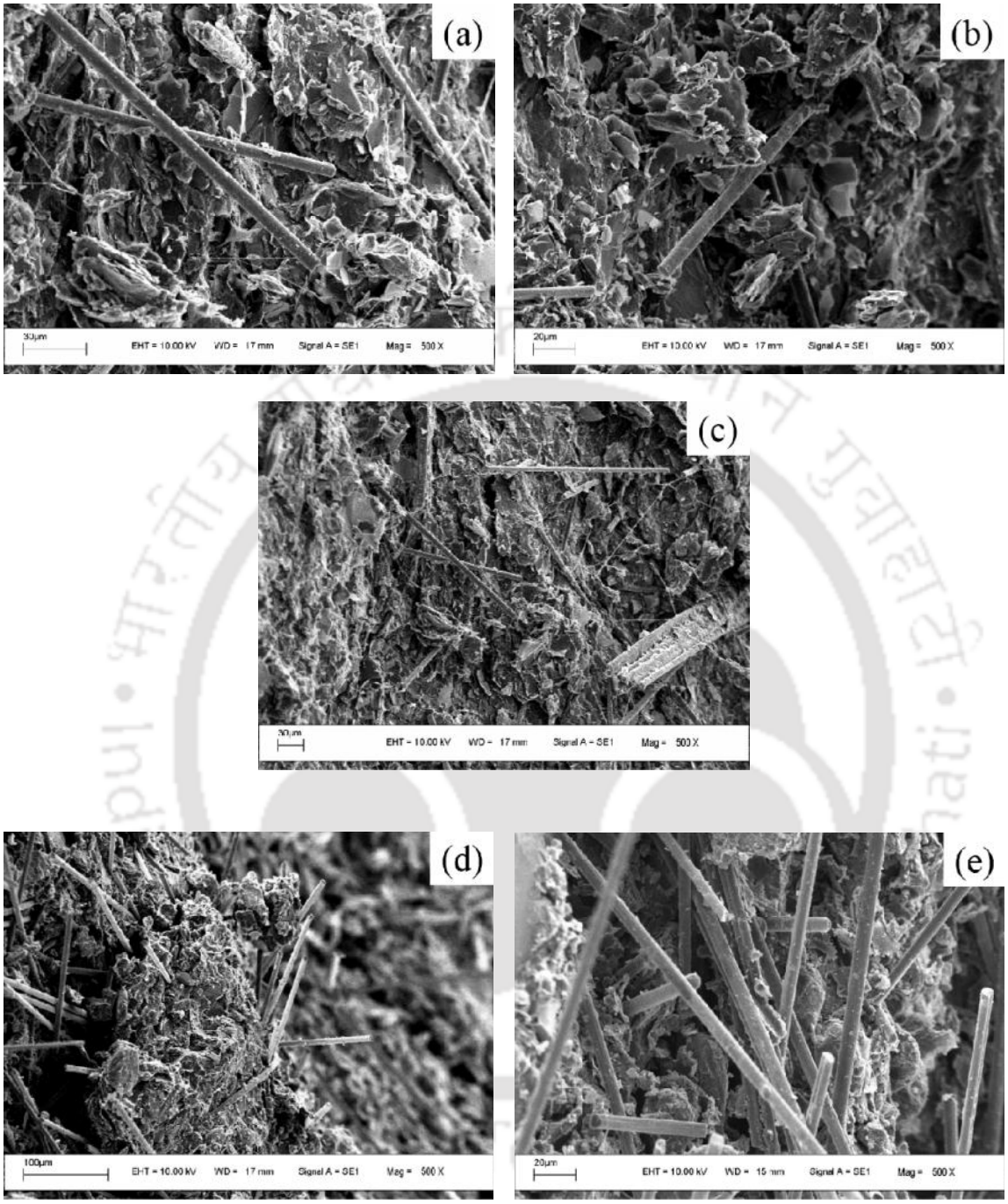

Figure 4.15: Representative FE-SEM images of fractured surface of CF(1mm)/CB/NG/NPFR composite bipolar plates for different CF lengths (a) 1 mm, (b) 2 mm, (c) 3 mm, (d) 4 mm, and (e) 5 mm

4.4.1.5 Electrical conductivity of the CF/CB/NG/polymer

The in-plane and through-plane electrical conductivities of CF/CB/NG/polymer composite bipolar plates for different length of the CF is shown in fig. 4.16, respectively. It can be seen from the figure that the in-plane as well as through-plane electrical conductivities of the developed composite were invariant up to 2 mm length of CF. However, the electrical conductivity decreased with the further increase in the CF length beyond 2 mm. It may be noted that 5% CF reinforcement (up to 2 mm length) at the expense of NG compensated the electrical conductivity almost exactly when there is no CF (corresponding to zero mm length). It may be due to uniform dispersion of CF in the composite up to 2 mm length as shown earlier in the fractured surface of the composite.

It was observed that the tendency of the CF agglomeration increased as the length of the CF increased beyond 2 mm length. It was experienced that the dispersion of long strands of CF into the slurry was difficult, as a result the electrical conductivity decreased at higher CF lengths. The electron can migrate from one end of the bipolar plate to the other end via NG-NG and/or NG-CB-NG and/or NG-CF-NG and/or NG-CF-CB-NG conducting path. Therefore, the electrical conductivities of the multi-filler (with different aspect ratios) composites are higher than the electrical conductivity of the single filler composites. However, at higher length of CF, the orientation of the CF becomes non-uniform due to agglomeration and decreases the electrical conductivity of the bipolar plate. The maximum in-plane electrical conductivities of the composite bipolar plates were 281.97, 415.05, and 349.25 $S \cdot cm^{-1}$, respectively. Similarly, the highest through-plane electrical conductivities at the optimum composition of the composite bipolar plates were 79.84, 97.47 and 92.14 $S \cdot cm^{-1}$, respectively.

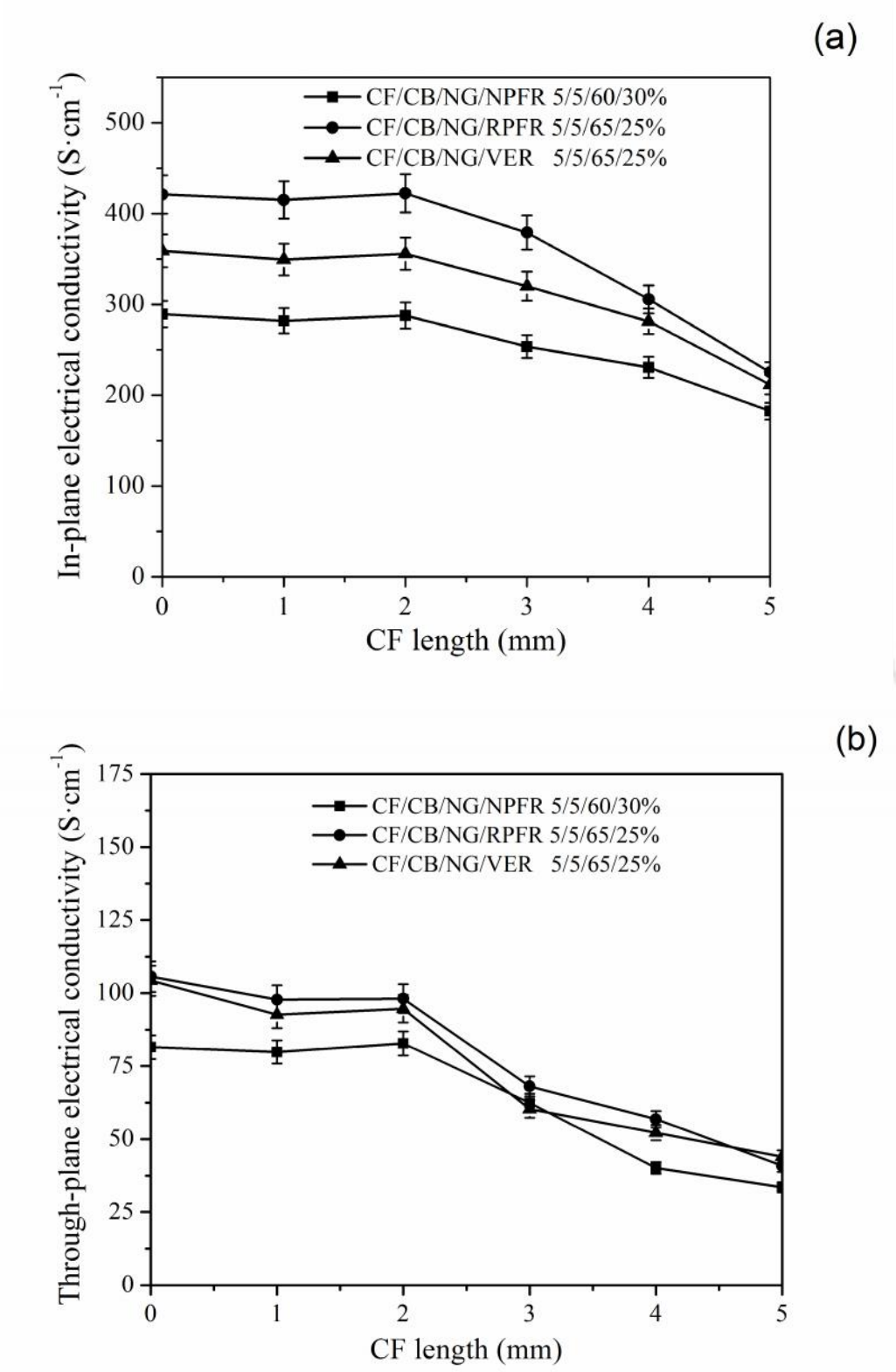

Figure 4.16: Effect of CF length on (a) in-plane and (b) through-plane electrical conductivities of the CF/CB/NG/polymer composite bipolar plates

It has been found that the in-plane electrical conductivities of the composite bipolar plates for all the polymer systems were well above the target values. However, the through-plane electrical conductivity of the composite bipolar plate for all the polymer matrix was still need to be improved to reach the target value.

4.4.1.6 Thermal conductivity of the CF/CB/NG/polymer

The thermal conductivity is also an important property of bipolar plate for heat dissipation during the functioning of fuel cell stack. It is a fact that during compression molding, the NG flakes are oriented in the pressure planes. Therefore, in-plane thermal conductivity of graphite-polymer composite is more than through-plane direction because of anisotropic structure of the NG (major reinforcement) based composite. Moreover, since the required thickness of the composite bipolar plate should be as small as possible to reduce the stack weight to volume ratio (US DoE 2012), the high in-plane thermal conductivity is required. Thus the heat generated in the fuel cell stack may be conducted efficiently using bipolar plate. Therefore, in-plane thermal conductivity was measured and represented here. Figure 4.17 shows that the thermal conductivity of the composites decreased at the higher length of CF (beyond 2 mm). The thermal conductivity of the composites was increased for 1 and 2 mm length of CF content as compared to when there is no CF content. However, there no significance difference was observed on the thermal conductivity of the composite for 1 and 2 mm length of CF. It may be because small length CF strands tend to align parallel to the surface of the bipolar plate, while owing to higher lengths of CF (at same loading) in the composite bipolar plate the number of CF strands reduced along with increased agglomeration result in reduced thermal conductivity of the composite.

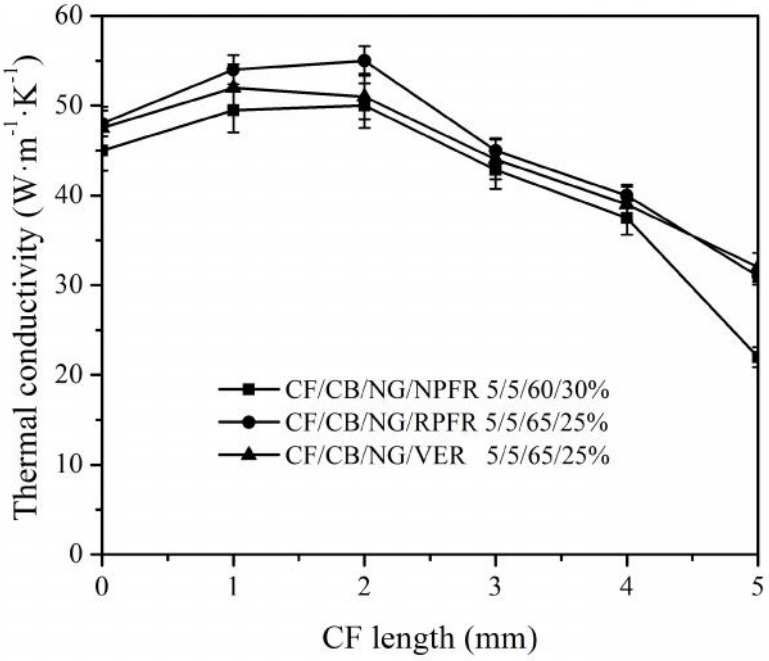

Figure 4.17: Effect of CF length on the thermal conductivity of the CF/CB/NG/polymer composite bipolar plates

The thermal conductivity of the CF, along the length, is 10.46 W·m^{-1}·K^{-1}, while it is 140–500 W·m^{-1}·K^{-1} for NG along the basal plane (datasheet, Torayca). Therefore, due to the agglomeration of CF strands at its higher length, the thermal conductivity of the composites adversely affected. The thermal conductivity pattern of different polymer based composite follow similar trend.

4.4.1.7 Hydrogen permeability of the CF/CB/NG/polymer

The hydrogen permeability of the composite bipolar plate was measured as per the method discussed in section 4.2.3.6. Figure 4.18 shows that the effect of CF length on the hydrogen permeability of the CF/CB/NG/polymer composite bipolar plates. It can be seen that the hydrogen permeability of the composite increases with the increase in the CF length for all three polymer matrix.

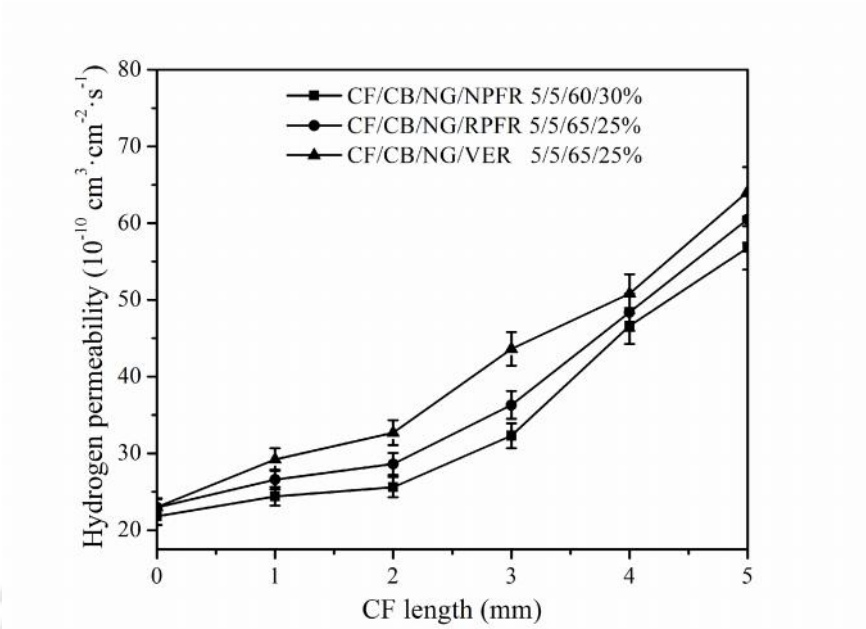

Figure 4.18: Effect of CF length on the hydrogen permeability of the CF/CB/NG/polymer composite bipolar plates

However, the CF mainly reinforced into the composite is to improve the mechanical strength of the bipolar plate keeping the hydrogen permeability within the required level. The long CF strands agglomerated within the composites, which may create small air pockets, led to high hydrogen permeability. Moreover, the length of CF need to optimized for the maximum improvement of the mechanical strength for the composite. However, the hydrogen permeability was well within the DoE target for the developed composite bipolar plate.

4.4.1.8 Corrosion current density of the CF/CB/NG/polymer

Potentiodynamic measurements were conducted to investigate the corrosion current densities of the CF/CB/NG/polymer composites. Figure 4.19 shows the effect of CF length on the anodic and cathodic corrosion current density of the composite bipolar plates.

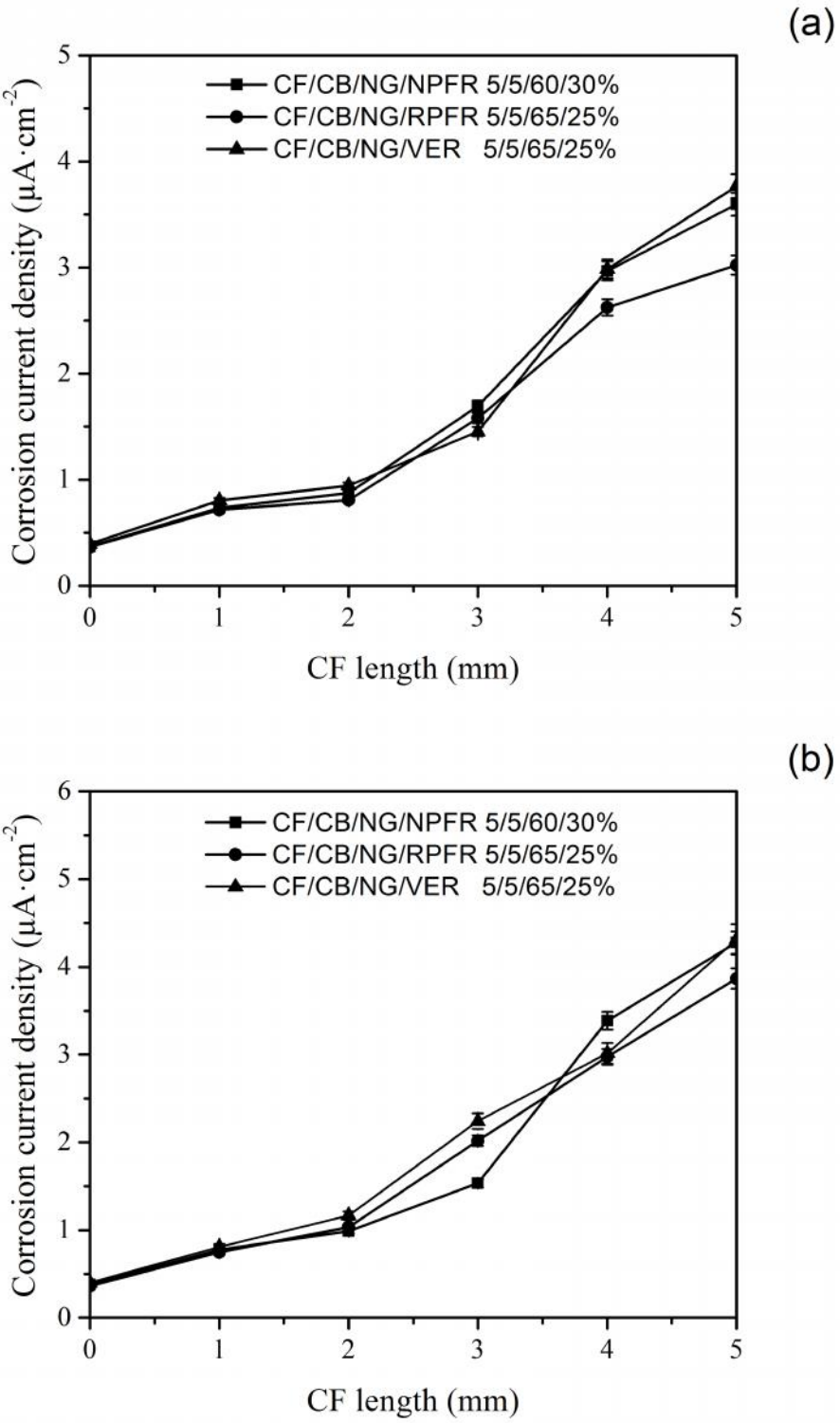

Figure 4.19: Effect of CF length on (a) anodic (hydrogen purged) and (b) cathodic (oxygen purged) corrosion current densities of the composite bipolar plates; tested in 1 M H_2SO_4 +2 ppm HF at 80°C; scan rate 1 $mV \cdot s^{-1}$

From the figures, it is clearly visible that the corrosion current densities of the composite bipolar plates increases with the increase in the CF length. Moreover, the corrosion current density increases rapidly when CF length was above 2 mm. The rapid increased in the corrosion current density may be due to the increased porosity of the composites, which is supported by the hydrogen permeability results (fig. 4.18). It can be noted that the VER based composites were found to be relatively more corrosive due to the use of metal catalyst used during VER curing reaction. Moreover, the anodic and cathodic current densities were well within the DoE target for the CF/CB/NG/polymer composite bipolar under investigation.

Considering, the various properties (especially mechanical) the CF length of 1 mm was used for all the further studies unless otherwise stated.

4.4.1.9 Interfacial electrical contact resistance of the CF(1mm)/CB/NG/polymer

The ICR of the composite was measured as per the procedure discussed in section 4.2.3.7. The fig. 4.20 shows the ICR of the composite bipolar plates optimized for 1 mm CF length was measured at various applied stacking pressure. It can be seen that the increase in applied stacking pressure decreases the ICR of the composite for all the three polymer matrix. However, the applied stacking pressure shown very meagre effect on the ICR above 2 MPa pressures. The decrease in the ICR with increase in the applied stacking pressure was due to the increase in contact points at different interfaces. At high pressure, carbon paper being a soft material entered into the rough surfaces (micro level) of composite and the copper plate and thus reduced the ICR. The ICR of the NPFR, RPFR, and VER based composite bipolar plates was found to be 22.11, 18.75, and 20.32 $m\Omega \cdot cm^2$, respectively, at 2 MPa applied stacking pressure.

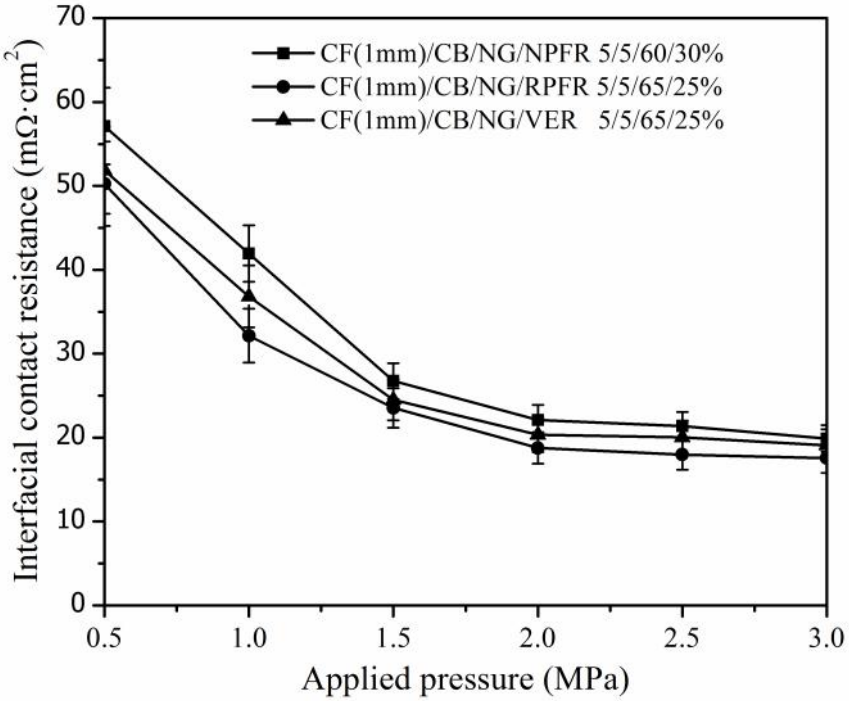

Figure 4.20: Effect of applied pressure on interfacial electrical contact resistance for optimum composite (CF(1mm)/CB/NG/polymer) bipolar plates

It may be noted that the ICR of the optimum composite (CF(1mm)/CB/NG/polymer) bipolar plates was far below the target value. Moreover, though the in-plane electrical conductivity, shore hardness, thermal conductivity, hydrogen permeability, and corrosion current density were well within the target values using the NPFR, RPFR, and VER based optimized composition (CF(1mm)/CB/NG/polymer) but the electrical properties (contact resistance as well as through-plane electrical conductivity) and flexural strength were not achieved by the above composition. The detailed properties of the CF(1mm)/CB/NG/polymer composite bipolar plates at their optimum compositions are summarized in table 4.7 and compared with the target values.

Table 4.7: Properties of optimized CF(1mm)/CB/NG/polymer composite bipolar plate

Properties		**DoE target 2017**	**CF(1mm)/CB/NG/NPFR 5/5/60/30%**		**CF(1mm)/CB/NG/RPFR 5/5/65/25%**		**CF(1mm)/CB/NG/VER 5/5/65/25%**	
Bulk density ($g \cdot cm^{-3}$)		< 2.0	1.827		1.848		1.846	
Flexural strength (MPa)		>59$^{\alpha}$	54.64		51.27		52.05	
Deflection at mid- span (%)		>3–5	3.25		3.05		2.89	
Shore hardness		>40$^{\alpha}$	58		55		53	
Electrical conductivity ($S \cdot cm^{-1}$)		>100	281.97 (∥)	79.84 (⊥)	415.05 (∥)	97.47 (⊥)	349.25 (∥)	92.14 (⊥)
Thermal conductivity ($W \cdot m^{-1} \cdot K^{-1}$)		>10	49.5		54		52	
H_2 permeability (10^{-10} $cm^3 \cdot cm^{-2} \cdot s^{-1}$)		10^4 (at 80°C and 3 bar)	24.4$^{\#}$		26.59$^{\#}$		29.2$^{\#}$	
Corrosion current density ($\mu A \cdot cm^{-2}$)	Anodic	<1	0.717		0.734		0.805	
	Cathodic		0.747		0.778		0.817	
Interfacial contact resistance (ICR) ($m\Omega \cdot cm^2$)		<10	22.11		18.75		20.32	

∥→ in-plane; ⊥ → through-plane

→ H_2 permeability at 80°C under 2 bar pressure

GP→ graphene; α→ Plug Power Inc.

NPFR → novolac phenol formaldehyde resin

RPFR → resol phenol formaldehyde resin

VER → vinyl ester resin

NG → natural graphite

CB → carbon black

CF → carbon fiber

4.4.2 Effect of graphene content on the properties of CF(1mm)/CB/(NG+GP)/polymer composite bipolar plate

It may be note that the DoE has not mentioned whether the target electrical conductivity is for in-plane or through-plane but considering the same value for both the cases, there is a need to improve the through-plane electrical conductivities of the composite bipolar plates. Moreover, the increased conductivity will always be desired if other properties do not deviate much. It was earlier found that the through-plane electrical conductivities of the composites were below 100 $S \cdot cm^{-1}$. Therefore, the above optimized compositions were used for further study improving the required properties of the composite bipolar plate. Therefore, graphene is used to further improve the desired properties. In this effort, a small amount of NG was replaced with the synthesized GP with an aim to at least achieve the electrical properties without hampering the other properties. The effect of GP reinforcement at the expense of NG into the above optimized composite bipolar plate is discussed in the subsequent section.

4.4.2.1 Bulk density of the CF(1mm)/CB/(NG+GP)/polymer

The effects of GP content on the bulk density of the CF(1mm)/CB/NG/polymer composite bipolar plates are shown in fig. 4.21. It can be seen that on increasing the GP content at the expense of NG, the bulk density of the composite continuously decreases almost linearly. The decreasing trend in the density of the composite was attributed due to the less density of GP (around 1-1.6 $g \cdot cm^{-3}$) (Shen and Lua 2013; Kakati and Verma 2011) in comparison to NG (2.26 $g \cdot cm^{-3}$). Moreover, it was found that the density of the composite followed the mixing law.

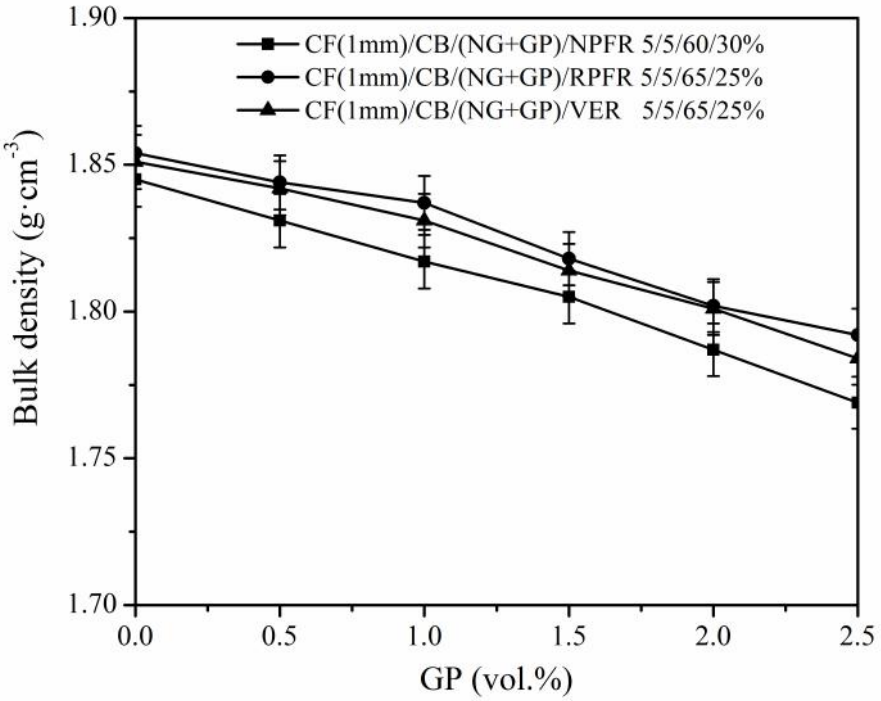

Figure 4.21: Effect of GP content on the bulk density of the CF(1mm)/CB/(NG+GP)/polymer composite bipolar plates

4.4.2.2 Flexural strength and deflection at mid-span of the CF(1mm)/CB/(NG+GP)/polymer

Figure 4.22 shows that effect of GP content on the flexural strength and deflection at mid-span of the developed composites. It can be seen that the flexural strength and deflection at mid-span of the composite bipolar plates (CF(1mm)/CB/(NG+GP)/polymer) initially increases up to 1.5% of GP content (at the expense of NG). It may be due to the high mechanical properties of GP as compared to NG.

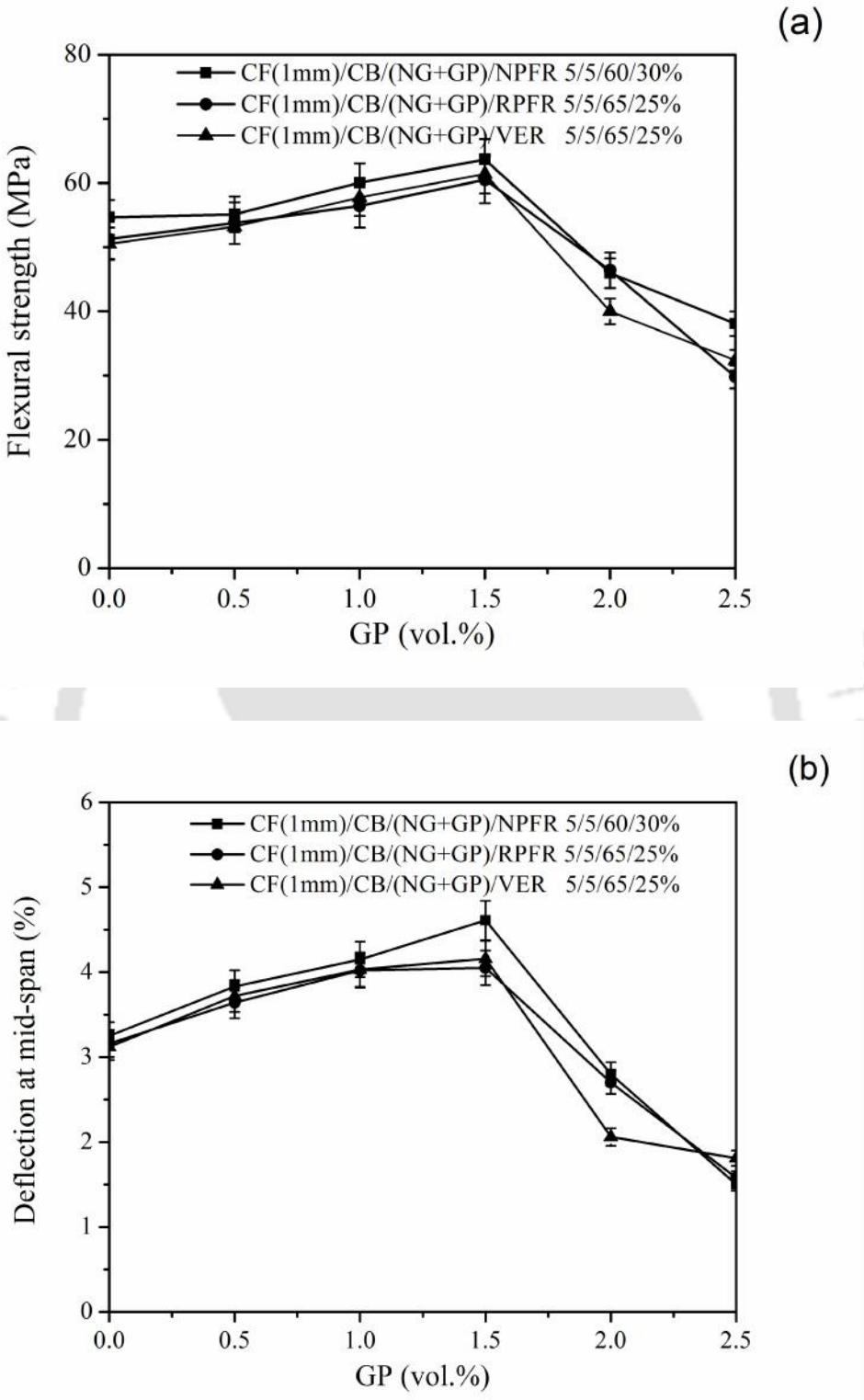

Figure 4.22: Effect of GP content on the (a) flexural strength, and (b) deflection at mid-span of the CF(1mm)/CB/(NG+GP)/polymer composite bipolar plates

Moreover, the high aspect ratio as well as good interfacial adhesion within the other constituents promotes formation of reinforced polymer network structure, and enables the composite bipolar plate more efficiently to handle the load transfer from the host polymer to reinforcement within the other constituents in the composite. As a results contributed to the enhancement of flexural strength and deflection at mid-span. Ramanathan et al., (2008) too have reported that the very small amount of GP is sufficient to significant improve the mechanical properties of the composite. However, it was observed that the flexural strength and deflection at mid-span of the above composite decreased beyond 1.5% of GP content. This may be attributed to the poor dispersion of GP nanosheets at the higher loading due to the lack of polymer matrix. The incomplete reinforcement packing may occurs during the fabrication process, which act as defect in the structure and as a result properties of the bipolar plate change from ductile to brittle (Choi et al., 2005). The maximum flexural strength of the NPFR, RPFR, and VER based composite bipolar plates was 63.66, 60.5, and 61.41 MPa, respectively (Ghosh and Verma 2014). Similarly, the corresponding deflection at mid-span at the optimum composition was 4.61, 4.05, and 4.16%, respectively.

4.4.2.3 Shore hardness of the CF(1mm)/CB/(NG+GP)/polymer

Figure 4.23 shows the effect of graphene content on the properties of shore hardness of the composite bipolar plates. It can be seen that the shore hardness of the composite increases with the increase in GP content (at the expense of NG) upto 1.5%. On further increase in GP content the shore hardness of the composite decreases. The increase in shore hardness can be attributed to the excellent structural and physical properties of GP nanosheets, which may act like a flexible net due to its two dimensional structure. Thus

when the indenter falls on to the composite surface, GP sheets carry the load uniformly and thus impede the motion of dislocations (Brownson et al., 2011).

However, the decrease of shore hardness beyond 1.5% of GP content can be attributed to the poor bonding of GP with the other constituents in the composite due to the lack of amount of binder matrix, which was fixed in all the compositions. It may be noted that GP having very high surface area as compared to NG, was added at the expense of NG. Therefore, at high GP loading, the polymer matrix was not sufficient to bind the reinforcements and resulted decreased hardness. The similar trend was found for all the polymer matrix based composite. The maximum shore hardness of the NPFR, RPFR, and VER based composite bipolar plates was found to be 65, 62, and 63, respectively.

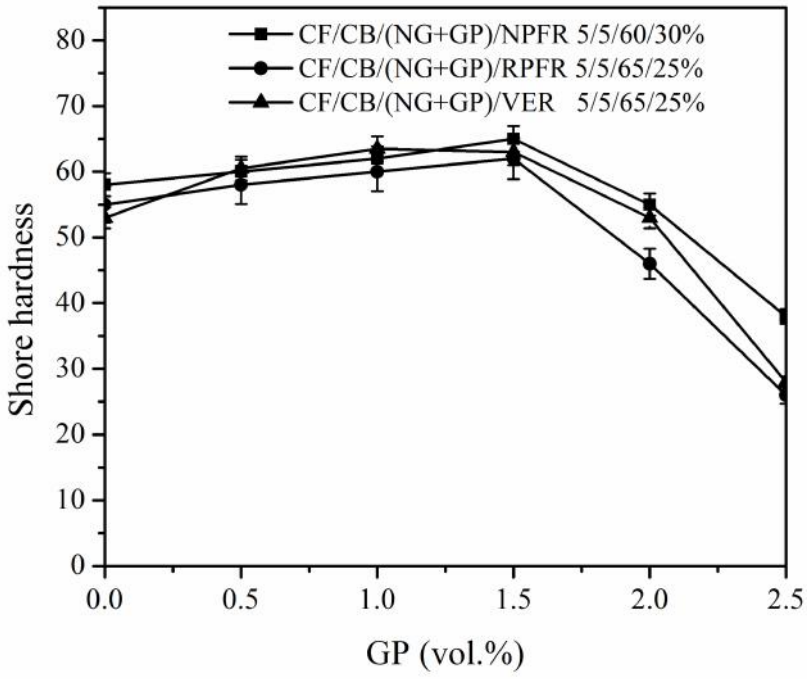

Figure 4.23: Effect of GP content on the shore hardness of the CF(1mm)/CB/(NG+GP)/polymer composite bipolar plates

4.4.2.4 Electrical conductivity of the CF(1mm)/CB/(NG+GP)/polymer

The high in-plane and through-plane electrical conductivity is the most essential feature for carbon-polymer composite bipolar plate. However, polymer resin often forms a thin insulating layer around the conductive reinforcement, thus decreases the effective essential conductive pathway within the reinforcement. A number of reports have indicated that the incorporation of graphite and/or CB and/or CF with other conductive materials, especially graphene, has been considered as an effective method to develop higher electrical conductivity of the carbon-polymer composite bipolar plates due to 2D conductive networks (Hsiao et al., 2010; Kakati et al., 2013). Therefore, the in-plane as well as through-plane electrical conductivity of CF(1mm)/CB/(NG+GP)/polymer composite bipolar plates with GP contents (at the expense of NG) were measured. It can be seen in the fig. 4.24 that the electrical conductivities of the composite is increased due to the reinforcement of GP content up to 1.5%. Thereafter a steep decrease was observed with the increase of GP content. It is known that GP is highly electrical conductive material (Geim 2009) and thus the addition of GP in the composite helps to easier electron mobility, which increases in-plane and through-plane electrical conductivities of the composite bipolar plate. The 1.5% GP content was suitable for better dispersion in the composite (having insulating polymer matrix) and thus forms conducting channels with the other conducting reinforcements such as CB and/or CF and/or NG in the composite (Kakati et al., 2013). However, higher GP loading (beyond 1.5% of GP) in polymer composites may cause serious GP aggregation, and the in-plane and through-plane electrical conductivities were found to be decreased. The 1.5% GP content showed highest electrical conductivities.

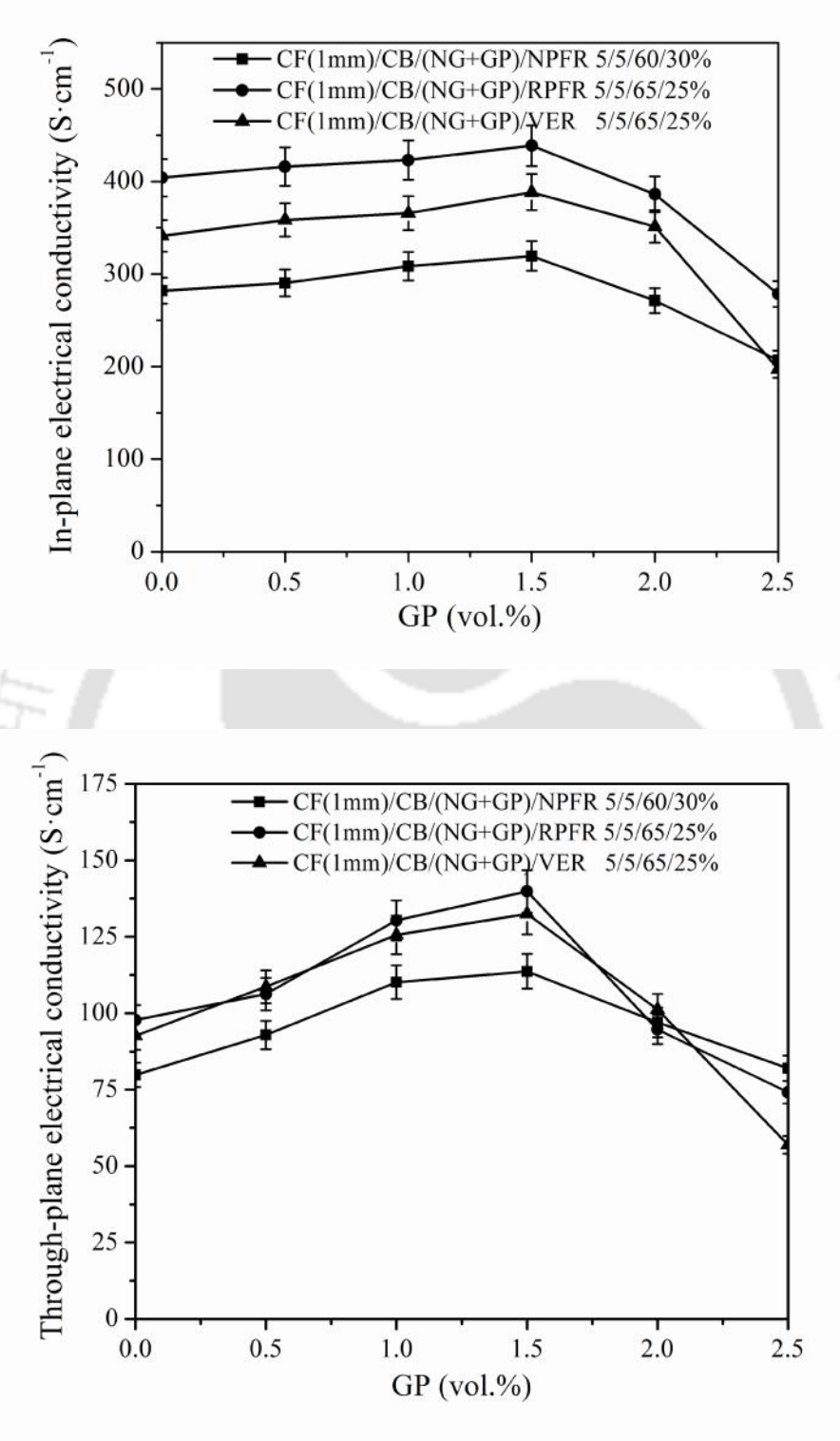

Figure 4.24: Effect of GP content on (a) in-plane and (b) through-plane electrical conductivity of the CF(1mm)/CB/(NG+GP)/polymer composite bipolar plates

The maximum in-plane electrical conductivities of the composite bipolar plates at 1.5% GP were 319.42, 438.37, and 388.42 $S \cdot cm^{-1}$, respectively, for NPFR, RPFR, and VER based polymer. Similarly, the corresponding highest through-plane electrical conductivities of the composite bipolar plates were 113.68, 139.87 and 132.45 $S \cdot cm^{-1}$, respectively.

4.4.2.5 Thermal conductivity of the CF(1mm)/CB/(NG+GP)/polymer

Figure 4.25 shows the in-plane thermal conductivity of composite plates with increasing graphene content. The thermal conductivity of the GP is around ten times higher than the NG. Therefore, the thermal conductivities of the bipolar plates were increased with the reinforcement of small amount of graphene content of the expense of NG.

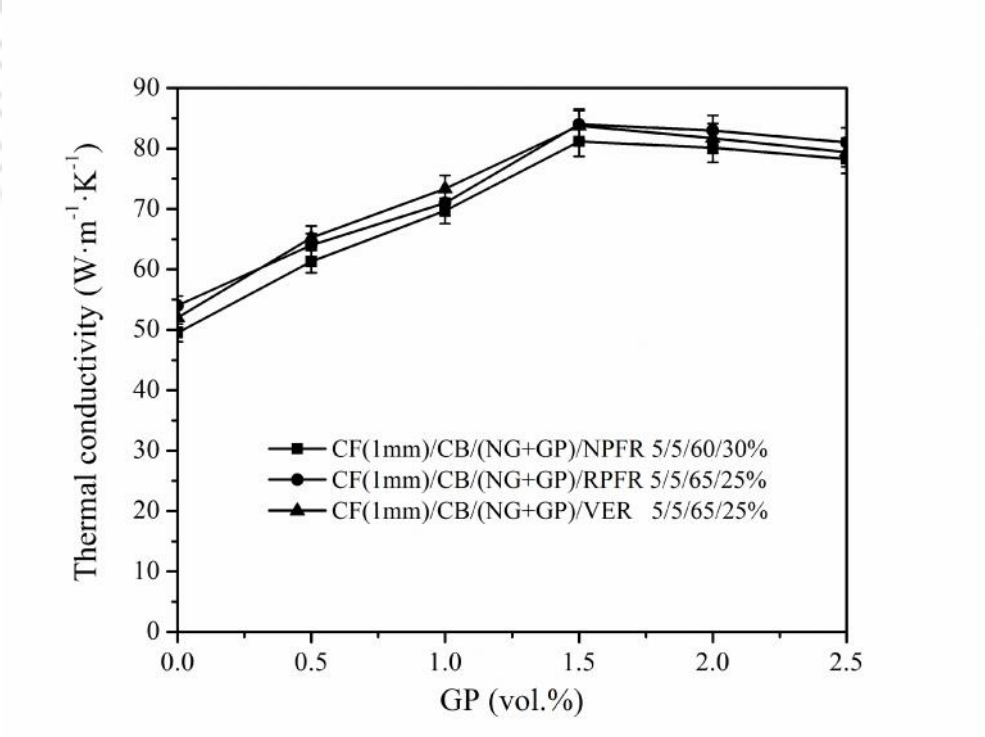

Figure 4.25: Effect of GP content on the thermal conductivity of the CF(1mm)/CB/(NG+GP)/polymer composite bipolar plates

Moreover, with the addition of 1.5% graphene content, thermal conductivity was increased around 40% for composite bipolar plate as compared to when there was no GP content present. However, it was found that beyond 1.5%, the thermal conductivity was not improved for all the three type polymer composites; it may be due to the formation of air pockets in the composite owing to high requirement of matrix by GP as compared to NG, which hinder the thermal transport in the composite.

4.4.2.6 Hydrogen permeability of CF(1mm)/CB/(NG+GP)/polymer

The effect of GP content on the hydrogen permeability of the composite bipolar plate is shown in fig. 4.26. The reinforcement with GP reduces the hydrogen permeabilities initially upto 1.5% GP loading.

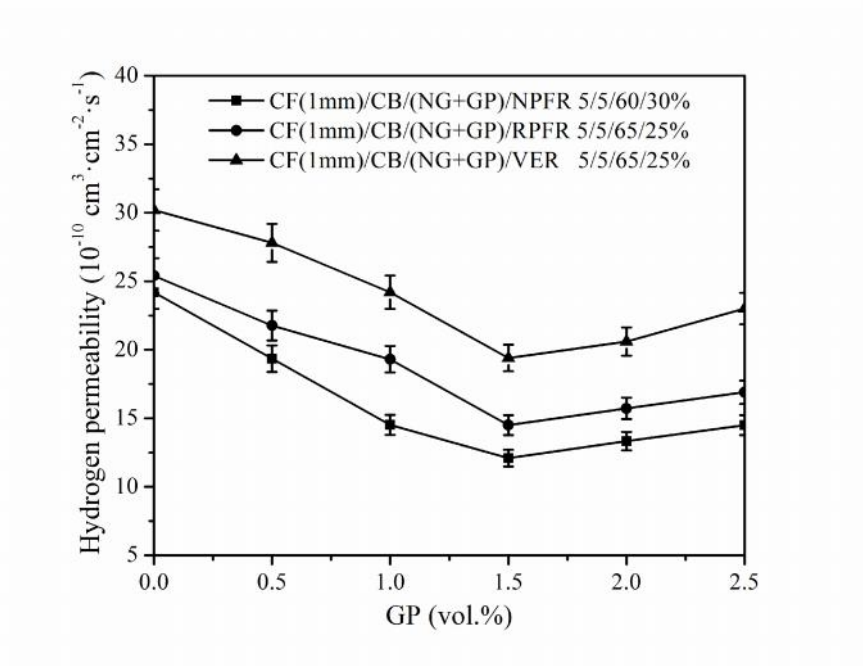

Figure 4.26: Effect of GP content on the hydrogen permeability of the CF(1mm)/CB/(NG+GP)/polymer composite bipolar plates

This can be attributed to the presence of impermeable GP sheets (Kim et al., 2010) with high aspect ratio that are uniformly dispersed in the penetrable polymer matrix along with other reinforcement leading to increase diffusion path length (tortuosity) and consequently, decreases permeability (Kalaitzidou et al., 2007). It is the intrinsic properties of GP sheet, which is impermeable to all gas molecules when there is no defects presents on the surface of GP sheets. The graphene's π-orbitals forms a dense, delocalized cloud that blocks the gap within its aromatic rings. This create repelling field, which does not allow even the smallest molecules including hydrogen (Berry 2013). The minimum hydrogen permeabilities of the GP/CF(1mm)/CB/NG/polymer composite bipolar plates were recorded as 12.09×10^{-10}, 15.5×10^{-10}, and 19.4×10^{-10} $cm^3\cdot cm^{-2}\cdot s^{-1}$, respectively for NPFR, RPFR, and VER based polymer composites. Kalaitzidou et al., (2007) reported GP can reduce oxygen permeability more efficient than CB and CNT. However, the hydrogen permeability of the composite increases for GP loading above 1.5%. This can be explained with the help of BET surface area analysis of the NG and GP. The surface area of the GP particles was 750.85 $m^2\cdot g^{-1}$, while it was only 249.64 $m^2\cdot g^{-1}$ for the NG particles. Therefore, at higher GP loading, the polymer content was not sufficient to bind all the filler content. This affects the hydrogen permeability of the composite negatively. The similar kind of detrimental effect was also observed in the case of mechanical strength, electrical conductivity, and thermal conductivity of the composite.

4.4.2.7 Corrosion current density of the CF(1mm)/CB/(NG+GP)/polymer

Figure 4.27 shows the corrosion current density for the GP reinforced composite bipolar plate in accelerated anodic, and cathodic environments.

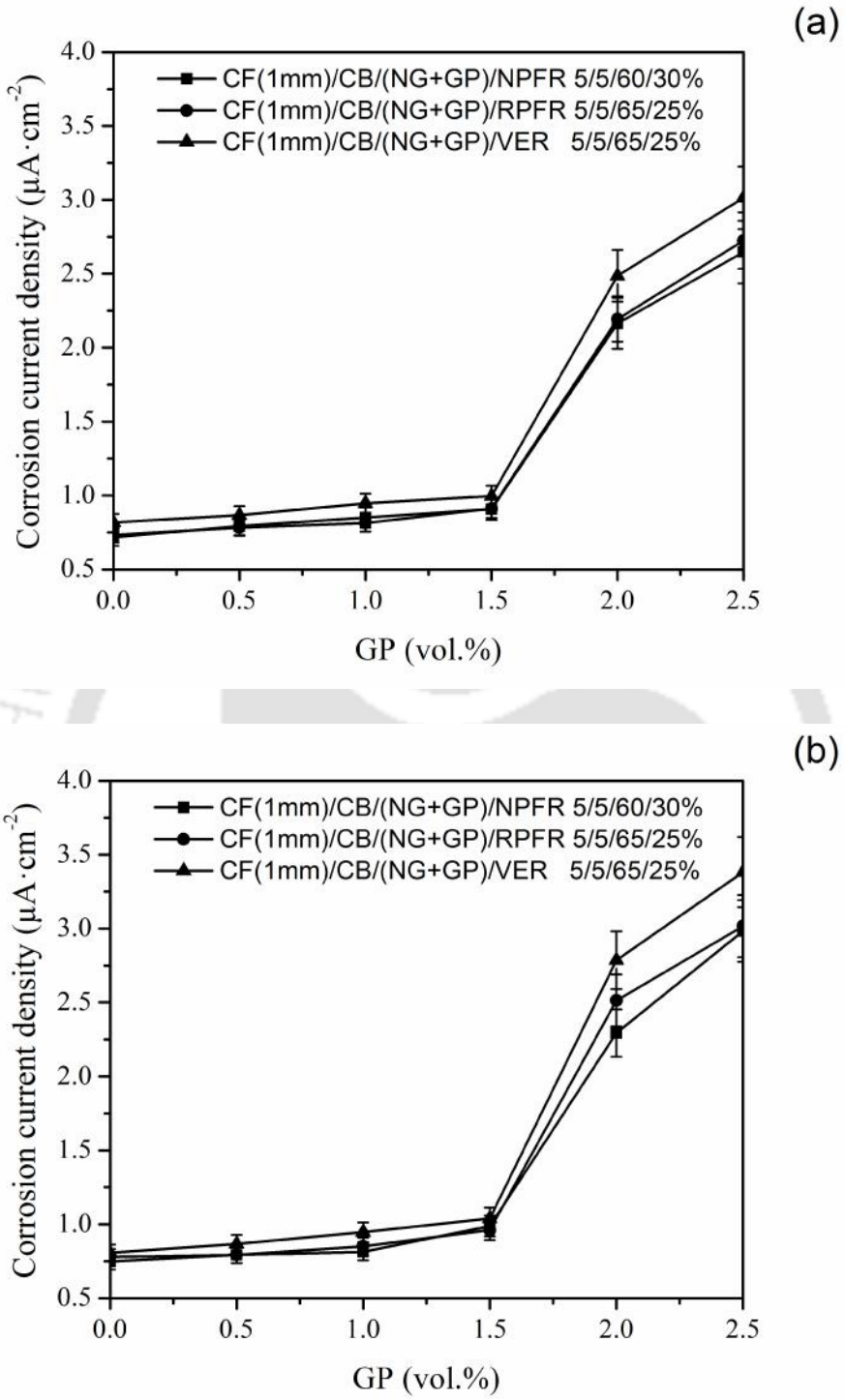

Figure 4.27: Effect of GP content on (a) anodic (hydrogen purged) and (b) cathodic (oxygen purged) corrosion current densities of the CF(1mm)/CB/(NG+GP)/polymer composite bipolar plates; tested in 1 M H_2SO_4 +2 ppm HF at 80°C; scan rate 1 $mV \cdot s^{-1}$

It can be seen that the anodic (H_2-purged), and cathodic (O_2-purged) corrosion current densities (i_{corr}) of the composite bipolar plate increases slightly as compared to without graphene content composite bipolar plate (Eguizábal et al., 2014). This behavior is consistent with the results obtained by Kakati et al., (2013) and Oliveira et al., (2013). It was observed that the electrical conductivity was increased by GP. However, the corrosion resistance of the composite bipolar plate was slightly affected but within the upper limit. However, increase the conductivity, one of the most desired properties of composite bipolar plate and balancing these effects with the other properties is a main challenge to the successful development of the composite bipolar plate. The PEMFC environment simulated corrosion current density for anodic condition and cathodic condition of the NPFR, RPFR, and VER based composite bipolar plate are shown in the fig. 4.27. It may be noted that i_{corr} values for anodic and cathodic environments for carbon-polymer composite bipolar plate are hardly discussed in any literature. Moreover, the anodic and cathodic corrosion current densities were well within the DoE target for the NPFR (anodic: 0.907 $\mu A \cdot cm^{-2}$; cathodic: 0.988 $\mu A \cdot cm^{-2}$), RPFR (anodic: 0.912 $\mu A \cdot cm^{-2}$; cathodic: 0.961 $\mu A \cdot cm^{-2}$) based developed composite bipolar plate under study. However, the cathodic corrosion current density for VER (anodic: 0.997 $\mu A \cdot cm^{-2}$; cathodic: 1.04 $\mu A \cdot cm^{-2}$) based polymer composite is just above the target for the composite bipolar plate.

It is found that 1.5% GP in the composition showed highest mechanical and electrical properties for all the three type of polymer composites. Therefore, the GP/CF(1mm)/CB/NG/polymer (GP/CF(1mm)/CB/NG/NPFR 1.5/5/5/58.5/30%, GP/CF(1mm)/CB/NG/RPFR 1.5/5/5/63.5/25%, and GP/CF(1mm)/CB/NG/VER

1.5/5/5/63.5/25%) was further studied for interfacial contact resistance to analyses any adverse effect owing to the reinforcement of the graphene.

4.4.2.8 Interfacial electrical contact resistance of the GP/CF(1mm)/CB/NG/polymer

Figure 4.28 shows the ICR analysis of the optimized graphene content reinforced composite bipolar plate (GP/CF(1mm)/CB/NG/polymer). The ICR of the composite decreases with the increase in applied stacking pressure as observed in the fig. 4.28. However, ICR of the composite decreases appreciably and significantly with the increase in applied stack pressure. It may be due to the alignment of highly conductive graphene particles parallel to the composite surface during compression moulding.

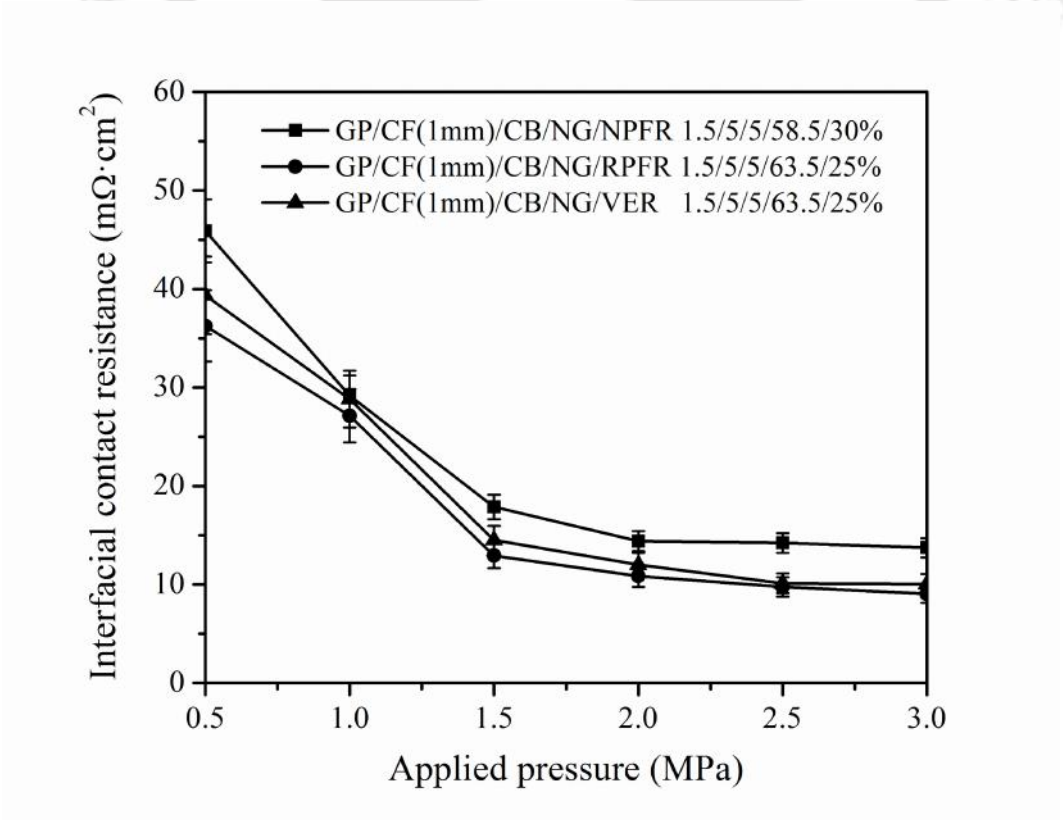

Figure 4.28: Effect of GP content on the interfacial electrical contact resistance of the optimum composite (GP/CF(1mm)/CB/NG/polymer) bipolar plates

The graphene particles aligned on to the surface create very high conductive path to the electrons and thus make the composite with very low ICR. The ICR of the optimum composite bipolar plate were 14.4, 10.75, and 12.86 $m\Omega \cdot cm^2$ at 2 MPa applied pressure, respectively for NPFR, RPFR, and VER based polymer composites. However, the ICR of the composite is just edge away from the benchmark.

Table 4.8 shows the results of the optimized composite bipolar plate and compared with the target properties. It is found that the composite bipolar plate achieved all the target properties. However, the ICR of the composites were slightly away from the target properties. Moreover, the cathodic corrosion current density for the VER based GP reinforced composite was insignificantly above the target value. Therefore, these composite bipolar plates were evaluated in the real PEMFC. The PEMFC performance analysis using developed and optimized composite bipolar plate is discussed in the subsequent section.

4.4.3 Fuel cell performance analysis

The PEMFC performance evaluation was conducted using CF optimized composite bipolar plate. Moreover, final GP optimized composite was evaluated in the PEMFC. The MEA was developed as per the procedure described in the section 4.3.2. The developed MEA was used to study the performance of the PEMFC. It is worthy to mention that a fresh MEA is fabricated with same composition and process to study the performance of the PEMFC for each pair of bipolar plates. It was done in order to avoid the aging effect of the MEA (if any) on the performance of the fuel cell. Figure 4.29 shows the *I-V* performance of unit cell PEMFC operated at around 50°C using optimum composition of composite bipolar plates.

Table 4.8: Properties of optimized GP/CF(1mm)/CB/NG/polymer composite bipolar plate

Properties		**DoE target 2017**	**GP/CF(1mm)/CB/NG/NPFR 1.5/5/5/58.5/30%**		**GP/CF(1mm)/CB/NG/RPFR 1.5/5/5/63.5/25%**		**GP/CF(1mm)/CB/NG/VER 1.5/5/5/63.5/25%**	
Bulk density ($g \cdot cm^{-3}$)		< 2.0	1.815		1.833		1.831	
Flexural strength (MPa)		>59[α]	63.66		60.05		61.41	
Deflection at mid- span (%)		3–5	4.61		4.05		4.16	
Shore hardness		>40[α]	65		62		63	
Electrical conductivity ($S \cdot cm^{-1}$)		>100	319.42 (∥)	113.68 (⊥)	438.37 (∥)	139.87 (⊥)	388.42 (∥)	132.45 (⊥)
Thermal conductivity ($W \cdot m^{-1} \cdot K^{-1}$)		>10	81.14		84		83.78	
H_2 permeability (10^{-10} $cm^3 \cdot cm^{-2} \cdot s^{-1}$)		10^4 (at 80°C and 3 bar)	12.09[#]		15.5[#]		19.4[#]	
Corrosion current density ($\mu A \cdot cm^{-2}$)	Anodic	<1	0.907		0.912		0.997	
	Cathodic		0.988		0.961		1.04	
Interfacial contact resistance (ICR) ($m\Omega \cdot cm^2$)		<10	14.4		10.75		12.86	

∥ → in-plane; ⊥→ through-plane

→ H_2 permeability at 80°C under 2 bar pressure

GP→ graphene; α→ Plug Power Inc.

NPFR → novolac phenol formaldehyde resin

RPFR → resol phenol formaldehyde resin

VER → vinyl ester resin

NG → natural graphite

CB → carbon black

CF → carbon fiber

The performance of the fuel cell could not be recorded above 50°C due to the limitation in the fabricated experimental setup. The performance of the fuel cell using developed bipolar plates with CF length optimized compositions of the CF(1mm)/CB/NG/polymer composites are shown in fig. 4.29. It can be seen from the figure that the RPFR based composite bipolar plate shows best performance among the three polymer based composite under study. This may be attributed due to the higher electrical conductivity and lower interfacial contact resistance.

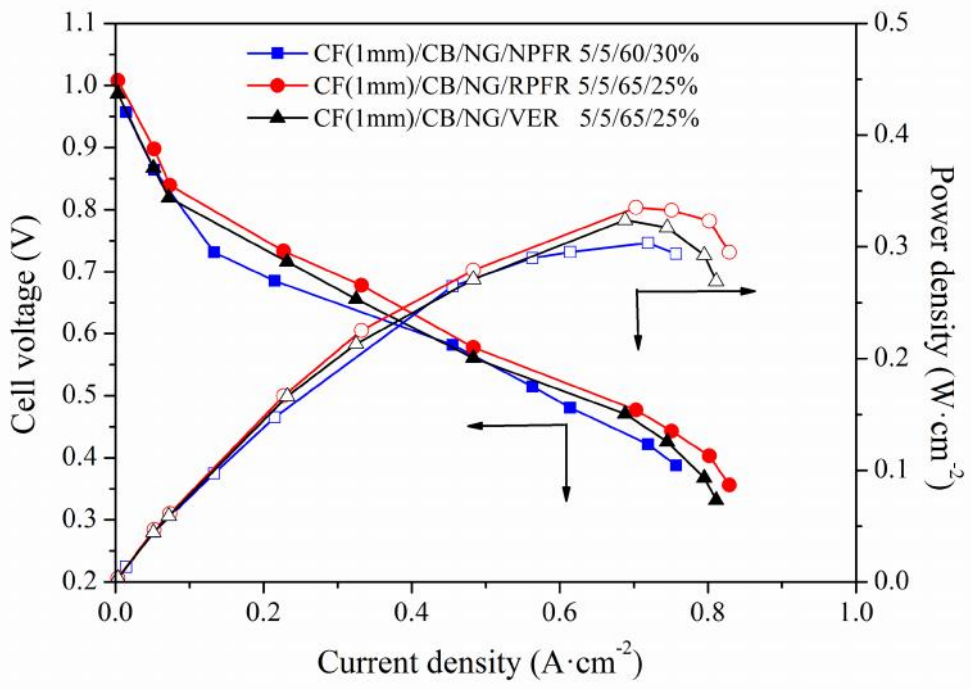

Figure 4.29: Performance of the PEMFC with optimized CF(1mm)/CB/NG/polymer composite bipolar plates at operating temperature of 50°C (filled symbols for current density and cell voltage; hollow symbols for current density and power density)

The maximum power densities of the single cell, with CF(1mm)/CB/NG/polymer composite bipolar plates, were around 303 (at 0.422 V), 335 (at 0.477 V), and 317 (at 0.426 V) $mW \cdot cm^{-2}$ for NPFR, RPFR, and VER based composites, respectively. The *I–V* performance analysis of the fuel cell was further studied with 1.5% GP reinforced optimized carbon-polymer composite bipolar plates to access the effect of GP. The unit cell PEMFC performance of GP reinforced composite bipolar plates are shown in fig. 4.30. It can be seen that reinforcement with 1.5% GP content to the CF(1mm)/CB/NG/polymer composite at the expense of NG improves the peak power output of the fuel cell.

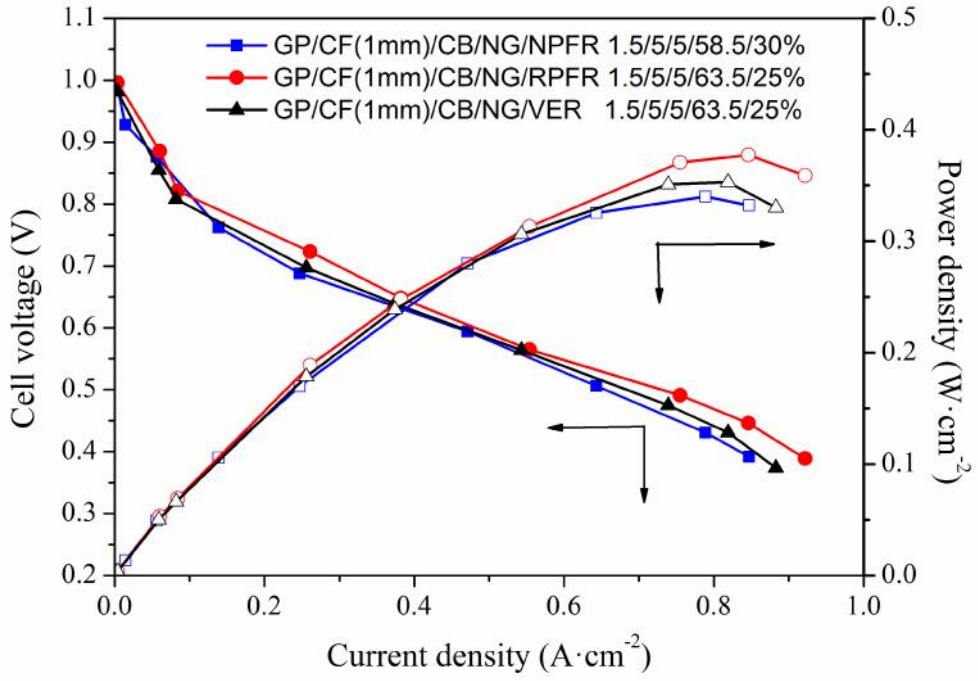

Figure 4.30: Performance of a single PEMFC with the optimized graphene (GP) reinforced GP/CF(1mm)/CB/NG/polymer composite bipolar plates at operating temperature of 50°C (filled symbol for current density and cell voltage; hollow symbol for current density and power density)

The maximum power densities of the single cell, with GP/CF(1mm)/CB/NG/polymer composite bipolar plates, were around 340 (at 0.431 V), 377 (at 0.446 V) and 353 (at 0.432 V) $mW \cdot cm^{-2}$ for NPFR, RPFR, and VER based composites, respectively. The peak power density of the fuel cell improved might be due to the significant increase in through-plane electrical conductivity and decrease in interfacial contact resistance. The figure shows that the maximum power density of the fuel cell was increased with the GP reinforced RPFR polymer composite (GP/CF(1mm)/CB/NG/RPFR 1.5/5/5/63.5/25%) bipolar plates. This improvement in the power densities can be attributed to the improvement in the in-plane as well through-plane electrical conductivities of the GP composites. Furthermore, the marginal improvement in the hydrogen permeability of the GP reinforced composite bipolar plates might have some positive synergetic effect on the performance of the PEMFC.

Table 4.9: Comparisons of PEMFC performances of optimized composite bipolar plate

Composite	Maximum power density of PEMFC along with corresponding current density and voltage			Increase in P_{max} with respect the composite without GP
	P_{max} ($mW \cdot cm^{-2}$)	j ($mA \cdot cm^{-2}$)	v (V)	
CF(1mm)/CB/NG/NPFR 5/5/60/30%	303	718	0.422	–
GP/CF(1mm)/CB/NG/NPFR 1.5/5/5/58.5/30%	340	788	0.431	12.22
CF(1mm)/CB/NG/RPFR 5/5/65/25%	335	702	0.477	–
GP/CF(1mm)/CB/NG/RPFR 1.5/5/5/63.5/25%	377	845	0.446	12.5
CF(1mm)/CB/NG/VER 5/5/65/25%	317	744	0.426	–
GP/CF(1mm)/CB/NG/VER 1.5/5/5/63.5/25%	353	817	0.432	11.5

P_{max}: maximum power density; j: current density; v: voltage

Table 4.9 shows comparative analysis of the different optimized composites along with the effect of GP (at the expense of NG) on the PEMFC performance. It can be seen that the power density was significantly increased for all the GP reinforced composite bipolar plate as compared to without GP composite bipolar plate.

Chapter 5

Graphene Reinforced Carbon-polymer Composite Bipolar Plate for HT-PEMFC

Chapter 5

Graphene Reinforced Carbon-polymer Composite Bipolar Plate for HT-PEMFC

In this chapter, the properties of the optimized graphene reinforced carbon-polymer composite bipolar plates are evaluated for possible application in high temperature PEMFC (HT-PEMFC).

5.1 Background

Proton exchange membrane fuel cells (PEMFCs) are recognized as a suitable alternative for distributed power generation due to advanced features such as high power density and low emission levels. Perfluorosulfonic acid (PFSA) based membranes such as nafion have been widely adopted in PEMFC development because they exhibit relatively high proton conductivity, mechanical strength, chemical stability, and longer durability. However, nafion membrane requires sufficient water content for effective proton conduction. Therefore, nafion based PEMFCs should operate at relatively low temperatures (at least below the boiling temperature of water). Therefore, the operating temperature for nafion membrane based PEMFC is normally within the range of 60–80°C. Several issues arise by the requirement of low temperature operation of the PEMFC are complicated water management, cooling loads, and importantly the CO issues (Larminie and Dicks 2003; Baschuk and Li 2001).

It may be noted that the major source of hydrogen as fuel is steam reforming of hydrocarbon (Larminie and Dicks 2003). The hydrogen produced by steam reforming generally contains trace amount (2500-5000 ppm) of carbon monoxide, which strongly

adsorbs onto the surface of Pt metal (Cross 1999). This high concentration of CO in the hydrogen renders the PEMFC inoperable due to the poisoning of the Pt catalyst at anode. It is also reported that the CO concentration for low temperature (around 80°C) PEMFC is needed to be less than 0.001% or 10 ppm, whereas the high temperature PEMFC (HT-PEMFC) can tolerate upto 30,000 ppm at 200°C (Zhang et al., 2006). The operative temperature of HT-PEMFC is defined as 120^{o}C for transportation and 150^{o}C for stationary application (US-DoE 2013). It is reported that the CO tolerance was increased from 10 ppm to 1000 ppm when the operating temperature of the PEMFC was enhanced from 80°C to 130°C (Li et al., 2003). Therefore, the researchers and scientists are attracted for HT-PEMFC research to increase the CO tolerance on Pt electrocatalyst (Song 2002; Zhang et al., 2006; Radhakrishnan et al., 2007; Barbir and Yazici 2008; Verma and Scott 2010; Atkinson et al., 2004; Li et al., 2003; Hansen et al., 2012). In addition, the use of non-noble metal catalyst, water management, and cooling systems can be simplified for HT-PEMFC as compared to PEMFC (Chandan et al., 2013).

In this regards, research is going on to develop PEMFC components, which can be used for HT-PEMFC application. The nafion membrane is most commonly used as a proton exchange membrane, which limits the operating temperature of PEMFC to 80°C. Therefore, research work is going on to synthesize suitable proton exchange membrane, which can be used in HT-PEMFC applications (Li et al., 2013; Yu and Benicewicz 2009). In this issues the phosphoric acid (PA) doped polybenzimidazole (PBI) membrane is commonly used as in HT-PEMFC applications owing to high operating temperature which is around 160^{o}C (Ergun et al., 2012; Qingfeng et al., 2001; Lin et al., 2013; Seo et al., 2013; Liao et al., 2013; Eguizábal et al., 2014; Ubeda et al., 2012). Moreover, owing to HT-PEMFC operation, the bipolar plate is also exposed to high temperature over a

long period of time. In view of this, it is required to evaluate the properties of the bipolar plate at high temperature for HT-PEMFC. Therefore, the most important properties such as mechanical strength, electrical conductivity, and corrosion resistance of carbon-polymer composite bipolar plate in HT-PEMFC operation is required to be satisfied as per stringent target (table 2.1).

Recently, Harting and Schmidt studied the effect of bipolar plate degradation on the performance of a HT-PEMFC. The study was conducted at 180^{o}C, which was at higher side of the recommended temperature so as to have accelerated degradation effects (Hartnig and Schmidt 2011). They have studied the effect of degradation of three type of bipolar plates (graphite composite; surface treated graphite; and gold coated stainless steel) on the PEMFC performance. It was found that the graphite composite degradation was comparatively high as compared to the other two plates. However, neither the composition of the graphite composite was reported nor the characterization of the composite was performed. Moreover, there is hardly any study available on the evaluation of composite bipolar plate for HT-PEMFC. Table 2.4 shows the recent and past literature data on the properties of carbon-polymer composite bipolar plates for PEMFC. However, these bipolar plates were not evaluated for the HT-PEMFC. Therefore, this chapter reports the preliminary evaluation of the bipolar plate for the possible application in HT-PEMFC. The optimized bipolar plate (GP/CF(1mm)/CB/NG/RPFR 1.5/5/5/63.5/25%) for the PEMFC was used further evaluation. The bipolar plate was mainly evaluated for mechanical, electrical, corrosion, and thermal tests.

5.2 Experimental

5.2.1 Materials and methods

The carbon-polymer composite bipolar plate was prepared using (GP/CF(1mm)/CB/NG/RPFR) of NG, CB, CF, and GP as the conductive fillers and RPFR as the polymer matrix. The details of the above materials and development of composite bipolar plate are already discussed in the chapter 4 (section 4.2.1).

5.2.2 Characterization of developed bipolar plate for HT-PEMFC

The bipolar plate under study was heat treated in a muffle furnace upto 200^{o}C temperature for 24 h. The heat treated bipolar plate was then tested for flexural strength, deflection at mid-span, shore hardness, in-plane electrical conductivity, and through-plane electrical conductivity analysis as explained in chapter 4 (section 4.2.3). It may be noted that different bipolar plate sample of the same composition was used for treatment at different temperature. Moreover, the characterization for thermal stability and corrosion current density in PA solution is described in subsequent section.

5.2.2.1 Thermal stability

The thermal stability of the developed composite (GP/CF(1mm)/CB/NG/RPFR 1.5/5/5/63.5/25%) bipolar plate was studied using thermo-gravimetric analyzer (TGA) as described in chapter 3 (section 3.2.3.5). Moreover, the thermal stability of the raw RPFR as well as cured RPFR (CRPFR) was analyzed. The RPFR was cured at its curing temperature for 1 h to get CRPFR and then analysed for thermal stability using TGA analyzer. The TGA analysis was conducted using 10 mg of sample in a 70 µL alumina crucible and heated in the range of 25–600°C at a heating rate of 10°C·min^{-1}. The thermal

stability of the composite was evaluated under air atmosphere too. The TGA analysis is discussed under nitrogen atmosphere unless otherwise stated.

5.2.2.2 Corrosion current density

It is well known that the phosphoric acid doped polybenzimidazole membrane is commonly used as in HT-PEMFC (Verma and Scott 2010). This PA doped PBI membrane can easily sustain upto 150^{o}C, which is required as per the DoE target for HT-PEMFC (table 2.1). Therefore, the corrosion resistance of the developed composite bipolar plate was measured using linear sweep voltammetry (LSV) in a simulated HT-PEMFC environment. The simulated HT-PEMFC environment was created using 85% phosphoric acid (PA) solution as an electrolyte at elevated temperature for the evaluation of corrosion current density of the developed composite bipolar plate. The details of corrosion current density measurement experimental set up is explained in chapter 4 (section 4.2.3.8). It may be noted that the corrosion current density measurements were conducted upto the temperature of 140^{o}C due to the obvious experimental constraint. The potential was swiped at a scan rate of 1 mV$\cdot$s^{-1}.

5.3 Results and discussion

5.3.1 Effect of temperature on flexural strength and deflection at mid-span

Figure 5.1(a,b) shows the effect of temperature on the flexural strength and deflection at mid-span of the composite (GP/CF(1mm)/CB/NG/RPFR 1.5/5/5/63.5/25%) bipolar plate. It can be seen that the composite maintains high flexural strength upto 175°C with the increase in temperature from 100^{o}C to 175^{o}C. However, as the temperature increases beyond 175^{o}C, the composite fails to maintain the high flexural strength.

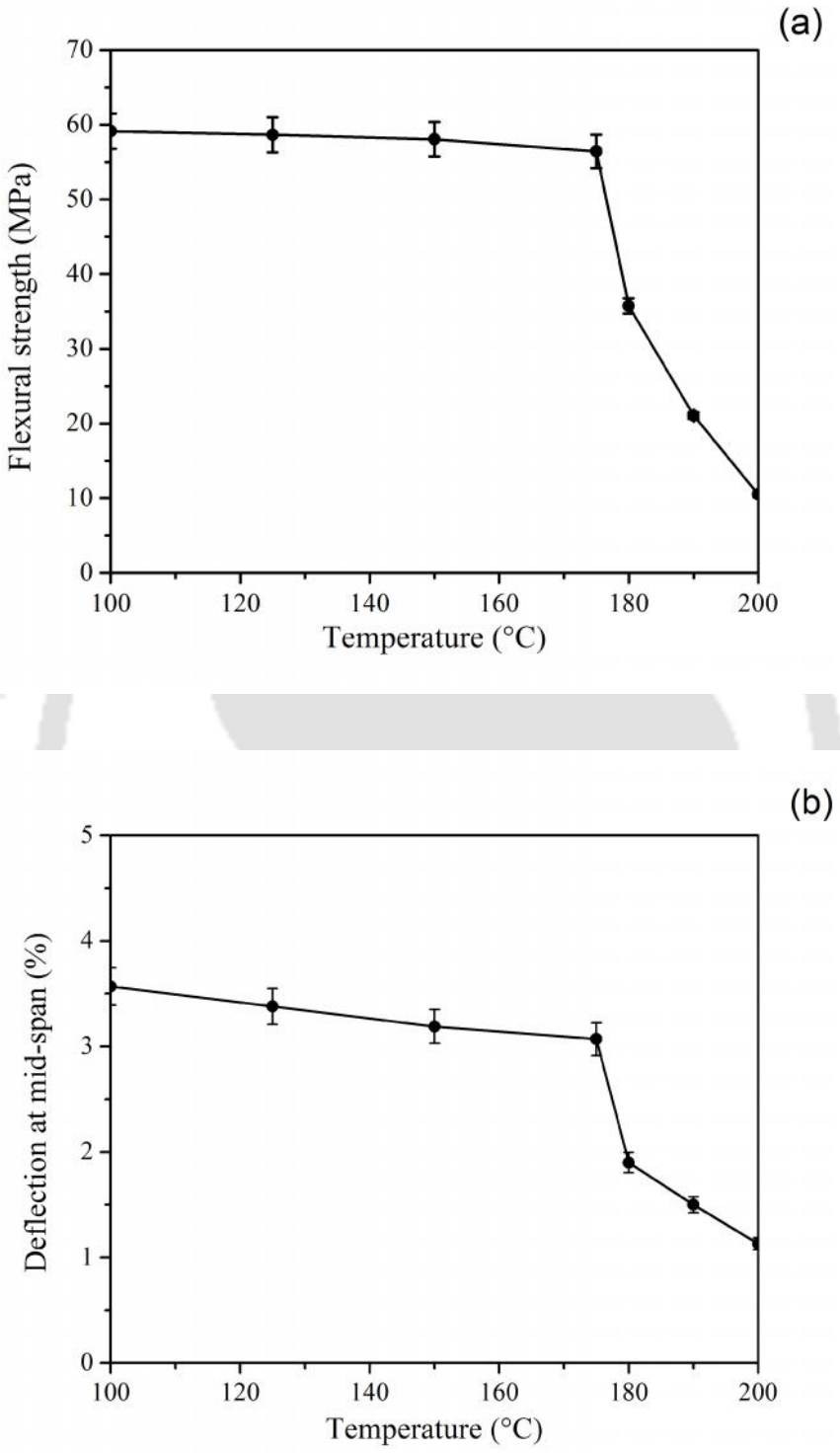

Figure 5.1: Effect of temperature on (a) flexural strength, and (b) deflection at mid-span of the composite (GP/CF(1mm)/CB/NG/RPFR 1.5/5/5/63.5/25%) bipolar plate

The deflection at mid-span also followed the similar trend (fig. 5.1(b)). It can be attributed to the failure of chemical attachment between the reinforcements and resin matrix due to the decomposition of polymer crosslinking at high temperature. The mechanical properties of the carbon-polymer composite bipolar plate need to be high so as to support thin membrane and electrode, and withstand the clamping forces for the HT-PEMFC stack assembly. The maximum flexural strength and deflection at mid-span was found to be 56.42 MPa and 3.07%, respectively, at 175^{o}C (Ghosh and Verma 2014).

5.3.2 Effect of temperature on shore hardness

Figure 5.2 shows the shore hardness of the composite bipolar plate (GP/CF(1mm)/CB/NG/RPFR 1.5/5/5/63.5/25%). Similar behavior was observed for the shore hardness with the increase in temperature as compared to flexural strength and deflection at mid-span. It can be seen that the shore hardness of the composite was hardly changed (considering the error involved in the process) with the increase in the temperature upto 175°C. However, the shore hardness sharply decreased with further increase in the temperature beyond 175°C. The decrease in shore hardness may be attributed to the thermal decomposition of cross-linkages between reinforcement and resin matrix at higher temperature, which results in failure to resist the dislocation of indentation load (Ghosh and Verma 2014). It may be noted that the shore hardness of the composite upto 175°C was well above the target values given in table 2.1.

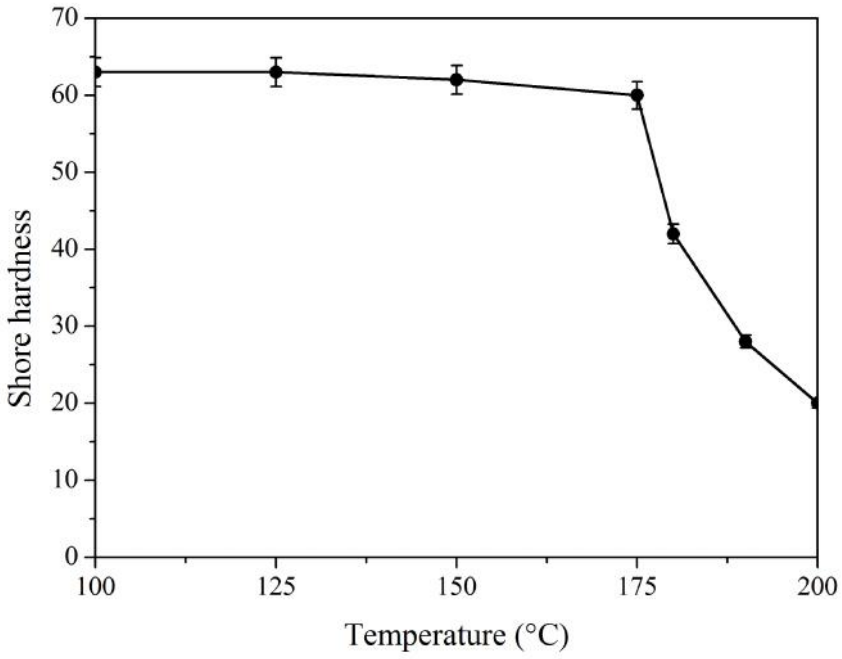

Figure 5.2: Effect of temperature on shore hardness of the composite bipolar plate (GP/CF(1mm)/CB/NG/RPFR 1.5/5/5/63.5/25%)

5.3.3 Effect of temperature on electrical conductivity

Figure 5.3 shows the effect of temperature on the in-plane and through-plane electrical conductivities of the composite bipolar plate (GP/CF(1mm)/CB/NG/RPFR 1.5/5/5/63.5/25%). It can be seen that the electrical conductivities of the composite bipolar plate upto 175°C are slightly affected with the increase in temperature. The in-plane and through-plane electrical conductivities of the composite at 175°C were around 409.25 and 98 $S \cdot cm^{-1}$, respectively. However, the conductivities decrease sharply with the increase in temperature of the composite bipolar plate beyond 175°C. It may be due to degradation of the polymer network causing isolation of the conducting path within the composite at high temperature.

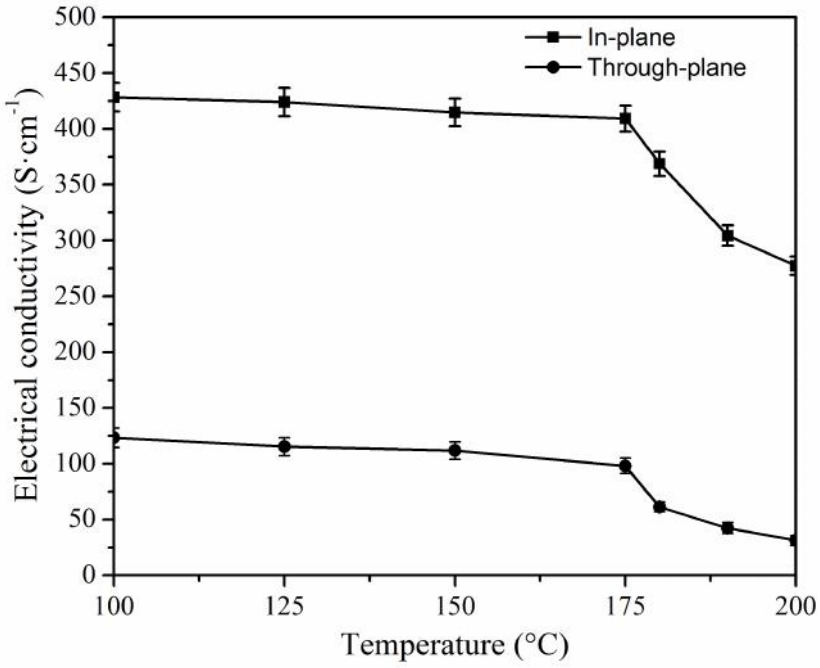

Figure 5.3: Effect of temperature on electrical conductivity of the composite bipolar plate (GP/CF(1mm)/CB/NG/RPFR 1.5/5/5/63.5/25%)

5.3.4 Effect of temperature on corrosion current density

Figure 5.4 shows the Tafel plots for the composite bipolar plate (GP/CF(1mm)/CB/NG/RPFR 1.5/5/5/63.5/25%) at different temperature. The corrosion current densities (i_{corr}) were found to be 0.501, 0.676, and 0.758 $\mu A \cdot cm^{-2}$ at temperature of 120, 130, and 140°C, respectively (Ghosh and Verma 2014). It showed that the developed bipolar plate was highly resistive to the phosphoric acid under redox environment and high temperature. It may be noted the i_{corr} was within the DoE target value (<1 $\mu A \cdot cm^{-2}$) though it was given for only PEMFC (Ghosh and Verma 2014).

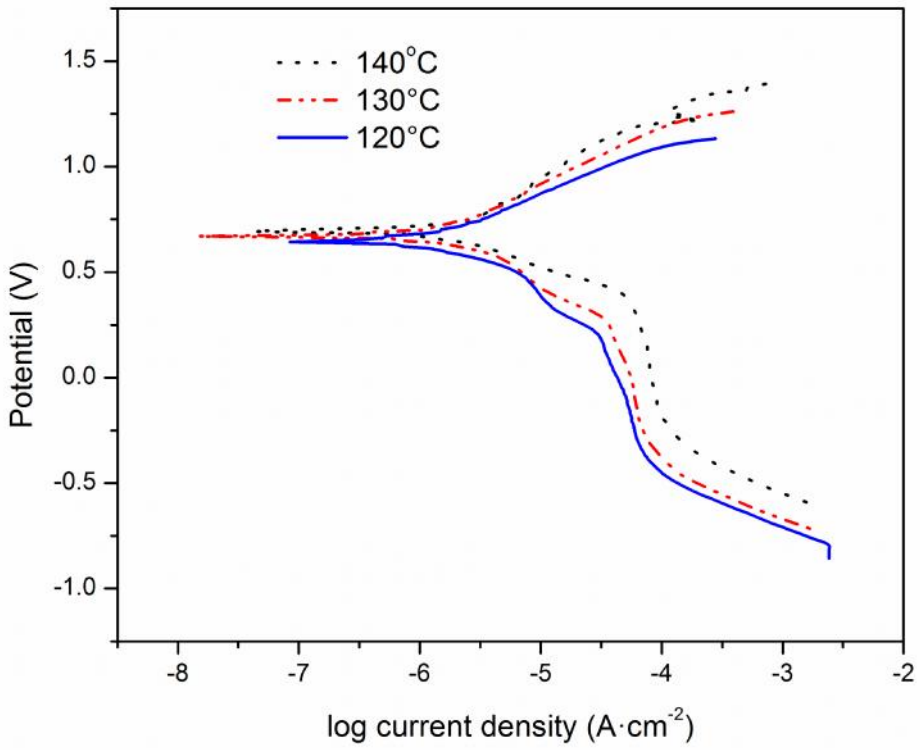

Figure 5.4: Tafel plots for measuring i_{corr} of the composite bipolar plate (GP/CF(1mm)/CB/NG/RPFR 1.5/5/5/63.5/25%) at different temperatures

5.3.5 Thermogravimetric analysis

In order to ascertain the rationale behind the properties shown by the composite bipolar plate, TGA of uncured liquid RPFR, cured RPFR (CRPFR), and the composite is shown in the fig. 5.5. The uncured liquid RPFR shows the distinct weight loss owing to the volatilization of the solvents in the temperature range of 80–210°C. During the above process, the curing of the RPFR occurs simultaneously in the region 120–210°C. The weight loss in the temperature range of 345–600°C is associated to the degrading (Knop and Pilato 1985; Lee et al., 2012) of the polymer. The weight loss associated to the

degradation of the polymer is due to the evolution of the products, which contains mixture of cresols and phenols, hydrogen, methane, carbon monoxide, water, and small amounts of carbon dioxide and ethane (Hermann et al., 2005).

The TGA curve of CRPFR is also included in the fig. 5.5. The initial weight loss as compared to the RPFR is obviously not observed. Moreover, weight loss was observed in the initial stage (upto around 210°C) due to the evaporation of any unbound and bound solvent and water, which was formed during condensation reaction of methylol groups (Knop and Pilato 1985; Lee et al., 2012). Further in the temperature range of 210-350°C, slight weight loss in CRPFR was observed.

Finally, the weight loss at higher temperature was observed due to the loss of carbon monoxide and methane formed by degradation of methylene-bridge, which can be seen in the CRPFR thermogram within the temperature range of 350-600°C.

The TGA plot of the composite shows that the onset temperature for the weight loss of the composite was increased in comparison to the raw RPFR and the residual weights of the composite bipolar plates at 300°C was around 98.06%.

On the other hand, the composite under air atmosphere shows that the degradation starts relatively early (at around 270^{o}C) as compared to nitrogen atmosphere. Therefore, the developed bipolar plates seems to be stable upto 270^{o}C temperature However, on correlating the thermal conductivity and mechanical strength results of the composite bipolar plate, it was observed that around 2% weight losses along with the cleavage of the crosslinking have a strong impact on the properties of the composite bipolar plate. Moreover, the similar kind of thermal stability was observed for the carbon-polymer composite bipolar plate by many researchers and scientists (Oliveira et al., 2013; Kim et

al., 2010; Kakati and Verma 2011). They also found good thermal stability upto 300°C that would be sufficient for application in HT-PEMFC. However, it was found that though the composite bipolar plate showed a good performance in TGA (in term of weight loss) but the performance of the bipolar plate showed the optimum performance upto 175°C. It was also experienced that the temperature beyond 175°C, the cracks were observed clearly on the composite bipolar plate. It may be due to the escape of the water or any solvent as well as entrapped air in the composite.

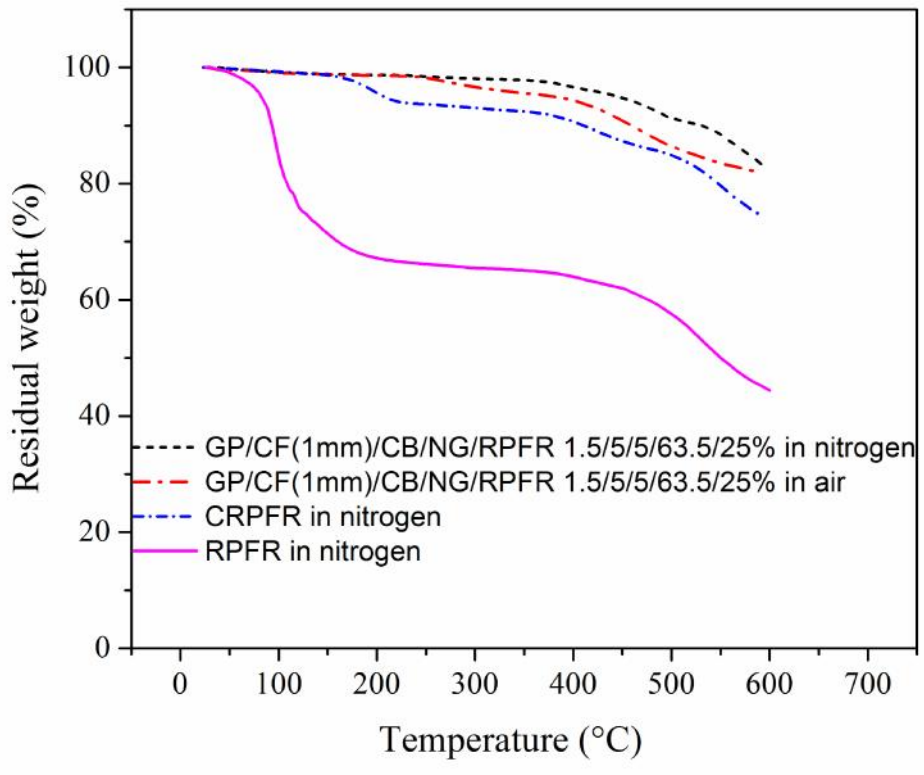

Figure 5.5: TGA of RPFR, CRPFR, and composite bipolar plate (GP/CF(1mm)/CB/NG/RPFR 1.5/5/5/63.5/25%)

Table 5.1 shows the comparison of the composite bipolar plate (GP/CF(1mm)/CB/NG/RPFR 1.5/5/5/63.5/25%) developed for HT-PEMFC in this study (IITG) with the commercial bipolar plate for PEMFC (Tjong 2011). The mechanical, electrical, and corrosion properties shown by the developed composite bipolar plate are comparatively better than the other composite bipolar plate.

Table 5.1: Comparison of composite bipolar plate properties with the commercial bipolar plates

Organization	**Mechanical properties**		**Electrical conductivity ($S \cdot cm^{-1}$)**		**Corrosion current density ($\mu A \cdot cm^2$)**
	Flexural strength (MPa)	**Shore hardness**	**In-plane**	**Through-plane**	
GE	42.7	-na-	109	-na-	-na-
Plug Power Inc.	40	-na-	55	20	-na-
DuPont	53.1	-na-	-na	25-33	-na-
IITG[a]	56.42	60	409.23	98	0.758[p]

[a]The properties of bipolar plate is reported at 175°C for HT-PEMFC application; na: not available; [p]phosphoric acid environment

Chapter 6

Graphene and Functionalized Graphene Supported Electrocatalyst

Chapter 6

Graphene and Functionalized Graphene Supported Electrocatalyst

This chapter discuss the synthesis and characterization of functionalized graphene (FGP) from as-synthesized graphene (GP), followed by the synthesis, characterization, and evaluation of GP and FGP supported Pt electrocatalyst for PEMFC applications. It is found that the Pt on FGP outperformed the Pt on GP. Therefore, in an attempt to reduce the Pt loading on the FGP, half of the Pt metal was replaced by the Au metal. The performance of this bimetallic electrocatalyst is evaluated and compared with other developed catalysts. It is also discussed that how the support material influence the electrochemical activity and stability of PEMFC anode as well as cathode electrocatalysts. Finally, the electrocatalysts supported on GP and FGP are tested in PEMFC.

6.1 Background

A multitude of new and improved electrocatalyst support materials for PEMFC electrocatalyst were investigated over the last decade. The requirements of these electrocatalyst supports are low cost, high electrochemical activity, and long term electrochemical stability. The unique physicochemical properties of GP suggests that it has great potential for providing new approaches and critical improvements in the many field of science and technologies including, fuel cell, and electrochemistry. For example, from the chapter 4 it was found that high electrically conductive graphene sheets enhanced the properties of bipolar plate significantly even at 1.5% loading. In this

chapter, GP is evaluated as an electrocatalyst support materials as mentioned in the chapter 2. Moreover, thermochemically synthesized graphene does not have very good interaction with the metal electrocatalyst when it is used to develop as an electrocatalyst support (Antolini 2012). Therefore, it is reported that the functionalized graphene may have better interaction than as-synthesized graphene (Kuila et al., 2012). Furthermore, it is well-known that graphene sheets, which have high specific surface area, unless well separated from each other, tend to form irreversible agglomerates or even restack to form graphite through strong π-π staking (Shan et al., 2009). Therefore, functionalization of graphene (FGP) was done to prevent restacking of graphene layer and used to develop electrocatalyst support. It is reported that the functionalization also improves the dispersion of metal nanoparticles on the support (Antolini 2012). The detailed methodology of the synthesis and characterization of functionalized graphene is described in the subsequent sections.

6.2 Experimental

6.2.1 Materials

H_2PtCl_6 (38–40wt.%) and aqueous solution of $HAuCl_4$ (1 mM) were purchased from Spectrochem and Merck, India, respectively, as electrocatalyst precursors. NaOH, $NaBH_4$, and citric acid (CA) were procured from Merck, India. Nafion solution 5wt.% was procured from DuPont, USA. The in-house synthesized GP was used for the development of FGP. The details synthesis of FGP is described in the next section.

6.2.2 Methods

6.2.2.1 Synthesis of functionalized graphene

The functionalization of as-synthesized GP was carried out by chemical treatment using citric acid as shown in fig. 6.1(a). Initially, as-synthesized GP nanosheets were dispersed in aqueous solution of citric acid followed by ultrasonic treatment to obtain a stable dispersion of GP nanosheets. The dispersion was then kept under vigorous stirring for 2 h using magnetic stirrer. The solvent was removed by filtering and the resultant mixture was washed, filtered, and subsequently heat treated at 300°C for 30 min to obtain functionalized graphene (FGP) sheets. This treatment improves the wetting characteristics by increasing oxygen containing functional groups including –COOH, –CO, and –OH on the GP surface (Poh et al., 2008). These functional groups act as an anchor for metal deposition (Poh et al., 2008). For comparison both GP and FGP of were used as an electrocatalyst support material for PEMFC. The subsequent section will discuss the use of GP and FGP as an electrocatalyst support in PEMFC.

6.2.2.2 Synthesis of graphene and functionalized graphene supported electrocatalyst

The synthesis of GP and FGP supported metal (Pt and/or Au) electrocatalyst can be categorized into two methods such as physical and chemical method (Saha et al., 2013). The physical methods are atomization of Pt in vacuum by thermal evaporation or sputtering on the support, whereas the chemical methods are used to form neutral Pt atom on the support by reducing Pt ions (Ghosh et al., 2013). The chemical methods have the significant advantages over physical method due to ease in controlling the size, shape, and composition as compared to physical methods (Subhramannia and Pillai 2008; Saha et al., 2013). Therefore, in this study, the electrocatalysts were prepared by chemical method using $NaBH_4$ reduction (Ghosh et al., 2013).

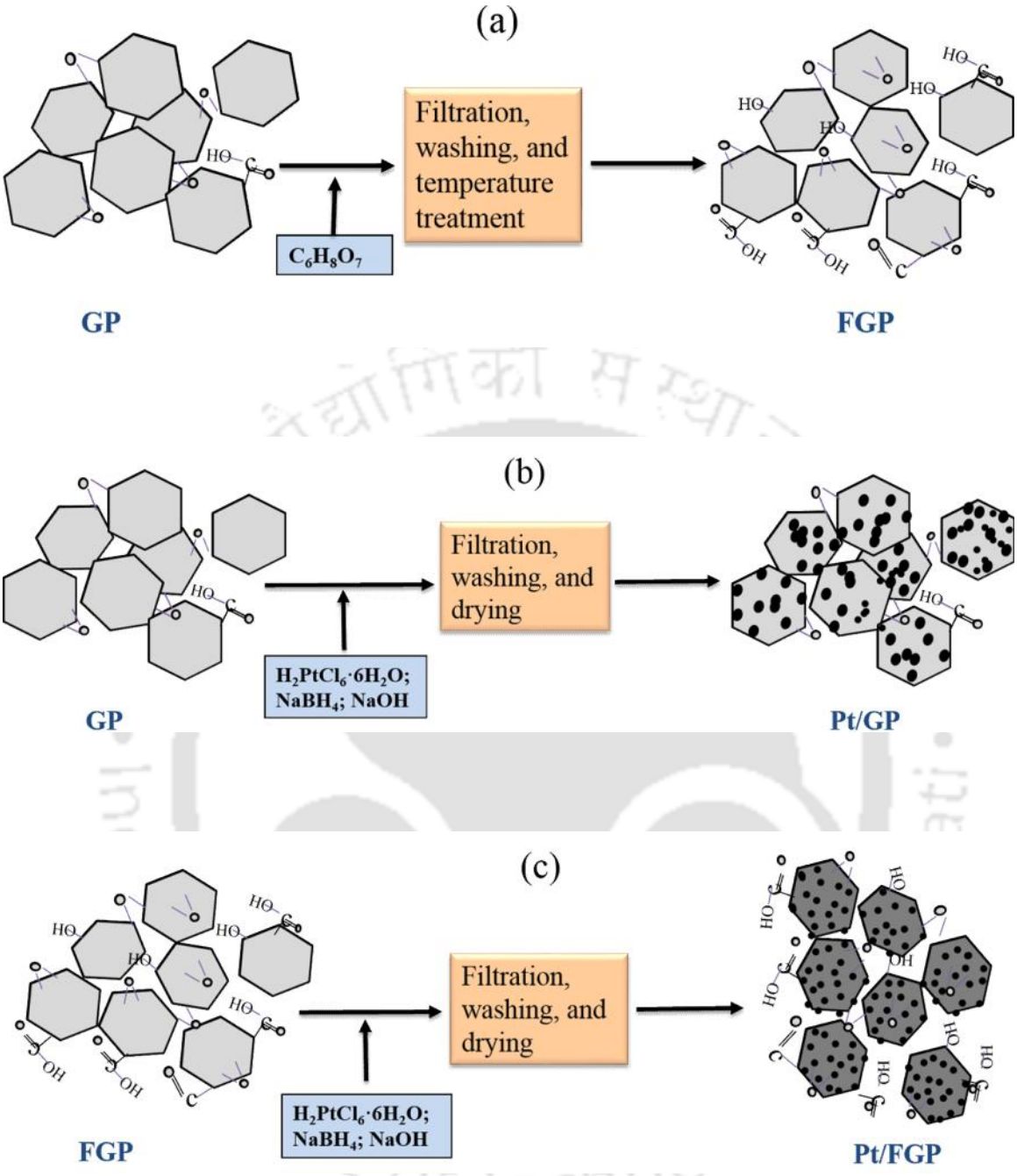

Figure 6.1: Schematic of synthesis of (a) FGP from GP, (b) Pt/GP from GP, and (c) Pt/FGP from FGP

The GP supported Pt electrocatalyst with 20wt.% was prepared *via* $NaBH_4$ reduction method (fig 6.1(b)) using GP, 40wt.% hexachloroplatinic acid ($H_2PtCl_6 \cdot 6H_2O$), and H_2O.

Initially, the as-synthesized GP was dispersed in ultra-pure millipore water by ultasonication for 1 h to make GP suspension slurry. The metal precursor ($H_2PtCl_6 \cdot 6H_2O$) was separately dissolve in water using ultrasonication. Then the obtained solution was drop-wise added to the GP slurry under continuous sonication. The pH of the mixture was adjusted at around 12 using 1 M NaOH solution. The reducing agent (0.8 M $NaBH_4$) was added into the above mixture under continuous stirring and slow heating upto 90°C under continuous stirring for 4 h. The resulting mixture was treated with N_2 for 30 min. Then the treated solution was filtered, washed copiously with water followed by ethanol, and dried in vacuum oven at 80°C to get Pt/GP electrocatalyst. The similar procedure was followed to synthesize Pt/FGP electrocatalyst as shown in fig. 6.1(c). The FGP supported Au and bimetallic (PtAu) electrocatalyst was prepared using aqueous $HAuCl_4$ as metal precursor source by following similar $NaBH_4$ reduction techniques as discussed earlier. The 20wt.% metal (Pt and/or Au) loading was kept for all the electrocatalysts. In case of PtAu electrocatalyst, the metal loading was selected 1:1 (Pt:Au) ratios.

6.2.3 Characterization

6.2.3.1 Characterization of functionalized graphene

The developed FGP was thoroughly characterized by FTIR, TGA, XRD, FE-SEM, TEM, and BET surface area analysis using similar experimental procedure as used for the characterization of GP and discussed in chapter 3.

6.2.3.2 Characterization of graphene and functionalized graphene supported electrocatalyst

Various physico-chemical characterization techniques were used to characterize the developed GP and FGP supported metal (Pt and/or Au) electrocatalyst. The surface morphologies (FE-SEM and TEM) and crystalline structure (XRD) analysis of developed

electrocatalysts were evaluated as per the procedure explained in chapter 3. *Ex-situ* electrochemical performance of the developed electrocatalysts were evaluated using rotating disc electrode (RDE) for oxygen reduction reaction (ORR) and cyclic voltammetry (CV) for hydrogen adsorption/desorption (HAD) using three electrode assembly as discussed earlier.

6.2.3.2.1 Oxygen reduction reaction analysis using linear sweep voltammetry

The oxygen reduction reaction (ORR) was carried-out using rotating disc electrode (RDE). The linear sweep voltammetry (LSV) was conducted using three electrodes RDE cell assembly connected to a potentiostat-galvanostat (Ghosh et al., 2013). The Ag/AgCl and Pt were used as reference and counter electrodes, respectively. The glassy carbon disc electrode (3 mm diameter) was used as working electrode substrate, which was pretreated prior to use. The pretreatment was done by polishing the electrode surface using 0.05 µm alumina paste and then thorough rinsing with ethanol and ultrapure water under sonication. The electrocatalyst slurry was prepared by mixing around 5 mg of Pt/C or Pt/GP or Pt/FGP or Au/FGP or PtAu/FGP powder with 5wt.% nafion-isopropyl alcohol (1:4) solution using sonication for 30 min. The electrocatalyst slurry was then drop cast on the surface of the pretreated glassy carbon electrode and dried to obtain the working electrode. An aqueous solution of 0.5 M H_2SO_4, saturated with O_2, was used as electrolyte. The LSV analysis was conducted using RDE at a scan rate of 10 $mV \cdot s^{-1}$ whereas the rotation speed of the disc electrode was kept at constant 1600 rpm.

6.2.3.2.2 Hydrogen adsorption/desorption analyses using cyclic voltammetry

The electrochemical hydrogen adsorption/desorption (HAD) activity of the developed electrocatalysts were conducted by CV technique at room temperature. The conventional three electrode cell assembly, as discussed in chapter 4 (fig. 4.7), was used for the HAD

evaluation. The Ag/AgCl and Pt electrodes were used as reference and counter electrodes, respectively. The working electrode was prepared by the developed electrocatalyst with metal (Pt and/or Au) loading of 0.6 $mg \cdot cm^{-2}$. To prepare working electrode, the Toray carbon paper (TGP-H-90) was coated with catalyst ink (Ghosh et al., 2012). The catalyst ink was prepared by mixing of required amount of catalyst, 5wt.% nafion solution, and isopropyl alcohol under continuous sonication for 15 min. Then the dispersed catalyst ink was sprayed on the toray carbon paper. Subsequently, the catalyst coated carbon paper was dried in hot air oven for overnight. An aqueous solution of 0.5 M H_2SO_4, saturated with N_2, was used as an electrolyte for CV analysis at a scan rate of 50 $mV \cdot s^{-1}$. Electrochemical surface area (ESA), one of the most important parameters for evaluating the activity of electrocatalysts, was measured from the CV plots using HAD on the Pt/GP electrocatalyst. Figure 6.2 shows a representative cyclic voltammogram of HAD using Pt electrocatalyst. The forward and reverse peaks in the voltammogram show the hydrogen desorption and adsorption peaks on the Pt catalyst surfaces (Ghosh et al., 2013). The ESA can be determined using eq. (6.1), where 210 $\mu C \cdot cm^{-2}$ Pt is a constant for the hydrogen adsorption charge (q_{Pt}) by polycrystalline Pt surface (eq. 6.2) (Sogaard et al., 2001). The schematic representation of hydrogen adsorption/desorption regions are shown in fig. 6.2. The charge associated with the hydrogen adsorption on Pt, which can be found out by integrating the hydrogen adsorption peak in the potential range of 0.05-0.4 V (SHE) for evaluating the electrochemical surface area (Chaparro et al., 2009; Ghosh et al., 2013).

The specific double layer capacitance was reported to be 40 $\mu F \cdot cm^{-2}$ and 8 $\mu F \cdot cm^{-2}$ for Pt and carbon black, respectively (Kangasniemi et al., 2004; Parthasarathy et al., 1992). However, since the capacitance is a function of potential, the double layer does not behave as an ideal capacitor.

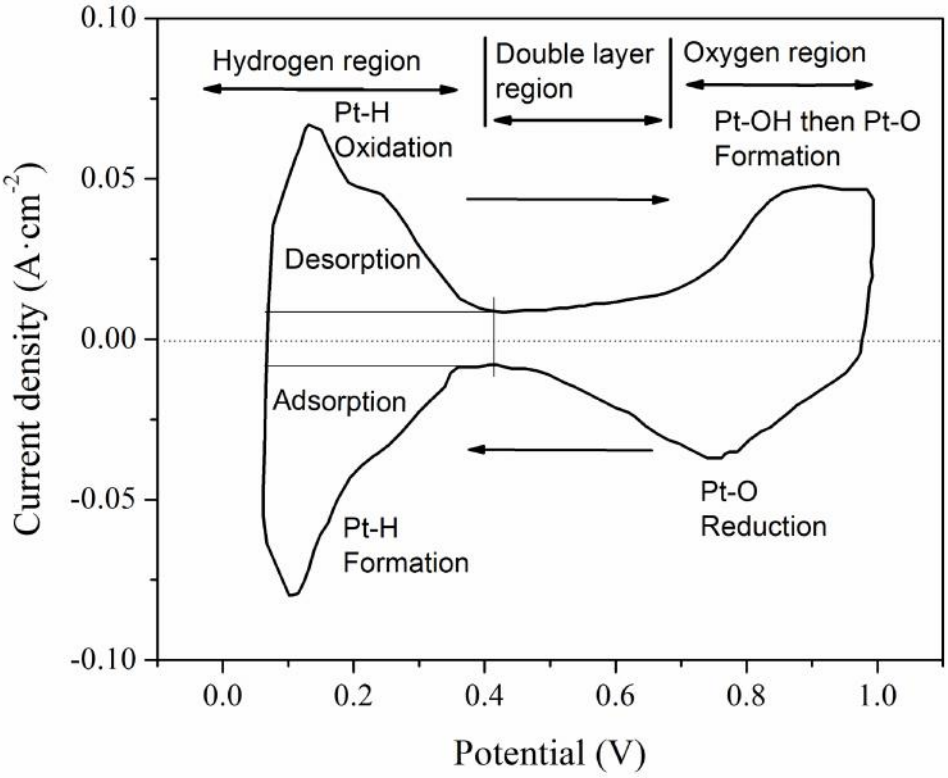

Figure 6.2: Representative cyclic voltammogram of PEMFC catalyst showing HAD

$$\mathrm{ESA}\,(\mathrm{m^2.g^{-1}Pt}) = \frac{q_{Pt}\,(\mu.\mathrm{cm^{-2}Pt})}{210\,(\mu.\mathrm{cm^{-2}Pt}) \times \mathrm{Pt\ loading}\,(\mathrm{g\,Pt.m^{-2}})} \qquad (6.1)$$

$$\mathrm{Pt} + \mathrm{H^+} + \mathrm{e^-} \rightarrow \mathrm{Pt\text{-}H} \qquad (6.2)$$

Moreover, the non-faradic or capacitive current generated due to charging/discharging the electrical double layer capacitance of electrode/electrolyte interface. Non-faradic current involves charge accumulation but not chemical reactions or charge transfer. The electrical charge associated with double layer charging must be considered for the analysis to avoid overestimating the charge attributed to the electrocatalytic activity (Cooper 2009). The potential in this report is reported with respect to standard hydrogen electrode (SHE) unless otherwise stated.

6.2.3.2.3 Electrochemical stability analysis

The electrochemical stability of the developed electocatalysts were measured using CV plots for HAD under simulated accelerated condition. These accelerated tests shows long-term degradation behavior of fuel cell electrocatalysts. All stability test experiments were conducted in nitrogen saturated 0.5 M H_2SO_4 at a scan rate of 50 $mV \cdot s^{-1}$ at room temperature. The CV potential scan for each electrocatalyst is reported for 1^{st}, 500^{th}, and 1000^{th} cycle.

6.3 Fuel cell performance evaluation using synthesized electrocatalyst

The performance of the developed electocatalysts were evaluated in a PEMFC. The preparation of MEA was conducted as explained in the chapter 4 (section 4.3.1). The electrodes were prepared by the carbon paper coated with the electrocatalysts. The noble metal catalyst loadings on the anode and cathode were kept as 0.4 $mg \cdot cm^{-2}$ and 0.6 $mg \cdot cm^{-2}$, respectively. It may be noted that a commercial PEMFC hardware controlled by a test station (fig. 6.3) was used to calculate the performance of the electrocatalyst. Therefore, the prepared MEA was installed in a 5 cm^2 PEMFC hardware having commercial graphite plate controlled by fuel cell test station (Fuel Cell Technologies, Inc., USA). The fuel cell was operated at 80°C. The H_2 and O_2 flow rates were 75 and 150 sccm, respectively, at 100% relative humidity. Figure 6.3 shows the snapshot of the fuel cell test station experimental setup.

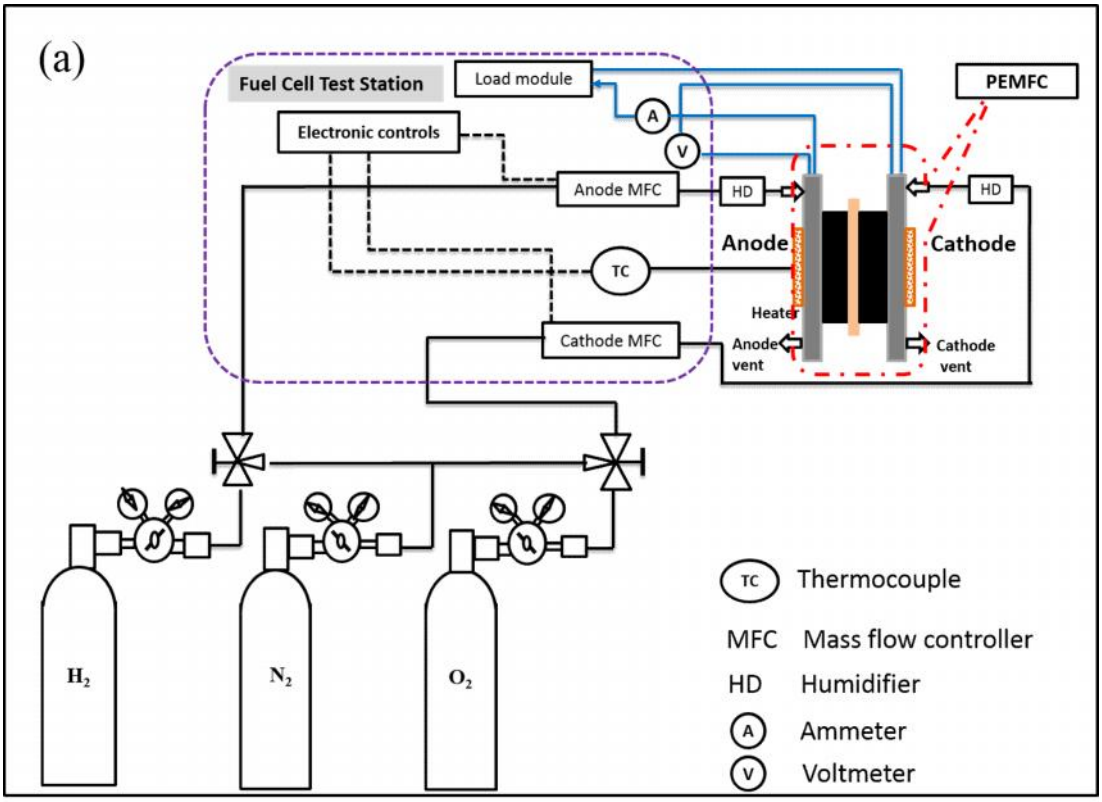

Figure 6.3: (a) Schematic of PEMFC testing station, and (b) snapshot of the PEMFC test station

6.4 Results and discussion

6.4.1 Functionalized graphene

6.4.1.1 FTIR analysis of the functionalized graphene

The fig. 6.4 shows the FTIR spectra of FGP and it is compared with GP. The peaks observed for GP are also present in the FTIR spectra of the FGP (fig. 6.4) along with two additional peaks at 1644 and 1378 cm^{-1}.

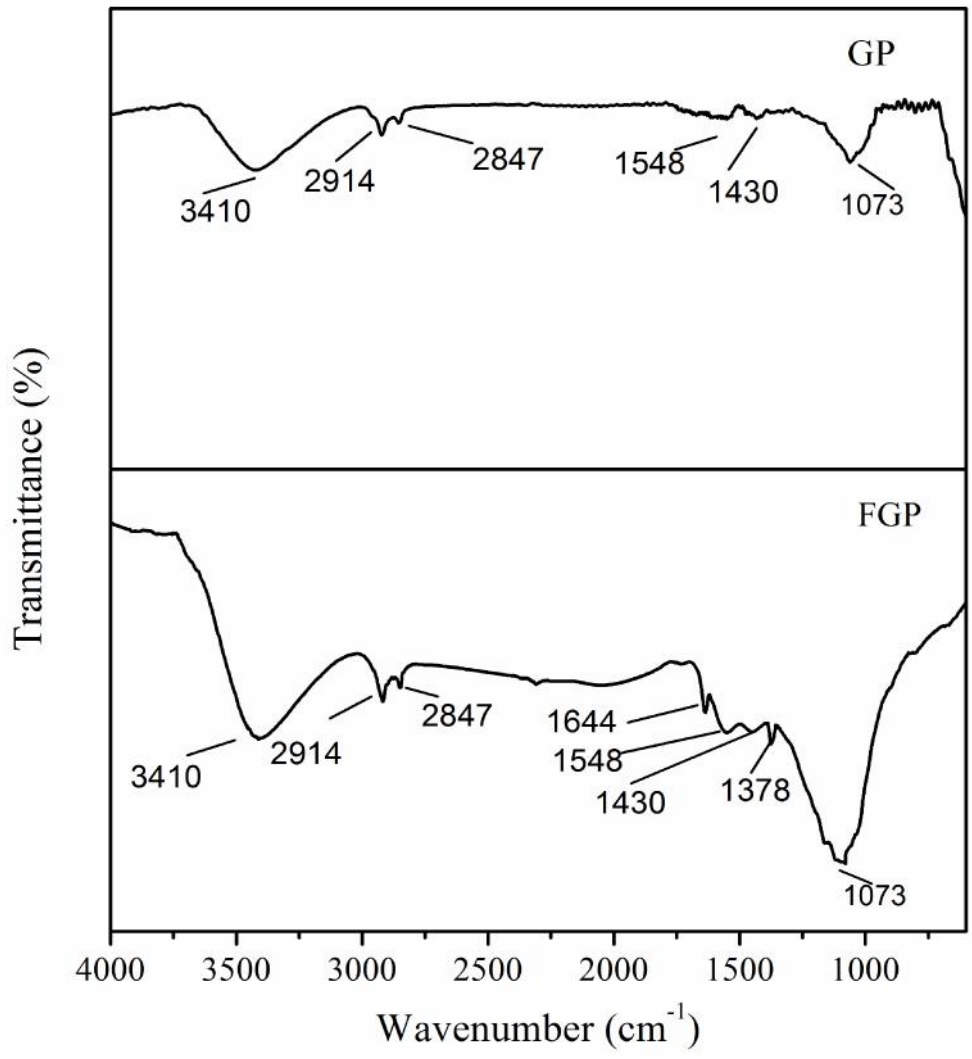

Figure 6.4: FTIR spectra of the GP, and FGP

Besides, the intensities of the FGP peaks at 3410 cm^{-1}, 2914 cm^{-1}, 2847 cm^{-1}, and 1730 cm^{-1} are increased as compared to GP spectra due to the increased strength of functional groups. The additional sharp peak at 1644 cm^{-1} is due to the C=O stretching of carbonyl (COOH) groups and peak at 1378 cm^{-1} is due to the stretching of carboxyl group (Ghosh et al., 2013).

6.4.1.2 Thermogravimetric analysis of the functionalized graphene

TGA is a useful tool to characterize the amount of functional groups grafted to FGP, because the organic substances covalently attached to the surface of GP start to thermally decompose at the temperature around 250°C (Teng et al., 2011). It can be seen in the fig. 6.5 that the FGP starts to lose more weight upon heating below 100°C as compared to GP.

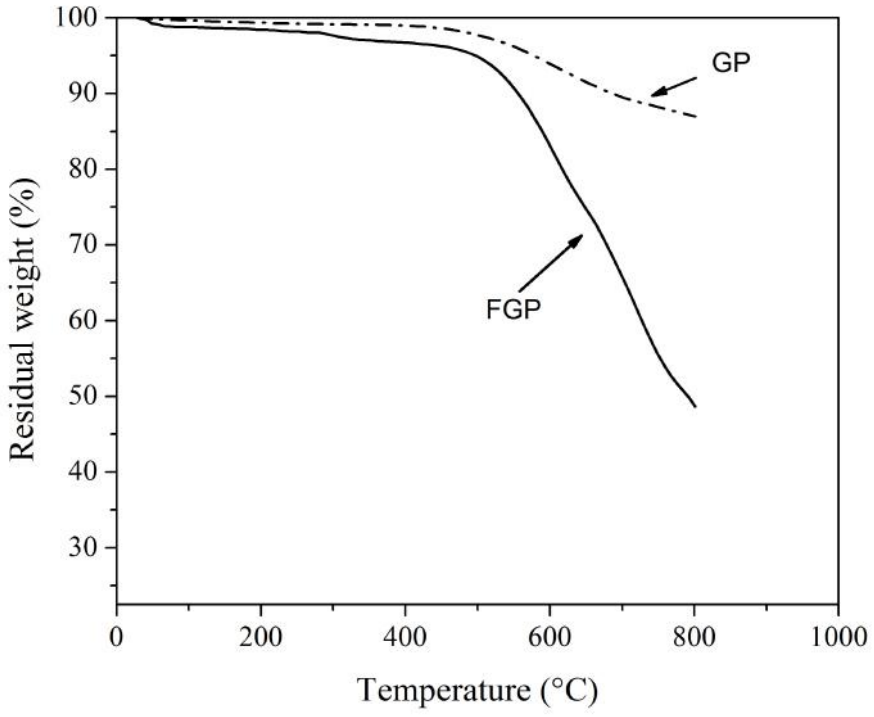

Figure 6.5: TGA thermograms of FGP, and GP

It may be due to the higher functionalized groups, which make the FGP more hydrophilic and thus FGP shows removal of physically adsorbed water as compared to GP (Pham et al., 2011). The weight loss for FGP in the temperature range from 250-500ºC can be attributed to the pyrolysis of oxygen containing functional group, yielding CO, CO_2, and steam (Teng et al., 2011). The higher mass loss over the temperature 500ºC can be attributed to the decomposition of highly efficient covalently functional groups (Shen et al., 2013). Moreover, the 48% residue was present at this high temperature (800ºC), which can be revels that the graphitized structure of GP sheets was not effected due to the functionalization which is in good agreement with the results of XRD analysis (fig. 6.6).

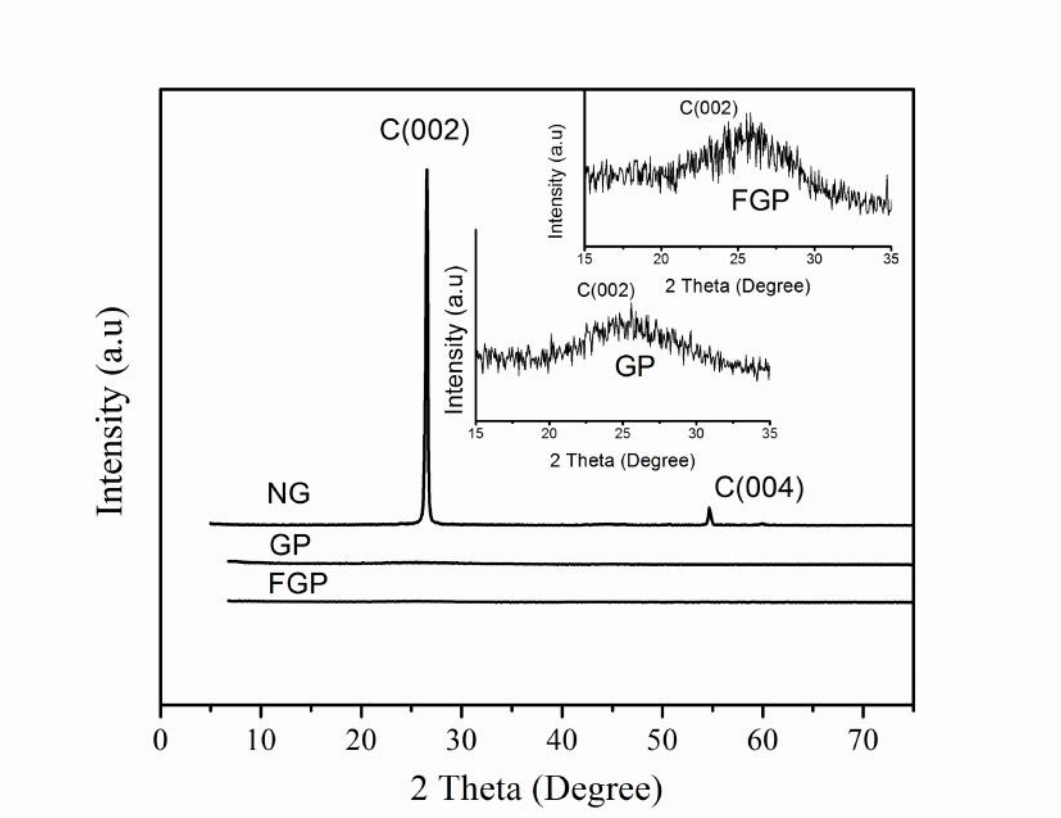

Figure 6.6: XRD diffraction patterns of NG, GP, and FGP

6.4.1.3 XRD analysis of the functionalized graphene

Figure 6.6 shows the XRD diffraction pattern of FGP and compared with the GP and NG. It appears from the fig. 6.6 that the FGP and GP diffraction peaks were disappeared as compared to the diffraction peak of NG. However, the GP (inset fig. 5.6) particles showed a broad diffraction peak C(002) at 25.75°, which was slightly shifted from the graphite C(002) peak at 26.5°. The lower side shifting of the C(002) peak signifies that the c-axis of graphite layer is exfoliated and carbon sp^2 bonds are reconstructed in GP (Ghosh et al., 2013). The similar diffraction pattern was observed for FGP particles shown in fig. 6.7 (inset). The diffraction patterns of FGP show that the carbon sp^2 hybridized 2D plane remain unchanged before and after the functionalization of the GP particles.

6.4.1.4 FE-SEM and TEM analysis of the functionalized graphene

From the fig. 6.7(a) it can be seen that similar type of the surface morphology was observed for FGP sheets as it was observed in the FE-SEM of GP (fig. 3.8(b,c)). The thin monolayer of FGP are semi-transparent in the FE-SEM micrograph, which indicate that the FGP sheet formed is atomically thin.

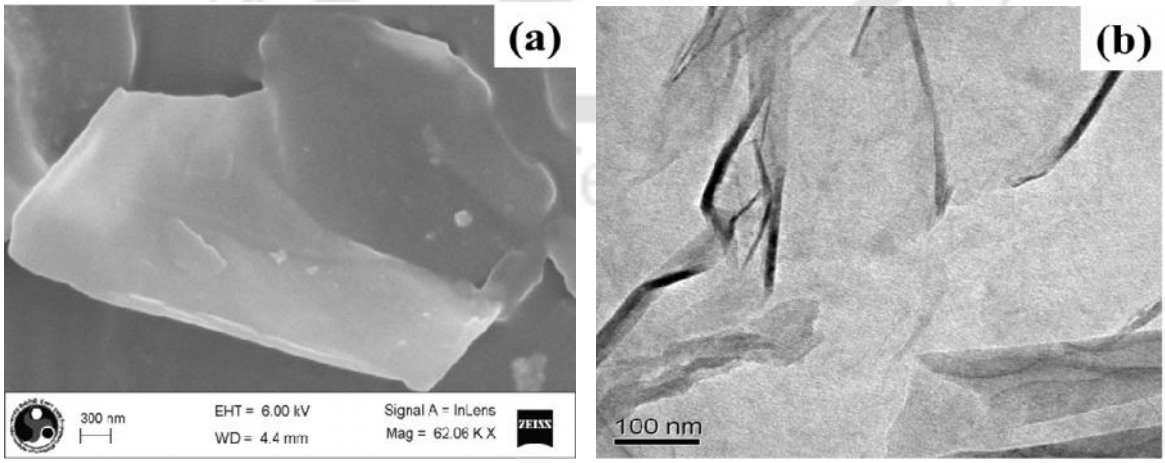

Figure 6.7: (a) FE-SEM, and (b) TEM analyses of FGP

Figure 6.7(b) shows the TEM morphology of FGP sheet. It can be seen that FGP exhibits crumpled and wrinkled flake-like structure due to the presence of functional groups on the GP surface. This structure is highly beneficial in maintaining a high surface area on the electrode since the sheets cannot readily collapse back to a graphitic structure (Cui et al., 2012; Ghosh et al., 2013).

6.4.1.5 BET analysis of the functionalized graphene

The specific surface area of FGP was calculated using BET surface area analyzer as explained in section 3.2.3.4. The BET surface area of FGP was found to be 910.32 $m^2 \cdot g^{-1}$ (Ghosh et al., 2013). High surface area of FGP suggests its utility as electrcatalyst support material for Pt electrocatalyst (Mishra et al., 2004).

6.4.2 Pt/GP and Pt/FGP electrocatalyst

The characterization using XRD, FE-SEM, TEM, EDX, and electrochemical activity (ORR and CV) analyses of developed Pt/GP and Pt/FGP electrocatalysts are discussed in the subsequent section.

6.4.2.1 XRD analyses of Pt/GP and Pt/FGP

The XRD diffraction patterns of synthesized Pt/GP and Pt/FGP are shown in the fig. 6.8, and compared with commercial Pt/C diffraction pattern. The synthesized of the electrocatalyst shows the presence of Pt(111), Pt(200), and Pt(220) crystalline phases of platinum (JCPDS 04-0802) along with broad peak for carbon C(002). It can be seen in the figure that the diffraction peaks of Pt in the Pt/FGP electrocatalyst are comparatively broad as compared to Pt/GP and Pt/C catalyst. It indicates that the average crystal size of the Pt particles in Pt/FGP catalyst is less than as compared to Pt/C and Pt/GP electrocatalyst (Liu et al., 2006).

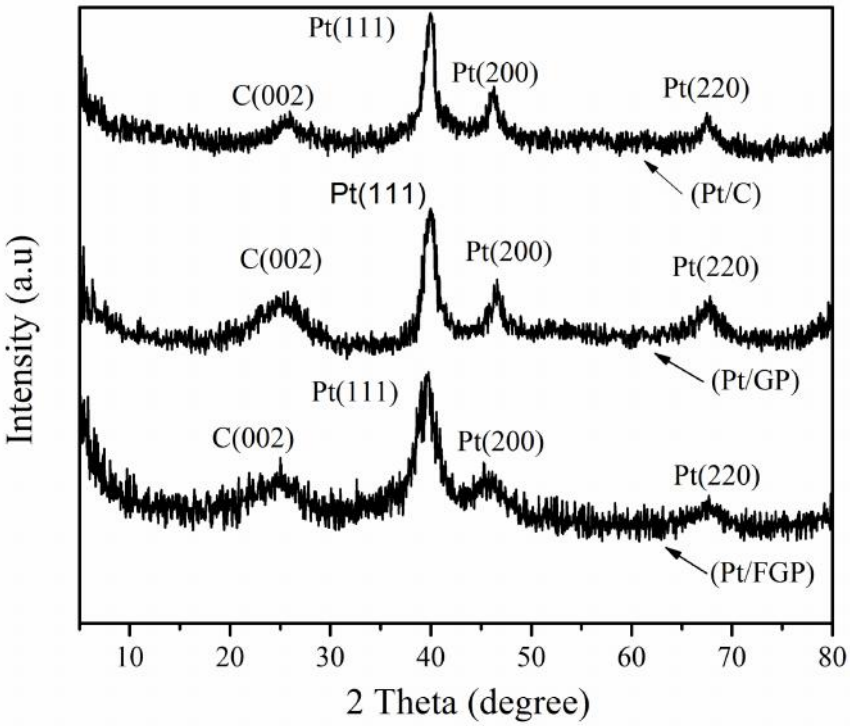

Figure 6.8: XRD patterns of Pt/C, Pt/GP, and Pt/FGP

The average crystallite size determination was done by measuring the broadening of a particular peak in a diffraction pattern. Typically, the narrower the peak, the larger the crystallite size. This is due to the periodicity of the individual crystallite domains, in phase, reinforcing the diffraction of the X-ray beam, resulting in a tall narrow peak (Qiling 2006). The average crystal sizes of the Pt particle for the Pt/C, Pt/GP, and Pt/FGP were about 4.8 nm, 4.3 nm, and 4 nm, respectively, using Scherrer formula.

6.4.2.2 Morphological analyses of Pt/GP and Pt/FGP

The typical FE-SEM micrograph of the Pt/GP and Pt/FGP are shown in the fig. 6.9(a,b). From the figure shows that Pt nanoparticles are well dispersed on the graphene and FGP surfaces.

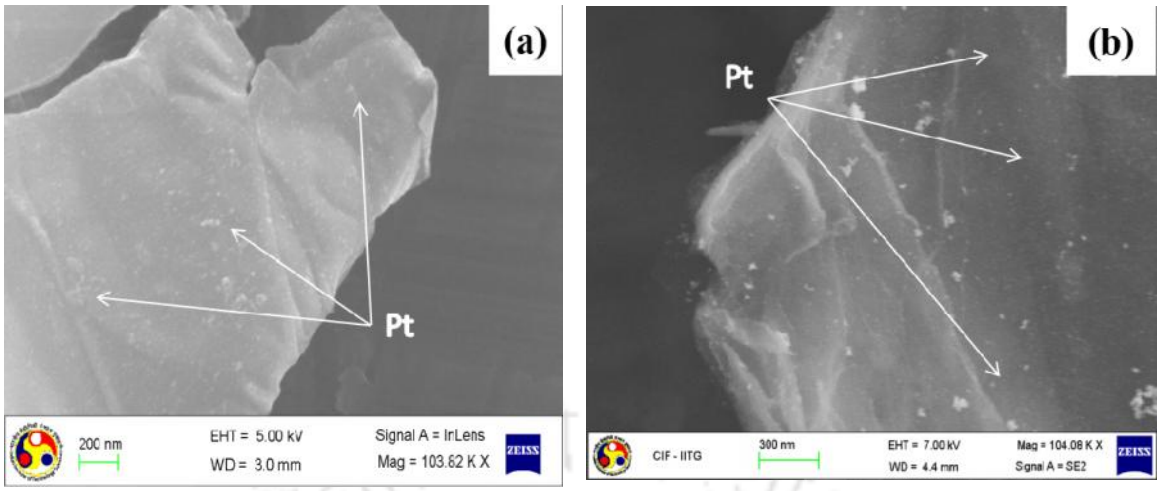

Figure 6.9: FE-SEM images of (a) Pt/GP, and (b) Pt/FGP

However, the presence of Pt particles on the GP and FGP surfaces are not very clearly visible in the FE-SEM. Further, TEM analysis was done to confirm the presence and distribution of platinum onto the support (GP and FGP). The TEM images of the Pt/GP and Pt/FGP are shown in fig. 6.10 and compared with micrograph of commercial Pt/C electrocatalyst. The fig. 6.10(a, b, and c) shows the presence of platinum particles on different support materials. It may be noted that carbon, GP, and FGP supports were having the same loading (20wt.%) of Pt. The high surface area support material is favorable for better dispersion of Pt nanoparticles. The TEM images of Pt/GP and Pt/FGP shows that the Pt particles are well distributed on GP and FGP as compared to carbon. The TEM images of Pt/GP and Pt/FGP shows that the Pt particles are well distributed on GP and FGP as compared to carbon. It may be due to the very less surface area of carbon (249.46 $m^2 \cdot g^{-1}$) in comparison to GP (750.85 $m^2 \cdot g^{-1}$) and FGP (910.32 $m^2 \cdot g^{-1}$) which are found by BET surface area analysis and reported in the section 3.3.4 and 6.4.1.5, respectively. The distribution of Pt on the carbon black shows large agglomeration of Pt particles at many places compared to graphene. However, the agglomeration of Pt particles on the FGP surface was even less than graphene surface.

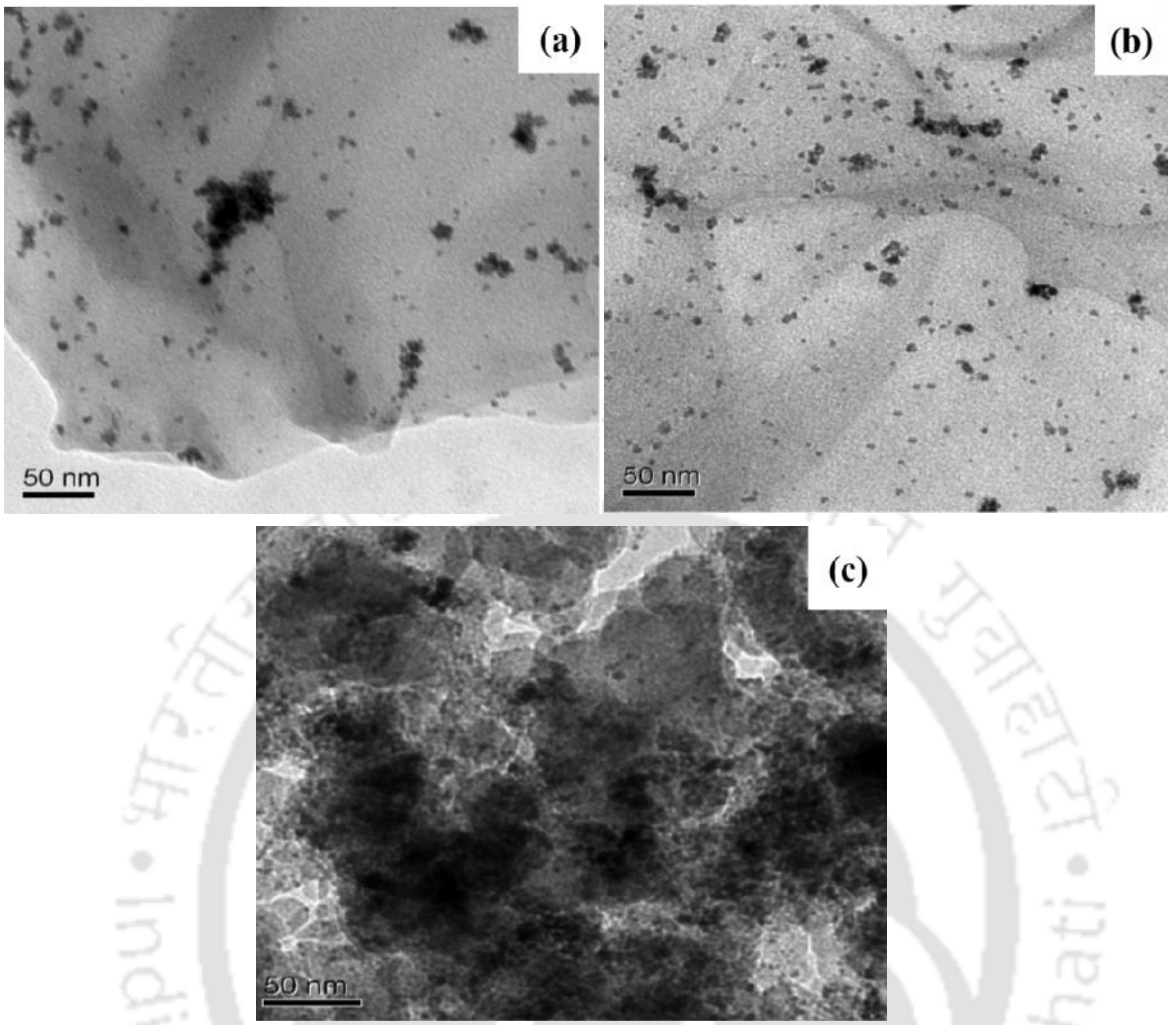

Figure 6.10: TEM surface morphology of (a) Pt/GP, (b) Pt/FGP, and (c) Pt/C

6.4.2.3 EDX analyses of Pt/GP and Pt/FGP

The evidence of the presence of Pt particles (fig. 6.11) on the GP and FGP surfaces was confirmed by Energy-dispersive X-ray spectroscopy (EDX). The EDX micrographs in fig. 6.11 clearly show the presence of carbon, Pt, and oxygen. The oxygen peak is observed due to the adsorption of oxygen by carbon. It may also be noted that the electrocatalysts were prepared by reducing hexachloroplatinic acid using $NaBH_4$ and the absence of other element such as chlorine or sodium in the EDX analyses confirmed the successful reduction of Pt on GP and FGP supports.

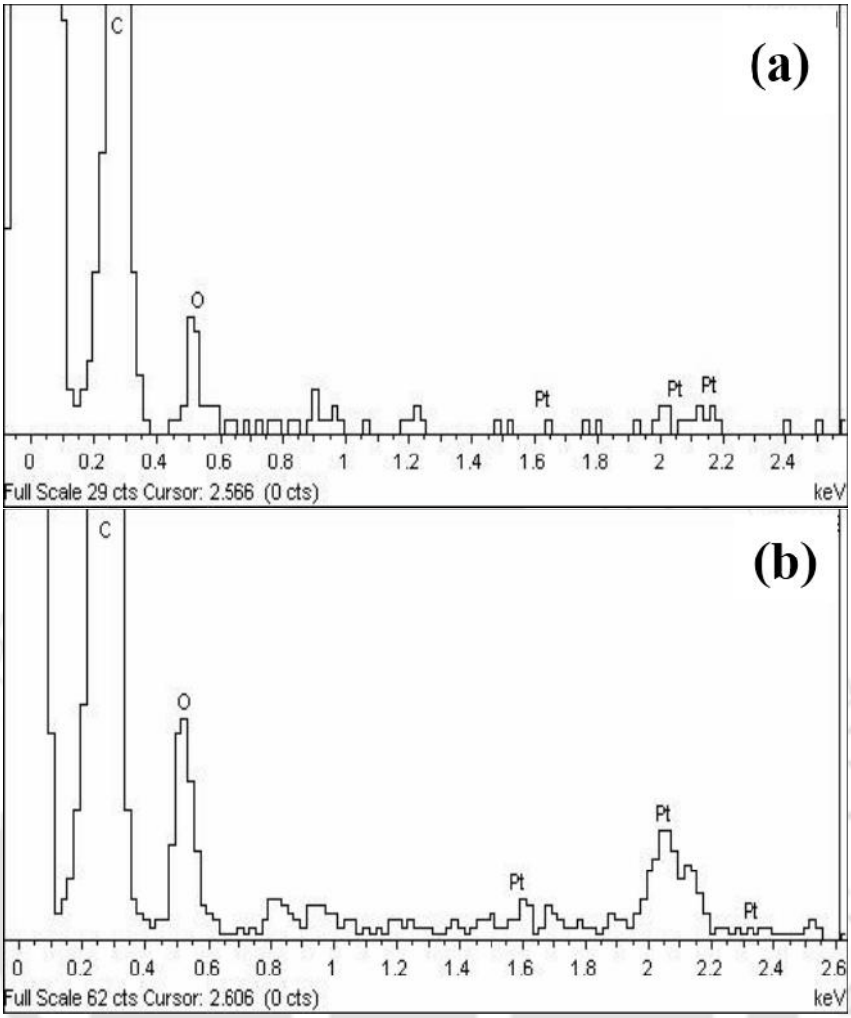

Figure 6.11: EDX micrograph of (a) Pt/GP, and (b) Pt/FGP

6.4.2.4 Oxygen reduction reaction (ORR) analyses of Pt/GP and Pt/FGP

To investigate the catalytic activity for the oxygen reduction reaction (ORR) study of the synthesized electrocatalysts (Pt/GP and Pt/FGP) are shown in fig. 6.12, and compared with commercial Pt/C electrocatalyst. The initial region is the kinetic control region and the oxygen reduction current density is not affected by the rate of mass transfer. The mixed control region can be seen in the plots (0.72-0.87 V for Pt/C; 0.72-0.9 V for Pt/GP; and 0.725-0.9 V for Pt/FGP), where the reduction current depends upon the rate of mass transport and kinetics of electron transport.

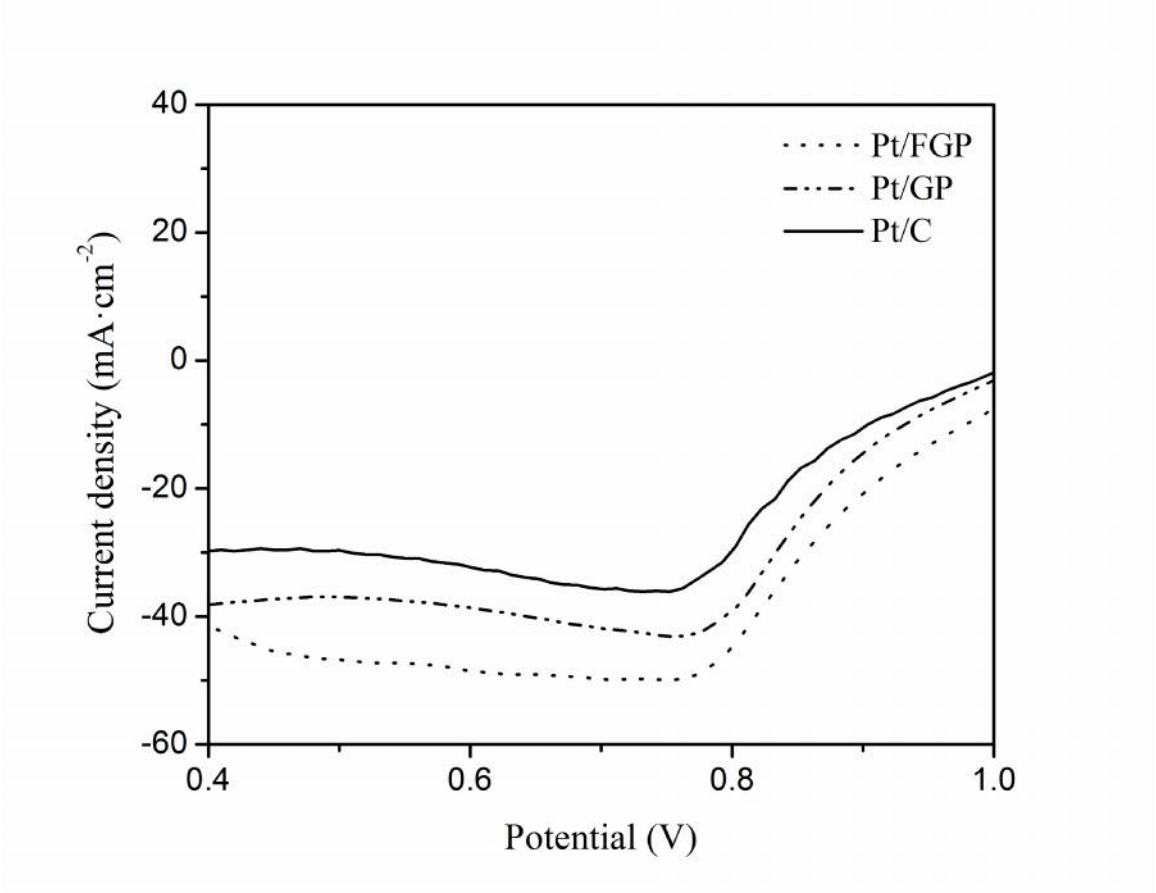

Figure 6.12: LSV for ORR of Pt/C, Pt/GP, and Pt/FGP at a scan rate of 10 mV·s^{-1} using RDE at 1,600 rpm (O_2 saturated 0.5 M H_2SO_4)

Finally, the region from beyond 0.72 V for Pt/C, 0.72 V for Pt/GP, and 0.725 V for Pt/FGP towards lower potential is the diffusion controlled region showing defined current plateau (Ghosh et al., 2013). It is clearly seen that the ORR activity of the Pt/GP and Pt/FGP is higher even at lower overpotential as compared to Pt/C electrocatalyst.

6.4.2.5 Hydrogen adsorption/desorption (HAD) analyses of Pt/GP and Pt/FGP

Cyclic voltammetry analyses of developed electrocatalysts (Pt/GP and Pt/FGP) are shown in fig. 6.13. Hydrogen adsorption/desorption can clearly be seen in the fig. 6.13 for Pt/C, Pt/GP, and Pt/FGP electrocatalysts in the potential range of 0.05 V to 0.4 V (Ghosh et al., 2013). The hydrogen adsorption/desorption processes were occurred on the

polycrystalline surfaces of Pt particles. The high electrochemical surface area is favorable for fuel cell electrocatalyst towards electrooxidation and electroreduction reaction. Therefore, the charge associated with the hydrogen adsorption on Pt was found out by integrating the hydrogen adsorption peak of cyclic voltamograms for evaluating the electrochemical surface area. The ESA was determined using the procedure explained in the section 6.2.3.2.2. The ESA for hydrogen adsorption on Pt/C, Pt/GP, and Pt/FGP were determined as 40, 53.96, and 57.93 $m^2 \cdot g^{-1}$Pt, respectively. Thus, as compared to commercial Pt/C electrocatalyst, the ESA of Pt/GP and Pt/FGP were found to be higher than 34.9% and 44.8%, respectively. In addition, the HAD (fig. 6.13) forward peak current densities of Pt/GP and Pt/FGP were found to be higher than 8.54% and 13.03%, respectively, as compared to the Pt/C. It shows that the electrochemical activity of the Pt/FGP is better than Pt/GP for HAD.

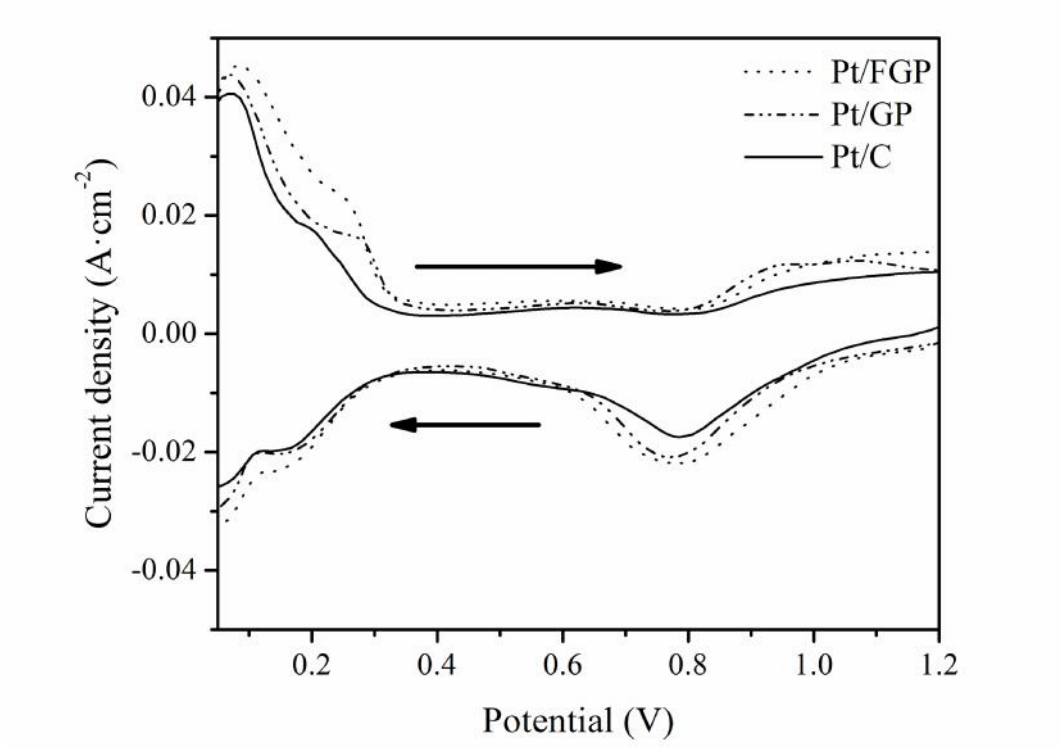

Figure 6.13: CV for HAD of Pt/C, Pt/GP, and Pt/FGP at a scan rate of 50 $mV \cdot s^{-1}$ (N_2 saturated 0.5 M H_2SO_4)

It may be due to the improved dispersion of Pt particles on FGP as the functionalization reduces the formation of stack of graphene. Henceforth, the surface area of the functionalized graphene was improved as compared to graphene and as a result the ESA of Pt/FGP was higher than that of Pt/GP as well as Pt/C.

It is found that the functionalized graphene support enhances the performance of the electrocatalyst. Therefore, FGP is used to further study the bimetallic electrocatalyst (PtAu) in comparison to Pt and Au.

6.4.3 Au/FGP and PtAu/FGP electrocatalyst

The different surface and electrochemical characterizations of the synthesized Au/FGP and PtAu/FGP are discussed in the following sections.

6.4.3.1 XRD analyses of Au/FGP and PtAu/FGP

Figure 6.14 shows the XRD diffraction patterns of as synthesized Au/FGP, PtAu/FGP, and compared with Pt/FGP electrocatalyst. The developed Au/FGP electrocatalyst show the face center cubic (fcc) crystalline Au diffraction peaks of (111), (200), and (220) at 2θ of 38.46, 44.5, and 65.7, respectively (JCPDS standard 04-0784) (Zhang et al., 2011a). The XRD patterns of PtAu/FGP electrocatalyst are similar to those of Au/FGP. The well-resolved peaks depicted in PtAu/FGP diffraction peaks of (111), (200), and (220) at 2θ of 38.8, 45.05, and 66.7, respectively. The broad peak for sp^2 hybridized carbon C(002) at around 2θ angle of 25.5 was observed for Au/FGP, and PtAu/FGP electrocatalyst, respectively. Each peak of PtAu/FGP electrocatalyst is in between corresponding peaks of Pt/FGP, and Au/FGP electrocatalysts. The shift of each peak of PtAu/FGP electrocatalyst to lower 2θ value compared to Pt/FGP and to higher 2θ value compared to Au/FGP (Basu and Basu 2011; Li et al., 2010). It indicates that a single phase bimetallic electrocatalyst is

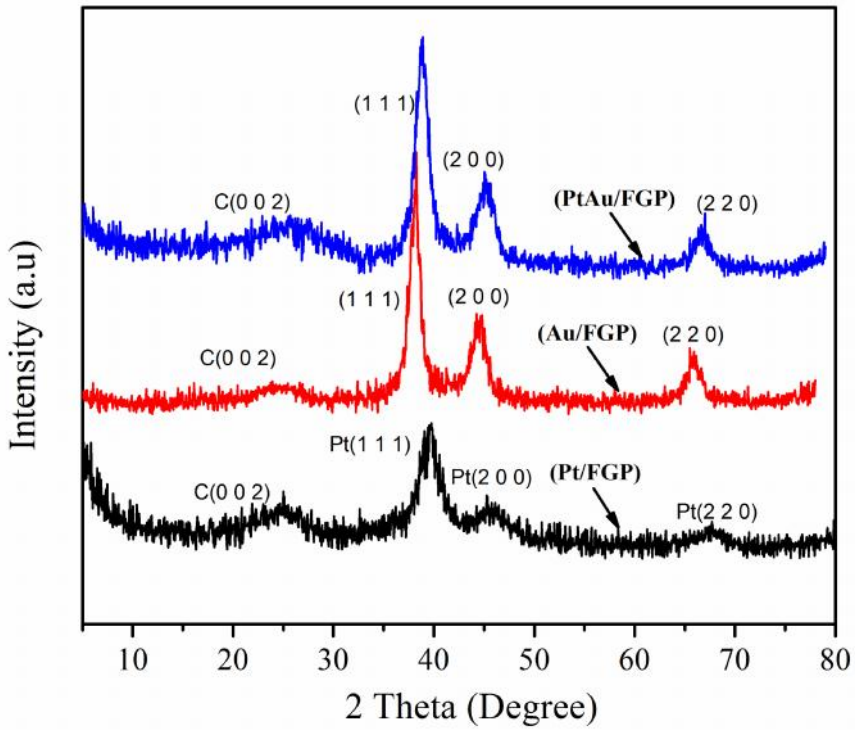

Figure 6.14: XRD patterns of Au/FGP, PtAu/FGP, and Pt/FGP

formed on the FGP support due to the incorporation of Au atoms into the Pt lattice, which leads to the formation of PtAu alloys (Zhang et al., 2011b). Moreover, due to the similarity of the Pt, and Au crystalline structures, the difference of the XRD peak positions for Pt and Au could not be distinguished. The Au and PtAu average crystallite sizes were calculated using broad diffraction peak of (111) as described in section 6.4.2.1. The average crystallite sizes of the Au and PtAu particle for the Au/FGP and PtAu/FGP were about 5.8 and 5 nm, respectively.

6.4.3.2 Morphological analyses of Au/FGP and PtAu/FGP

The typical FE-SEM and TEM micrographs were recorded for the Au/FGP and PtAu/FGP and shown in the fig. 6.15. FE-SEM images show the good dispersion of metallic nanoparticles over FGP sheets (fig. 6.15a,b), however, cannot be clearly seen.

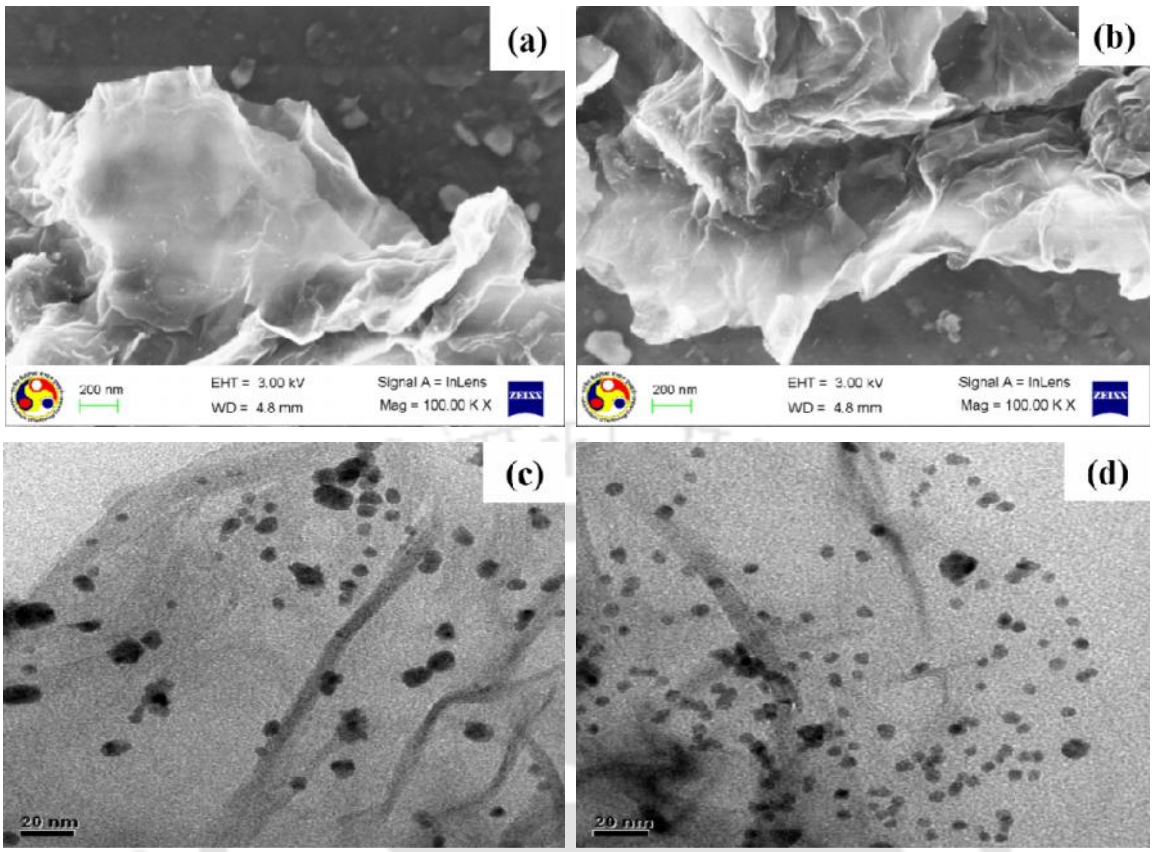

Figure 6.15: (a,b) FE-SEM and (c,d) TEM morphology of Au/FGP and PtAu/FGP, respectively

Therefore, TEM analysis was carried out for a more detailed morphological observation. Figure 6.15(c,d) shows the TEM images of Au/FGP and PtAu/FGP, respectively. It can be seen in the fig 6.15 that the PtAu alloy nanoparticles are comparatively well dispersed on FGP as compared to Au nanoparticles (fig. 6.15c,d).

6.4.3.3 EDX analyses of Au/FGP and PtAu/FGP

The EDX micrographs of as prepared Au/FGP and PtAu/FGP are shown in fig. 6.16. The EDX pattern confirms the presence of Pt, Au, and C and no other element. This indicates that the metal precursors were successfully reduced to form the electrocatalyst on the FGP (Xu et al., 2008).

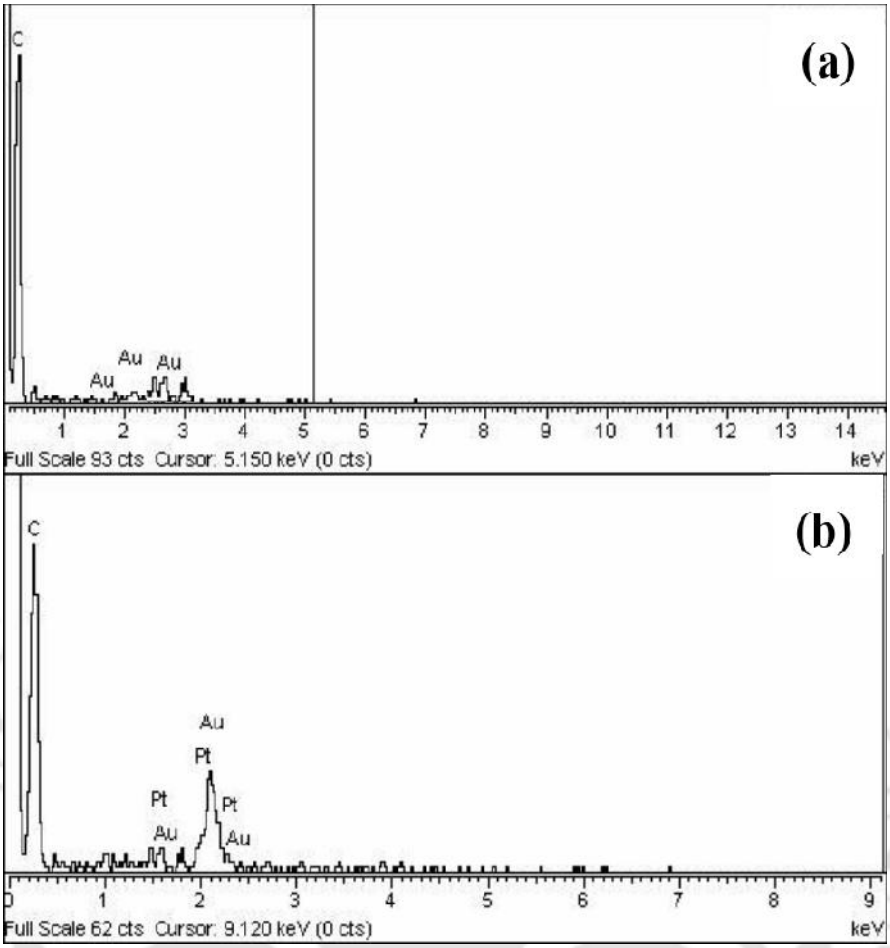

Figure 6.16: EDX micrograph of (a) Au/FGP, and (b) PtAu/FGP

6.4.3.4 Oxygen reduction reaction (ORR) analyses of Au/FGP and PtAu/FGP

The electrocatalytic activity of developed Au/FGP, PtAu/FGP, and Pt/FGP electrocatalysts were characterized by ORR using RDE as shown in fig. 6.17. The linear sweep voltammetry was conducted in the potential range of 1 V to 0.4 V at scan rate of 10 $mV \cdot s^{-1}$. It is clearly seen from the fig. 6.17 that the ORR on the Au/FGP has high overpotential and very low current density, which indicate very weak ORR activity as compared to PtAu/FGP electrocatalyst. The oxygen reduction of PtAu/FGP was started gradually at a potential around 1.0 V and reached a limiting plateau at a potential around 0.75 V. The mixed control region can be seen in the voltammograms between 0.77 and

0.91 V, and the diffusion control is started beyond 0.77 V towards lower potential. The ORR diffusion current density at 0.75 V for PtAu/FGP electrocatalyst is observed around 50 $mA \cdot cm^{-2}$, which is marginally higher that Pt/FGP current density (48 $mA \cdot cm^{-2}$) and significantly higher than Pt/GP (40 $mA \cdot cm^{-2}$) and Pt/C (34 $mA \cdot cm^{-2}$) electrocatalysts (fig. 6.12). It can be seen that though the 50% Pt was replaced by Au but the ORR performance of the PtAu/FGP is almost maintained. The similar electrocatalytic activity of the Pt and/or PtAu can also be explained based on the synergetic effect of the Au and Pt in ORR.

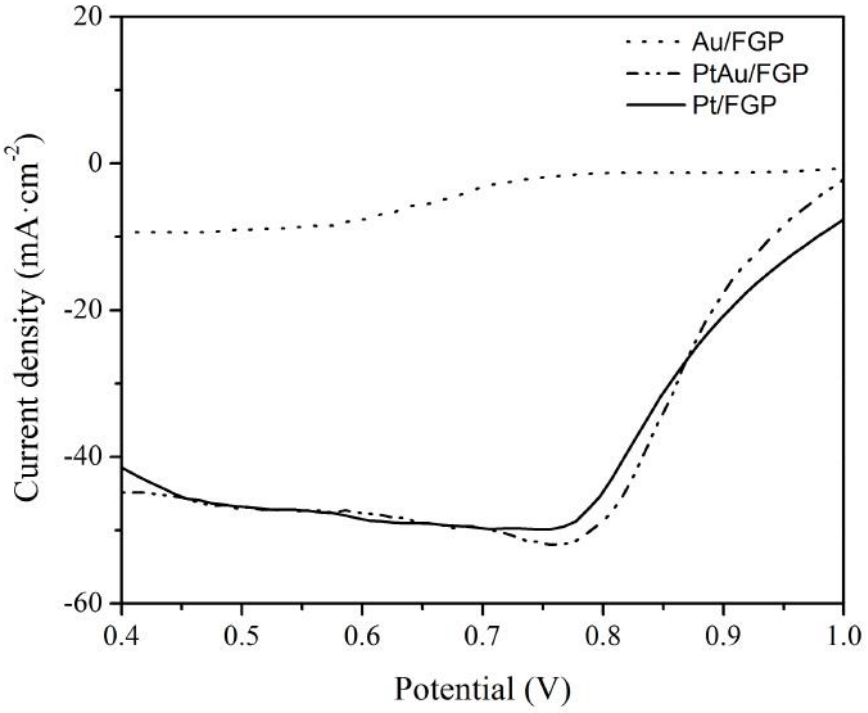

Figure 6.17: LSV for ORR of Au/FGP, PtAu/FGP, Pt/FGP at a scan rate of 10 $mV \cdot s^{-1}$ using RDE at 1,600 rpm (O_2 saturated 0.5 M H_2SO_4)

It can be seen that the Au/FGP electrocatalyst is hardly active for ORR electrocatalyst because Au is not capable of providing adsorption sites for the formation of Au-OH (Teliska et al., 2005). Moreover, the Au in PtAu electrocatalyst can facilitate the breaking

of Pt-OH thus allowing Pt to act efficiently in the ORR electrocatalytic process. Therefore, in comparison with Pt/FGP, Pt/GP, and Pt/C electrocatalyst, the higher ORR activity was observed for PtAu/FGP electrocatalyst (fig. 6.12 and fig. 6.17) (Ma et al., 2010).

6.4.3.5 Hydrogen adsorption/desorption (HAD) analyses of Au/FGP and PtAu/FGP

The HAD on Au/FGP and PtAu/FGP electrocatalysts were conducted as explained in section 6.4.2.5 and shown in the fig. 6.18. The CV plots display characteristics of a polycrystalline Au electrode, showing formation of Au surface oxides in the anode region and a cathodic peak around 1.1 V corresponding to the subsequent reduction of Au oxides. However, no significant hydrogen adsorption/desorption peaks were observed for Au/FGP electrocatalyst. It can also be found that the Au/FGP is showing hardly any hydrogen adsorption/desorption peak in the voltammogram (Senthil Kumar and Phani 2009; Khosravi and Amini 2010). However, for PtAu/FGP electrocatalyst, the characteristic peak intensity of Au is considerably reduced and the typical characteristic peaks of Pt are clearly observed (fig. 6.18). Therefore, it can be suggested that the surface of the bimetallic nanoparticles has a Pt-rich composition and Au is preferentially distributed in the inner region. It indicates that the Au surface has been mostly covered with Pt. The ESA of PtAu/FGP electrocatalyst was calculated for hydrogen adsorption on Pt, assuming that hydrogen is adsorbed on the Pt polycrystalline and not on Au polycrystalline nanostructure. The ESA for hydrogen adsorption on PtAu/FGP was found to be 48.15 $m^2.g^{-1}$Pt. The ESA for HAD of developed electrocatalyst was in increasing

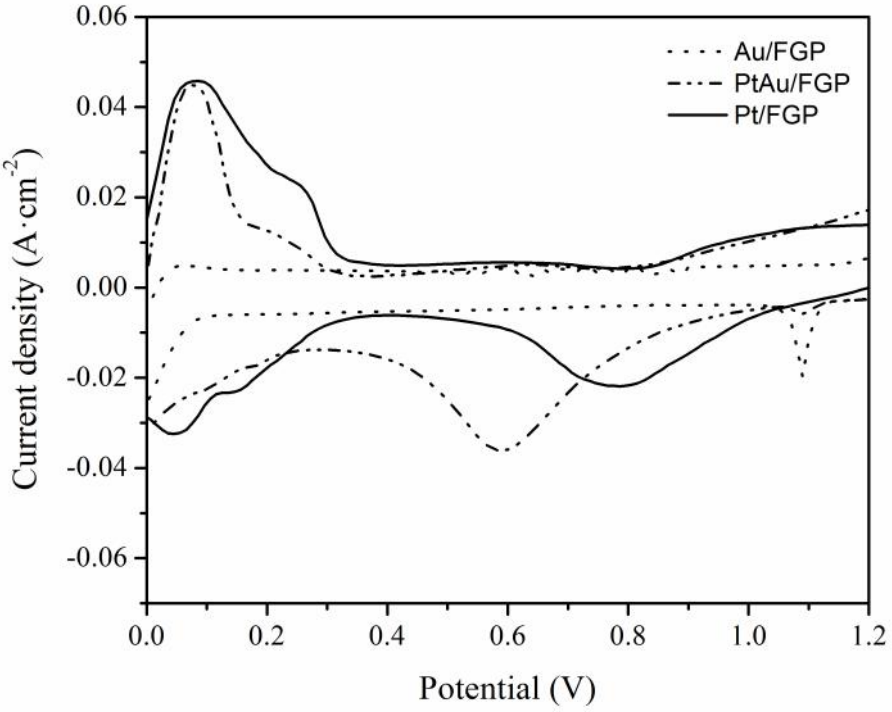

Figure 6.18: CV for HAD of Au/FGP, PtAu/FGP, and Pt/FGP at a scan rate of 50 $mV \cdot s^{-1}$ (N_2 saturated 0.5 M H_2SO_4)

order of Pt/FGP (57.93 $m^2 \cdot g^{-1}Pt$)>Pt/GP (53.96 $m^2 \cdot g^{-1}Pt$)>PtAu/FGP (48.15 $m^2 \cdot g^{-1}Pt$)>Pt/C (40 $m^2 \cdot g^{-1}Pt$) (refer fig. 6.13 and fig. 6.18). The plot for Pt/FGP is also shown for comparison. Moreover, the electrochemical stability of the Pt/GP, Pt/FGP, and PtAu/FGP was conducted using CV hydrogen adsorption/desorption and result compared with commercial Pt/C electrocatalyst, which are discussed in the subsequent section.

6.4.4 Electrochemical stability analyses of different electrocatalyst

In this section, the electrochemical stability of the electrocatalysts (Pt/C, Pt/GP, Pt/FGP, and PtAu/FGP) are reported and compared. It may be noted that due to insignificant HAD activity, the Au/FGP was not further characterized. The cyclic voltammetry of the developed electrocatalysts was conducted up to 1000 cycles and the results are reported

for 1st, 500th, and 1000th cycles (fig. 6.19). Figure 6.19 shows that with the increase in number of cycles, the peak height as well as ESA decreases for all the electrocatalysts. The vital data pertaining to the electrocatalysts are given in table 6.1 for better understanding and comparison. Table 6.1 shows the comparison of the ESA and HAD forward peak current densities of Pt/C, Pt/GP, Pt/FGP, and PtAu/FGP electrocatalysts for different CV cycles.

It can be seen (table 6.1) that the ESA and forward peak current density for Pt/C, Pt/GP, Pt/FGP, and PtAu/FGP electrocatalysts decreases with increase in scan cycles. In the 500th scan (table 6.1a) the percentage decrease in ESA was lowest for the functionalized graphene supported Pt and PtAu electrocatalyst. The percentage decrease (cumulative) in ESA for Pt/GP, Pt/FGP, and PtAu/FGP at 1000th scan was significantly low as compared to the commercial Pt/C.

Table 6.1(b) shows that the electrocatalyst performances are more or less similar for 500th scan cycle. However, for a long run (1000th scan cycle) the Pt/GP, Pt/FGP, and PtAu/FGP outperformed as compared to Pt/C. Moreover, FGP supported metal (Pt and/or PtAu) electrocatalysts performed better than Pt/GP. It is evident that the interaction between Pt and graphene was improved due to functionalization of the developed graphene. As a result, the stability of the Pt/FGP and PtAu/FGP were improved as compared to Pt/GP.

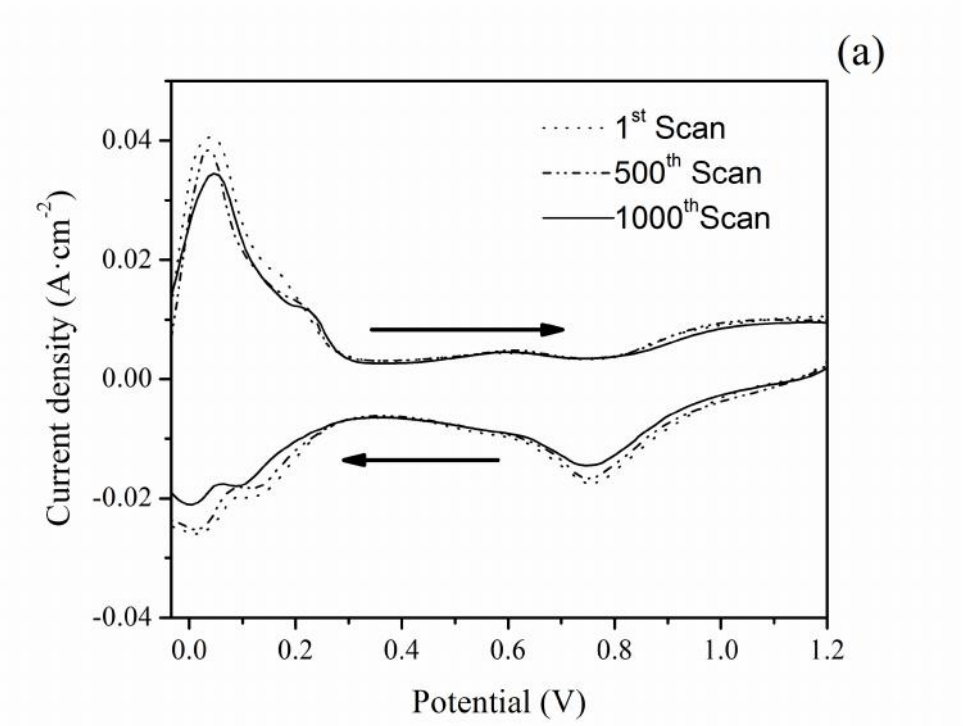

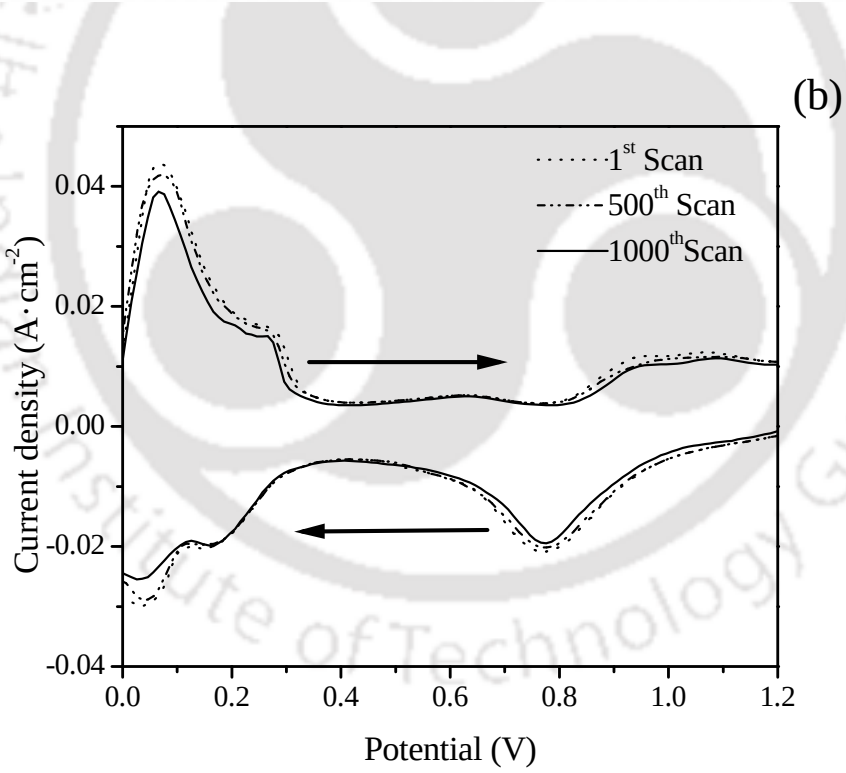

(Figure continued in next page)

Contd…

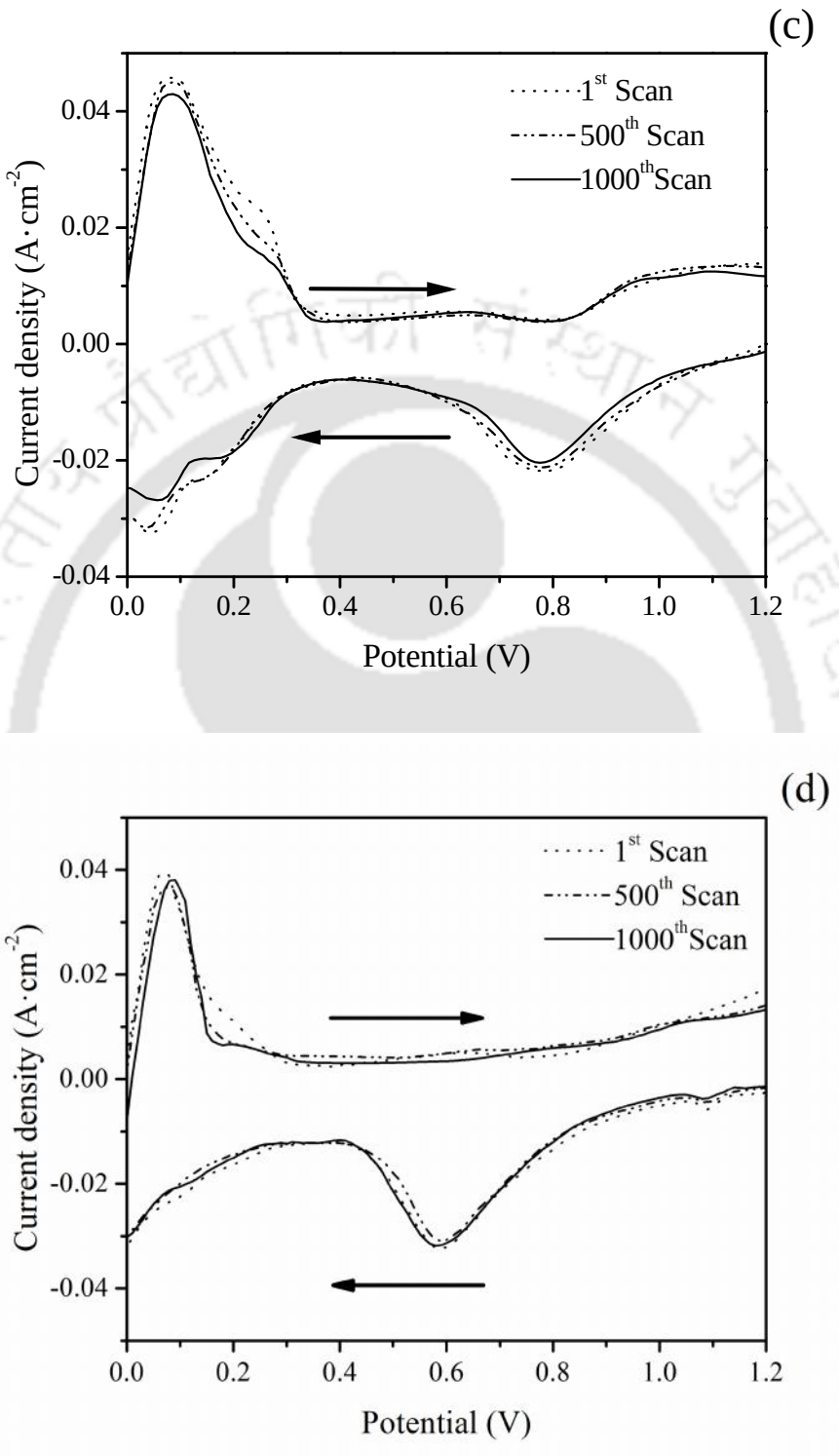

Figure 6.19: CV of (a) Pt/C, (b) Pt/GP, (c) Pt/FGP, and (d) PtAu/FGP at a scan rate of 50 $mV \cdot s^{-1}$ (N_2 saturated 0.5 M H_2SO_4)

Table 6.1: Comparison of (a) electrochemical surface area for HAD, and (b) catalysts stability in terms of forward peak current density for HAD

(a)	**1st Scan**				**500th Scan**				**1000th Scan**			
	Pt/C	Pt/GP	Pt/FGP	PtAu/FGP	Pt/C	Pt/GP	Pt/FGP	PtAu/FGP	Pt/C	Pt/GP	Pt/FGP	PtAu/FGP
ESA ($m^2 \cdot g^{-1}$Pt)	40	53.96	57.93	48.15	36.05	50.53	56.44	45.7	32.22	47.30	53.33	43.21
% decrease in ESA with respect to 1st scan of respective catalyst					10.95	6.78	2.63	5.36	24.14	14.08	8.62	11.45
(b)												
Forward peak current density ($mA \cdot cm^{-2}$)	40.5	43.96	45.78	41.54	38.42	41.92	43.96	39.85	34.48	39.12	42.06	38.04
% decrease in forward peak current density with respect to 1st scan of respective catalyst					5.41	4.86	4.05	4.82	17.45	12.37	8.84	9.2

6.4.5 Fuel cell performance evaluation using developed electrocatalysts

Figure 6.20 shows the performance of the unit cell PEMFC achieved using synthesized Pt/GP or Pt/FGP or PtAu/FGP at both the electrodes and compared with the Pt/C. It can be seen in the fig. 6.20 that the performance of the cell using Pt/GP or Pt/FGP or PtAu/FGP is better than the Pt/C. The maximum power densities using Pt/C, Pt/GP, Pt/FGP, and PtAu/FGP were obtained as 314, 426, 455, 411 $mW \cdot cm^{-2}$, respectively. At the maximum power density, the Pt mass-specific activity of Pt/C, Pt/GP, Pt/FGP, and PtAu/FGP electrolcatalyst is 0.52, 0.71, 0.76, and 1.37 $W \cdot mg^{-2}$, respectively. The Pt mass-specific activity of PtAu/FGP at the maximum power density is around 1.8 times higher than Pt/FGP and around 2.5 times higher than commercial Pt/C. This may be attributed to the improvement for the utilization of the Pt metal with the core-shell structure. The interaction between the Pt and Au may also contribute to its high performance. Furthermore, the probable reason for the better performance of Pt/GP, Pt/FGP, and PtAu/FGP as compared to Pt/C can be understand by the results of the ORR and HAD analysis discussed earlier. The kinetics of the ORR was quite high as well as the overpotential for the ORR was lower for Pt/GP, Pt/FGP, and PtAu/FGP as compared to the Pt/C.

Moreover, the HAD shown that the electrochemical surface area of the Pt/GP, Pt/FGP, and PtAu/FGP was around 34.9%, 44.8%, and 24% as compared to the Pt/C electrocatalyst. Therefore, the overall performance of the PEMFC was increased significantly for the Pt/GP, Pt/FGP, and PtAu/FGP. It may also be seen that the functionalization of the graphene produced the better results as compared to the as-synthesized graphene as an electrocatalyst support. It may be due to the even distribution and higher ESA of Pt nanoparticles onto the FGP as compared to GP.

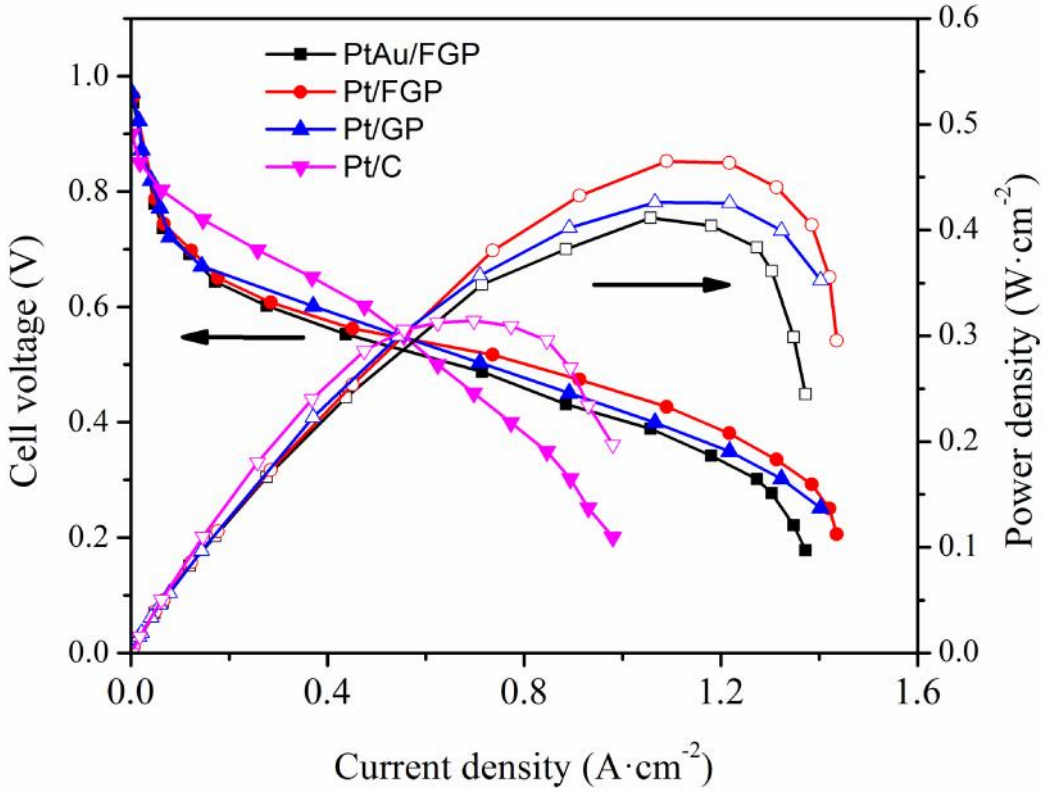

Figure 6.20: PEMFC performance of PtAu/FGP, Pt/FGP, Pt/G, and Pt/C (filled symbol for current density and cell voltage; hollow symbol for current density and power density) at 1 atm and 80^{o}C using loading of particular electrocatalyst (0.4 mg·cm^{-2} at anode; 0.6 mg·cm^{-2} at cathode)

The other observation of the $I-V$ plots (fig. 6.20) is that at low to moderate current densities the performance of the cell is fairly good for Pt/C as compared to Pt/GP or Pt/FGP or PtAu/FGP. The inferior performance of the cell using Pt/GP or Pt/FGP or PtAu/FGP was due to the flaky nature of graphene, whereas the carbon particles were spherical in nature (Ghosh et al., 2013). Thus anisotropic behavior of graphene and FGP for electrical conductivity dominates in the low to moderate current density region. At

high current density, the anisotropic and flaky behavior diminishes and thereafter the performance of the cell having GP and FGP supported platinum electrocatalyst improves significantly (Ghosh et al., 2013). Overall, the performance of the fuel cell was found to be superior for Pt/FGP and then for Pt/GP and PtAu/FGP electrocatalysts as compared to Pt/C.

Chapter 7

Conclusions and Future Scope

Chapter 7

Conclusions and Future Scope

7.1 Conclusions

In this study, the graphene was synthesized and characterized for the potential evaluation in PEMFC components particularly in polymer composite bipolar plate and as an electrocatalyst support material. Moreover, the suitability of the developed bipolar plate was also evaluated for HT-PEMFC. The main findings emanating from this study are summarized below:

The GP, being one of the highest electrically conductive materials, has been synthesized using chemical oxidation followed by thermal exfoliation of NG and was incorporated into the carbon-polymer composite bipolar plate as well as used as an electrocatalyst support material. The XRD, Raman, AFM, FE-SEM, and TEM analyses showed that monolayer graphene was produced. The absence of graphite C(002) peak in the XRD diffractogram confirmed that the developed GP was monolayer in nature, which was further confirmed by Raman analysis. The measured thickness of the developed GP was around 0.5 nm, which confirmed that monolayer GP was developed.

The composite bipolar plates were developed using three different polymer matrix, *viz.* NPFR, RPFR, and VER. Various reinforcements like CF, CB, and NG were used to develop the composite bipolar plate. The composite bipolar plate were fabricated using compression molding technique. The compositions of the optimized composites were taken from the literature and used as based compositions. However, the effect of CF length in the composite was evaluated in order to further improve the performance. More

specifically, the effect of CF length on the properties of composite (CF/CB/NG/NPFR 5/5/60/30%, CF/CB/NG/RPFR 5/5/65/25%, and CF/CB/NG/VER 5/5/65/25%) bipolar plates were studied to optimize the CF length for better mechanical strength. The maximum mechanical strength was found at 1 mm of CF length. Therefore, the optimum compositions for three polymer system were considered as CF(1mm)/CB/NG/NPFR 5/5/60/30%, CF(1mm)/CB/NG/RPFR 5/5/65/25%, and CF(1mm)/CB/NG/VER 5/5/65/25%. The detailed properties of these composites were given in table 4.7. It was found that the density, deflection at mid-span, shore hardness, in-plane electrical conductivity, thermal conductivity, hydrogen permeability, and corrosion current density for these composites were reached to stringent target. However, the flexural strength, through-plane electrical conductivity, and interfacial electrical contact resistance of the composite bipolar plates were lacking in comparison with the target. Moreover, the deflection of mid-span of the VER based composite was below the target. Therefore, the synthesized GP was reinforced at the expense of NG into the above optimized CF(1mm)/CB/NG/polymer composite bipolar plate primarily to improve the desired properties. It was found that not only electrical conductivity but also the flexural strength, and deflection at mid-span increased with the increase in GP content upto 1.5%. However, the flexural strength and electrical conductivity of the composite decreased rapidly after 1.5% GP content. Similarly, hydrogen permeability and corrosion current density was increased rapidly above 1.5% GP content. Therefore, the optimum compositions for three polymer system were considered as GP/CF(1mm)/CB/NG/NPFR 1.5/5/5/58.5/30%, GP/CF(1mm)/CB/NG/RPFR 1.5/5/5/63.5/25%, and GP/CF(1mm)/CB/NG/VER 1.5/5/5/63.5/25%. The properties of the GP/CF/CB/NG/polymer composite bipolar plates were shown in table 4.8. It was found that the in-plane as well as the through-plane electrical conductivities of the composite

bipolar plates were increased substantially at 1.5% GP. The electrical conductivity of the multiple component system could be explained by the simple resistive network as explained in the section 4.4.1.5. It was found that the GP had a little impact on the hydrogen permeabilities of the composite bipolar plates. It can be seen that the target values for all the properties have been achieved. However, the interfacial contact resistance of the composite bipolar plate was edge below the target value (14.4, 10.85, and 12.02 $m\Omega \cdot cm^2$ against 10 $m\Omega \cdot cm^2$, for NPFR, RPFR, and VER based composite, respectively).

In order to evaluate the performance of the composite bipolar plate in fuel cell, a PEMFC system was developed. It was found that the power density of the fuel cell was increased for GP reinforced composite bipolar plate as compared to when there was no GP content present. The peak power densities of the fuel cell were 340, 377, and 355 $mW \cdot cm^{-2}$ for GP/CF(1mm)/CB/NG/NPFR 1.5/5/5/58.5/30%, GP/CF(1mm)/CB/NG/RPFR 1.5/5/5/63.5/25%, and GP/CF(1mm)/CB/NG/VER 1.5/5/5/63.5/25%, respectively.

It can be seen that the maximum power density was shown by the fuel cell having GP/CF(1mm)/CB/NG/RPFR composite bipolar plate. Therefore, this RPFR based optimized composite bipolar plate (GP/CF(1mm)/CB/GP/RPFR 1.5/5/5/63.5/25%) was further evaluated to find its suitability in HT-PEMFC. The composite was exposed to elevated temperature and the properties were evaluated for HT-PEMFC. The TGA analysis showed that the composite bipolar plate was quite stable upto 270^oC. However, the evaluation of the mechanical and electrical properties showed that the composite was suitable upto 175^oC and just retained the desired properties. The composite bipolar plate was suitable for the temperature upto 175^oC only. It may be concluded that the composite

bipolar plate may be used for the HT-PEMFC operating upto 150^{o}C with a margin of 25^{o}C. Moreover, there is a need to study the performance of the composite in a HT-PEMFC for the evaluation of the fuel cell performance using the composite bipolar plate.

The synthesized GP was further used as an electrocatalyst support material for PEMFC. It was also found that GP do not have very good interaction with the metal nanoparticles. Therefore, FGP was developed using chemical method and characterized using FTIR, XRD, TGA, FE-SEM, and TEM.

The synthesis route to form nanophase electrocatalyst as well as the preparation method and the physical and electrochemical characterization of GP and FGP supported Pt and/or Au electrocatalsts were explained. The GP and FGP supported Pt and/or Au electrocatalst was prepared using precipitation method. The XRD analyses confirmed the formation of metal (Pt and/or Au) polycrystalline structure on the support material. The BET surface area of GP and FGP was found to be 3-4 times higher as compared to carbon black. The higher surface area led to uniform and well dispersed platinum particles on GP and FGP as compared to carbon black as support material for same loading of Pt. The electrochemical activity of Pt/GP, Pt/FGP, and PtAu/FGP (towards HAD and ORR) was better than Pt/C. The stability of the catalysts was measured at 500th and 1000th scan cycle of the CV and reported in terms of the peak current density of the forward scan. It was found that the decrease in forward peak current density was nearly same for 500th cycle. However, for 1000th cycle the decrease in the forward peak current density was only 12.37%, 8.84%, and 9.1% for Pt/GP, Pt/FGP, and PtAu/FGP as compared to Pt/C (17.45%). Therefore, it was concluded that the stability of the GP was better but for FGP the stability was best in the long run. It may be because FGP had better interaction with

the Pt as compared to as-synthesized GP. The developed Pt/GP or Pt/FGP or PtAu/FGP catalyst was used at the anode as well as at the cathode of a PEMFC developed for the purpose using standard components. The maximum power density using Pt/C, Pt/GP, Pt/FGP, and PtAu/FGP were obtained 314, 426, 455, and 411 $mW \cdot cm^{-2}$, respectively. Moreover, the total mass-specific activity of PtAu/FGP at the maximum power density was around 1.8 times higher that Pt/FGP and around 2.5 times higher than commercial Pt/C. Surprisingly, at low to moderate current densities, the performance of the cell for Pt/C was better than that of Pt/GP or Pt/FGP or PtAu/FGP, probably due to the anisotropic behavior of graphene for electrical conductivity. However, for higher current densities the anisotropic behavior diminished and the Pt/GP, Pt/FGP, and PtAu/FGP performance improved significantly.

It was found that the GP played an important role to enhance the properties of the composite bipolar plate and electrocatalyst support of PEMFC. It can be seen that the properties of graphene reinforced carbon-polymer composite bipolar plate was achieved almost all the stringent target and listed in table 4.8. Moreover, the developed electrocatalyst showed higher electrochemical activity as compared to commercial electrocatalyst. The composite bipolar plate was found suitable to the HT-PEMFC especially for PBI/PA based electrolyte. Thus the study fulfill the aim of the research work along with all the objective. It may be noted that though all the properties were achieved as per the bench mark but the ICR of the composite bipolar plate could not be achived but the cathodic corrosion current density was on the edge. However, in order to further make the effective bipolar plate and electrocatalyst, some future scope along with future direction for the research is shown in the next section.

7.2 Future scope

- A study on the properties of composite bipolar plate using conductive polymer may be conducted to decrease the interfacial contact resistance.

- The performance of the developed bipolar plates was tested in a unit cell of PEMFC and thus there is a need to thoroughly study the bipolar plates in a fuel cell stack.

- The preliminary study showed that the developed graphene reinforced carbon-polymer composite bipolar plate may be used in HT-PEMFC application. Therefore, the fuel cell performance in HT-PEMFC may be evaluated using developed bipolar plate.

- In the present study, the noble metal was used for the development of graphene and functionalized supported electrocatalyst. The development of graphene supported non-noble metal electrocatalyst may be synthesized and analyzed.

- The graphene was used in bipolar plate and as an electrocatalyst support. A study on the graphene as a microporous layer may be conducted.

References

References

Accorsi J and Yu M. Carbon black. In: Pritchard G, editor. Plastics additives: Springer Netherlands; 1998. p. 153-161.

Akhavan O. The effect of heat treatment on formation of graphene thin films from graphene oxide nanosheets. *Carbon*. 2010; **48** (2), 509-519.

Allaoui A, Bai S, Cheng HM, Bai JB. Mechanical and electrical properties of a MWNT/epoxy composite. *Composites Science and Technology*. 2002; **62** (15), 1993-1998.

Allen MJ, Tung VC, Kaner RB. Honeycomb carbon: A review of graphene. *Chemical Reviews*. 2009; **110** (1), 132-145.

Antolini E. Carbon supports for low-temperature fuel cell catalysts. *Journal of The Electrochemical Society* 2009; **88** (1-2), 1-24.

Antolini E. Graphene as a new carbon support for low-temperature fuel cell catalysts. *Applied Catalysis B: Environmental*. 2012; **123-124** (0), 52-68.

Antunes RA, de Oliveira MCL, Ett G, Ett V. Carbon materials in composite bipolar plates for polymer electrolyte membrane fuel cells: A review of the main challenges to improve electrical performance. *Journal of Power Sources*. 2011; **196** (6), 2945-2961.

Aravind SSJ, Baby TT, Arockiadoss T, Rakhi RB, Ramaprabhu S. A cholesterol biosensor based on gold nanoparticles decorated functionalized graphene nanoplatelets. *Thin Solid Films*. 2011; **519** (16), 5667-5672.

Atkinson A, Barnett S, Gorte RJ, Irvine JTS, McEvoy AJ, Mogensen M, Singhal SC, Vohs J. Advanced anodes for high-temperature fuel cells. *Nature Materials*. 2004; **3** (1), 17-27.

Avasarala B and Haldar P. Effect of surface roughness of composite bipolar plates on the contact resistance of a proton exchange membrane fuel cell. *Journal of Power Sources*. 2009; **188** (1), 225-229.

Avinash MB, Subrahmanyam KS, Sundarayya Y, Govindaraju T. Covalent modification and exfoliation of graphene oxide using ferrocene. *Nanoscale*. 2010; **2** (9), 1762-1766.

Barbir F. PEM fuel cells: Theory and practice. Burlington: MA: Elsevier Academic Press; 2005.

Barbir F and Yazici S. Status and development of PEM fuel cell technology. *International Journal of Energy Research*. 2008; **32** (5), 369-378.

Baschuk JJ and Li X. Carbon monoxide poisoning of proton exchange membrane fuel cells. *International Journal of Energy Research*. 2001; **25** (8), 695-713.

Basu D and Basu S. Synthesis and characterization of Pt-Au/C catalyst for glucose electro-oxidation for the application in direct glucose fuel cell. *International Journal of Hydrogen Energy*. 2011; **36** (22), 14923-14929.

Berry V. Impermeability of graphene and its applications. *Carbon*. 2013; **62** (0), 1-10.

Blunk R, Abd Elhamid MH, Lisi D, Mikhail Y. Polymeric composite bipolar plates for vehicle applications. *Journal of Power Sources*. 2006a; **156** (2), 151-157.

Blunk R, Zhong F, Owens J. Automotive composite fuel cell bipolar plates: Hydrogen permeation concerns. *Journal of Power Sources*. 2006b; **159** (1), 533-542.

Blunk RHJ, Lisi DJ, Yoo Y-E, Tucker CL. Enhanced conductivity of fuel cell plates through controlled fiber orientation. *AIChE Journal*. 2003; **49** (1), 18-29.

Bockris JOM and Srinivasan S. Fuel cells: Their electrochemistry. New York: McGraw-Hill; 1969.

Bong S, Kim Y-R, Kim I, Woo S, Uhm S, Lee J, Kim H. Graphene supported electrocatalysts for methanol oxidation. *Electrochemistry Communications*. 2010; **12** (1), 129-131.

Borup R, John D, Hui X, Axel O, Fernando G, Pivovar B. PEM fuel cell durability. 2008 doe hydrogen program review. *June 9-13*. 2008; (http://www.hydrogen.energy.gov/pdfs/review08/fc_26_borup.pdf).

Brownson DAC, Kampouris DK, Banks CE. An overview of graphene in energy production and storage applications. *Journal of Power Sources*. 2011; **196** (11), 4873-4885.

Caillard A, Coutanceau C, Brault P, Mathias J, Léger JM. Structure of Pt/C and PtRu/C catalytic layers prepared by plasma sputtering and electric performance in direct methanol fuel cells (DMFC). *Journal of Power Sources*. 2006; **162** (1), 66-73.

Chandan A, Hattenberger M, El-kharouf A, Du S, Dhir A, Self V, Pollet BG, Ingram A, Bujalski W. High temperature (HT) polymer electrolyte membrane fuel cells (PEMFC) - a review. *Journal of Power Sources*. 2013; **231** (0), 264-278.

Chandra S, Sahu S, Pramanik P. A novel synthesis of graphene by dichromate oxidation. *Materials Science and Engineering: B*. 2010; **167** (3), 133-136.

Chaparro AM, Martín AJ, Folgado MA, Gallardo B, Daza L. Comparative analysis of the electroactive area of Pt/C PEMFC electrodes in liquid and solid polymer contact by underpotential hydrogen adsorption/desorption. *International Journal of Hydrogen Energy*. 2009; **34** (11), 4838-4846.

Chen C-K and Kuo J-K. Nylon 6/CB polymeric conductive plastic bipolar plates for PEM fuel cells. *Journal of Applied Polymer Science*. 2006; **101** (5), 3415-3421.

Chen E. Fuel cell technology handbook. Florida: CRC Press 2003.

Chen H, Botef I, Zheng H, Maaza M, Vasudeva RV, Srinivasu VV. Thermal conductivity and stability of nano size carbon black filled PDMS: fuel cell perspective. International Journal of *Nanotechnology*. 2011; **8**, 437 - 445.

Cheng QF, Wang JP, Wen JJ, Liu CH, Jiang KL, Li QQ, Fan SS. Carbon nanotube/epoxy composites fabricated by resin transfer molding. *Carbon*. 2010; **48** (1), 260-266.

Choi SM, Seo MH, Kim HJ, Kim WB. Synthesis of surface-functionalized graphene nanosheets with high Pt-loadings and their applications to methanol electrooxidation. *Carbon*. 2011; **49** (3), 904-909.

Choi Y-K, Sugimoto K-i, Song S-M, Gotoh Y, Ohkoshi Y, Endo M. Mechanical and physical properties of epoxy composites reinforced by vapor grown carbon nanofibers. *Carbon*. 2005; **43** (10), 2199-2208.

Chung DDL. Review graphite. *Journal of Materials Science*. 2002; **37** (8), 1475-1489.

Chung DDL. Electrical applications of carbon materials. *Journal of Materials Science*. 2004; **39** (8), 2645-2661.

Cooper JS. Design analysis of PEMFC bipolar plates considering stack manufacturing and environment impact. *Journal of Power Sources*. 2004; **129** (2), 152-169.

Cooper KR. In situ PEMFC electrochemical surface area and catalyst utilization measurement. Fuel Cell Magazine2009. p. 1-3.

Costamagna P and Srinivasan S. Quantum jumps in the PEMFC science and technology from the 1960s to the year 2000: Part i. Fundamental scientific aspects. *Journal of Power Sources*. 2001; **102** (1-2), 242-252.

Cross J. Gasoline fuel processing: A system perspective. *IQPC Fuel Cells Infrastructure Conference*. 1999.

Cui L, Chen L, Xu M, Su H, Ai S. Nonenzymatic amperometric organic peroxide sensor based on nano-cobalt phthalocyanine loaded functionalized graphene film. *Analytica Chimica Acta*. 2012; **712** (0), 64-71.

Cunningham BD and Baird DG. Development of bipolar plates for fuel cells from graphite filled wet-lay material and a compatible thermoplastic laminate skin layer. *Journal of Power Sources*. 2007; **168** (2), 418-425.

Dai L, Chang DW, Baek J-B, Lu W. Carbon nanomaterials for advanced energy conversion and storage. *Small*. 2012; **8** (8), 1130-1166.

Davies DP, Adcock PL, Turpin M, Rowen SJ. Bipolar plate materials for solid polymer fuel cells. *Journal of Applied Electrochemistry*. 2000a; **30** (1), 101-105.

Davies DP, Adcock PL, Turpin M, Rowen SJ. Stainless steel as a bipolar plate material for solid polymer fuel cells. *Journal of Power Sources*. 2000b; **86** (1-2), 237-242.

Devanathan R. Recent developments in proton exchange membranes for fuel cells. *Energy & Environmental Science*. 2008; **1** (1), 101-119.

Dhakate SR, Mathur RB, Kakati BK, Dhami TL. Properties of graphite-composite bipolar plate prepared by compression molding technique for PEM fuel cell. *International Journal of Hydrogen Energy*. 2007; **32** (17), 4537-4543.

Dhakate SR, Sharma S, Borah M, Mathur RB, Dhami TL. Expanded graphite-based electrically conductive composites as bipolar plate for PEM fuel cell. *International Journal of Hydrogen Energy*. 2008; **33** (23), 7146-7152.

Dhakate SR, Sharma S, Chauhan N, Seth RK, Mathur RB. CNTs nanostructuring effect on the properties of graphite composite bipolar plate. *International Journal of Hydrogen Energy*. 2010; **35** (9), 4195-4200.

Dicks AL. The role of carbon in fuel cells. *Journal of Power Sources*. 2006; **156** (2), 128-141.

Dong L, Gari RRS, Li Z, Craig MM, Hou S. Graphene-supported platinum and platinum-ruthenium nanoparticles with high electrocatalytic activity for methanol and ethanol oxidation. *Carbon*. 2010; **48** (3), 781-787.

Du L. Highly conductive epoxy/graphite polymer composite bipolar plates in proton exchange membrane fuel cells: The University of Maryland; 2008.

Du L and Jana SC. Highly conductive epoxy/graphite composites for bipolar plates in proton exchange membrane fuel cells. *Journal of Power Sources*. 2007; **172** (2), 734-741.

Dutta A, Mahapatra SS, Datta J. High performance PtPdAu nano-catalyst for ethanol oxidation in alkaline media for fuel cell applications. *International Journal of Hydrogen Energy*. 2011; **36** (22), 14898-14906.

Dweiri R and Sahari J. Electrical properties of carbon-based polypropylene composites for bipolar plates in polymer electrolyte membrane fuel cell (PEMFC). *Journal of Power Sources*. 2007; **171** (2), 424-432.

Eguizábal A, Sgroi M, Pullini D, Ferain E, Pina MP. Nanoporous pbi membranes by track etching for high temperature PEMs. *Journal of Membrane Science*. 2014; **454** (0), 243-252.

El-kharouf A, Mason TJ, Brett DJL, Pollet BG. Ex-situ characterisation of gas diffusion layers for proton exchange membrane fuel cells. *Journal of Power Sources*. 2012; **218** (0), 393-404.

Emtsev KV, Bostwick A, Horn K, Jobst J, Kellogg GL, Ley L, McChesney JL, Ohta T, et al.,. Towards wafer-size graphene layers by atmospheric pressure graphitization of silicon carbide. *Nature Materials*. 2009; **8** (3), 203-207.

Ergun D, Devrim Y, Bac N, Eroglu I. Phosphoric acid doped polybenzimidazole membrane for high temperature PEM fuel cell. *Journal of Applied Polymer Science*. 2012; **124** (S1), E267-E277.

Ferrari AC. Raman spectroscopy of graphene and graphite: Disorder, electron-phonon coupling, doping and nonadiabatic effects. *Solid State Communications*. 2007; **143** (1-2), 47-57.

Frysz CA, Shui X, Chung DDL. Carbon filaments and carbon black as a conductive additive to the manganese dioxide cathode of a lithium electrolytic cell. *Journal of Power Sources*. 1996; **58** (1), 41-54.

Fu Y, Hou M, Lin G, Hou J, Shao Z, Yi B. Coated 316l stainless steel with CrxN film as bipolar plate for PEMFC prepared by pulsed bias arc ion plating. *Journal of Power Sources*. 2008; **176** (1), 282-286.

FuelCellToday. http://www.Fuelcelltoday.Com/analysis/analyst-views/2013. 2013; Access on October 2013.

Gardziella A, Pilato LA, Knop A. Phenolic resins: Chemistry, applications, standardization, safety and ecology. Springer; 2000.

Geim AK. Graphene: Status and prospects. *Science*. 2009; **324** (5934), 1530-1534.

Geim AK and Novoselov KS. The rise of graphene. *Nature Materials*. 2007; **6** (3), 183-191.

Geng D, Yang S, Zhang Y, Yang J, Liu J, Li R, Sham T-K, Sun X, et al.,. Nitrogen doping effects on the structure of graphene. *Applied Surface Science*. 2011; **257** (21), 9193-9198.

Geng X, Guo Y, Li D, Li W, Zhu C, Wei X, Chen M, Gao S, et al.,. Interlayer catalytic exfoliation realizing scalable production of large-size pristine few-layer graphene. *Scientific Reports*. 2013; **3**.

Geng Y, Wang SJ, Kim J-K. Preparation of graphite nanoplatelets and graphene sheets. *Journal of Colloid and Interface Science*. 2009; **336** (2), 592-598.

Ghosh A, Basu S, Verma A. Graphene and functionalized graphene supported platinum catalyst for PEMFC. *Fuel Cells*. 2013; **13** (3), 355-363.

Ghosh A, Srinath A, Verma A. Synthesis and evaluation of graphene for PEMFC catalyst support. *International Journal of Innovative Research and Development*. 2012; **1** (7), 7-12.

Giorgio S and Henry CR. Core-shell bimetallic particles, prepared by sequential impregnations. *The European Physical Journal - Applied Physics*. 2002; **20** (01), 23-27.

Gittleman C, Mastenand D, Jorgensen S, Waldecker J, Hirano S, Mehall M. 2010. Automotive fuel cell R&D needs. In: DOE fuel cell pre-solicitation workshop. (Lakewood, Colorado), https://www1.eere.energy.gov/hydrogenandfuelcells/fc_wkshp_mar10.html, Access on October 2013.

Gong K, Du F, Xia Z, Durstock M, Dai L. Nitrogen-doped carbon nanotube arrays with high electrocatalytic activity for oxygen reduction. *Science*. 2009; **323** (5915), 760-764.

Grove WR. On voltaic series and the combination of gases by platinum. *Philosophical Magazine and Journal of Science*. 1839; **14** (86), 127-130.

Guo H-L, Wang X-F, Qian Q-Y, Wang F-B, Xia X-H. A green approach to the synthesis of graphene nanosheets. *ACS Nano*. 2009; **3** (9), 2653-2659.

Guo J, Ren L, Wang R, Zhang C, Yang Y, Liu T. Water dispersible graphene noncovalently functionalized with tryptophan and its poly(vinyl alcohol) nanocomposite. *Composites Part B: Engineering*. 2011; **42** (8), 2130-2135.

Guo N and Leu MC. Effect of different graphite materials on the electrical conductivity and flexural strength of bipolar plates fabricated using selective laser sintering. *International Journal of Hydrogen Energy*. 2012; **37** (4), 3558-3566.

Ha H-W, Kim IY, Hwang S-J, Ruoff RS. One-pot synthesis of platinum nanoparticles embedded on reduced graphene oxide for oxygen reduction in methanol fuel cells. *Electrochemical and Solid-State Letters*. 2011; **14**, B70.

Hansen MK, Aili D, Christensen E, Pan C, Eriksen S, Jensen JO, von Barner JH, Li Q, Bjerrum NJ. PEM steam electrolysis at 130°C using a phosphoric acid doped short side chain PFSA membrane. *International Journal of Hydrogen Energy*. 2012; **37** (15), 10992-11000.

Hartnig C and Schmidt TJ. On a new degradation mode for high-temperature polymer electrolyte fuel cells: How bipolar plate degradation affects cell performance. *Electrochimica Acta*. 2011; **56** (11), 4237-4242.

Hasche F, Oezaslan M, Strasser P. Activity, structure and degradation of dealloyed PtNi3 nanoparticle electrocatalyst for the oxygen reduction reaction in PEMFC. *Journal of The Electrochemical Society*. 2011; **159** (1), B24-B33.

He W, Jiang H, Zhou Y, Yang S, Xue X, Zou Z, Zhang X, Akins DL, Yang H. An efficient reduction route for the production of Pd-Pt nanoparticles anchored on graphene nanosheets for use as durable oxygen reduction electrocatalysts. *Carbon*. 2012; **50** (1), 265-274.

Hermann A, Chaudhuri T, Spagnol P. Bipolar plates for PEM fuel cells: A review. *International Journal of Hydrogen Energy*. 2005; **30** (12), 1297-1302.

Hogarth MP and Ralph TR. Catalysis for low temperature fuel cells *Platinum Metals Review*. 2002; **46** (4), 146-164.

Hong S-T and Weil KS. Niobium-clad 304l stainless steel PEMFC bipolar plate material: Tensile and bend properties. *Journal of Power Sources*. 2007; **168** (2), 408-417.

Hou J, Shao Y, Ellis MW, Moore RB, Yi B. Graphene-based electrochemical energy conversion and storage: Fuel cells, supercapacitors and lithium ion batteries. *Physical Chemistry Chemical Physics*. 2011; **13** (34), 15384-15402.

Hsiao M-C, Liao S-H, Yen M-Y, Teng C-C, Lee S-H, Pu N-W, Wang C-A, Sung Y, et al.,. Preparation and properties of a graphene reinforced nanocomposite conducting plate. *Journal of Materials Chemistry*. 2010; **20** (39), 8496-8505.

Huang J, Baird DG, McGrath JE. Development of fuel cell bipolar plates from graphite filled wet-lay thermoplastic composite materials. *Journal of Power Sources*. 2005; **150** (0), 110-119.

Huang K-J, Niu D-J, Sun J-Y, Han C-H, Wu Z-W, Li Y-L, Xiong X-Q. Novel electrochemical sensor based on functionalized graphene for simultaneous determination of adenine and guanine in DNA. *Colloids and Surfaces B: Biointerfaces*. 2011; **82** (2), 543-549.

Hui C, Hong-bo L, Li Y, Jian-xin L. Study on the preparation and properties of novolac epoxy/graphite composite bipolar plate for PEMFC. *International Journal of Hydrogen Energy*. 2010; **35** (7), 3105-3109.

Hummers WS and Offeman RE. Preparation of graphitic oxide. *Journal of the American Chemical Society*. 1958; **80** (6), 1339-1339.

Hwang IU, Yu HN, Kim SS, Lee DG, Suh JD, Lee SH, Ahn BK, Kim SH, Lim TW. Bipolar plate made of carbon fiber epoxy composite for polymer electrolyte membrane fuel cells. *Journal of Power Sources*. 2008; **184** (1), 90-94.

IEO. Http://www.Eia.Gov/forecasts/ieo/. 2013; Access november 2013.

Jafri IR, Rajalakshmi N, Ramaprabhu S. Nitrogen doped graphene nanoplatelets as catalyst support for oxygen reduction reaction in proton exchange membrane fuel cell. *Journal of Materials Chemistry*. 2010; **20** (34), 7114-7117.

James L and Andrew D. Fuel cell system explained: John Wiley & Son; 2003.

Jayakumar K, Pandiyan S, Rajalakshmi N, Dhathathreyan KS. Cost-benefit analysis of commercial bipolar plates for PEMFC's. *Journal of Power Sources*. 2006; **161** (1), 454-459.

Jiang X and Drzal LT. Exploring the potential of exfoliated graphene nanoplatelets as the conductive filler in polymeric nanocomposites for bipolar plates. *Journal of Power Sources*. 2012; **218** (0), 297-306.

John FR, Radhakrishnan V, Haridoss P. Effect of electrochemical aging on the interaction between gas diffusion layers and the flow field in a proton exchange membrane fuel cell. *International Journal of Hydrogen Energy*. 2011; **36** (12), 7207-7211.

Kakati BK, Ghosh A, Verma A. Graphene reinforced composite bipolar plate for polymer electrolyte membrane fuel cell. *ASME 2011 9th International Conference on Fuel Cell Science, Engineering and Technology*. 2011; **FuelCell2011-54661**, 301-307.

Kakati BK, Ghosh A, Verma A. Efficient composite bipolar plate reinforced with carbon fiber and graphene for proton exchange membrane fuel cell. *International Journal of Hydrogen Energy*. 2013; **38** (22), 9362-9369.

Kakati BK, Sathiyamoorthy D, Verma A. Electrochemical and mechanical behavior of carbon composite bipolar plate for fuel cell. *International Journal of Hydrogen Energy*. 2010; **35** (9), 4185-4194.

Kakati BK and Verma A. Carbon-polymer composite bipolar plate for PEM fuel cell: Development, characterization and performance evaluation. Germany: LAP Lambert Academic Publishing; 2011.

Kakati BK, Yamsani VK, Dhathathreyan KS, Sathiyamoorthy D, Verma A. The electrical conductivity of a composite bipolar plate for fuel cell applications. *Carbon*. 2009; **47** (10), 2413-2418.

Kalaitzidou K, Fukushima H, Drzal LT. Multifunctional polypropylene composites produced by incorporation of exfoliated graphite nanoplatelets. *Carbon*. 2007; **45** (7), 1446-1452.

Kamarudin SK, Daud WRW, Md. Som A, Takriff MS, Mohammad AW. Technical design and economic evaluation of a PEMFC fuel cell system. *Journal of Power Sources*. 2006; **157** (2), 641-649.

Kang S-J, Kim DO, Lee J-H, Lee P-C, Lee M-H, Lee Y, Lee JY, Choi HR, et al.,. Solvent-assisted graphite loading for highly conductive phenolic resin bipolar plates for proton exchange membrane fuel cells. *Journal of Power Sources*. 2010; **195** (12), 3794-3801.

Kangasniemi K, Condit D, Jarvic T. Characterization of vulcan electrochemically oxidized under simulated PEM fuel cell conditions. *Journal of The Electrochemical Society*. 2004; **151** (4), E125-E132.

Kaniyoor A, Baby TT, Ramaprabhu S. Graphene synthesis via hydrogen induced low temperature exfoliation of graphite oxide. *Journal of Materials Chemistry*. 2010; **20** (39), 8467-8469.

Katz HS and Brandmaier HE. "Concise fundamentals of fiber-reinforces composites." handbook of reinforcements for plastics. New York: NY: Van Nostrand Reinhold Company, ; 1987.

Khosravi M and Amini MK. Carbon paper supported Pt/Au catalysts prepared via cu underpotential deposition-redox replacement and investigation of their

electrocatalytic activity for methanol oxidation and oxygen reduction reactions. *International Journal of Hydrogen Energy*. 2010; **35** (19), 10527-10538.

Kim H, Abdala AA, Macosko CW. Graphene/polymer nanocomposites. *Macromolecules*. 2010a; **43** (16), 6515-6530.

Kim H, Park J-N, Lee W-H. Preparation of platinum-based electrode catalysts for low temperature fuel cell. *Catalysis Today*. 2003; **87** (1-4), 237-245.

Kim JW, Kim NH, Kuilla T, Kim TJ, Rhee KY, Lee JH. Synergy effects of hybrid carbon system on properties of composite bipolar plates for fuel cells. *Journal of Power Sources*. 2010b; **195** (17), 5474-5480.

Kim KS, Zhao Y, Jang H, Lee SY, Kim JM, Kim KS, Ahn J-H, Kim P, et al.,. Large-scale pattern growth of graphene films for stretchable transparent electrodes. *Nature*. 2009; **457** (7230), 706-710.

Knop A and Pilato L. Phenolic resin. Berlin: Springer Verlag; 1985.

Kou R, Shao Y, Wang D, Engelhard MH, Kwak JH, Wang J, Viswanathan VV, Wang C, et al.,. Enhanced activity and stability of Pt catalysts on functionalized graphene sheets for electrocatalytic oxygen reduction. *Electrochemistry Communications*. 2009; **11** (5), 954-957.

Kraytsberg A, Auinat M, Ein-Eli Y. Reduced contact resistance of PEM fuel cell's bipolar plates via surface texturing. *Journal of Power Sources*. 2007; **164** (2), 697-703.

Kuan H-C, Ma C-CM, Chen KH, Chen S-M. Preparation, electrical, mechanical and thermal properties of composite bipolar plate for a fuel cell. *Journal of Power Sources*. 2004; **134** (1), 7-17.

Kuila T, Bose S, Mishra AK, Khanra P, Kim NH, Lee JH. Chemical functionalization of graphene and its applications. *Progress in Materials Science*. 2012; **57** (7), 1061-1105.

Kuilla T, Bhadra S, Yao D, Kim NH, Bose S, Lee JH. Recent advances in graphene based polymer composites. *Progress in Polymer Science*. 2010; **35** (11), 1350-1375.

Kulikovsky AA. A simple model for carbon corrosion in PEM fuel cell. *Journal of The Electrochemical Society*. 2011; **158** (8), B957-B962.

Kurachenkov VI and Igonin LA. Curing mechanism for phenol—formaldehyde resins. *Journal of Polymer Science Part A-1: Polymer Chemistry*. 1971; **9** (8), 2283-2289.

Lafront AM, Ghali E, Morales AT. Corrosion behavior of two bipolar plate materials in simulated PEMFC environment by electrochemical noise technique. *Electrochimica Acta*. 2007; **52** (15), 5076-5085.

Larminie J and Dicks AL. Fuel cell system explained, 2nd edition: John Wiley & Sons Ltd.,Wiltshire; 2003.

Lee JH, Jang YK, Hong CE, Kim NH, Li P, Lee HK. Effect of carbon fillers on properties of polymer composite bipolar plates of fuel cells. *Journal of Power Sources*. 2009; **193** (2), 523-529.

Lee SH, Kakati N, Jee SH, Maiti J, Yoon Y-S. Hydrothermal synthesis of PtRu nanoparticles supported on graphene sheets for methanol oxidation in direct methanol fuel cell. *Materials Letters*. 2011; **65** (21-22), 3281-3284.

Lee W-J, Chang K-C, Tseng IM. Properties of phenol-formaldehyde resins prepared from phenol-liquefied lignin. *Journal of Applied Polymer Science*. 2012; **124** (6), 4782-4788.

Li D, Muller MB, Gilje S, Kaner RB, Wallace GG. Processable aqueous dispersions of graphene nanosheets. *Nature Nanotechnology*. 2008; **3** (2), 101-105.

Li Q, He R, Gao J-A, Jensen JO, Bjerrum NJ. The co poisoning effect in PEMFCs operational at temperatures up to 200°c. *Journal of The Electrochemical Society*. 2003; **150** (12), A1599-A1605.

Li X. Thermodynamic performance of fuel cells and comparison with heat engines. Oxford: Elsevier Science; 2007.

Li X, Chen X, Benicewicz BC. Synthesis and properties of phenylindane-containing polybenzimidazole (PBI) for high-temperature polymer electrolyte membrane fuel cells (PEMFCs). *Journal of Power Sources*. 2013; **243** (0), 796-804.

Li X, Liu J, He W, Huang Q, Yang H. Influence of the composition of core-shell Au-Pt nanoparticle electrocatalysts for the oxygen reduction reaction. *Journal of Colloid and Interface Science*. 2010; **344** (1), 132-136.

Li X and Sabir I. Review of bipolar plates in PEM fuel cells: Flow-field designs. *International Journal of Hydrogen Energy*. 2005; **30** (4), 359-371.

Li Y, Tang L, Li J. Preparation and electrochemical performance for methanol oxidation of Pt/graphene nanocomposites. *Electrochemistry Communications*. 2009; **11** (4), 846-849.

Liao J, Yang J, Li Q, Cleemann LN, Jensen JO, Bjerrum NJ, He R, Xing W. Oxidative degradation of acid doped polybenzimidazole membranes and fuel cell durability in the presence of ferrous ions. *Journal of Power Sources*. 2013; **238** (0), 516-522.

Liao S-H, Hsiao M-C, Yen C-Y, Ma C-CM, Lee S-J, Su A, Tsai M-C, Yen M-Y, Liu P-L. Novel functionalized carbon nanotubes as cross-links reinforced vinyl ester/nanocomposite bipolar plates for polymer electrolyte membrane fuel cells. *Journal of Power Sources*. 2010a; **195** (23), 7808-7817.

Liao S-H, Hung C-H, Ma C-CM, Yen C-Y, Lin Y-F, Weng C-C. Preparation and properties of carbon nanotube-reinforced vinyl ester/nanocomposite bipolar plates

for polymer electrolyte membrane fuel cells. *Journal of Power Sources*. 2008a; **176** (1), 175-182.

Liao S-H, Weng C-C, Yen C-Y, Hsiao M-C, Ma C-CM, Tsai M-C, Su A, Yen M-Y, et al.,. Preparation and properties of functionalized multiwalled carbon nanotubes/polypropylene nanocomposite bipolar plates for polymer electrolyte membrane fuel cells. *Journal of Power Sources*. 2010b; **195** (1), 263-270.

Liao S-H, Yen C-Y, Weng C-C, Lin Y-F, Ma C-CM, Yang C-H, Tsai M-C, Yen M-Y, et al.,. Preparation and properties of carbon nanotube/polypropylene nanocomposite bipolar plates for polymer electrolyte membrane fuel cells. *Journal of Power Sources*. 2008b; **185** (2), 1225-1232.

Lin B, Chu F, Yuan N, Shang H, Ren Y, Gu Z, Ding J, Wei Y, Yu X. Phosphoric acid doped polybenzimidazole/imidazolium- modified silsesquioxane hybrid proton conducting membranes for anhydrous proton exchange membrane application. *Journal of Power Sources*. 2013; (0).

Liu C, Xue X, Lu T, Xing W. The preparation of high activity DMFC Pt/C electrocatalysts using a pre-precipitation method. *Journal of Power Sources*. 2006; **161** (1), 68-73.

Liu J, Xue Y, Zhang M, Dai L. Graphene-based materials for energy applications. *MRS Bulletin*. 2012; **37**, 1265-1272.

Liu N, Luo F, Wu H, Liu Y, Zhang C, Chen J. One-step ionic-liquid-assisted electrochemical synthesis of ionic-liquid-functionalized graphene sheets directly from graphite. *Advanced Functional Materials*. 2008; **18** (10), 1518-1525.

Liu S, Wang J, Zeng J, Ou J, Li Z, Liu X, Yang S. “Green” electrochemical synthesis of Pt/graphene sheet nanocomposite film and its electrocatalytic property. *Journal of Power Sources*. 2010; **195** (15), 4628-4633.

Liu Z-W, Peng F, Wang H-J, Yu H, Zheng W-X, Yang J. Phosphorus-doped graphite layers with high electrocatalytic activity for the O_2 reduction in an alkaline medium. *Angewandte Chemie International Edition*. 2011; **50** (14), 3257-3261.

Lobato J, Canizares P, Ubeda D, Pinar FJ, Rodrigo MA. Testing Pt Ru/CNF catalysts for a high temperature polybenzimidazole-based direct ethanol fuel cell. Effect of metal content. *Applied Catalysis B: Environmental*. 2011; **106** (1-2), 174-180.

Lotya M, Hernandez Y, King PJ, Smith RJ, Nicolosi V, Karlsson LS, Blighe FM, De S, et al.,. Liquid phase production of graphene by exfoliation of graphite in surfactant/water solutions. *Journal of the American Chemical Society*. 2009; **131** (10), 3611-3620.

Lu W and Chung DDL. A comparative study of carbons for use as an electrically conducting additive in the manganese dioxide cathode of an electrochemical cell. *Carbon*. 2002; **40** (3), 447-449.

Ma Y, Zhang H, Zhong H, Xu T, Jin H, Geng X. High active PtAu/C catalyst with core-shell structure for oxygen reduction reaction. *Catalysis Communications*. 2010; **11** (5), 434-437.

Maget HJR. Handbook of fuel cell technology. In: Berger C, editor. Englewood Cliffs, NJ, USA: Prentice-Hall; 1968.

Maheshwari PH, Mathur RB, Dhami TL. Fabrication of high strength and a low weight composite bipolar plate for fuel cell applications. *Journal of Power Sources*. 2007; **173** (1), 394-403.

Mamlouk M and Scott K. Phosphoric acid-doped electrodes for a PBI polymer membrane fuel cell. *International Journal of Energy Research*. 2011; **35** (6), 507-519.

Mani P, Srivastava R, Strasser P. Dealloyed Pt−Cu core−shell nanoparticle electrocatalysts for use in PEM fuel cell cathodes. *The Journal of Physical Chemistry C*. 2008; **112** (7), 2770-2778.

Marinkas A, Arena F, Mitzel J, Prinz GM, Heinzel A, Peinecke V, Natter H. Graphene as catalyst support: The influences of carbon additives and catalyst preparation methods on the performance of PEM fuel cells. *Carbon*. 2013; **58** (0), 139-150.

Mathur RB, Dhakate SR, Gupta DK, Dhami TL, Aggarwal RK. Effect of different carbon fillers on the properties of graphite composite bipolar plate. *Journal of Materials Processing Technology*. 2008; **203** (1-3), 184-192.

Mehta V and Cooper JS. Review and analysis of PEM fuel cell design and manufacturing. *Journal of Power Sources*. 2003; **114** (1), 32-53.

Metin Ö, Kayhan E, Özkar S, Schneider JJ. Palladium nanoparticles supported on chemically derived graphene: An efficient and reusable catalyst for the dehydrogenation of ammonia borane. *International Journal of Hydrogen Energy*. 2012; **37** (10), 8161-8169.

Meyer JC, Geim AK, Katsnelson MI, Novoselov KS, Obergfell D, Roth S, Girit C, Zettl A. On the roughness of single- and bi-layer graphene membranes. *Solid State Communications*. 2007; **143** (1-2), 101-109.

Middelman E, Kout W, Vogelaar B, Lenssen J, de Waal E. Bipolar plates for PEM fuel cells. *Journal of Power Sources*. 2003; **118** (1-2), 44-46.

Mighri F, Huneault MA, Champagne MF. Electrically conductive thermoplastic blends for injection and compression molding of bipolar plates in the fuel cell application. *Polymer Engineering & Science*. 2004; **44** (9), 1755-1765.

Min Y, Zhigang S, Xiaojing Z, Shulin M. Achieving concentrated graphene dispersions in water/acetone mixtures by the strategy of tailoring hansen solubility parameters. *Journal of Physics D: Applied Physics*. 2013; **46** (2), 025301.

Mishra V, Yang F, Pitchumani R. Measurement and prediction of electrical contact resistance between gas diffusion layers and bipolar plate for applications to PEM fuel cells. *Journal of Fuel Cell Science and Technology*. 2004; **1** (1), 2-9.

Nam D-G and Lee H-C. Thermal nitridation of chromium electroplated AISI316L stainless steel for polymer electrolyte membrane fuel cell bipolar plate. *Journal of Power Sources*. 2007; **170** (2), 268-274.

Novoselov KS, Geim AK, Morozov SV, Jiang D, Zhang Y, Dubonos SV, Grigorieva IV, Firsov AA. Electric field effect in atomically thin carbon films. *Science*. 2004; **306** (5696), 666-669.

Oliveira MCLd, Ett G, Antunes RA. Materials selection for bipolar plates for polymer electrolyte membrane fuel cells using the ashby approach. *Journal of Power Sources*. 2012; **206** (0), 3-13.

Oliveira MCLd, Ett G, Antunes RA. Corrosion and thermal stability of multi-walled carbon nanotube-graphite-acrylonitrile-butadiene-styrene composite bipolar plates for polymer electrolyte membrane fuel cells. *Journal of Power Sources*. 2013; **221** (0), 345-355.

Pander J. 2009. Hamburg speeds-up preparation for fuel-cell cars.

Papageorgopoulos D. Doe fuel cell technology program overview and introduction to the 2010 fuel cell pre-solicitation workshop in doe fuel cell pre-solicitation workshop. *Department of Energy, Lakewood, Colorado*. 2010; (https://www1.eere.energy.gov/hydrogenandfuelcells/pdfs/fuelcell_pre-solicitation_wkshop_mar10_papageorgopoulos.pdf), Access on August 2013.

Park S, Lee K-S, Bozoklu G, Cai W, Nguyen ST, Ruoff RS. Graphene oxide papers modified by divalent ions—enhancing mechanical properties via chemical cross-linking. *ACS Nano*. 2008; **2** (3), 572-578.

Park S and Ruoff RS. Chemical methods for the production of graphenes. *Nature Nanotechnology*. 2009; **4** (4), 217-224.

Park S, Shao Y, Wan H, Rieke PC, Viswanathan VV, Towne SA, Saraf LV, Liu J, et al.,. Design of graphene sheets-supported Pt catalyst layer in PEM fuel cells. *Electrochemistry Communications*. 2011; **13** (3), 258-261.

Parthasarathy A, Davé B, Srinivasan S, Appleby AJ, Martin CR. The platinum microelectrode/nafion interface: An alectrochemical impedance spectroscopic analysis of oxygen reduction kinetics and nafion characteristics. *Journal of The Electrochemical Society*. 1992; **139** (6), 1634-1641.

Pham TA, Kim JS, Kim JS, Jeong YT. One-step reduction of graphene oxide with l-glutathione. *Colloids and Surfaces A: Physicochemical and Engineering Aspects*. 2011; **384** (1-3), 543-548.

Poh CK, Lim SH, Pan H, Lin J, Lee JY. Citric acid functionalized carbon materials for fuel cell applications. *Journal of Power Sources*. 2008; **176** (1), 70-75.

Qiling Y. Preparation and characterization of highly active nano Pt/C electrocatalyst for proton exchange membrane fuel cell (*Ph.D*). South Africa: University of the Western Cape; 2006.

Qingfeng L, Hjuler HA, Bjerrum NJ. Phosphoric acid doped polybenzimidazole membranes: Physiochemical characterization and fuel cell applications. *Journal of Applied Electrochemistry*. 2001; **31** (7), 773-779.

Radhakrishnan S, Ramanujam BTS, Adhikari A, Sivaram S. High-temperature, polymer-graphite hybrid composites for bipolar plates: Effect of processing conditions on electrical properties. *Journal of Power Sources*. 2007; **163** (2), 702-707.

Rafiee MA, Rafiee J, Srivastava I, Wang Z, Song H, Yu Z-Z, Koratkar N. Fracture and fatigue in graphene nanocomposites. *Small*. 2010; **6** (2), 179-183.

Rafiee MA, Rafiee J, Wang Z, Song H, Yu Z-Z, Koratkar N. Enhanced mechanical properties of nanocomposites at low graphene content. *ACS Nano*. 2009; **3** (12), 3884-3890.

Ramanathan T, Abdala AA, StankovichS, Dikin DA, Herrera Alonso M, Piner RD, Adamson DH, Schniepp HC, et al.,. Functionalized graphene sheets for polymer nanocomposites. *Nature Nanotechnology*. 2008; **3** (6), 327-331.

Rao CV, Reddy ALM, Ishikawa Y, Ajayan PM. Synthesis and electrocatalytic oxygen reduction activity of graphene-supported Pt_3Co and Pt_3Cr alloy nanoparticles. *Carbon*. 2011; **49** (3), 931-936.

Reina A, Jia X, Ho J, Nezich D, Son H, Bulovic V, Dresselhaus MS, Kong J. Large area, few-layer graphene films on arbitrary substrates by chemical vapor deposition. *Nano Letters*. 2008; **9** (1), 30-35.

Ren YJ and Zeng CL. Corrosion protection of 304 stainless steel bipolar plates using tic films produced by high-energy micro-arc alloying process. *Journal of Power Sources*. 2007; **171** (2), 778-782.

Rodwick LBC. Development and moleding of electrical conductivity resins for fuel cell bipolar plate applications: Michigan Technological University; 2008.

Saha MS, Neburchilov V, Ghosh D, Zhang J. Nanomaterials-supported Pt catalysts for proton exchange membrane fuel cells. *Wiley Interdisciplinary Reviews: Energy and Environment*. 2013; **2** (1), 31-51.

Sao-Joao S, Giorgio S, Penisson JM, Chapon C, Bourgeois S, Henry C. Structure and deformations of Pd−Ni core−shell nanoparticles. *The Journal of Physical Chemistry B*. 2004; **109** (1), 342-347.

Schmittinger W and Vahidi A. A review of the main parameters influencing long-term performance and durability of PEM fuel cells. *Journal of Power Sources*. 2008; **180** (1), 1-14.

Schniepp HC, Li J-L, McAllister MJ, Sai H, Herrera-Alonso M, Adamson DH, Prud'homme RK, Car R, et al.,. Functionalized single graphene sheets derived from splitting graphite oxide. *The Journal of Physical Chemistry B*. 2006; **110** (17), 8535-8539.

Seger B and Kamat PV. Electrocatalytically active graphene-platinum nanocomposites. Role of 2-D carbon support in PEM fuel cells. *The Journal of Physical Chemistry C*. 2009; **113** (19), 7990-7995.

Senthil Kumar S and Phani KLN. Exploration of unalloyed bimetallic Au-Pt/C nanoparticles for oxygen reduction reaction. *Journal of Power Sources*. 2009; **187** (1), 19-24.

Seo DW, Lim YD, Lee SH, Jang HH, Choi SY, Jeon YT, Ju H, Kim WG. Preparation and properties of phosphoric acid doped sulfonated poly(tetra phenyl phthalazine ether sulfone) copolymers for high temperature proton exchange membrane application. *International Journal of Hydrogen Energy*. 2013; **38** (14), 6261-6267.

Shan C, Yang H, Han D, Zhang Q, Ivaska A, Niu L. Water-soluble graphene covalently functionalized by biocompatible poly-l-lysine. *Langmuir*. 2009; **25** (20), 12030-12033.

Shao J-J, Li Z-J, Zhang C, Zhang L-F, Yang Q-H. A wavy graphene/platinum hybrid with increased electroactivity for the methanol oxidation reaction. *Journal of Materials Chemistry A*. 2014.

Shao Y, Zhang S, Wang C, Nie Z, Liu J, Wang Y, Lin Y. Highly durable graphene nanoplatelets supported Pt nanocatalysts for oxygen reduction. *Journal of Power Sources*. 2010; **195** (15), 4600-4605.

Sharma S and Pollet BG. Support materials for PEMFCc and DMFC electrocatalysts-A review. *Journal of Power Sources*. 2012; **208** (0), 96-119.

Shen X-J, Pei X-Q, Fu S-Y, Friedrich K. Significantly modified tribological performance of epoxy nanocomposites at very low graphene oxide content. *Polymer*. 2013; **54** (3), 1234-1242.

Shen Y and Lua AC. A facile method for the large-scale continuous synthesis of graphene sheets using a novel catalyst. *Scientific Reports*. 2013; **3**.

Sobal NS, Ebels U, Möhwald H, Giersig M. Synthesis of core−shell PtCo nanocrystals. *The Journal of Physical Chemistry B*. 2003; **107** (30), 7351-7354.

Sogaard M, Odgaard M, Skou EM. An improved method for the determination of the electrochemical active area of porous composite platinum electrodes. *Solid State Ionics*. 2001; **145** (1), 31-35.

Sohi NJS, Bhadra S, Khastgir D. The effect of different carbon fillers on the electrical conductivity of ethylene vinyl acetate copolymer-based composites and the applicability of different conductivity models. *Carbon*. 2011; **49** (4), 1349-1361.

Soldano C, Mahmood A, Dujardin E. Production, properties and potential of graphene. *Carbon*. 2010; **48** (8), 2127-2150.

Solin SA. Clays and clay intercalation compounds:Properties and physical phenomena. *Annual Review of Materials Science*. 1997; **27** (1), 89-115.

Song C. Fuel processing for low-temperature and high-temperature fuel cells: Challenges, and opportunities for sustainable development in the 21st century. *Catalysis Today*. 2002; **77** (1-2), 17-49.

Song L, Guo J, Zhamu A, Jang ZB. Highly conductive nano-scaled graphene plate nanocomposites. USA2009.

Spendelow J and Jacos M. Fuel cell transportation cost analysis, preliminary results. http://www.hydrogen.energy.gov/pdfs/12020_fuel_cell_system_cost_2012.pdf: U.S. DOE hydrogen and fuel cells program annual merit review and peer evaluation; 2012.

Stankovich S, Dikin DA, Dommett GHB, Kohlhaas KM, Zimney EJ, Stach EA, Piner RD, Nguyen ST, Ruoff RS. Graphene-based composite materials. *Nature*. 2006; **442** (7100), 282-286.

Strasser P, Koh S, Anniyev T, Greeley J, More K, Yu C, Liu Z, Kaya S, et al.,. Lattice-strain control of the activity in dealloyed core-shell fuel cell catalysts. *Nat Chem*. 2010; **2** (6), 454-460.

Subhramannia M and Pillai VK. Shape-dependent electrocatalytic activity of platinum nanostructures. *Journal of Materials Chemistry*. 2008; **18** (48), 5858-5870.

Suherman H, Sulong AB, Sahari J. Effect of the compression molding parameters on the in-plane and through-plane conductivity of carbon nanotubes/graphite/epoxy nanocomposites as bipolar plate material for a polymer electrolyte membrane fuel cell. *Ceramics International*. 2013; **39** (2), 1277-1284.

Sun Y, Wu Q, Shi G. Graphene based new energy materials. *Energy & Environmental Science*. 2011; **4** (4), 1113-1132.

Taherian R, Golikand AN, Hadianfard MJ. The effect of mold pressing pressure and composition on properties of nanocomposite bipolar plate for proton exchange membrane fuel cell. *Materials & Design*. 2011; **32** (7), 3883-3892.

Taherian R, Golikand AN, Hadianfard MJ. Preparation and properties of a phenolic/graphite nanocomposite bipolar plate for proton exchange membrane fuel cell. *ECS Journal of Solid State Science and Technology*. 2012; **1** (6), M39-M46.

Tan C, Huang X, Zhang H. Synthesis and applications of graphene-based noble metal nanostructures. *Materials Today*. 2013; **16** (1-2), 29-36.

Tawfik H, Hung Y, Mahajan D. Metal bipolar plates for PEM fuel cell—a review. *Journal of Power Sources*. 2007; **163** (2), 755-767.

Teliska M, Murthi VS, Mukerjee S, Ramaker DE. Correlation of water activation, surface properties, and oxygen reduction reactivity of supported Pt-M/C bimetallic electrocatalysts using XAS. *Journal of The Electrochemical Society*. 2005; **152** (11), A2159-A2169.

Teng C-C, Ma C-CM, Lu C-H, Yang S-Y, Lee S-H, Hsiao M-C, Yen M-Y, Chiou K-C, Lee T-M. Thermal conductivity and structure of non-covalent functionalized graphene/epoxy composites. *Carbon*. 2011; **49** (15), 5107-5116.

Thepkaew J, Therdthianwong A, Therdthianwong S. Key parameters of active layers affecting proton exchange membrane (PEM) fuel cell performance. *Energy*. 2008; **33** (12), 1794-1800.

Tjong SC. Polymer nanocomposite bipolar plates reinforced with carbon nanotubes and graphite nanosheets. *Energy & Environmental Science*. 2011; **4** (3), 605-626.

Toyota. 2009. Toyota advanced fuel cell hybrid vehicle completes government field evaluation.

Ubeda D, Pinar FJ, Canizares P, Rodrigo MA, Lobato J. An easy parameter estimation procedure for modeling a HT-PEMFC. *International Journal of Hydrogen Energy*. 2012; **37** (15), 11308-11320.

US-DoE. 2013. Fuel cell technologies office:The high temperature membrane working group. (http://www1.eere.energy.gov/hydrogenandfuelcells/htmwg.html), Access on September 2013.

Vallés C, Drummond C, Saadaoui H, Furtado CA, He M, Roubeau O, Ortolani L, Monthioux M, Pénicaud A. Solutions of negatively charged graphene sheets and ribbons. *Journal of the American Chemical Society*. 2008; **130** (47), 15802-15804.

Verma A and Scott K. Development of high-temperature PEMFC based on heteropolyacids and polybenzimidazole. *Journal of Solid State Electrochemistry*. 2010; **14** (2), 213-219.

Vinayan BP, Jafri RI, Nagar R, Rajalakshmi N, Sethupathi K, Ramaprabhu S. Catalytic activity of platinum-cobalt alloy nanoparticles decorated functionalized multiwalled carbon nanotubes for oxygen reduction reaction in PEMFC. *International Journal of Hydrogen Energy*. 2012; **37** (1), 412-421.

Wang H, Brady MP, Teeter G, Turner JA. Thermally nitrided stainless steels for polymer electrolyte membrane fuel cell bipolar plates: Part 1: Model Ni-50Cr and austenitic 349™ alloys. *Journal of Power Sources*. 2004; **138** (1-2), 86-93.

Wang H and Turner JA. Reviewing metallic PEMFC bipolar plates. *Fuel Cells*. 2010; **10** (4), 510-519.

Wang M-x, Xu F, Liu Q, Sun H-f, Cheng R-h, He H, Stach EA, Xie J. Enhancing the catalytic performance of Pt/C catalysts using steam-etched carbon blacks as a catalyst support. *Carbon*. 2011; **49** (1), 256-265.

Wang S, Chen Z-H, Ma W-J, Ma Q-S. Influence of heat treatment on physical-chemical properties of pan-based carbon fiber. *Ceramics International*. 2006; **32** (3), 291-295.

Wang S, Zhang L, Xia Z, Roy A, Chang DW, Baek J-B, Dai L. Bcn graphene as efficient metal-free electrocatalyst for the oxygen reduction reaction. *Angewandte Chemie International Edition*. 2012; **51** (17), 4209-4212.

Wolf H and Willert-Porada M. Electrically conductive LCP-carbon composite with low carbon content for bipolar plate application in polymer electrolyte membrane fuel cell. *Journal of Power Sources*. 2006; **153** (1), 41-46.

Wu B, Fu Y, Xu J, Lin G, Hou M. Chromium nitride films on stainless steel as bipolar plate for proton exchange membrane fuel cell. *Journal of Power Sources*. 2009; **194** (2), 976-980.

Wu HH and Chu PP. Degradation kinetics of functionalized novolac resins. *Polymer Degradation and Stability*. 2010; **95** (9), 849-1855. .

Wu M and Shaw LL. A novel concept of carbon-filled polymer blends for applications in PEM fuel cell bipolar plates. *International Journal of Hydrogen Energy*. 2005; **30** (4), 373-380.

Xin Y, Liu J-g, Zhou Y, Liu W, Gao J, Xie Y, Yin Y, Zou Z. Preparation and characterization of Pt supported on graphene with enhanced electrocatalytic activity in fuel cell. *Journal of Power Sources*. 2011; **196** (3), 1012-1018.

Xing Y. Synthesis and electrochemical characterization of uniformly-dispersed high loading Pt nanoparticles on sonochemically-treated carbon nanotubes. *The Journal of Physical Chemistry B*. 2004; **108** (50), 19255-19259.

Xu JB, Zhao TS, Liang ZX. Carbon supported platinum-gold alloy catalyst for direct formic acid fuel cells. *Journal of Power Sources*. 2008a; **185** (2), 857-861.

Xu Y, Bai H, Lu G, Li C, Shi G. Flexible graphene films via the filtration of water-soluble noncovalent functionalized graphene sheets. *Journal of the American Chemical Society*. 2008b; **130** (18), 5856-5857.

Yang B, Brady MP, Wang H, Turner JA, More KL, Young DJ, Tortorelli PF, Payzant EA, Walker LR. Protective nitride formation on stainless steel alloys for proton exchange membrane fuel cell bipolar plates. *Journal of Power Sources*. 2007; **174** (1), 228-236.

Yang L, Jiang S, Zhao Y, Zhu L, Chen S, Wang X, Wu Q, Ma J, et al.,. Boron-doped carbon nanotubes as metal-free electrocatalysts for the oxygen reduction reaction. *Angewandte Chemie International Edition*. 2011a; **50** (31), 7132-7135.

Yang S-Y, Chang K-H, Lee Y-F, Ma C-CM, Hu C-C. Constructing a hierarchical graphene-carbon nanotube architecture for enhancing exposure of graphene and electrochemical activity of Pt nanoclusters. *Electrochemistry Communications*. 2010; **12** (9), 1206-1209.

Yang Z, Yao Z, Li G, Fang G, Nie H, Liu Z, Zhou X, Chen Xa, Huang S. Sulfur-doped graphene as an efficient metal-free cathode catalyst for oxygen reduction. *ACS Nano*. 2011b; **6** (1), 205-211.

Yano H, Inukai J, Uchida H, Watanabe M, Babu PK, Kobayashi T, Chung JH, Oldfield E, Wieckowski A. Particle-size effect of nanoscale platinum catalysts in oxygen reduction reaction: An electrochemical and 195Pt EC-NMR study. *Physical Chemistry Chemical Physics*. 2006; **8** (42), 4932-4939.

Yin Q, Li A-j, Wang W-q, Xia L-g, Wang Y-m. Study on the electrical and mechanical properties of phenol formaldehyde resin/graphite composite for bipolar plate. *Journal of Power Sources*. 2007; **165** (2), 717-721.

Yoo E, Okada T, Akita T, Kohyama M, Honma I, Nakamura J. Sub-nano-Pt cluster supported on graphene nanosheets for Co tolerant catalysts in polymer electrolyte fuel cells. *Journal of Power Sources*. 2011; **196** (1), 110-115.

Yoo E, Okata T, Akita T, Kohyama M, Nakamura J, Honma I. Enhanced electrocatalytic activity of Pt subnanoclusters on graphene nanosheet surface. *Nano Letters*. 2009; **9** (6), 2255-2259.

Yu S and Benicewicz BC. Synthesis and properties of functionalized polybenzimidazoles for high-temperature PEMFCs. *Macromolecules*. 2009; **42** (22), 8640-8648.

Zhang G, Wang Y, Wang X, Chen Y, Zhou Y, Tang Y, Lu L, Bao J, Lu T. Preparation of Pd-Au/C catalysts with different alloying degree and their electrocatalytic performance for formic acid oxidation. *Applied Catalysis B: Environmental*. 2011a; **102** (3-4), 614-619.

Zhang J, Lima FHB, Shao MH, Sasaki K, Wang JX, Hanson J, Adzic RR. Platinum monolayer on nonnoble metal−noble metal core−shell nanoparticle electrocatalysts for O_2 reduction. *The Journal of Physical Chemistry B*. 2005; **109** (48), 22701-22704.

Zhang J, Xie Z, Zhang J, Tang Y, Song C, Navessin T, Shi Z, Song D, et al.,. High temperature PEM fuel cells. *Journal of Power Sources*. 2006; **160** (2), 872-891.

Zhang L-S, Liang X-Q, Song W-G, Wu Z-Y. Identification of the nitrogen species on n-doped graphene layers and Pt/NG composite catalyst for direct methanol fuel cell. *Physical Chemistry Chemical Physics*. 2010; **12** (38), 12055-12059.

Zhang S, Shao Y, Yin G, Lin Y. Stabilization of platinum nanoparticle electrocatalysts for oxygen reduction using poly(diallyldimethylammonium chloride). *Journal of Materials Chemistry*. 2009; **19** (42), 7995-8001.

Zhang S, Shao Y, Yin G, Lin Y. Recent progress in nanostructured electrocatalysts for PEM fuel cells. *Journal of Materials Chemistry A*. 2013; **1** (15), 4631-4641.

Zhang Y, Gu Y-e, Lin S, Wei J, Wang Z, Wang C, Du Y, Ye W. One-step synthesis of PtPdAu ternary alloy nanoparticles on graphene with superior methanol electrooxidation activity. *Electrochimica Acta*. 2011b; **56** (24), 8746-8751.

Zhu Y, Murali S, Cai W, Li X, Suk JW, Potts JR, Ruoff RS. Graphene and graphene oxide: Synthesis, properties, and applications. *Advanced Materials*. 2010; **22** (35), 3906-3924.

Research Output

Papers published in peer reviewed international journals

1. **Avijit Ghosh,** Anil Verma. Carbon-polymer composite bipolar plate for high temperature PEMFC, Fuel Cells (2014), DOI: 10.1002/fuce.201300186.
2. **Avijit Ghosh**, Suddhasatwa Basu, Anil Verma. Graphene and functionalized graphene supported Pt electrocatalyst for PEMFC, Fuel Cells (2013)13, 352-361.
3. Biraj Kumar Kakati, **Avijit Ghosh**, Anil Verma. Efficient composite bipolar plate reinforced with carbon fiber and graphene for proton exchange membrane fuel cell, International Journal of Hydrogen Energy (2013) 38, 9362-9369.
4. **Avijit Ghosh**, Srinath A, Anil Verma. Synthesis and evaluation of graphene for PEMFC catalyst Support, International Journal of Innovative Research and Development (2012)7, 7-13.
5. Biraj Kumar Kakati, **Avijit Ghosh**, Anil Verma. Graphene reinforced carbon-polymer composite bipolar plate for PEMFC, ASME Proceedings, Fuel Cell (2011), 301-307.

Manuscript submitted

1. **Avijit Ghosh,** Anil Verma. Effect of carbon fiber length and graphene on carbon-polymer composite bipolar plate for PEMFC (Journal of Solid State Electrochemistry, Springer).
2. One invited book chapter on "Potential applications of graphene in polymer electrolyte membrane fuel cell", Authors by **Avijit Ghosh,** Anil Verma, is submitted to CRC Press Hand Book of Graphene Science.

Presentation in international conferences

1. **Avijit Ghosh**, Shaik Md. Ehtesham Hussain, Kshetrimaum Punicha, Anil Verma. in: **ICHNRSD 2014,** International Conference on Harnessing Natural Resources for Sustainable Development: Global trends, 29-31 January 2014, Cotton College, Guwahati, Assam.
2. **Avijit Ghosh,** Anil Verma. in: **NANOSMAT 2013**, 22-25 September 2013, Granada, Spain.
3. **Avijit Ghosh,** Anil Verma. in: **ISWESD 2012**, International seminar and workshop on energy, sustainability, and development, 10-12 October 2012, Sibsagar, Assam, India.
4. Biraj Kumar Kakati**, Avijit Ghosh,** Anil Verma. in: **ASME 2011**, 5th International Conference on Energy Sustainability & 9th Fuel Cell Science, Engineering and Technology Conference 2011**, 7**–10 August 2011,Washington DC, USA.
5. **Avijit Ghosh**, Biraj Kumar Kakati, Anil Verma. in: **ICANN 2010,** International conference on advance nanomaterial and nanotechnology, 8-10 December 2010, IIT Guwahati, India.

Presentation in National Conferences

1. **Avijit Ghosh,** Anil Verma. in: **GFCET 2013**, Green Fuels & Clean Energy Technologies, 15-16 December 2013, Institute of Engineers India, Guwahati, Assam.
2. **Avijit Ghosh**, Anil Verma. in: **REFLUX 2013**, Annual chemical engineering festival, 6-7 April 2013, IIT Guwahati, India.
3. **Avijit Ghosh**, Anil Verma. in: **REFLUX 2013**, Annual chemical engineering festival, 6-7 April 2013, IIT Guwahati, India.

4. **Avijit Ghosh**, Leela Manohar Aeshala, Anil Verma. in: **CHEMCON 2012**, 65th Annual Meeting of Indian Institute of Chemical Engineers, 27-30 December 2012, NIT Jalandhar, and India.
5. **Avijit Ghosh**, Biraj Kumar Kakati, Anil Verma. in: **CHEMCON 2011,** 64th Annual Meeting of Indian Institute of Chemical Engineers, , 27-29 December 2011, Bangalore, India.

Award

Received 2nd best poster presentation award in the **REFLUX 2013**, The Annual Technical Festival, 6-7 April 2013, IIT Guwahati, India.

About the Author

The author joined Sustainable Environergy Electrochemical Research Group (*SEERG*) in the Department of Chemical Engineering, Indian Institute of Technology Guwahati, Guwahati, Assam, India, as a full time Ph.D. scholar in January 2009. Before joining IIT Guwahati, the author completed M. Tech. in Chemical Engineering in 2008 from University of Calcutta, West Bengal, Kolkata, India.

The author published 5 research papers in peer reviewed high impact factor international journals. He has also presented several scientific and technical research papers in national and international seminars and symposiums. Moreover, the author is working as an Assistant Professor in Department of Chemical Engineering at Haldia Institute of Technology, West Bengal, India.